NANYANG TECHNOLOGICAL UNIVERSITY

HYBRID TiO_2 PHOTOCATALYTIC CERAMIC MEMBRANES: FABRICATION, CHARACTERIZATION AND PERFORMANCE EVALUATION

RONN GOEI

SCHOOL OF CIVIL AND ENVIRONMENTAL ENGINEERING

2014

HYBRID TiO_2 PHOTOCATALYTIC CERAMIC MEMBRANES: FABRICATION, CHARACTERIZATION AND PERFORMANCE EVALUATION

RONN GOEI

School of Civil and Environmental Engineering

A thesis submitted to the Nanyang Technological University
in partial fulfilment of the requirement for the degree of
Doctor of Philosophy

2014

[23] *Whatever you do, work heartily, as for the Lord and not for men,* [24] *knowing that from the Lord you will receive the inheritance as your reward. You are serving the Lord Christ.*
*(**Colossians 3:23-24, ESV**)*

ACKNOWLEDGEMENT

This thesis work was accomplished with the involvement of many people. First and foremost, I am truly grateful for my advisor Assoc. Prof. Lim Teik Thye that had inspired me to pursue this graduate studies under his guidance. His patience, sharp remarks, striving for excellence and constant encouragement was greatly appreciated. I'm grateful to NTU for providing me with a PhD research scholarship. I also thank the National Research Foundation (NRF), Singapore for the financial support through project EWI RFP 0802-11.

Secondly, I would like to thank my research group members who have been working together with me during my PhD study. Special thanks to Dr. Alvin Goh Kok Hui, Dr. Yap Pow Seng, Dr. Wang Penghua, and Loo Siew Leng for their willingness to share their knowledge, technical skills, and friendship with me. I would also like to thank members of Nanyang Environment and Water Research Institute (NEWRI) for their help.

Thirdly, I wish to sincerely thank all the staffs from the Environment Laboratory for their kind support and friendship during this graduate study. They are Mrs. Lim-Tay Chew Wang, Mr. Tan Han Kiang, Mr. Ong Chee Yung, Mrs. Maria Chong Ai Shing, Mrs. Phang-Tay Beng Choo, Ms. Pearlyn See Shen Yen, Mrs. Choy Mei Ling, Mr. Yong Fook Yew, Mr. Aidil bin Md. Idris, and Mrs. Koh-Tang Lai Sim.

Fourthly, I would like to thank my family: my mom, Mrs. Hasniati Goei, my aunt, Ms. Masnawaty Joe, my late grandparents, Mr. Goh Boon Kuan and Mrs. I Joe Kam, and my dear brother, Shimon. Thanks for your continuous prayer, encouragement, understanding, support and unconditional love during the highs and lows in this period. These have been a source of motivation to me to take every single step in this journey. I thank my wife-to-be Diana Koh for her moral support and encouragement that give me strength to progress.

Last but not least, I would like to thank the Lord for HIS unceasing providence and blessing, without which this thesis would not have been possible. SOLI DEO GLORIA.

SUMMARY

Titanium dioxide (TiO_2) photocatalyst has been used extensively in many environmentally-sustainable applications owing to its sterling characteristics such as its excellent chemical and thermal stability, low toxicity, low cost and high quantum yield. The most photoactive polymorph of TiO_2, anatase, would initiate photocatalytic degradation of many noxious environmental pollutants upon the generation of the electron-hole (e^--h^+) pairs under ultraviolet (UV) irradiation. The photocatalytic activity of TiO_2 is highly dependent on its physico-chemical characteristics such as crystal structure, crystallite size, surface area, pore volume, and porosity. The integration of TiO_2 photocatalysis and membrane separation process in a hybrid treatment system could be achieved either by a tandem operation of sequential photoreactor and membrane reactor or by operating a hybrid photocatalytic membrane reactor (PMR) in which the photocatalyst was anchored onto the membrane support. The PMR system allows simultaneous photocatalytic degradation and membrane separation of the pollutants in the feed water without the need of catalyst recovery at the end of each treatment process. This study aims to fabricate a hybrid TiO_2 photocatalytic membrane to be used in the PMR treatment system. Thin layers of TiO_2 photocatalyst were coated onto the macroporous alumina membrane support to obtain a dual-functional membrane that exhibits high water permeability, good photocatalytic degradation and good membrane separation performances.

In the first part of this study, Pluronic P-123, a tri-block copolymer, was used as the structure directing agent (SDA) in the preparation of TiO_2 sols via acid-catalyzed sol-gel method. The mesoporosity of the resulting TiO_2 layer was formed by the spontaneous self-assembly of the SDA. The SDA was subsequently removed during the calcination process leaving behind a porous architecture of mesoporous TiO_2 layer. Generally, an increase in the amount of SDA added during the preparation of the TiO_2 sol would result in TiO_2 layer with higher overall surface area, larger porosity and pore sizes. A hierarchically porous hybrid photocatalytic membrane was fabricated via layer-by-layer coating of different TiO_2 layers formed with sols of varying SDA contents onto the macroporous alumina ceramic membrane support, starting from the TiO_2 layer of largest porosity and pore size on the support-TiO_2 interface followed by subsequent TiO_2 layers of decreasing porosity and pore size. Different hierarchical architectures of the P-123-based TiO_2 hybrid photocatalytic ceramic membranes were fabricated to obtain the optimum membrane performance. Various characterization techniques were employed to elucidate the physico-chemical and morphological characteristics of the resulting TiO_2 layer. The performance of the membrane was evaluated both in the batch photoreactor and continuous flow PMR operated in the dead-end filtration mode. All membranes exhibited a photo-induced super-hydrophilicity which was important for the photocatalytic degradation of the target pollutant. The membrane (Plu D) that consists of 3 sub-layers of P-123-10wt% TiO_2, 2 sub-layers of P-123-5wt% TiO_2, and a thin P-123-2wt% TiO_2 top layer exhibited the optimum membrane performance. The result suggested that the performance of the TiO_2 membrane could be optimized by tailoring the hierarchical architecture of the membrane.

In the second part of this study, various types of SDAs (i.e. Pluronic P-123, Triton X-100, Tween 20 and Tween 80) were used to prepare different TiO_2 sols. Four specimens of the TiO_2 photocatalytic membranes were prepared by multilayer coating of different TiO_2 sols prepared with single SDA. Two of the membrane specimens were prepared by coating TiO_2 sub-layers prepared with different SDAs. The TiO_2 sols prepared using different SDAs exhibited a good compatibility between the sub-layers, allowing flexibility of fabricating the

TiO_2 membrane that exhibited favorable operating parameters, i.e., high permeability, good photocatalytic performances or good membrane retention.

Finally, different types of Ag-decorated TiO_2 (Ag-TiO_2) membranes were fabricated. The incorporation of Ag nanoparticles (Ag NPs) into the TiO_2 matrix enhanced the photocatalytic activity of TiO_2 and added an additional anti-bacterial functionality. The porous characteristics of the resulting Ag-TiO_2 layer could be fine-tuned by altering the amount of Ag and/or P-123 added into the sols. The Ag-TiO_2 membrane displayed a good chemical stability, leaching out 9.5 μg L^{-1} of Ag after 6 h operation in the PMR and 27 μg L^{-1} of Ag after 168 h of immersion in deionized (DI) water. The anti-bacterial property of the Ag-TiO_2 membrane was evaluated through the diffusion inhibition zone test and experiments using both batch reactor and PMR. In the batch reactor operated in dark, the membrane was able to remove a minimum of 5-logs of Escherichia *coli* (E. *coli*), a common water-borne pathogen. The membrane with the highest amount of incorporated Ag was able to remove close to 7-logs of E. *coli* when operated in the PMR.

The integration of the TiO_2 heterogeneous photocatalysis and membrane process in the membrane photoreactor offers simultaneous photodegradation and membrane separation, simpler system configuration with less mechanical and hydraulic fittings, and smaller overall footprint. The hierarchically porous TiO_2 photocatalytic membrane shows a great potential for use in water and wastewater treatment owing to its anti-fouling capability, high-flux performance, good photocatalytic activity, good anti-bacterial activity and reusability.

TABLE OF CONTENT

LIST OF TABLES

LIST OF FIGURES

LIST OF SYMBOLS AND ABBREVIATIONS

Ads-MR	Adsorptive-membrane retention
Ag NPs	Silver nanoparticles
Ag-TiO_2	Silver-decorated titanium dioxide
AOPs	Advanced oxidation processes
BET	Brunauer-Emmett-Teller
BJH	Barrett-Joyner-Halenda
CB	Conduction band
CMC	Critical micelle concentration
CS	Crystallite size
DI H_2O	Deionized water
DRS	Diffuse reflectance spectra
EDX	Energy dispersive x-rays
E_g	Band-gap energy
EtOH	Ethanol
FESEM	Field emission scanning electron microscopy
FTIR	Fourier transform infrared
FWHM	Full width at half maximum
HLB	Hydrophile-lipophile balance
HAP	hydroxyapatite
$h\nu$	photon energy
HPC	Hydroxypropyl cellulose
HRTEM	High-resolution transmission electron microscopy
ICP-MS	Inductively coupled plasma-mass spectroscopy
ICP-OES	Inductively coupled plasma-optical emission spectroscopy
IPA	Isopropanol

K_{ads}	Langmuir adsorption constant
k_{app}	Pseudo first-order rate constant
λ	Wavelength
MB	Methylene blue
MF	Microfiltration
MW	Molecular weight
MWCO	Molecular weight cut-off
NF	Nanofiltration
NHE	Normal hydrogen electrode
NOM	Natural organic matter
P25	Degussa/Evonik P25 (TiO_2)
PCA	Photocatalytic activity
PCD	Photocatalytic degradation
PCO	Photocatalytic oxidation
PEG	Polyethylene glycol
PL	Photoluminescence
P-123	Pluronic P-123
PMR	Photocatalytic membrane reactor
PSH	Photo-induced super-hydrophilicity
PVA	Polyvinyl alcohol
PWP	Pure water permeability
RhB	Rhodamine B
RO	Reverse osmosis
ROS	Reactive oxygen species
rpm	Rotation per minute
SAED	Selected area electron diffraction
SDA	Structure directing agent
T20	Tween 20

T80	Tween 80
TGA	Thermogravimetric analysis
TMP	Trans-membrane pressure
TOC	Total organic carbon
TTIP	Titanium tetraisopropoxide
UF	Ultrafiltration
UV	Ultraviolet
UV-LED	Ultraviolet light emitting diode
VB	Valence band
VCA	Video contact angle
Vis	Visible light
V_p	Pore volume
X100	Triton X-100
XPS	X-rays photoelectrons spectroscopy
XRD	X-rays diffraction
ρ	Density

LIST OF PUBLICATIONS

Parts of the findings presented in this thesis have been published in the following journal papers:

R. Goei, and T.-T. Lim. Ag-decorated TiO_2 photocatalytic membrane with hierarchical architecture: Photocatalytic and anti-bacterial activities. *Water Research*. 59 (2014) 207-218.

R. Goei, and T.-T. Lim. Asymmetric TiO_2 hybrid photocatalytic ceramic membrane with porosity gradient: Effect of structure directing agent on the resulting membranes architecture and performances. *Ceramics International*. 40 (2014) 6747-6757.

R. Goei, Z. Dong, T. -T. Lim, High-permeability pluronic-based TiO_2 hybrid photocatalytic membrane with hierarchical porosity: Fabrication, characterizations and performances. *Chemical Engineering Journal*. 228 (2013) 1030-1039.

Co-authorship in others' work:

D. Hou, **R. Goei**, X. Wang, P. Wang, T. -T. Lim, Preparation of carbon-sensitized and Fe-Er codoped TiO_2 with response surface methodology for bisphenol A photocatalytic degradation under visible-light irradiation. *Applied Catalysis B: Environmental*. 126 (2012) 121-133.

T. -T. Lim, K. H. Goh, **R. Goei**, Z. Dong, Mechanistic and thermodynamic studies of oxyanion sorption by various synthetic Mg/Al layered double hydroxides. *Water Science & Technology*. 59 (2009) 1011-1017.

CHAPTER 1 INTRODUCTION

1.1 Background

Water shortage is one of the major issues faced both by the developed as well as the developing countries. Clean water is needed for domestic usage, agricultural development, and industrial processes. Water reclamation has been considered as an alternative source of water and its potential usage in a land scarce country like Singapore has preceded over other traditional sources of water supply to overcome the problem of water shortage (PUB 2014). In order to fully realize the potential of water reclamation, the removal of different types of water-borne pollutants from domestic and industrial wastewater needs to be considered. A novel and robust wastewater treatment is required to overcome the problem caused by different emerging contaminants. Commonly used water treatment processes include chemical and physical treatment and biological treatment (Aksu 2005, Appels et al. 2008, Bailey et al. 1999, Chen 2004, Chong et al. 2010, Gogate and Pandit 2004, Haritash and Kaushik 2009, Malato et al. 2009). Some of these treatments would introduce various types of chemicals into the treatment system or produce some secondary pollutants, which maybe more toxic than the primary pollutants (Magdeburg et al. 2014, Malato et al. 2003, Xiao et al. 2014, Zong et al. 2013).

The use of membrane separation for water purification has gained much interest in the last decades. Microporous membrane was first used to pre-treat drinking water supply during World War II in Europe (Baker 2004). Industrial scale wastewater reclamation using reverse osmosis (RO) membrane was triggered by the work of Loeb and Sourirajan (1963) who fabricated a defect free, high flux anisotropic RO membrane. Since then, membrane separation has been used widely in water filtration, medical separation process, gas separation, chemical purification and many other applications. The advantages of membrane technology are low energy consumption, allowing continuous operation, easy to upscale and combine with other processes, good effluent quality and adjustable membrane properties (Baker 2004, Mulder 1996). However, inherent drawback of membrane fouling has led to higher operational and overall energy consumption in the treatment process (Gander et al. 2000, Le-Clech et al. 2006, Seidel and Elimelech 2002).

On the other hand, heterogeneous photocatalysis is deemed as an environmental friendly method to degrade many types of noxious and recalcitrant pollutants (Fox and Dulay 1993, Herrmann 1999, 2005). Heterogeneous photocatalysis is characterized by the formation of highly reactive radicals that are able to oxidize and degrade by mineralizing various recalcitrant contaminants (Herrmann 1999). These radicals include hydroxyl, superoxide and hydroperoxyl radicals. Characteristic features of the hydroxyl radical are highly reactive, powerful oxidant, easy to produce, ubiquitous in nature, possessing electrophilic property, non-selective reagent, relatively short lifespan, and its reaction with appropriate substrate molecules are kinetically controlled (Oppenländer 2003). Various advantages of heterogeneous photocatalysis over other advanced oxidation processes are zero/minimum usage and production of hazardous chemicals, and the opportunity to tap into abundant solar irradiation as the source of energy for the treatment process (Gaya and Abdullah 2008, Liu et al. 2006, Pirkanniemi and Sillanpää 2002, Rajeshwar et al. 2008). This is despite the possible limitation arising from the large scale applications.

The interest to couple photocatalytic processes and membrane separation has started with the introduction of photocatalytic oxidation treatment in tandem with a membrane separation treatment (Azrague et al. 2005, Molinari et al. 2004, Rivero et al. 2006). In this process configuration, the photocatalyst was introduced in the suspension prior to the membrane reactor. The main disadvantage of photocatalyst in suspension system is the need to recover the photocatalyst after the treatment process. The integration of photocatalytic oxidation and membrane separation in a single hybrid treatment system was advocated.

Polymeric membranes have been used extensively in water/wastewater treatment process. However the disadvantages of the polymeric membrane are its poor chemical, thermal and photo-stability under UV irradiation which limits its used for the hybrid photocatalytic membrane process (Artale et al. 2001). The need to fabricate membrane that is chemically stable and able to withstand UV irradiation had brought interest to the usage of ceramic membrane. Ozdemir et al. (2006) reported that inorganic membrane (ceramic and metal) are used extensively in the study that combine membrane and catalyst, most of which involve gas phase reaction at elevated temperature. Ceramic membrane has shown superior quality in terms of its heat stability, mechanical properties, biological stability, easy to clean, stability to UV light irradiation and chemical stability in different corrosive environments (Anderson et al. 1988, Buekenhoudt 2008). Other advantages are its high selectivity, longer life span and therefore long term cost competitiveness.

1.2 Motivation and knowledge gap

TiO_2 photocatalyst has been used extensively in many environmentally-sustainable applications owing to its sterling characteristics such as its excellent chemical and thermal stability, low toxicity, low cost and high quantum yield. The integration of the TiO_2 photocatalysis and membrane separation process in a hybrid treatment system could be achieved either by the operation of separate photo- and membrane reactor in succession or by the operation of hybrid photoreactor that carry out simultaneous photocatalytic degradation reaction and membrane separation (Lim et al. 2011). The former requires photocatalyst recovery from the treated water. The latter could suffer from possible mass transfer limitation and lower photocatalytic degradation efficiency due to its smaller number of active sites.

Immobilizing TiO_2 photocatalyst onto the membrane support could overcome the requirement of catalyst recovery for the separate reactor system. Besides, the immobilization of TiO_2 may overcome the issue of mass transfer limitation through the forced permeation of pollutants across the photocatalytic layers of the membrane activated by UV irradiation.

However, the synergistic coupling of the hybrid photocatalytic membrane has long standing operational issues that need to be addressed: low water permeability and adverse loss of permeation over a prolonged usage period caused by membrane fouling. In order to address the above-mentioned issues and to fabricate an effective hybrid photocatalytic membrane, the following strategies could be adopted:

- The membrane support should be chemically stable under UV irradiation.
- The membrane should be as thin as possible to minimize the intrinsic resistance of the membrane without compromising the integrity of the membrane during operation.
- The hybrid membrane should possess a hierarchically porous architecture which can improve the water permeation through the membrane. The hierarchical architecture can be achieved through coating of multiple TiO_2 sub-layers of different porous structures.
- The microstructural of the TiO_2 photocatalytic sub-layer must be controllable during the fabrication process. This would allow easy fine-tuning of fabrication parameters in order to achieve an optimum membrane performance.
- The coated photocatalytic TiO_2 sub-layers must be of uniform thickness with minimal presence of cracks, pinholes, or other defects.
- A flow-through membrane reactor should be setup to carry out simultaneous photocatalytic degradation reaction and membrane separation.

- The pollutant should be photocatalytically degraded when they travel through the hierarchically porous membrane.
- The membrane reactor setup should be able to treat various types of environmental noxious micropollutants.

Therefore, it is important to develop a TiO_2 hybrid photocatalytic membrane which allows effective removal of environmental pollutants through simultaneous degradation and separation process. The membrane system should operate in the high flux condition and allow re-utilization after appropriate cleaning. The flexibility to optimize the resulting membrane performance by controlling various membrane fabrication parameters is desirable.

1.3 Objectives and scopes

This research aimed to fabricate, characterize, and evaluate the performances of a hierarchically porous TiO_2 hybrid photocatalytic ceramic membrane. Different structure directing agents (SDAs) were employed to achieve the hierarchical architecture. At the later stage, this study also aimed to further enhance the functionality of the TiO_2 membrane by the addition of Ag in the TiO_2 photocatalytic layers. The Ag-decorated TiO_2 (Ag-TiO_2) membrane could effectively inactivate bacterial cells through different anti-bacterial actions. The performances of membranes are to be tested both in the batch photoreactor and the flow-through PMR.

The detailed scope of works for this study is as follows:

1. Designing and commissioning of photocatalytic membrane reactor (PMR)
    i. To design and commission a hybrid PMR system comprising an UV irradiation source, pumps, valves, and monitoring system;

    ii. To design and fabricate a membrane cell module to allow performance evaluation of the TiO_2 / Ag-TiO_2 membranes in the PMR;
    iii. To establish performance evaluation protocol using the PMR both for PCD and anti bacterial experiments.

2. Fabrication and performance evaluation of the hierarchically porous TiO_2 photocatalytic ceramic membrane
    i. To synthesize and characterize TiO_2 membrane layers prepared by sol-gel method using Pluronic P-123 (P-123) as the SDA;
    ii. To fabricate a hierarchically porous TiO_2 photocatalytic ceramic membrane via layer-by-layer coating of the different TiO_2 sub-layers;
    iii. To characterize photo-induced super-hydrophilicity (PSH) of the TiO_2 membrane;
    iv. To evaluate pure water permeability and membrane retention capability of the TiO_2 membrane;
    v. To evaluate photocatalytic degradation (PCD) performance of the TiO_2 membrane both in the batch photoreactor and PMR;
    vi. To evaluate reusability potential of the TiO_2 membrane.
3. Fabrication and performance evaluation of various hierarchically porous TiO_2 photocatalytic ceramic membranes which were prepared using different types of SDAs
    i. To synthesize and characterize TiO_2 membrane layers prepared by sol-gel method using different types of SDAs;

ii. To fabricate different types of hierarchically porous TiO_2 photocatalytic ceramic membranes with the photocatalytic TiO_2 sub-layers prepared using different SDAs;

iii. To evaluate the PCD performance of the composite membranes both in the batch photoreactor and PMR;

iv. To evaluate the reusability potential of the composite membrane.

4. Fabrication and performance evaluation of Ag-TiO_2 membrane
    i. To prepare various types of Ag-TiO_2 sols;
    ii. To fabricate different types of the Ag-TiO_2 membranes;
    iii. To evaluate the PCD performance of the Ag-TiO_2 membranes in the PMR;
    iv. To quantify the amount of total-Ag leaching from the Ag-TiO_2 membranes;
    v. To evaluate the diffusion inhibition zone of the Ag-TiO_2 membranes;
    vi. To evaluate the anti-bacterial performance of the Ag-TiO_2 membranes both in the batch reactor and PMR based on Escherichia *coli* (E. *coli*) inactivation.

1.4 The organization of Thesis

This thesis comprises seven chapters. Chapter 1 presents the background, motivation, knowledge gap, objectives, scope of works of this study and the organization of this thesis. Chapter 2 provides a review of the fundamentals of heterogeneous photocatalysis, the usage of TiO_2 as efficient photocatalyst, as well as brief introduction to the ceramic membrane and its usage as the support in a hybrid treatment system utilizing TiO_2 as the photocatalysis. Chapter 2 also discusses the recent findings in the research area of the TiO_2 hybrid photocatalytic ceramic membrane. Chapter 3 describes the materials and methods used in this study, including the experimental procedures adopted to fabricate, characterize and evaluate the performance of the TiO_2 hybrid photocatalytic ceramic membrane. Chapter 4 presents the synthesis and characterization of high permeability TiO_2 hybrid photocatalytic ceramic membrane that possesses a hierarchical porous architecture. Chapter 5 presents the studies on the effect of different SDAs in tailoring the resulting performance of TiO_2 hybrid photocatalytic ceramic membrane. Chapter 6 elucidates the facile preparations of Ag-TiO_2 hybrid photocatalytic ceramic membrane and their physico-chemical characteristics, pollutant removal capabilities and the anti-bacterial functionality of the Ag-TiO_2 membrane against E. *coli*. Chapter 7 presents a summary of important conclusions derived from this study and also several recommendations for the future work.

CHAPTER 2 LITERATURE REVIEW

2.1 Fundamental of heterogeneous photocatalysis

Heterogeneous photocatalysis is a subset of advanced oxidation processes (AOPs) in which the catalyst used and the reactants are of different phases. Heterogeneous photocatalysis could be carried out either in the aqueous solution, pure organic liquid phase, or in the gas phase. Fujishima and Honda (1972) through their pioneering discovery of water splitting in the irradiated TiO_2 electrode without any externally applied voltage, has triggered a worldwide intensive researches on the heterogeneous photocatalysis. The detailed studies of heterogeneous photocatalysis have been widely discussed in the literature (Carp et al. 2004, Fujishima and Zhang 2006, Herrmann 1999, 2005, Hoffmann et al. 1995, Linsebigler et al. 1995, Ollis and Al-Ekabi 1993). Photocatalytic degradation (PCD) reaction of pollutant in water consists of 5 major sequential steps (Herrmann 1999): (1) transfer of reactants from the bulk fluid phase to the surface of the catalyst, (2) adsorption of the reactants, (3) reaction in the adsorbed phase, (4) desorption of the products, and lastly (5) removal of the products from the interface region.

PCD of organic pollutants, microorganisms and other recalcitrant environmental pollutants was caused by the attack of the non-selective radicals generated on the surface of the photocatalyst via a photonic activation. The main advantage of the PCD reaction is the possibility of the complete mineralization of the pollutants resulting in an efficient treatment process with minimal handling of the secondary pollutants. Furthermore, PCD process can be carried out in a very mild operating temperature and pressure condition. Complete degradation occurred when all chemical constituents of the pollutant are mineralized into its inorganic forms i.e. carbon to carbon dioxide (CO_2), hydrogen to water (H_2O), nitrogen to nitrate (NO_3^-), halogen to halide ions (X^-), sulfur to sulfates (SO_4^{2-}), and phosphorus to phosphate (PO_4^{3-}) (Carp et al. 2004). PCD reaction of an organic compound can be generalized as follows (Hoffmann et al. 1995):

$$C_xH_yX_z + \left(x + \frac{y-z}{4}\right) O_2 \xrightarrow{hv} xCO_2 + zH^+ + zX^- + \left(\frac{y-z}{2}\right) H_2O \tag{2.1}$$

Characteristics of a good photocatalyst are high photo-reactivity, efficient utilization of visible or near UV irradiation, biologically and chemically inert, good photo-stability, low toxicity, and low production cost (Gaya and Abdullah 2008, Vinod and Anirudhan 2002). Semiconductor materials possess a unique electronic structure which consists of valence band (VB) and conduction band (CB) separated by an energy gap known as band gap. This unique characteristic allowed effective utilization of photonic energy to produce the reactive non-selective agents for PCD reaction.

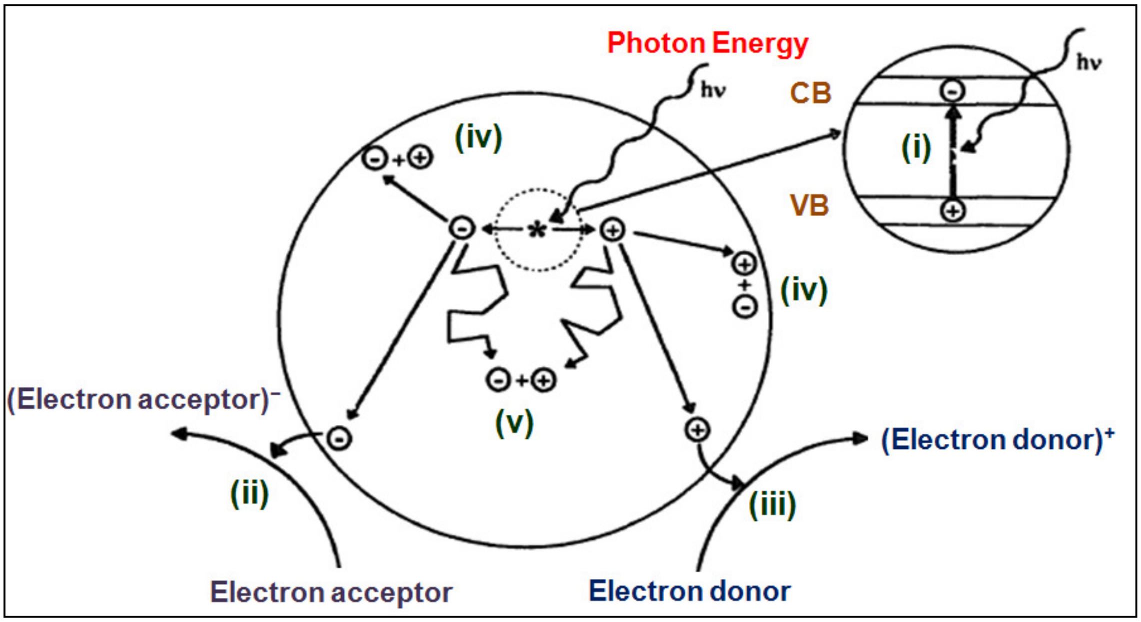

Figure 2.1 Schematic of the PCD mechanism: (i) generation of charge carriers, (ii) reduction reaction involving photo-generated electrons, (iii) oxidation reaction involving photo-generated holes, (iv) recombination of charge carriers at the surface of photocatalyst, and (v) recombination of charge carriers in the bulk (modified from Mills and Le Hunte (1997)).

A graphical illustration of the photocatalytic processes in the semiconductor materials is presented in Fig 2.1. The photocatalytic process starts with the absorption of photonic energy that is equal or greater than the prescribed intrinsic band gap energy of the semiconductor materials. The absorbed energy is utilized to excite a photo-generated electron (e^{-}) overcoming the band gap energy to the CB, leaving behind a photo-generated hole (h^{+}) in its VB (Eq. 2.2). A reduction reaction (Eq. 2.3) between the e^{-} and electron acceptors (e.g. dissolved O_2) produces superoxide radicals ($\bullet O_2^-$). On the other hand, an oxidation reaction (Eg. 2.4) occurred between h^{+} with electron donors (e.g. adsorbed H_2O or hydroxide ions (OH–)) produces hydroxyl radicals ($\bullet OH$). These radicals are the non-selective reagents that would react and mineralize the target pollutants.

$$Semiconductor + hv \rightarrow e^- + h^+ \tag{2.2}$$

$$e^- + O_2 \rightarrow \bullet O_2^- \tag{2.3}$$

$$h^+ + H_2O \rightarrow \bullet OH + H^+ \tag{2.4}$$

The $\bullet O_2^-$ would trigger the formation of other chemical species (Eq. 2.5 - 2.8) in water such as hydroperoxyl radicals ($\bullet OOH$), hydrogen peroxide (H_2O_2), singlet oxygen species ($^1O_2$) and eventually form the $\bullet OH$. The hydroperoxyl radicals would further prolong the life time of h^{+} by acting as an electron scavenger (Gaya and Abdullah 2008). The formation of $\bullet OH$ is essential to ensure non-selective oxidation of the target pollutants. The $\bullet OH$ radical possesses a very high standard redox potential of +2.8 V vs NHE (normal hydrogen electrode), second only to fluorine (of +3.03 V vs NHE) (Egerton and Christensen 2004). All the reactive oxygen species (ROS) generated (Eq. 2.5 – 2.8) holds a significant role in the PCD of the target pollutants depending on the exact experimental condition (Fujishima and Zhang 2006).

In the acidic condition:

$$\bullet O_2^- + H^+ \rightarrow \bullet OOH \tag{2.5}$$

$$\bullet OOH + e^- \rightarrow HO_2^- \tag{2.6}$$

$$\bullet OOH + H^+ \rightarrow H_2O_2 \tag{2.7}$$

$$H_2O_2 + e^- + H^+ \rightarrow \bullet OH + H_2O \tag{2.8}$$

Besides the above mentioned mechanisms, the photogenerated e^--h^+ pairs could recombine either at the surface of the photocatalyst or in the bulk. The recombination steps could hinder the efficiency of the photocatalytic process (Herrmann 1999). Additionally, the charge carriers could be trapped in the meta-stable surface state of the dopant element in the case of metal/non-metal decorated photocatalyst (Hoffmann et al. 1995).

The general scheme of PCD reaction can be classified into 4 fundamental processes: generation of the charge carriers, trapping of the charge carriers, recombination process, and the interfacial charge transfer. The characteristic timescales for each fundamental process are delineated in Table 2.1. The efficiency of PCD reaction is limited by the recombination of the photogenerated e^--h^+ pairs prior to the important activation of the superoxide species (Gerischer and Heller 1991). The recombination of e^--h^+ pairs occur rapidly with the timescale in the order of nanoseconds (Rothenberger et al. 1985). It would result in overall lower quantum efficiency. It is generally accepted that the target pollutant undergo oxidation reaction by the surface-bound $\bullet OH$, although a direct oxidation via direct h^+ transfer is also plausible (Turchi and Ollis 1989). Thus, it is vital that the target pollutants are in the vicinity of the photocatalyst surface and the electron donor or acceptor are presence sufficiently in the aqueous reactor for the generation of $\bullet OH$ to ensure effective PCD reaction with high quantum efficiency (Jing et al. 2006).

Table 2.1 Fundamental processes of heterogeneous photocatalysis and its characteristic timescale (Hoffmann et al. 1995, Mills and Le Hunte 1997)

Fundamental Processes	Characteristic Timescale	
Charge-carrier Generation		
$TiO_2 + hv \rightarrow e^- + h^+$	fs (very fast)	(2.9)
Charge-carrier Trapping		
$h^+ + >Ti^{IV}OH \rightarrow (>Ti^{IV}OH^{\bullet +})$	10 ns (fast)	(2.10)
$e^- + >Ti^{IV}OH \leftrightarrow (> Ti^{III}OH)$	100 ps (shallow trap, dynamic equilibrium)	(2.11a)
$e^- + >Ti^{IV} \rightarrow > Ti^{III}$	10 ns (deep trap, irreversible)	(2.11b)
Charge-carrier Recombination		
$e^- + (Ti^{IV}OH\bullet)^+ \rightarrow >Ti^{IV}OH$	100 ns (slow)	(2.12)
$h^+ + (> Ti^{III}OH) \rightarrow Ti^{IV}OH$	10 ns (fast)	(2.13)
Interfacial Charge Transfer		
$(Ti^{IV}OH\bullet)^+ + Red \rightarrow >Ti^{IV}OH + Red^{\bullet +}$	100 ns (slow)	(2.14)
$e_{trap}^- + Ox \rightarrow Ti^{IV}OH + Ox^{\bullet -}$	ms (very slow)	(2.15)

Note: **>TiOH** = primary hydrated surface functionality of TiO_2; **e^-** = conduction band electron; **h^+** = valence band hole; **e_{trap}^-** = trapped conduction band electron; **Red** = electron donor; **Ox** = electron acceptor; **($Ti^{IV}OH^{\bullet +}$)** = surface trapped valence band hole and (**> Ti^{III}OH**)= surface trapped conduction band electron

2.2 TiO_2-assisted heterogeneous photocatalysis

2.2.1 Semiconductor photocatalysis

Semiconductor materials with its unique electronic states are appraised as suitable candidates for a good photocatalyst. Unlike the continuum electronic state of metallic materials, semiconductor materials have an energy band gap. Band gap values signify the amount of energy to be supplied for photo excitation process to take place. The band-gap energy of some common semiconductor materials is summarized in Table 2.2.

The relation between band gap and energy of radiation required to excite the e^{-}-h^{+} pairs is governed by classical physics law (Eq. 2.16):

$$E = h\nu \tag{2.16}$$

$$\lambda = \frac{1237}{E_g} \tag{2.17}$$

where E is the photon energy, h is Planck's constant of 6.626×10^{-34} m^2 kg s^{-1}, and ν is the frequency of the electromagnetic wave oscillation contained in the incoming photon. Photon frequency can be further expanded as the ratio of speed of light with respect to the photon energy wavelength. The minimum wavelength (nm) of the photon required for the photo-generation of the e^{-} and h^{+} pairs for a given band-gap energy of the semiconductor material is delineated in Eq. 2.17.

Table 2.2 Band gap energy of various common semiconductor materials (summarized from Linsebigler et al.(1995), Vinod and Anirudhan (2002), Kabra et al. (2004), Gaya and Abdullah (2008), and Thiruvenkatachari et al. (2008))

Types	E_g (eV)	λ (nm)	Types	E_g (eV)	λ (nm)
CdS	2.30-2.50	538 - 495	SiC	3.00	412
CdSe	1.70	728	SnO_2	3.50-3.80	353 - 326
Cu_2O	3.90	317	$SrTiO_3$	2.40-3.20	515 - 387
Fe_2O_3	2.20-2.80	562 - 442	TiO_2 (Rutile)	3.00	412
α-Fe_2O_3	3.10-3.50	399 - 353	TiO_2 (Anatase)	3.20	387
GaAs	1.40	884	WO_3	2.80-3.40	442 - 364
GaP	2.25	550	WSe_2	1.20	1030
PbS	2.20	562	ZnO	3.20-3.40	387 - 364
PbSe	0.20-0.30	6200	ZnS	3.10-3.70	400 - 334
Si (metal)	1.10	1125	ZrO_3	5.00	25

From the Equation 2.17 and Table 2.2, it can be deduced that the range of electromagnetic spectrum that could be utilized for the photo-excitation process falls between 170 nm to 1000 nm. The range could be classified into different sub-bands of the electromagnetic spectrum i.e. vacuum UV, visible light (760-380 nm/ 1.63-3.26 eV), UVA (400-315 nm/ 3.10-3.94 eV), UVB (315-280 nm / 3.94-4.43 eV), and UVC (280-100 nm/ 4.43-12.4 eV). (Oppenländer 2003).

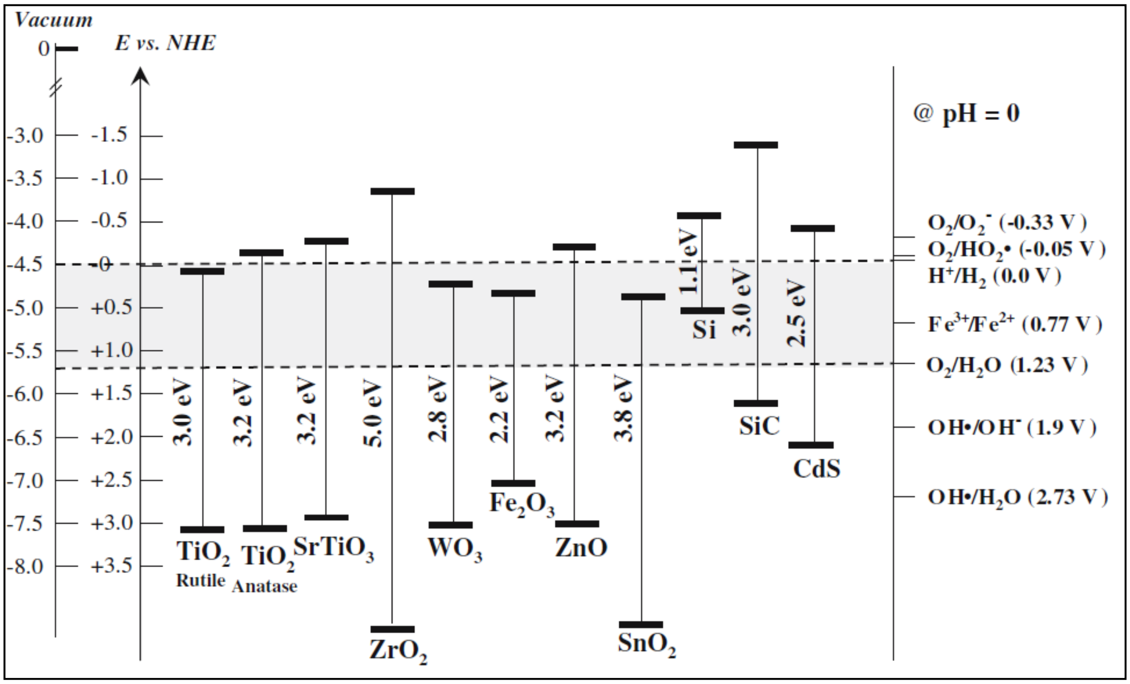

Figure 2.2 Energy level diagrams of various semiconductor materials with selected redox potential. The energy scales is referenced against vacuum and the normal hydrogen electrode (NHE) (taken from Choi et al.(2006a)).

Among the chalcogenides (metal oxide/selenide/sulfide) semiconductor, CdS, TiO_2 and ZnO have been found to exhibit high photocatalytic activity (Hoffmann et al. 1995, Klavarioti et al. 2009, Thiruvenkatachari et al. 2008) . However, not all semiconductor materials are suitable to be used as photocatalyst. ZnO and CdS have a low solubility in the aqueous media. ZnO in the aqueous system would produce $Zn(OH)_2$ on the ZnO surface that could inactivate the photocatalyst over a prolonged usage. CdS, similar to the majority of the metal sulfides, undergo the photoanodic corrosion. Furthermore, Cd is a very toxic metal, second only to mercury (Hg). α-Fe_2O_3 experiences photocathodic corrosion (Fox and Dulay 1993).

It has been proposed that the band-gap energy of the semiconductor photocatalyst must extend through the redox potential of $H_2O/{\bullet}OH$ and $O_2/HO_2{\bullet}$ couple to allow efficient generation of the reactive radicals. Energy level diagram of various semiconductor materials is shown in Fig 2.2. As can be observed from Fig. 2.2, not all semiconductor materials satisfy the band-gap span requirement (e.g. Fe_2O_3, SnO_2, rutile TiO_2, and WO_3).

TiO_2 has received much attention as an ideal photocatalyst due to its high oxidation potential of VB holes ($E_{vb} = + 2.7\ V_{NHE}$ at pH 7) (Choi 2006b). Besides, TiO_2 possesses high surface activity, good biocompatibility, high chemical stability, high photo-stability, low cost, and low toxicity (Chen et al. 2009, Habibi et al. 2007a, Thiruvenkatachari et al. 2008). The first attempt of using TiO_2 for the PCD application was by Frank and Bard for the decomposition of cyanide and sulfite (Frank and Bard 1977b, a). Since then, TiO_2 photocatalyst has been used extensively in many environmental applications.

Types of pollutants which could be effectively mineralized in the TiO_2 photocatalysis system are aliphatic compounds, aromatic compounds, detergents, dyes, polymers, pharmaceuticals, pesticides, and herbicides (Byrappa et al. 2000, Haque et al. 2006, Haque and Muneer 2007, Horikoshi et al. 2001, Lim et al. 2011, Molinari et al. 2006, Vinod and Anirudhan 2002). Table 2.3 summarizes different characterization techniques that can be used to monitor the extent of PCD reaction of various types of pollutants. These techniques can be combined with total organic carbon (TOC) measurement to determine the overall extent of mineralization of organic pollutants.

The PCD reaction can happen only if the molecules of target pollutant are adsorbed to the surface of the photocatalyst. The adsorption of the pollutant to the photocatalyst can be modeled by the Langmuir adsorption isotherm (Langmuir 1932) as follow:

$$\theta = \frac{K_{ads} C_{eq}}{1 + K_{ads} C_{eq}} \tag{2.18}$$

The adsorbed target pollutant would then be degraded following the Langmuir-Hinshelwood (L-H) model (Houas et al. 2001, Xu and Langford 2001) as follow:

$$r = k\theta = k\left(\frac{K_{ads} C_{eq}}{1 + K_{ads} C_{eq}}\right) \tag{2.19}$$

where θ = the fraction coverage of the photocatalyst surface by pollutant, C_{eq} = the concentration of the pollutant at equilibrium, K_{ads} = Langmuir adsorption constant, and k = reaction rate constant.

Table 2.3 Characterization tools for the determination of the extent of TiO_2-assisted PCD reaction

Techniques / instruments	**Type of molecules/target pollutants/intermediates studied**	**Selected references**
Chemical Oxygen Demand (COD)	Organic compounds	(Ghanem et al. 2014, Giri and Golder 2014, Wu et al. 1998, Yuan et al. 2014)
UV-visible spectrophotometry (UV/Vis)	Dyes (e.g. methylene blue, Rhodamine B, methyl orange, etc) and other organic compounds	(Choi et al. 2006b, Goei et al. 2013, Konstantinou and Albanis 2004)

Gas chromatography (GC) / Gas chromatography-mass spectrometry (GC-MS)	Gas-phase pollutants (e.g. acetaldehyde, formaldehyde) and PCD end product (CO_2)	(Jardim et al. 1997, Konstantinou and Albanis 2003, Sleiman et al. 2009, Stylidi et al. 2004, Zhao et al. 2008)
Gel filtration chromatography (GFC)	Molecular size distribution of NOM or other model pollutants and their intermediates with high MW (between 1 – 50 kDa)	(Amama et al. 2004, Syafei et al. 2008, Yu et al. 2009)
Ultra-filtration membrane fractionation	Molecular size of NOM or other pollutant with high MW (between 1 – 50 kDa)	(Syafei et al. 2008)
High performance liquid chromatography (HPLC)	Organic compounds	(Gao et al. 2010, Hou et al. 2012, Subagio et al. 2010, Zhao et al. 2008)
Specific ultraviolet absorbance (SUVA)	Fraction of unsaturated carbon bonds (degree of aromaticity) in the aromatic organic pollutant	(Abellán et al. 2007, Choo et al. 2008, Huang et al. 2008, Syafei et al. 2008, Yigit and Inan 2009)
Liquid chromatography-mass spectrometry (LC-MS/MS)	Organic compounds and its intermediates.	(Abellán et al. 2007, Antoniou et al. 2008, Calza et al. 2006, Konstantinou and Albanis 2003, Kouloumbos et al. 2003)
Excitation-emission matrix (EEM)	Changes in composition and reactivity of large organic compounds	(Bosco et al. 2006, Li and Sun 2014, Valencia et al. 2013, 2014)

The overall efficiency of the PCD of various organic pollutants was governed not only by inherent properties of the photocatalyst but also by operating parameters of the PCD experiment. The effect of different operating parameters such as light (energy) source, light intensity, photocatalyst dosage, concentration of target pollutants, operating pH, aqueous matrix species and various up-scaling parameters have been discussed in detail elsewhere

(Bhatkhande et al. 2002, 2003, Gaya and Abdullah 2008, Konstantinou and Albanis 2004, Sin et al. 2012).

2.2.2 TiO_2: structures, properties and syntheses.

TiO_2 exist either in its natural polymorphs (i.e. anatase, brookite, or rutile) or in its artificial polymorphs (i.e. TiO_2(B), TiO_2(H), TiO_2(R), etc) (Herrmann 1999). The properties of three different naturally-occurred TiO_2 polymorphs are summarized in Fig. 2.3.

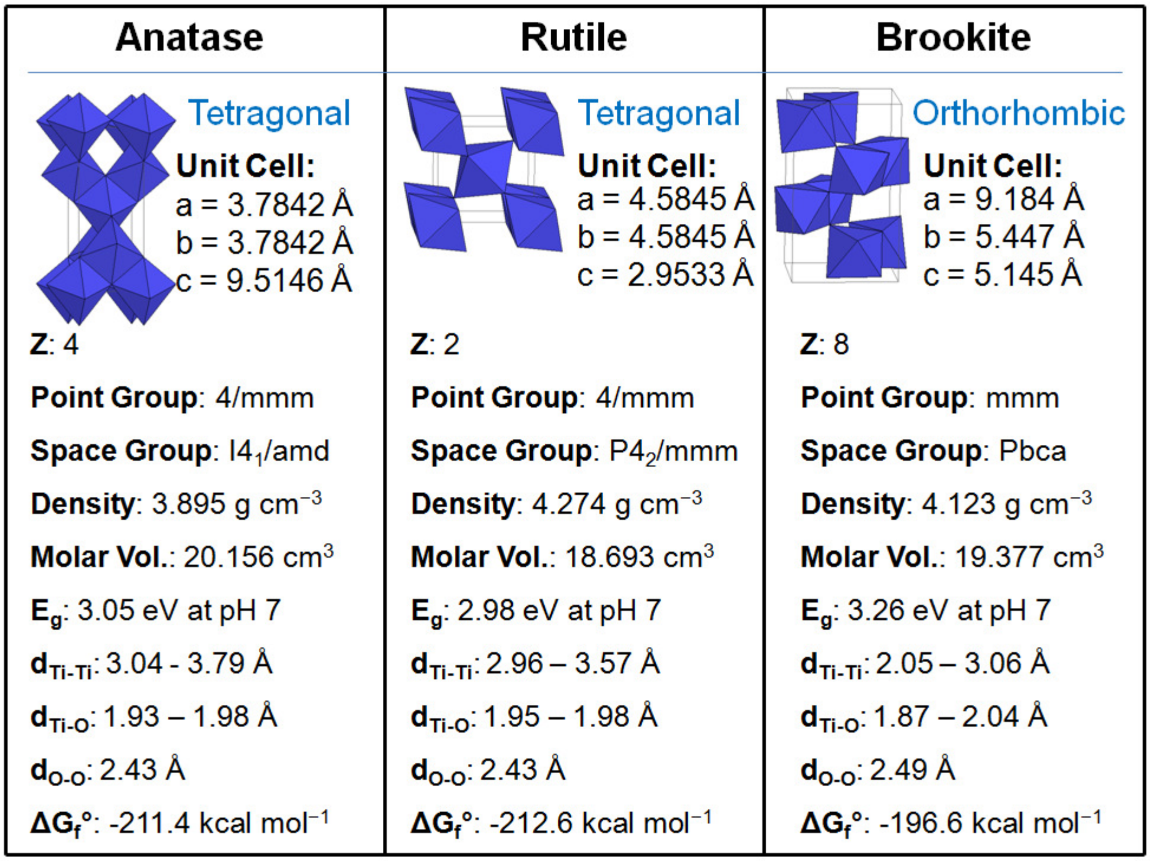

Anatase	**Rutile**	**Brookite**
Tetragonal	Tetragonal	Orthorhombic
Unit Cell: a = 3.7842 Å b = 3.7842 Å c = 9.5146 Å	**Unit Cell:** a = 4.5845 Å b = 4.5845 Å c = 2.9533 Å	**Unit Cell:** a = 9.184 Å b = 5.447 Å c = 5.145 Å
Z: 4	**Z**: 2	**Z**: 8
Point Group: 4/mmm	**Point Group**: 4/mmm	**Point Group**: mmm
Space Group: $I4_1/amd$	**Space Group**: $P4_2/mmm$	**Space Group**: Pbca
Density: 3.895 g cm^{-3}	**Density**: 4.274 g cm^{-3}	**Density**: 4.123 g cm^{-3}
Molar Vol.: 20.156 cm^3	**Molar Vol.**: 18.693 cm^3	**Molar Vol.**: 19.377 cm^3
E_g: 3.05 eV at pH 7	**E_g**: 2.98 eV at pH 7	**E_g**: 3.26 eV at pH 7
$d_{Ti\text{-}Ti}$: 3.04 - 3.79 Å	**$d_{Ti\text{-}Ti}$**: 2.96 – 3.57 Å	**$d_{Ti\text{-}Ti}$**: 2.05 – 3.06 Å
$d_{Ti\text{-}O}$: 1.93 – 1.98 Å	**$d_{Ti\text{-}O}$**: 1.95 – 1.98 Å	**$d_{Ti\text{-}O}$**: 1.87 – 2.04 Å
$d_{O\text{-}O}$: 2.43 Å	**$d_{O\text{-}O}$**: 2.43 Å	**$d_{O\text{-}O}$**: 2.49 Å
$\Delta G_f°$: -211.4 kcal mol^{-1}	**$\Delta G_f°$**: -212.6 kcal mol^{-1}	**$\Delta G_f°$**: -196.6 kcal mol^{-1}

Figure 2.3 Properties of different naturally-occurred TiO_2 polymorphs (summarized from Linsebigler et al. (1995), Di Paola et al. (2009), Park et al. (2009), and Smyth (2009)).

Anatase and rutile polymorphs of TiO_2 exist in the tetragonal structure, while brookite and TiO_2 (B) exist in the orthorhombic structure. The atoms in the anatase, brookite and rutile were in the [TiO_2^{6-}] intrinsic octahedral arrangement (Fig. 2.3). The Ti-Ti distance in the anatase is wider than those in the [TiO_2^{6-}] octahedral arrangement of rutile. The number of neighboring octahedrons that are in contact with the octahedral structure of anatase and rutile are 8 (4 sharing a corner and 4 sharing an edge) and 10 (8 sharing a corner and 2 sharing an edge) respectively. This would lead to a denser rutile structure. The dense structure of rutile is able to withstand a high temperature and pressure up to 60 kBar (Jamieson and Olinger 1968, Navrotsky et al. 1967).

Although anatase is thermodynamically less stable than rutile, the formation of anatase is much favored at lower temperature (< 600°C) (Herrmann 1999). The formation of TiO_2 crystals at a lower temperature would yield TiO_2 with a higher surface area and hence, a higher surface density of the active sites for effective adsorption and photocatalytic degradation reaction. Therefore, anatase was found to be the most photocatalytically active polymorph of TiO_2 (Gaya and Abdullah 2008, Schindler and Kunst 1990, Tanaka et al. 1993a). The high photocatalytic activity of anatase could be ascribed to its triangular atomic arrangement that allowed effective adsorption of pollutants (Di Valentin et al. 2007). Both anatase and brookite polymorph would be transformed to the rutile structure when subjected to a higher temperature (Linsebigler et al. 1995). The detailed review on the anatase to rutile transformation has been published elsewhere (Hanaor and Sorrell 2011). The differences in the electronic and optical responses of different TiO_2 polymorphs are discussed in detail elsewhere (Landmann et al. 2012). TiO_2 showed an amphoteric characteristic (i.e. its surface charge are pH dependent). The iso-electric point of TiO_2 is in between pH 5 and 7. At acidic condition (pH < 5), the surface charge of TiO_2 will be positive ($\equiv$Ti-OH_2^+); while in the alkaline condition (pH > 7), the surface charge will turn negative ($\equiv$Ti-OH^-) (Choi 2006a).

Surface defects of the TiO_2 crystals also play a critical role in the adsorption of reactive adsorbates (Nash 2008). For example, the presence of oxygen vacancy in the TiO_2 surface would allow the non-dissociative adsorption of O_2 molecules generating a superoxide radical upon reaction with the photogenerated electron. This phenomenon coupled with the high electron transfer rates from TiO_2 to the adsorbed molecule is responsible for the high photocatalytic activity of TiO_2.

TiO_2 could be prepared in different shapes and morphologies such as nanocrystals/nanodots, nanowires/nanorods (when TiO_2 was synthesized with templating agent), nanosheets, or nanofilms. Nano-sized TiO_2 demonstrates unique optical, electronic, mechanical, thermal, and structural properties which are size-, shape-, and microstructure-dependent. Different techniques to prepare TiO_2 are aerogel method, chemical vapor deposition, direct oxidation method, electro-deposition, hydrothermal method, microwave irradiation method, micelles/inverse-micelles method, physical vapor deposition, sol method, sol-gel method, solvothermal method, and sonochemical method (Chen and Mao 2007).

Sol-gel technique has notable advantages such as high purity, good homogeneity of the film microstructure, low temperature synthesis, controlled reaction condition, low-cost and simple technology, low processing temperature for film densification, controllable properties and versatility for coating on large surface area (Chen et al. 2009, Răileanu et al. 2009, Sharma et al. 2009). Besides, sol-gel method allows an uniform mixing, even at molecular level, of different precursors resulting in a homogeneous multi-components ceramic materials (Vankelecom et al. 2005). Besides TiO_2, sol-gel method has been used to prepare different types of ceramic materials such as silica (SiO_2), yttria (Y_2O_3), zirconia (ZrO_2), and many other composite ceramics (Van Gestel et al. 2010).

Sols is a stable dispersion of nanometer-sized colloidal particles in a liquid solution. Drying of the sol at the ambient pressure (thermal evaporation of the liquid) will cause shrinkage in the dispersion producing an intermediate xerogel phase. A final gel will be produced by the complete removal of the water/solvent at a higher temperature. The sol-gel preparation of TiO_2 could be divided into two major reaction steps i.e. hydrolysis and condensation (Eq 2.18 and 2.19).

Hydrolysis: $$Ti(OR)_4 + H_2O \rightarrow Ti(OR)_3OH + ROH \tag{2.18}$$

Condensation: $$Ti(OR)_4 + Ti(OR)_3OH \rightarrow (RO)_3TiOTi(OR)_3 + ROH \tag{2.19}$$

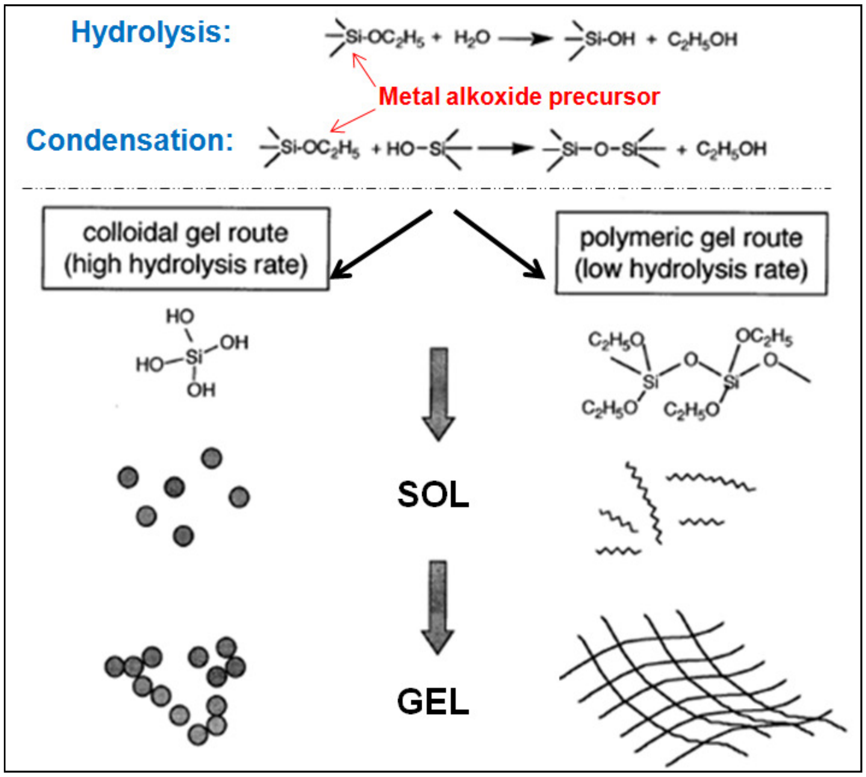

Figure 2.4 Colloidal and polymeric route of sol-gel synthesis using metal alkoxide as precursor (modified from Tsuru (2001)).

The formation of TiO_2 using sol-gel method could happen either through the particulate/colloidal sol route or a polymeric sol route (Anderson et al. 1988, Tsuru et al.

2001b). Fig. 2.4 illustrates sol-gel preparation routes. In the particulate sol, the hydrolysis reaction takes place in the condition of high water concentration followed by gelation of the titania network. The fast hydrolysis and condensation reaction would result in the formation of highly branched network. The size of primary colloidal particles is usually in the range of 5-15 nm. In the case of the polymeric sol, hydrolysis reaction occurrs in the solvent (i.e. low water content) to form a soluble intermediate product before the condensation reaction to form a linear inorganic polymeric network. Polymeric sol route is preferred for the fabrication of mesoporous TiO_2 thin film due to the formation of smaller size gel network at the end of the synthesis process. This will result in the formation of micropores. It was suggested that the size of individual nanoparticles were to be less than 10 nm for the formation of a well connected microporous structure (De Lange et al. 1995). The hydrolysis rate can also be slowed down by the addition of chelating agent (e.g. acetylacetone) or the selection of precursor with slower hydrolysis rate (Cot et al. 2000, Vankelecom et al. 2005).

Sol-gel technique allows a one-pot synthesis by combining different types of precursors and solvent to yield a desired gel network. Different types of titanium precursors such as titanium alkoxides or non-alkoxide titanium source could be used to prepare the TiO_2 sol (Chen and Mao 2007, Guillén-Santiago et al. 2010, Raut et al. 2009). Different of organic solvents have been incorporated in the preparation of TiO_2 sol including ethanol, benzyl alcohol, butanol, ethylene glycol, 2-propanol, and 1-methoxy-2-propanol (Beyers et al. 2005, Han et al. 2014, Hung et al. 2010, Jiang et al. 2003, Niederberger et al. 2002, Zhong et al. 2005).

The final appearance of titania sol is highly dependent on two parameters: the initial hydrolysis ratio ($r_w = [H_2O] / [Ti]$) and the inhibitor ratio ($r_a = [H^+] / [Ti]$). A higher initial hydrolysis ratio r_w would give rise to a larger particle size and surface area. The r_w ratio has to be kept below 2 to avoid early gelation of the sol. pH is an important parameter to control sol-gel process. A low pH is favorable for hydrolysis reaction (Sekulic et al. 2004).An optimum pH value of 2 is required to form a stable sol (Kermanpur et al. 2008). HCl (or other acids) could be incorporated in the sol preparation to control the condensation rate and to prevent fast gelation of the sol (Habibi et al. 2007a, Van Gestel et al. 2002). The final solid gel phase would be obtained upon the completion of polymerization reaction or due to the solvent vaporization.

Acetic-acid catalyzed sol-gel route was employed by Choi and coworkers (2006b) to prepare TiO_2 sol. In this route, the rate of hydrolysis was controlled by the slow release of H_2O via the esterification reaction between alcohol and acetic acid (Barboux-Doeuff and Sanchez 1994, Sanchez et al. 1988). Chelating agent such as acetylacetone could be added to retard the hydrolysis and condensation reaction (Habibi et al. 2007a, Habibi and Nasr-Esfahani 2007, Habibi et al. 2007b).

The properties of TiO_2 can be elucidated using a wide range of characterization tools. The important characterization techniques employed are summarized in Table 2.4.

Table 2.4 Characterization tools for TiO_2 materials

Technique / instrument	**Characteristic studied**	**Findings/characteristic peaks**
Atomic Force Microscope (AFM)	Surface morphology	The grain appear elongated along the direction of withdrawal of dip coating (Chrysicopoulou et al. 1998). TiO_2 appear as uniform and dense spherical grain (Sun et al. 2009). Three important parameters to characterize the morphology of thin film from AFM image are the maximum height (R_{max}), the average roughness value (R_a) and the root mean square roughness (R_{rms}) (Tsoukleris et al. 2007).

N_2 porosimetry analysis	Specific surface area and pore size distribution	Titania film shows good potential for composite membrane fabrication with low hydraulic resistance and effective organic retention (Choi et al. 2006a). N_2 adsorption at low relative pressure ($P/P_0 < 0.4$) is accounted for monolayer adsorption of N_2 on the pore walls. The sharp inflection at $0.4 < P/P_0 < 0.75$ is characteristic of capillary condensation within uniform pores. The sharpness of the step indicates the uniformity of the pore size distribution (Zhao et al. 2005).
Fourier transformed Infra Red Spectroscopy (FTIR)	Chemical bonding	–O–H stretching @ 3450 cm^{-1}; Ti–O–Ti network absorption @ 450-700 cm^{-1}; rutile @ 650 cm^{-1}; 1634, 1638, 2360, 2922 cm^{-1} due to stretching and bending of C=C, –C=O, –CH, and –CH_2 respectively (Wang et al. 2008). Ti(O–C) – stretching vibration @ 1100 cm^{-1} (Zhang et al. 2006).
Laser Light Scattering / dynamic light scattering	Colloidal diameter, particle size distribution.	Colloidal diameter could be controlled by temperature of aging process (Tsuru et al. 2001b).
Mastersizer	Average particle size	Average size titania nanoparticles cluster on the suspension was found to be 65 nm (Ding et al. 2006).
^{1}H / ^{13}C / ^{17}ONuclear magnetic resonance (NMR)	Chemical changes of Ti(IV) environment, chemical structure	Selected references (Almeida et al. 2014, Crepaldi et al. 2003, Sun et al. 2014a, Sun et al. 2014b, Wu et al. 1998)
Powder X-Ray Diffraction (XRD) with Rietveld Analysis	Crystal phase and composition	TiO_2 → ***Anatase*** [JCPDS 21-1272]: 25.28° (101), 48.05° (200), 37.80° (004), 53.89° (105), 55.06° (211), and 62.69° (204); *Brookite* [JCPDS 29-1360]: 25.34° (120), 30.81° (121), 25.69° (111), 48.01° (231), 55.23° (241); *Rutile* [JCPDS 21-1276]: 27.45° (110), 54.32° (211), 36.09° (101), 41.23° (111), 56.64° (220), 69.01° (301). Al_2O_3 → *Corundum* [JCPDS 10-0173]: 43.36° (113), 35.13° (104), 57.52° (116), 25.58° (012), 68.19° (300), 52.55° (024), 37.78° (110). Ag → [JCPDS 74-1828]: 38.4° (111),

		64.2° (220), and 77.4° (311).
Raman Spectroscopy	Structure of composites	Anatase: 143, 196, 395, 513, 519, and 638 cm^{-1} ; Rutile: 611 cm^{-1} (Bosc et al. 2003, Kment et al. 2010).
Rotary viscosimeter	Suspension viscosity and rheology	Viscosity of titania sol 5.45×10^{-3} Pa s = 5.45 cP (Ding et al. 2006)
Scanning Electron Microscopy (SEM) with Energy Dispersive X-Rays (EDX)	Surface morphology and elemental composition	Coating of TiO_2 thin film supported on different ceramic substrate could be observed.
Scanning Tunneling Microscopy (STM)	Surface morphology	The morphology of TiO_2 thin film could be observed by STM.
Transmission Electron Microscopy (TEM)	Film thickness and coating inside the membrane pores	Highly porous titania film with distinct pore structure with mean diameter 3-7 nm was observed (Choi et al. 2006a).
Thermo-gravimetric Analysis (TGA) with differential thermal analysis (DTA)	Thermal stability	Weight loss: (1) < 200°C is due to water evaporation and thermal decomposition of the remnant organic solvent, (2) 200-280°C is due to carbonization / combustion of organic compounds in the composite and (3) > 280°C is due to evaporation of physically absorbed water and further combustion of organic additives (Habibi et al. 2007a). DTA Analysis**:** endothermic: removal of water and alcohol. Exothermic: thermo-oxidative degradation of organics, crystallization process (Rǎileanu et al. 2009).
UV-Vis Diffuse Reflectance Spectrophotometer (UV-DRS)	UV-Vis light absorbance, bandgap and light utilization characteristic	E_g=3.23 eV (λ=385 nm) for anatase; E_g=3.34 eV (λ=372.5 nm) for titania catalyst (Choi et al. 2006a). Two main absorption bands at 233 and 304 nm assigned to titanium species in octahedral $[TiO_2^{6-}]$ environment signified the formation of anatase titania (Zhao et al. 2005).

X-ray Photoelectron Spectroscopy (XPS)	Elemental surface chemistry	Ti^{4+} is confirmed by Ti $2p_{3/2}$ at binding energy of 453-460 eV with Ti $2p_{1/2}$ peak at 458.8 eV (Choi et al. 2006a).

PCD performance of TiO_2 photocatalyst is strongly influenced by the crystal structure, lattice defects, particle size, porosity, overall surface area, and the density of hydroxyl group on the surface of the photocatalysts (Răileanu et al. 2009, Shankar et al. 2004). An optimum TiO_2 crystallite size in the range of 8-10 nm for efficient PCD reaction was postulated (Bosc et al. 2003). The crystallite size (CS) could also be estimated from the BET surface area by assuming spherical crystallite with no or minimal aggregation among the particles (Ivanda et al. 1999). Other method to estimate CS of TiO_2 is by using Scherrer's equation (Scherrer 1918) from the XRD peak broadening of (101) anatase crystal plane at 25.3°.

TiO_2 under UV irradiation displayed photocatalytic disinfection property (Fujishima et al. 2000). Matsunaga and co-workers (1985) was the first to report the anti-bacterial activity of UV-irradiated TiO_2. Since then, large numbers of research works have been dedicated to study the disinfection capability of TiO_2 photocatalyst. Photocatalytic disinfection capability of TiO_2 has been tested against different types of microorganisms such as bacteria, fungi, algae, protozoa, and virus (Foster et al. 2011, Yao and Lun Yeung 2011). The mechanisms of photocatalytic disinfection capability of TiO_2 are direct oxidation of coenzymes in cells, destruction of cell structure and damaging the cell DNA (Hu et al. 2007, Matsunaga et al. 1985).

2.2.3 Improving photocatalytic activity and functionality of TiO_2

2.2.3.1 Metal doped TiO_2

Attempt to improve the photocatalytic activity of TiO_2 include synthesizing nano-sized TiO_2 in various shapes and morphologies (Joo et al. 2005, Wu 2007), doping with metal (Lahiri et al. 2006, Subramanian et al. 2004) and non-metal, coupling with other semiconductor materials, surface modification, etc. Different metals (e.g. Ag, Al, Au, Ce, Co, Cr, Cu, Fe, Mn, Nb, Ni, Pd, Pt, V, W), lanthanides (e.g. Ce, Eu, Nd, La) and non-metal (e.g. B, C, F, N, S) have been used as the dopant materials. Various co-doped TiO_2 have also been reported (Wang and Lim 2010, Wang et al. 2011a, Wang et al. 2011b).

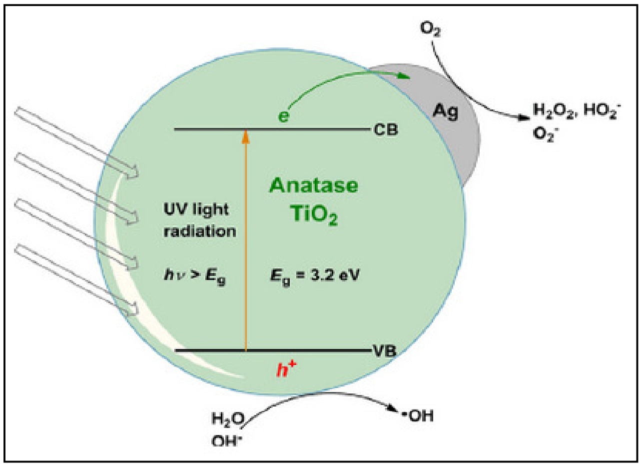

Figure 2.5 Metal-semiconductor (Ag-TiO_2) complexes that would prolong the life-time of photogenerated e^- and h^+ pairs (taken from Zhao and Chen (2011)).

The formation of metal cluster and semiconductor complex (Fig. 2.5) has been reported to enhance the PCD reaction efficiency by trapping the photo-generated charge carriers and improving overall charge transfer process (Subramanian et al. 2001). The dopant creates an additional intermediate energy level that prolongs the lifetime of the photogenerated e^--h^+ pairs by acting as an electron traps. They also might introduce oxygen vacancies that would improve the number of active sites thus improving overall PCD efficiency. Among the metallic materials, Ag provides the highest Schottky barrier which is important for effective inhibition of e^{-}-h^{+} pairs recombination (Nasr-Esfahani and Habibi 2008). Ag-doping also allowed the PCD reaction to be carried out under visible light ($\lambda > 400$ nm) irradiation. Besides, Ag is preferred as the metal dopant due to its excellent anti-bacterial properties that could reduce biofouling in the membrane separation process (Liu et al. 2013b, Yin et al. 2013).

Kubacka et al. (2008) have combined Ag and TiO_2 via impregnation and photodeposition method. They found that combining Ag and TiO_2 by photodeposition method displayed higher anti-bacteria performance over the impregnated Ag-TiO_2 composite. Photodeposition of Ag nanoparticles improved the PCD performance of TiO_2 coating (Arabatzis et al. 2003). In other study, Ag-modified P25 coating displayed an improved PCD performance of o-cresol over the Ag-less coating (Liu et al. 2004). The incorporation of photoreduced Ag on mesoporous anatase has significantly enhanced the anti-bacterial activity (Liu et al. 2008).

The incorporation of Ag into the TiO_2 matrix by direct photoreduction process has some disadvantages because of its poor adhesion, inability to yield uniform Ag nanoparticles distribution and the length of time required for effective photoreduction (Hou et al. 2009). A modified sol-gel method has been used instead to incorporate Ag^{+} in the preparation of TiO_2. Ag^{+} would be deposited on the surface of TiO_2 during calcination while the remaining Ag^{+} would diffuse into the TiO_2 lattice. The diffused Ag^{+} could be photoreduced during the post treatment. Ag^{+} ion could also be reduced to Ag^{0} during the calcination due to the high redox potential of Ag (Ao et al. 2008). Deposited Ag nanoparticles were found to agglomerate near the surface of the Ag-TiO_2 composite due to its high surface energy (Chao et al. 2003).

The need of anti-bacterial actions of Ag was aggravated by the evolution of new bacteria strains that are resistant to antibiotic (Kyriacou et al. 2004). The anti-bacterial properties of Ag-TiO_2 composite is mainly contributed by Ag^+ ions dissolving from the surface of Ag (Feng et al. 2000). Dissolved Ag^+ can be adsorbed onto the surface of the bacteria cells and damage the cell membrane and solid structures of its protein. Ag^+ can also permeate into bacteria cells, interacting with various enzymes within the cells and may interfere with the DNA (Feng et al. 2000, Li et al. 2008) .

The main drawback of the application of Ag as an anti-bacterial agent in the water-related application is the high rate of Ag^+ release. High Ag^+ release rate would shortened the lifespan of anti-bacterial activity (Wang et al. 1998). Besides, the stringent potable water standards have prescribed a maximum level of Ag in potable water supply as 100 $\mu g\ L^{-1}$ (USEPA 2009, WHO 2011). Therefore, the need to immobilize Ag nanoparticles in the mesoporous support matrix is imminent in order to delay the release of Ag^+. The supported Ag composite could prolong the duration of anti-bacterial activity which would lower the overall treatment cost (Akhavan and Ghaderi 2010, Zhang et al. 2004).

2.2.3.2 Structure directing agent (SDA)-modified TiO_2

Ordered mesoporous TiO_2 can be prepared using a process known as evaporation-induced self-assembly. In this process, an SDA is added during the preparation of the TiO_2 sol. The SDA assembles to form a micellar structure that can be removed during calcination steps, leaving behind an ordered mesoporous TiO_2 structure. The addition of SDA in the sol preparation allows fine-tuning the porosity and porous structure of the resulting TiO_2. Besides, the addition of SDA would increase the overall specific surface area of the TiO_2. The increase of specific surface area of the TiO_2 would promote better adsorption of pollutants onto photocatalyst resulting in higher overall PCD rate. Different types of SDAs that could be used to assist the pore formation are classified into block copolymers and cationic, anionic and nonionic surfactants. Table 2.5 summarizes common types of SDAs that have been used in the preparation of TiO_2.

Table 2.5 Common types of SDA used in the preparation of mesoporous TiO_2

Class	Examples (Scientific/Trade)	Selected references
Polymer	Polyethylene glycol (PEG)	(Arconada et al. 2009, Chen and Dionysiou 2007, Jahromi et al. 2009)
Di-block copolymer	Poly(ethylene-co-butylene)-block-poly(ethylene oxide) / KLE	(Coquil et al. 2010, Fattakhova-Rohlfing et al. 2007, Ortel et al. 2012a)
Tri-block copolymer	Poly(ethylene oxide)-block-polybutadiene-block-poly(ethylene oxide)/ PEO-PB-PEO	(Ortel et al. 2012b)
	Polystyrene-block-polybutadiene-block-polystyrene/ SBS	(Zakaria et al. 2013)
	Poly(ethylene oxide)-block-poly(propylene oxide)-block-poly(ethylene oxide)/ Pluronic P-123	(Goei et al. 2013, Liu et al. 2009, Procházka et al. 2008, Sun et al. 2009, Wu and Rankin 2011)
	Poly(ethylene oxide)-block-poly(propylene oxide)-block-poly(ethylene oxide)/ Pluronic F-127	(Castro and Durán 2013, Rahimi et al. 2013, Wang et al. 2013)

Cationic surfactant	Cetyl trimethyl-ammonium bromide/ CTAB	(Lee et al. 2013, Rashad and Shalan 2013, Shao et al. 2013)
	Poly(ethyleneimine)/ PEI	(Chang and Hsiang 2010)
Anionic surfactant	Sodium dodecyl sulfate/ SDS	(Rashad and Shalan 2013)
Nonionic surfactant	Polyethylene glycol p-(1,1,3,3-tetramethylbutyl)-phenyl ether/ Triton X-100	(Li et al. 2011, Sanguanruang et al. 2011, Xu et al. 2013)
	Polyoxyethylene (20) sorbitan monolaurate/ Tween 20	(Chen and Dionysiou 2008, García-Benjume et al. 2009)
	Polyoxyethylene (20) sorbitan monooleate / Tween 80	(Choi et al. 2006c, Choi et al. 2006d, Han et al. 2011)
	Poly(ethylene glycol) hexadecyl ether/ Brij58	(Arconada et al. 2010, Castro and Durán 2013)

The usage of copolymer as SDA in the past has been limited due to the low thermal stability of the polymer, resulting in the amorphous TiO_2 at a low calcination temperature or TiO_2 with smaller surface area and pore volume due to the collapse of the SDA scaffolding at a higher calcination temperature (Shamaila et al. 2011). The possibility of the high temperature calcination while maintaining a high-porosity TiO_2 was demonstrated by Lee et al. (2008) using a mixture of soft and hard templates as the SDA. The materials were able to withstand a calcination temperature of 1000°C while maintaining a high porosity. Zhang and coworkers (2010) carbonized the copolymer template using H_2SO_4 to yield amorphous carbon inside the mesoporous structure of TiO_2 that has strengthened TiO_2 framework during calcination. Other efforts were noted to improve the thermal stability of the template (Yoshitake et al. 2002).

Among different types of SDAs, a non-ionic SDA was generally preferred due to the weaker interactions between the SDA and the TiO_2 scaffold allowing easy removal of the SDA during calcination step. Besides, the use of non-ionic SDA would increase the structural stability of the meso-structure (Habibi et al. 2007a, Habibi and Nasr-Esfahani 2007, Habibi et al. 2007b). Generally, the increase in the SDA chain length would result in a structure with a larger porosity. The increase in the SDA concentration has the similar effect as the increase in the SDA chain length (Choi et al. 2006b, Zhang et al. 2003a). Zhang and coworkers (2003b) studied the effect of the molecular weight of polyethylene glycol (PEG) and the molar ratio of the SDA to the Ti content on the performances of the resulting TiO_2 photocatalytic film. The capping effect of SDA on the titanium precursor was found to reduce the hydrolysis and condensation reaction during the sol-gel synthesis (Dag et al. 2003, Stathatos et al. 2004).

During the preparation of the sol, the hydrated head group of the SDA (e.g. poly(ethylene oxide) of P-123 copolymer) interacts directly with the metal alkoxide precursor. This interaction promote the formation of a micellar structure even at a concentration lower than the critical micelle concentration (Wu and Rankin 2011). The resulting pore diameter is relatively uniform while the wall thickness of the resulting microstructure is solely dependent on the overall concentration of SDA in the sol (thicker wall for lower concentration of SDA).

2.3 TiO_2-based hybrid photocatalytic ceramic membrane

The integration of TiO_2 heterogeneous photocatalysis and membrane separation process in a hybrid treatment system is advocated in order to achieve effective water treatment solution. The integration could be achieved either using a separated membrane reactor with photoreactor in tandem as well as an integrated membrane photoreactor (Lim et al. 2011). In each case, TiO_2 photocatalyst could be either used in a suspension or in an immobilized system. The former requires catalyst recovery after the photocatalytic treatment process. The latter suffers from mass transfer limitation and has a much smaller number of active sites compared to the former.

The usage of suspended TiO_2 nanoparticles in a tandem photocatalyst-membrane reactor treatment system has been limited due to possible particles aggregation, possible membrane fouling and the need of particle recovery at the end of the treatment process (Linsebigler et al. 1995, Zhang et al. 1998). By anchoring the TiO_2 photocatalyst onto a porous membrane support, the issue of catalyst recovery can be solved. In addition, it also allows the synergistic coupling of photocatalytic reaction and membrane filtration which promotes mass transfer process through forced permeation. In this context, the crystallite size of the anchored TiO_2 photocatalyst must be optimized in order to achieve a high photocatalytic activity while not incurring a high membrane resistance. In addition, there is a need to produce a thin and uniform layer of nano-sized photocatalyst anchored on the highly porous membrane surface in order to maintain high water permeation through the TiO_2 membrane.

TiO_2 nanoparticles can be anchored onto different types of supports such as polymeric and ceramic membrane. An attempt to anchor TiO_2 nanoparticles on different types of flat-sheet polymeric membranes have resulted in partial membrane damage caused by radical attack triggered by UV-irradiation (Molinari et al. 2000). Photostable ceramic membrane has since been used for hybrid photocatalytic membrane application.

The ceramic membrane has many notable advantages such as its good permeability (due to good surface wettability and relatively uniform pore size), chemical stability (able to withstand organic solvents, chlorines, and extreme pH condition), thermal stability, mechanical stability, easy to clean, anti-fouling and anti-microbial property (Anderson et al. 1988, Bhave 1991, Burggraaf and Cot 1996, Chang et al. 1994, Guizard et al. 1992). Besides, membrane process using ceramic membrane is cheaper over a long term application despite its high membrane cost compared to the polymeric membrane system. A comprehensive economic assessment of membrane process for water and wastewater treatment has been published elsewhere (Owen et al. 1995).

Ceramic membrane for water and wastewater treatment normally consists of an asymmetric structure coated on a macroporous support. The support provides a mechanical strength to the membrane. Among different types of ceramic porous support materials, α-Al_2O_3 was commonly chosen due to its high chemical stability in extreme pH condition (Tsuru et al. 2001b).

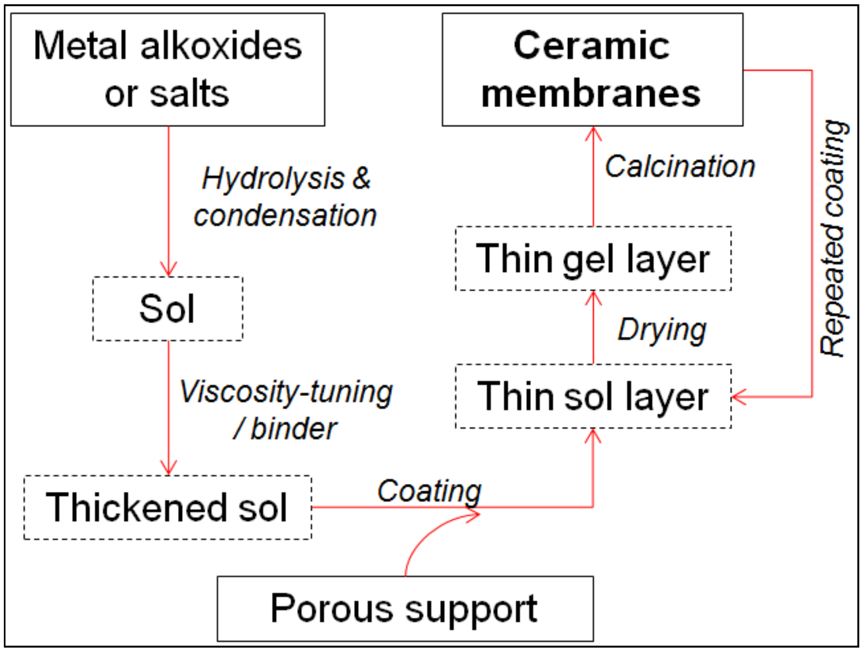

Figure 2.6 Flow diagram to prepare micro-/meso-porous ceramic membranes via the sol-gel technique (modified from Hsieh (1996)).

The flow diagram of the typical preparation steps of micro/mesoporous membranes via the sol-gel technique is presented in Fig. 2.6. In the typical preparation, a thickened sol is coated onto the porous support. The asymmetrical structure is obtained through coating of 2 or more layers with different porosities. Usually, more than 1 layer of coating is required for each type of the sol to ensure the smoothness and uniformity of the coating. A mesoporous intermediate layer is coated prior to the microporous top layer to reduce the surface roughness. This will result in a multi-layered ceramic membrane with a hierarchically porous architecture. The presence of porosity gradient is important to prevent early clogging of the composite membrane during the treatment process.

Leenaars and coworkers were the first to prepare an alumina ceramic membrane with ultrafine pores of diameter 3-5 nm by controlling the condition during sol-gel synthesis and the subsequent heat treatment (Keizer et al. 1984, Leenaars et al. 1984, Leenaars and Burggraaf 1985). Hashizume and Kunitake (2003) prepared a self-supporting ultrathin titania film by spin coating. They used different types and concentrations of spin-coating solutions to achieve a titania thin film with a controllable thickness. Meulenberg and coworkers (2006) produced a hybrid membrane with porosity gradient combining a stainless steel substrate, screen-printed ceramic layer, and a thick photoactive TiO_2 layer.

Coating of TiO_2 photocatalytic layers is an important step in the fabrication of the hybrid membrane. Delamination of TiO_2 layer from the support layer is to be avoided. Different coating techniques have been used to prepare and coat the TiO_2 thin film layer on the ceramic membrane support such as dip coating, spin coating (Fretwell and Douglas 2001, Pan and Lee 2006, Wang et al. 2002), slip casting (Alem et al. 2009b, Zaspalis et al. 1992), in-situ hydrothermal/solvothermal synthesis (Shen et al. 2014, Zhan et al. 2013), aerosol spraying (Cho and Yoon 2013, Kavan and Grätzel 1995, Kubo et al. 2013), chemical vapor deposition

(Diesen et al. 2013, Mills et al. 2002), physical vapor deposition (Moser et al. 2013, Weng and Huang 2013), radio-frequency magnetron sputtering (Dholam et al. 2008), spray pyrolysis (Ennaoui et al. 2006, Kavan and Grätzel 1995), reactive sputtering (Awitor et al. 2008), electrochemical deposition (Hepel and Kumarihamy 2007, Palmas et al. 2010), plasma spraying (Znamirowski et al. 2013, Zou et al. 2007), etc.

Different preparation and coating techniques used would result in the TiO_2 thin film of various thicknesses and morphologies. The final microstructure and the performance of the TiO_2 thin film is strongly dependent of the preparation condition. Zhao and coworkers (2004) investigated different preparation conditions that would affect the microstructure of the resulting TiO_2 thin film such as amount of SDA added, amount of the hydrolysis retardants added, aging time, pH, and calcination temperature. Liu and coworkers (2005) optimized the relative amount of the TiO_2 sol constituent to control the porosity of the resulting thin film.

Recurrently, binder such as hydroxypropyl cellulose (HPC) or polyvinyl alcohol (PVA) was added into the TiO_2 sol as a binder (Alem et al. 2009b). Binder could help to adjust the viscosity of the sol, lower the surface tension of the sol and increase the mechanical strength of the resulting membrane (Larbot et al. 1988, Sekulic-Kuzmanovic 2004).

Heat treatment plays an important role in the fabrication of crack-free membrane. A lower calcination temperature would yield membrane with a smaller pore and crystallite size. Also, the lower calcination temperature would prevent transformation of anatase to rutile. By controlling the heating rate during the calcination step, one can avoid the development of thermally induced stress possibly caused by unequal thermal expansion of the composite membrane or layer shrinkage due to thermal decomposition of organic additives. For the multi-layer coating process, the repeated thermal treatments performed after each coating could cause a partial collapse of the porous structure thus reducing its PCD efficiency

(Arconada et al. 2010). It was suggested that the calcination temperature is the ultimate control porosity structure of the resulting membrane (Puhlfürß et al. 2000).

It is important to ensure that the surface of the composite membrane is hydrophilic to allow easy access of the target organic pollutant to the catalytic sites (Hata et al. 2000). Surface of the TiO_2 exhibits photo-induced super-hydrophilicity (PSH) when irradiated with UV source (Irie et al. 2003, Watanabe et al. 1999). According to the Laplace equation, the wettability of porous materials is inversely proportional to the contact energy (surface energy) of the materials (Mulder 1996).

Table 2.6 summarizes different characterization techniques that can be used to study various characteristics of ceramic membrane composite.

Table 2.6 Characterization of ceramic membranes

Technique / instrument	Characteristic studied	Findings
Gas bubble pressure (GBP) method (ASTM F316-80)	Mean pore size and pore size distribution	Pore size decreases or can be plugged as the deposition of TiO_2 increases (Ha et al. 1996).
ASTM F316	Pore size characteristic	Permeability of the TiO_2 composite membrane was evaluated (Alem et al. 2009b).
Nano-permporometry (humid gas permeation)	Pore size and pore size distribution	Nano-order pore size of silica-zirconia membrane is evaluated (Tsuru et al. 2001a).
Pencil hardness testing (ASTM D3363-92a) / Tensile testing (ASTM C633-01) / Scratch adhesion testing	Mechanical properties / coating strength	Pencil hardness testing is more suitable for porous film; porous film shows fair adhesion strength but relatively weak mechanical properties as compared to dense membrane (Ryu et al. 2010).
Static angle goniometer	Hydrophilicity /	Hydrophilic membrane is compatible with

	hydrophobicity	polar pollutant.
Spectral ellipsometry and environmental ellipsometric porosimetry	Thickness and porosity of the coating	Different information of TiO_2 film could be obtained via ellipsometry (Boissiere et al. 2005).
Three-points bend test	Mechanical strength	The mechanical strength of the composite membrane was reinforced by the alumina support (Alem et al. 2009b).
Water absorption method (ASTM C373-88)	Apparent porosity and bulk density	Apparent porosity of TiO_2 composite membrane was evaluated. Result was complimentary to BET porosimetry analysis (Alem et al. 2009b).
Zeta potential analyzer	Electrical potential difference (streaming potential)	Zeta potential depends of types of the electrolyte; titania shows amphoteric properties with isoelectric point of 6.5 (Tsuru et al. 2001b).

Table 2.7 summarizes selected works on the TiO_2-based thin films and photocatalytic ceramic membranes. Majority of works listed on Table 2.7 mainly deal with TiO_2-based thin films or TiO_2-based membranes used to treat various types of pollutants in a batch photoreactor. In the batch reactor, the efficacy of supported-TiO_2 photocatalyst is limited to the mass-transfer limitation of the pollutants to the surface of the photocatalysts. A continuous flow treatment system can be achieved by coating TiO_2 onto a porous membrane support. The overall improvement on direct contact between target pollutants and photocatalysts due to the forced permeation through the membrane will result in an enhanced photocatalytic degradation efficiency of the treatment system.

The anti-bacterial application of traditional ceramic membrane treatment process was limited to the molecular sieve functionality. It does not inactivate bacteria cells. Bacteria cells deposited on the membrane surface can grow into structured community known as bio-film which is more difficult to remove than individual bacteria cells in suspension (Costerton et al. 1999). The inclusions of Ag nanoparticles (Ag NPs) into TiO_2 photocatalytic ceramic membrane could enhance the anti-bacterial property and inhibit the growth of bio-film. Table 2.8 summarizes selected works on Ag-decorated TiO_2-based thin films and photocatalytic ceramic membranes.

Table 2.7 TiO_2-based thin film and photocatalytic ceramic membrane: preparation, properties and performances

References	Synthesis / fabrication highlights	Important physico-chemical properties	Photocatalytic and membrane performances
(Anderson et al. 1988)	• Two types of membrane were prepared: from particulate sols and polymeric sols.	• The size of the particles in the particulate sols is strongly dependent on the pH condition (early precipitation and possible particle aggregation occurred respectively at low and high pH condition). • For the polymeric sols, a transparent gel could only be obtained when $[H_2O]/[Ti] \leq 4$, acid do not significantly affect the properties of the polymeric gels.	• The membrane pores whose diameter are in the 1.8 – 5.0 nm range.
(Zhao et al. 2004, Zhao et al. 2005)	• TiO_2 mesoporous thin film was prepared using P-123 as the SDA. • TiO_2 sol was dip-coated on glass slides and/or silicon wafer.	• Optimum molar concentration of SDA was found to be 0.03 with respect to Ti. • Different parameters (i.e. amount of SDA, aging time, pH, aging temperature, and amount of acetylacetone (chelating agent)) were investigated in relation to the properties of the final TiO_2 film. • Template removal by solvent extraction	• Thin film composite was tested against methylene blue. • Ethanol-extracted membranes calcined at 350-400°C have the highest PCD efficiency due to its larger surface area.

		followed by calcination improved the overall structural stability of the TiO_2 scaffold. • TiO_2 crystallite size (CS) ranged between 5 and 30 nm for solvent-extracted samples.	
(Zhang et al. 2006)	• TiO_2/Al_2O_3 composite membranes were prepared from colloidal titania sols.	• Uniform pore size around 50-100 nm. • The dissolution of TiO_2 microstructure was observed after 6 times usage resulting in membrane with larger pore size. • Membrane consists of TiO_2 tubules with average thickness of 50 µm.	• Different retention rates were observed for model pollutant Direct Black168 when treated at different pH. • Immediate decline in flux was observed followed by a stable sustainable flux for the rest duration of the experimental run. • The presence of H_2O_2 accelerates the PCD reaction of organic pollutant.
(Choi et al. 2006b)	• TiO_2 sol was prepared using acetic-acid based sol-gel route with non-ionic surfactant as SDA. • TiO_2 sol was dip-coated on borosilicate glass. • Among the non-ionic SDAs, Tween-80	• TiO_2 CS range between 8.3 and 15.6 nm. • Slow hydrolysis reaction enhanced the structure of the resulting TiO_2. • Capping effect from the SDA reduce the hydrolysis and condensation reaction rate.	• Higher removal of methylene blue (MB) for higher loading of SDA up to 2.0 molar ratios (with respect to TiO_2), above which the PCD efficiency was reversed.

	showed the best pore structure and film thickness controllability.		
(Habibi et al. 2007a, Habibi and Nasr-Esfahani 2007, Habibi et al. 2007b)	• TiO_2 thin film composite was prepared by sol-gel method utilizing methylcellulose (MC, a non-ionic polymer) as the SDA. • TiO_2 sol was spin-coated onto borosilicate glass.	• The addition of MC improved the stability of the TiO_2 sol and the resulting coating quality. • The addition of MC improved the adhesion of the TiO_2 layer to the support. • TiO_2 CS of the composite film was 16.3 nm	• Thin film composite was tested against 3 types of diazo dyes. • First order kinetic of PCD of C.I. Reactive Yellow 2 dye was observed. • More efficient PCD was observed for thin film composite prepared with MC. • Photodecoloration was much faster than the photomineralization (which includes aromatic ring opening reaction).
(Zhao et al. 2008)	• A micro-nano hierarchical TiO_2 film was fabricated with Si-coated borosilicate glass as support. • Electro-hydrodynamic (EHD) coating technique (Zhao et al. 2006). • For comparison, nano-structured TiO_2 thin film was also prepared by spin coating.	• TiO_2 layer consist of array of TiO_2 nanoparticles. • TiO_2 loading of 12 ± 1 mg. • Pore size < 100 nm. • Thickness of the hierarchically porous and nanoporous TiO_2 thin films were 2 and 1.5 µm respectively.	• PCD capability of the thin film was evaluated against liquid phenol and gaseous acetaldehyde. • Hierarchical porous thin film showed a better PCD performance (especially in treating phenol).
(Syafei et al.	• Commercial Degussa P25 suspended in	• Commercial membrane with MWCO 1,	• Higher flux decline for the TiO_2 coated

2008)	acetylacetone solution with Triton X-100 as the SDA. • Coating by immersing TAMI ATZ (alumina, titania, zirconia) ceramic membrane disk.	15, and 30 kDa was used.	membrane which could be attributed to the adsorption of organic pollutant. • Higher humic acid removal by the TiO_2 coated membrane which mainly was contributed by the membrane rejection.
(Sun et al. 2009)	• Usage of DoE (design of experiment) to find an optimal synthesis condition for maximum photocatalytic activity. • Factors considered: amount of acetic acid added, amount of ethanol added, amount of SDA (P-123) added, and calcination temperature. • TiO_2 film was coated on ITO glass.	• The presence of residual OH groups bonded with Ti was found in the FTIR spectrum of all samples. • TiO_2 CS range between 12.0 and 38.7 nm. • TiO_2 loading range between 33 and 211 $\mu g\ cm^{-2}$. • TiO_2 exist as uniform and dense spherical grain.	• Calcination temperature has the most significant influence for the photocatalytic activity of both methyl orange and gaseous toluene.
(Alem et al. 2009b)	• TiO_2/Al_2O_3 composite membrane prepared from TiO_2 colloidal sol with HPC and PVA added as binder. • TiO_2 layer was coated using slip casting method.	• Optimum thickness of 1µm for membrane with good integrity. • Composite membrane with large surface area (75 $m^2\ g^{-1}$) and small pore size (4.7 nm) was fabricated.	• Membrane showed permeability of 30 mL min^{-1} Bar^{-1} cm^{-2} with Knudsen diffusion observed at low TMP. • Removal of methyl orange in the batch photoreactor was observed despite the issue of mass transfer limitation.

(Alem et al. 2009a)	- Multilayer TiO_2/Al_2O_3 composite membrane prepared using TiO_2 polymeric and TiO_2 colloidal sol as the top and intermediate layer respectively. - Aging to increase the viscosity of the sol and thus minimizing sol infiltration to the underlying layer.	- Composite membrane with improved surface area (83 $m^2 g^{-1}$) and smaller pore size (4 nm) was fabricated.	- Addition of top TiO_2 layer had a minimum impact on the membrane permeability. - Improved PCD of methyl orange in the batch photoreactor due to the presence of top TiO_2 layer prepared from polymeric sol.
(Arconada et al. 2010)	- TiO_2 mesoporous thin film was prepared using different types of SDAs: Pluronic F-127, Brij56/58, CTAB and SDS. - Two types of chelating agents were used: acetylacetone and acetic acid. - TiO_2 was dip-coated to glass and silicon wafer substrate, prior SiO_2 coating was applied to the glass substrate to prevent diffusion of Na^+.	- All sol displayed an excellent stability (a relatively constant viscosity of 2 mPa.s for more than 1 month). - Coating thickness was varied between 200 and 300 nm. Thickest coating was obtained for TiO_2-acetic acid-F-127 combination. - Porosity profile of the film was determined using spectral ellipsometry. - Specific surface area range between 28 and 68 $m^2 g^{-1}$.	- The efficacy of PCD reaction is highly dependent of the total surface area effectively irradiated with UV. - There exists an optimum coating thickness above which, the light shielding effect and higher material cost hinder the overall efficacy of the PCD reaction.

(Arconada et al. 2011)	• TiO_2 mesoporous thin film was prepared using different types of SDAs: F-127, Brij58 and Triton X-100. • TiO_2 was dip-coated to glass in different relative humidity (RH) and withdrawn at different rate.	• TiO_2 CS range between 16 and 19 nm. • Total pore volume range between 30 and 45% with pore size distribution between 2.4 and 6.4 were obtained.	• TiO_2 film prepared with Brij58 at RH 50% displayed highest initial PCD rate while maximum amount of methylethyl ketones was degraded by Brij58, RH 20% TiO_2 film.
(Wang et al. 2013)	• TiO_2 mesoporous thin film was prepared using F-127 as the SDA. • TiO_2 sol was spin-coated onto ITO glass slides and/or silicon wafer.	• Highly ordered TiO_2 mesoporous framework was obtained after calcination at 350°C. • The mesoporous framework was stable even after calcination at 600°C. • TiO_2 CS ranged between 7.6 and 29.6 nm with pore walls ~13 nm.	• Thin film calcined at 350°C showed poor PCD of methyl orange due to the presence of amorphous TiO_2 and organic residues. • There exists an optimum calcination temperature 500°C for excellent PCD activity, above which the mesoporous structure collapsed.
(Castro and Durán 2013)	• TiO_2 mesoporous thin film was prepared using F-127 and Brij58 as the SDA. • TiO_2 sol was dip-coated to glass slides and/or silicon wafer, 6 mm s^{-1} withdrawal rate. An intermediate SiO_2 layer was coated to prevent the diffusion of Na^+ from the glass substrate to the TiO_2 coating.	• TiO_2 CS ranged between 7 and 12 nm. TiO_2 layer prepared with F-127 showed larger pore sizes (6-10 nm). • TiO_2 layer prepared with F-127 showed highly ordered TiO_2 framework while the layer prepared with Brij58 showed a homogeneous mesoporous structure without pore ordering.	• TiO_2 layer prepared with Brij58 showed higher PCD efficiency when treating gaseous pollutants: TCE (trichloroethene), H_2S (hydrogen sulfide) and methyl-ethyl-ketone. • TiO_2 layer prepared with Brij58 showed a higher PCD efficiency when treating aqueous methyl orange dye solution.

Table 2.8 Ag-decorated TiO_2-based thin film and photocatalytic ceramic membrane: preparation, properties and performances

References	**Synthesis / fabrication highlights**	**Important physico-chemical properties**	**Photocatalytic, anti-bacterial and membrane performances**
(Page et al. 2007)	• Ag-TiO_2 film was prepared by a modified sol-gel method. $AgNO_3$ was added in the preparation of TiO_2 sol. • Ag-TiO_2 sol was dip-coated to different types of substrates.	• Ag present in the Ag-TiO_2 films as Ag_2O. • Ag-TiO_2 films displayed a photo-induced super-hydrophilicity property.	• Anti-bacteria property was tested against gram-positive (B. *cereus*, and S. *aureus)* and gram-negative bacteria (E. *coli*) using UV 365 nm as irradiation sources. • Gram-positive bacteria were more susceptible to the anti-bacterial activity of Ag-TiO_2 film mainly due to its more porous membrane structure.
(Liu et al. 2008)	• TiO_2 was prepared by sol-gel method using P-123 as SDA. • TiO_2 was spin-coated onto glass substrate. • Ag-doping was done by immersing coated substrate in the $AgNO_3$ solution.	• Concentration of Ag^+ released was determined using anodic stripping voltametry. Higher initial Ag^+ release rate was observed. • Homogeneous worm-like 3-dimensional pores were formed. Pore size was 5 nm in diameter. Ag NPs were incorporated in the TiO_2 mesopores. • Pore volume and surface area of the Ag-TiO_2 thin film was 0.26 $cm^3\ g^{-1}$ and 157 $m^2\ g^{-1}$.	• Anti-bacterial activity of the Ag-TiO_2 composite was tested against E. *coli* and Ag-resistant E. *coli*. • Extent of anti-bacterial activity was determined by viable-bacteria cells imaging using epifluorescence microscopy. • Ag-TiO_2 composite was equally effective in killing both E. *coli* and Ag-resistant E. *coli*.

		- TiO_2 CS was 10 nm.	
(Nasr-Esfahani and Habibi 2008)	- Ag-TiO_2 materials were prepared by sol-gel method, using MC as SDA and TiO_2 nanoparticles (3 types) as fillers. - Ag was introduced by soaking of film in the $AgNO_3$ solution.	- TiO_2 nanoparticles filler aggregate and grow to form a larger TiO_2 crystal during calcination. - The addition of nanoparticles fillers enhances the growth of TiO_2 crystals.	- Improved photocatalytic activity as compared with the undoped TiO_2.
(Akhavan 2009)	- TiO_2 thin film was prepared by dip-coating of TiO_2 sol on glass substrate. - Ag was introduced by soaking of film in the $AgNO_3$ solution. - Other type of Ag-TiO_2 thin film was prepared by a direct incorporation of Ag sol in the sol preparation.	- TiO_2 crystallite size (CS) was ~11 nm. The mean size of Ag NPs was ~12 nm. - Based on XPS analysis, Ag species exist as AgO, Ag_2O and Ag^0. - Ag was found to aggregate on the surface of Ag-TiO_2 film. - Surface Plasmon resonance phenomenon due to Ag NPs was observed at 412 nm.	- Anti-bacterial activity of the Ag-TiO_2 composite was tested against E. *coli* in the presence of visible light irradiation (425 nm). - Enhanced anti-bacterial activity was observed for Ag-TiO_2 thin film. - Ag-TiO_2 thin film prepared by a direct incorporation of Ag source in the sol preparation displayed a higher anti-bacteria activity.

(Krylova et al. 2009)	• Ag NPs were incorporated in various ceramic-based thin films: SiO_2, TiO_2, and ZrO_2 prepared by sol-gel method. P-123 was incorporated as SDA. • Thin films were deposited onto different supports (i.e. glass, silicon wafer and aluminum) by dip-coating method.	• Ag inhibited the growth of TiO_2 crystals. • The mean pore size of TiO_2 was 12 nm with pore wall thickness of 5.5 nm. • Mixture of anatase and brookite phases was observed for Ag-TiO_2 thin film. • TiO_2 CS ranged between 15 and 25 nm. Average size of Ag NPs was 4-10 nm. • Surface Plasmon resonance phenomenon was observed at 400 nm.	• No performance evaluation was performed in this work.
(Rǎileanu et al. 2009)	• Ag-doped (2% wt) TiO_2 thin film supported on glass. • Two types of thin film: direct Ag doping (in-situ co-gelation) and addition of Ag into the TiO_2 sol.	• Smoother TiO_2 thin film was observed for film prepared by direct Ag doping • Ag was present as Ag^+. • Ag inhibited the growth of TiO_2 crystals. • Ag was found to promote anatase-rutile transformation.	• Improved photocatalytic activity as compared with undoped TiO_2. • Early anatase-rutile transformation decreases the overall PCD efficiency.

(Hou et al. 2009)	- Ag-TiO_2 film was prepared by a modified sol-gel method. $AgNO_3$ was added in the preparation of TiO_2 sol. - Ag-TiO_2 sol was dip-coated 3 times to a glass substrate.	- TiO_2 CS ranged between 10 and 40 nm. - Formation of Ag cluster was observed for sample with Ag/Ti molar ratio = 0.48. - Based on XPS analysis, Ag species exist as AgO, Ag_2O and Ag^0. - Ag was found to aggregate on the surface of Ag-TiO_2 film.	- There exists an optimum level of Ag loading for maximum PCD performance both when irradiated with UV or visible light. - PCD performance of Ag/TiO_2 film was better under visible light irradiation.
(Ma et al. 2009a)	- Ag-TiO_2 sol was prepared by sol-gel method. Hydroxyapatite (HAP) sol was prepared by precipitation method. - Alumina support was coated with two-step approach: first with HAP sol and calcined followed by coating of Ag-TiO_2 sol and final calcination.	- Thickness of HAP/Ag-TiO_2 composite layer was ~10µm. - No Ag^0 phase was observed in XRD spectra due to small amount of Ag^0 present. - Amount of HAP deposited varied from 2.8 to 5.5 g m^{-2} depending on the dip time. Amount of Ag-TiO_2 deposited ~49 g m^{-2} (not affected by the dip-time. - Mean pore size ~790 nm.	- Ag-TiO_2 sol with 1wt% Ag exhibits higher photoactivity than the one with 5wt% Ag and pure TiO_2. - Anti-bacterial activity of the Ag-TiO_2 composite was tested against E. *coli*. - HAP was found to increase bacterial adsorption capacity of the membrane. - The removals of E. coli were approximately 6 and 4-logs under UV Irradiation and in the dark respectively.

(Akhavan and Ghaderi 2010)	• Ag-TiO_2 was prepared by sol-gel method. • Ag-TiO_2 was dip-coated to glass substrate.	• TiO_2 CS was ~11 nm. The mean size of Ag NPs was ~10 nm. • Majority of the Ag species were Ag^0. Ag^0 were found to agglomerate on the surface of TiO_2. • Pore volume and surface area of the Ag-TiO_2 thin film was 0.30 cm^3 g^{-1} and 213 m^2 g^{-1}. • Ag^+ release was found to reach saturation after 8 days.	• Enhanced anti-bacterial activity was observed for Ag-TiO_2 thin film mainly due to slow Ag^+ release and slower recombination rate of photo-generated e^--h^+ pairs. • Anti-bacterial activity of the Ag-TiO_2 composite was tested against E. *coli*.
(Kment et al. 2010)	• Ag acetylacetone was added during the preparation of TiO_2 sol. Ag-TiO_2 sol was dip-coated to a glass slide. • Fe- and Zr-doped TiO_2. Were also prepared/	• TiO_2 CS ranged between 10 and 14 nm. • Ag was found to suppress the growth of anatase crystals.	• Ag-TiO_2 film displayed a relatively high quantum high, second only to Zr-TiO_2 based on electrochemistry experiment. • Ag-TiO_2 film displayed the highest PCD activity among the metal-doped TiO_2 film.
(Zhao and Chen 2011)	• Ag-TiO_2 sol was prepared by sol-gel method utilizing H_2O_2 as peptizing agent to allow preparation at neutral pH. • Ag-TiO_2 sol was dip-coated to a glass slide.	• Ag NPs were found deposited on the surface of TiO_2. • Rhombus-shape TiO_2 were synthesized (diagonal lengths of 10 and 40 nm).	• Enhanced photocatalytic activity was observed for Ag-TiO_2 thin film even at low Ag loading (0.5 wt%).

(Yu et al. 2011)	- Ag-TiO$_2$ was prepared by sol-gel method using P-123 as SDA and acetylacetone as chelating agent. - Ag-TiO$_2$ was spin-coated onto silicon wafer.	- Ag species exists as Ag^0. After UV exposure, Ag$_2$O was formed through oxidation. - Average size of TiO$_2$ range between 10 and 20 nm. Ag NPs of various sizes (range between 10 and 30 nm) exist as agglomerated granules. Ag NPs agglomeration could be avoided at higher Ag concentration. Ag NPs were concentrated on the surface of the TiO$_2$.	- Anti-bacteria property was tested against E. *coli* using UV 365 nm as the irradiation sources. - Anti-bacterial activity of Ag-TiO$_2$ composites were studied by diffusion inhibition zone and batch reactor. - Anti-bacterial activity was proportional to the [Ag] on the TiO$_2$ surface.
(Piwoński et al. 2011)	- TiO$_2$ was dip-coated on silicon wafer. - TiO$_2$ thin film was immersed in the AgNO$_3$ solution (from 0.05 – 500 mM) followed by UV irradiation or irradiation with excimer laser.	- Three Ag- photodeposition parameters were studied: [AgNO$_3$], irradiation time, and irradiation source. - Number of photodeposited Ag increase by 10 folds when [AgNO$_3$] increased by 10,000. Prolonged irradiation time increase the size of deposited Ag. - UV-assisted photodeposition was more effective.	- TiO$_2$ film displayed a weak anti-bacterial activity in the dark. - Anti-bacterial activity is proportional to the [Ag] on the TiO$_2$ surface.

(Kubacka et al. 2011)	• TiO_2 was prepared using a micro-emulsion synthetic route supported on ethylene-vinyl alcohol copolymer. • Ag was photodeposited up to 1% wt% with respect to Ti.	• Characteristic TiO_2 primary particle size was ~10 nm. • No structural changes were observed for Ag-decorated film. The inclusion of Ag only alters the optical property of the film.	• Anti-bacteria property was tested against E. *coli* and S. *aureus* using UV (280) nm and visible light (500 nm) as irradiation sources. • Ag decorated film remove up to 7 and 6 logs E. *coli* and S. *aureus* respectively when irradiated with UV. • Ag decorated film remove up to 3 logs E. *coli* and S. *aureus* when irradiated with visible light.
(Emadi and Raeissi 2011)	• TiO_2 layer was prepared by anodic oxidation of titanium plate support. • Ag was deposited by electro-deposition.	• Average size of electro-deposited Ag was 32 nm.	• Ag-TiO_2 effectively killed E. *coli* and S. *aureus* bacteria cells. • Bio-medical application.
(Wu et al. 2011)	• Microporous TiO_2 thin film was prepared by anodizing titanium plate. • Ag-doping was done by immersing anodized Ti plate in the $AgNO_3$ solution.	• The TiO_2 thin film consists of 80% anatase and 20% rutile. • The size of micropores range between 90 and 300 nm.	• Extent of PCD reaction was determined by measuring concentration of hydroxyl radical. • Disinfection capability of Ag-TiO_2 composite was determined by the level of lipid peroxidation, K^+ and protein leakage from the cells.

(Joya et al. 2012)	• TiO_2 was dip-coated on glass substrate. • TiO_2 thin film was immersed in the $AgNO_3$ solution followed by irradiation with KrF excimer laser.	• Thin film thickness was in the range between 250-300 nm. • TiO_2 CS ranged between 38 and 43 nm. • Cubic and hexagonal Ag NPs size was ranged between 5 and 20 nm. • Surface Plasmon resonance phenomenon was observed at 516 nm (due to localized SPR of Ag NPs formed during the laser irradiation).	• Anti-bacteria property was tested against E. *coli* and S. *aureus* using normal daylight as the irradiation source. • The Ag-TiO_2 thin film composite completely eliminated E. *coli* and S. *aureus* (4×10^4 cfu mL^{-1}) within 60 min.
(Gutiérrez et al. 2013)	• Ag-TiO_2 was prepared by sol-gel method. • Ag-TiO_2 was dip-coated to glass substrate.	• TiO_2 CS ranged between 13 and 18 nm. • There exists an optimum Ag loading for which the photocurrent would be maximized (indicating maximum PCD capability).	• Enhanced photocatalytic decomposition of methanol and Basic Orange II were observed for Ag-TiO_2 thin film.
(Obalová et al. 2013)	• Ag-TiO_2 was prepared by sol-gel method. • Ag-TiO_2 was dip-coated to glass substrate.	• Ag was found to improve crystallinity while suppressing crystal growth of TiO_2.	• Enhanced photocatalytic decomposition of N_2O was observed for Ag-TiO_2 thin film. • There exists an optimum amount of Ag-doping for efficient decomposition of N_2O.

2.4 Conclusion

TiO_2 has been used extensively in the water and wastewater treatment due to its ability to generate electron and hole pairs when irradiated with UV. The photogenerated e^- and h^+ pairs could generate different types of non-selective reactive radicals upon reaction with suitable electron and holes acceptor. These radicals are responsible for the decomposition and possible complete mineralization of wide range of environmental recalcitrant and noxious pollutants.

The need of post-separation of the powdered photocatalyst during application had prompted many research efforts on supported TiO_2. Ceramic support has been used as an ideal support material due to its stability and potential long term application. The idea of supported TiO_2 on a ceramic membrane to allow continuous treatment processes has been explored extensively.

Different method can be employed to increase the PCD capability of TiO_2. Among which are the usage of SDA and chelating agent during the preparation of the sol, and doping with various metal/non-metal elements. Ag has been an excellent dopant candidate due to its anti-bacterial activity and visible light responsiveness. Different aspects of incorporation of SDA and Ag dopant have been discussed in this chapter.

In the following chapters, effort to immobilized TiO_2 into a ceramic membrane support will be described. Different types of SDAs will be used to improve overall performance of the photocatalyst. Various preparation steps will be carefully considered in order to obtain a hybrid membrane that shows an optimum photocatalytic and membrane performance. Lastly, the addition of Ag is considered to improve the PCD capability as well as to introduce an additional anti-bacterial activity to the hybrid membrane.

CHAPTER 3 MATERIALS AND METHODS

3.1 Materials and synthesis techniques

3.1.1 Chemicals and materials

All chemicals used in this study were of analytical grade. The following chemical were used in the preparation of TiO_2 sol without further purification unless it is stated otherwise: titanium tetraisopropoxide (TTIP, Merck), 2-propanol (IPA, Merck), hydrochloric acid 37% (HCl, Aldrich), and nitric acid 67% (HNO_3, Merck). Silver nitrate ≥98% ($AgNO_3$, Merck) was used as the Ag source for the Ag-decorated TiO_2 (Ag-TiO_2). MilliQ water (18.2 MΩ.cm at 25°C) was used throughout in the sol preparation and other experiments in this study. Four types of structure directing agents (SDAs) were employed to produce mesoporous TiO_2 layer, i.e. poly(ethylene glycol)–block–poly(propylene glycol)–block–poly(ethylene glycol) (Pluronic® P-123, P-123, Aldrich), polyethylene glycol p-(1,1,3,3-tetramethylbutyl)-phenyl ether (Triton X-100™, X100, Aldrich), Polyoxyethylene (20) sorbitan monolaurate (Tween® 20, T20, Aldrich), and Polyoxyethylene (20) sorbitan monooleate (Tween® 80, T80, Aldrich).

The macroporous alumina ceramic membrane support was prepared from aluminum oxide (α-Al_2O_3, Aldrich) with a relative density of 4 g cm^{-3} and average particle size of 0.05 µm. Poly vinyl alcohol 88%-hydrolyzed (MW 88,000 g mol^{-1}, PVA, Acros Organics) was used as pores filler during the coating of TiO_2 photocatalytic layers in the membrane fabrication. The membrane retention capability was evaluated using poly(ethylene glygol) (PEG, Alfa Aesar) of MW 1,500, 6,000, 10,000, and 20,000 g mol^{-1}. Rhodamine B (Fig. 3.1) (MW 479.02 g mol^{-1}, λ_{max} 553 nm, RhB, Merck), a common tracer dye and bio-marker, was used as the model organic pollutant without further purification.

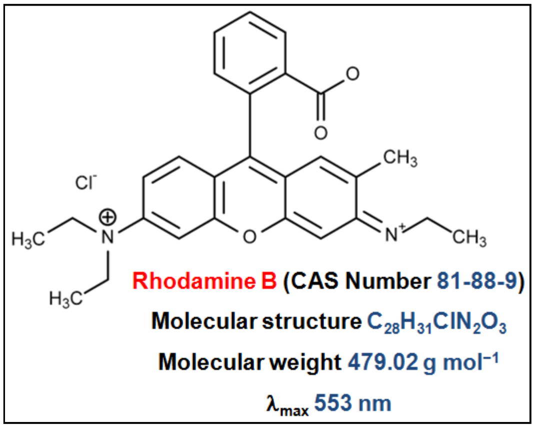

Figure 3.1 Molecular structure of Rhodamine B.

3.1.2 Preparation of macroporous alumina ceramic support

The macroporous alumina ceramic membrane support was fabricated by molding a predetermined amount of Al_2O_3 powder on a custom-made pellet pounder assembly. The pellet pounder assembly was pressed at 50 kN for 3 min and 100 kN for the subsequent 3 min by the uni-axial hydraulic press (Perkin Elmer). The diameter and thickness of the resulting ceramic membrane support were 23 mm and 2 mm respectively.

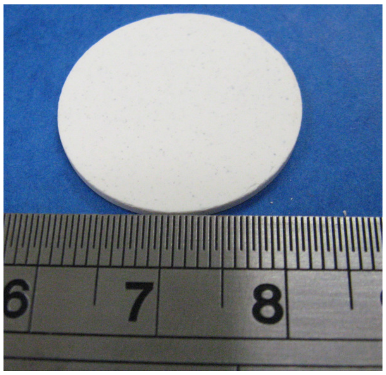

Figure 3.2 Photograph of alumina ceramic membrane support.

The pelletized ceramic membrane support was calcined and sintered at 1280°C in a programmable muffle furnace (Nabertherm LHT04/16) for 24 h, and was cooled down naturally to the room temperature. Finally, the ceramic membrane support was subjected to the multi-step sandpaper polishing (ISO grit sizes of P360, P600, P1000 and P1500) in order to obtain a smooth surface for the subsequent dip coating process. Fig. 3.2 shows photograph of the as-fabricated alumina ceramic membrane support.

3.1.3 Preparation of TiO_2 sols

TiO_2 sol was prepared using an acid-catalyzed sol-gel method. Fig. 3.3 summarizes the sol-gel preparation of the TiO_2 sol. TTIP was used as the titanium alkoxide precursor with IPA as the solvent. Different types of SDAs (i.e. P-123, X100, T20 and T80) were employed in the preparation of the TiO_2 sol as the pore forming agents.

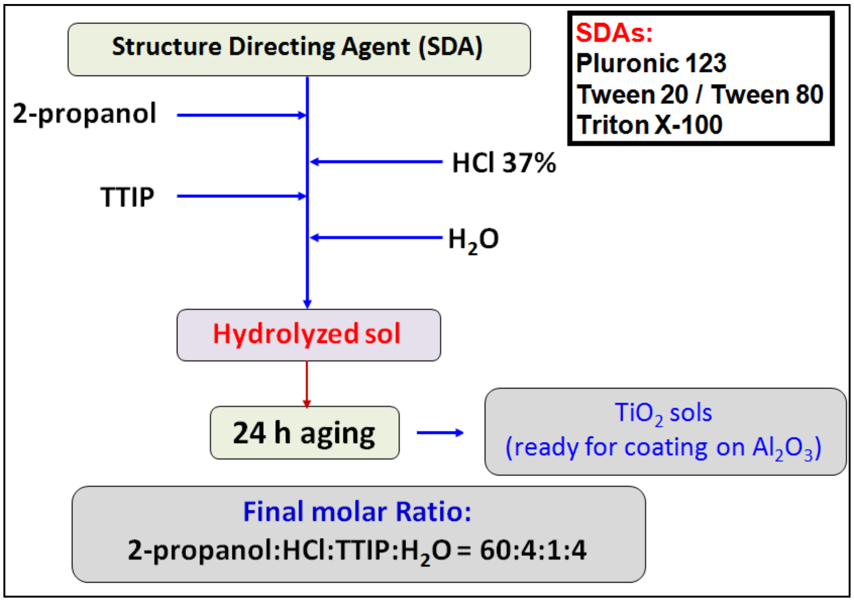

Figure 3.3 Schematic of preparation of the TiO_2 sol using sol-gel method.

In a typical preparation of the TiO_2 sol, a predetermined amount of SDA was dissolved in IPA. The mixture was stirred for 1 h at the room temperature to ensure complete dissolution of the SDA. After which, HCl was added drop-wise to the mixture. Finally, the hydrolysis and condensation reactions were initiated by the drop-wise addition of TTIP and MilliQ water under vigorous stirring. The homogeneity of the resulting sols was enhanced by continuous stirring at the room temperature for 12-24 h. After the aging period, the final sols were ready for coating and had a constant molar ratio of IPA:HCl:TTIP:H_2O equals to 60:4:1:4.

3.1.4 Preparation of Ag-TiO_2 sols

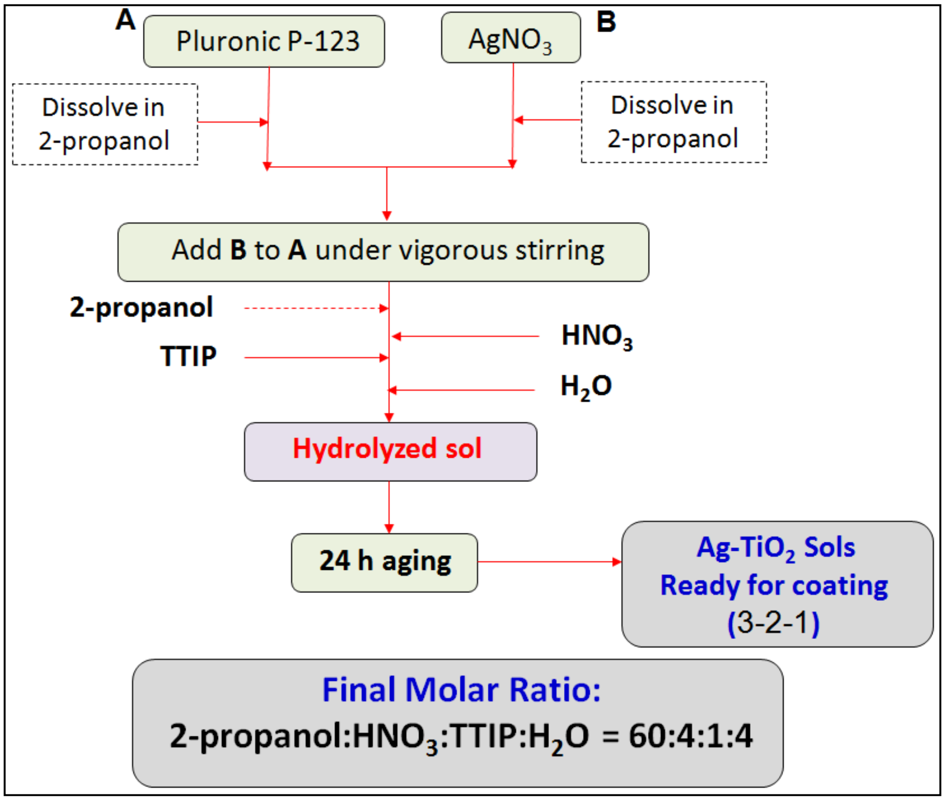

Figure 3.4 Schematic of preparation of the Ag-decorated TiO_2 sol using sol-gel method.

Ag-TiO_2 sol was prepared using the modified acid-catalyzed sol-gel method. Fig. 3.4 summarizes the preparation of the Ag-TiO_2 sol. A predetermined amount of P-123 was dissolved in IPA to obtain solution A. Solution B was prepared by dissolving $AgNO_3$ in IPA and was stirred continuously at room temperature for 1 h to ensure complete dissolution of $AgNO_3$. Solution B was then added drop-wise to the solution A under vigorous stirring. After which, HNO_3 was added into the mixture. Finally, TTIP and H_2O were added drop-wise to the mixture for the hydrolysis and condensation reaction under a vigorous stirring. The resulting sols were stirred continuously for 12-24 h at room temperature to improve its homogeneity. The final Ag-TiO_2 sols had a molar ratio of IPA:HNO_3:TTIP:H_2O equal to 60:4:1:4. Variable amounts of P-123 and $AgNO_3$ were used in the preparation of different sols to obtain Ag-TiO_2 sols that contained 0.5, 1.0, 2.0, 5.0, or 10 wt% of P-123 and 0.5, 1.0, 2.0, 3.0 mol% of Ag (with respect to TiO_2) respectively.

3.1.5 Fabrication of hierarchically porous TiO_2 photocatalytic ceramic membrane

The hierarchical architecture of the TiO_2 photocatalytic ceramic membrane was obtained by coating different sols on the alumina ceramic membrane support. In this architecture, the porosity gradient was obtained through the coating of multiple TiO_2 photocatalytic sub-layers of different pore structures starting from coating of the layer of largest pore size on the Al_2O_3 support, followed by coating of subsequent layers of decreasing pore sizes.

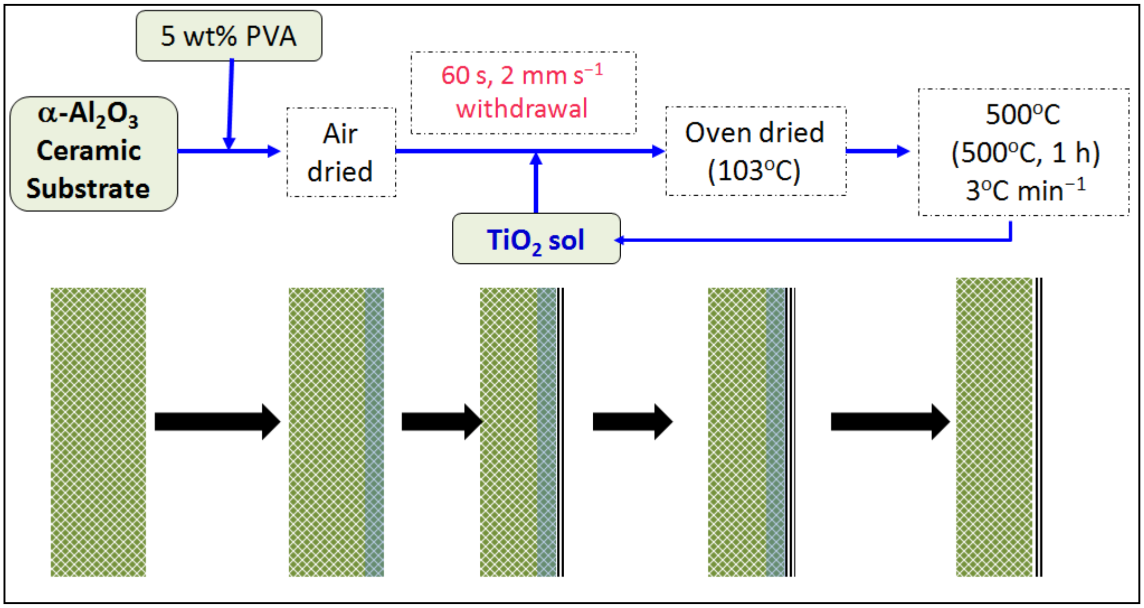

Figure 3.5 Fabrication of hierarchically porous TiO_2 photocatalytic ceramic membrane.

Fig. 3.5 illustrates the step-by-step fabrication of the TiO_2 membrane. One side of the ceramic membrane support was covered with liquid-proof tape to allow only a single-side coating of TiO_2 sols. Prior to the coating, the smoothened alumina ceramic membrane support was first wetted with 5% PVA solution which would fill up the pores of Al_2O_3. This pre-wetting step is essential in order to prevent the possible infiltration of the TiO_2 sol into the macroporous support which would cause pore blocking and decreased porosity of the resulting membrane. The membrane support was dried at the room temperature and then dipped into the designated TiO_2 sol for 60 s using a home-fabricated dip-coater. The coated membrane was withdrawn from the sol at a rate of 2 mm s^{-1}. The coated membrane was first oven dried (103°C, 15 min), then calcined in the muffle furnace (Nabertherm LHT04/16) at 500°C for 1 h (3°C min^{-1} heating rate). The membrane was cooled down naturally to the room temperature and ready for the coating of the subsequent sub-layer. The process was repeated until all the sub-layers have been coated. Ag-TiO_2 membranes were prepared with the similar fabrication steps with the details are delineated in Section 6.2.1.

In order to characterize the microstructure of the TiO_2 layer, a thick TiO_2 layer was coated onto a Petri dish. The resulting TiO_2 layer was then scrapped off, heat treated, pulverized, and stored for its subsequent characterizations. Different TiO_2 layers were also coated on a borosilicate glass for the evaluation of their hydrophilicity. The glass support was cleaned thoroughly and dried at the room temperature and then dipped into the designated TiO_2 sol for 60 s using a home-fabricated dip-coater. The coated glass was withdrawn from the sol at a rate of 2 mm s^{-1}. The coated borosilicate glass was then heat-treated by the same method used for the TiO_2 membrane.

3.1.6 Preparation of microbial strain

Escherichia *coli* (E. *coli*, ATCC® 25922™), a gram-negative bacteria, was chosen as the model bacteria for the anti-bacterial study of Ag-TiO_2 membrane. E. *coli* was inoculated in the tryptic soy broth at 37°C until their mid-exponential growth phase. E. *coli* cells were collected by centrifugation at 10,000 rpm and washed multiple times with 0.9 wt% NaCl (Merck) solution. After decanting the supernatant, the bacterial cell pellet was re-suspended in a 0.9 wt% NaCl solution. The E. *coli* stock solution of approximately 1×10^8 colony-forming units per mL (cfu mL^{-1}) was then prepared for the subsequent anti-bacterial experiments.

3.2 Photocatalytic membrane reactor (PMR) setup

The performance of the hybrid TiO_2 photocatalytic ceramic membrane was evaluated using a photocatalytic membrane reactor (PMR) setup. The membrane cell module (Fig. 3.6) was fabricated using stainless steel SS316 alloy. The chamber volume was 15 mL. The top side of the module (feed chamber) was made of transparent Suprasil® quartz that allows UV penetration to the surface of the mounted membrane. The TiO_2 photocatalytic ceramic membrane was mounted and tightly secured in the membrane cell. A perforated SS316 disk was used as the mechanical support to the TiO_2 membrane.

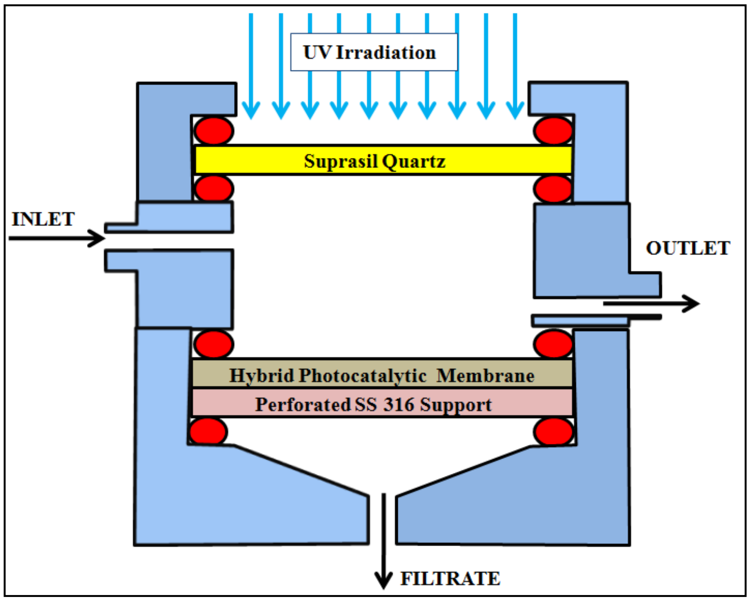

Figure 3.6 Schematic diagram of the membrane cell module.

The cell module was connected to the PMR setup (Fig. 3.7). A high-pressure metering pump (up to 400 bar, 5979 Optos Pump 2HM, Eldex Laboratories) was connected to deliver the feed water. The permeate flux was monitored using an electronic balance and then re-circulated back to the feed tank. The transmembrane pressure (TMP) was recorded using a pressure transducer. Air stream was supplied into the feed tank to provide mixing and oxygen supply that would assist the photocatalytic reaction. The PMR setup with its various safety features was fully controlled by the computer setup.

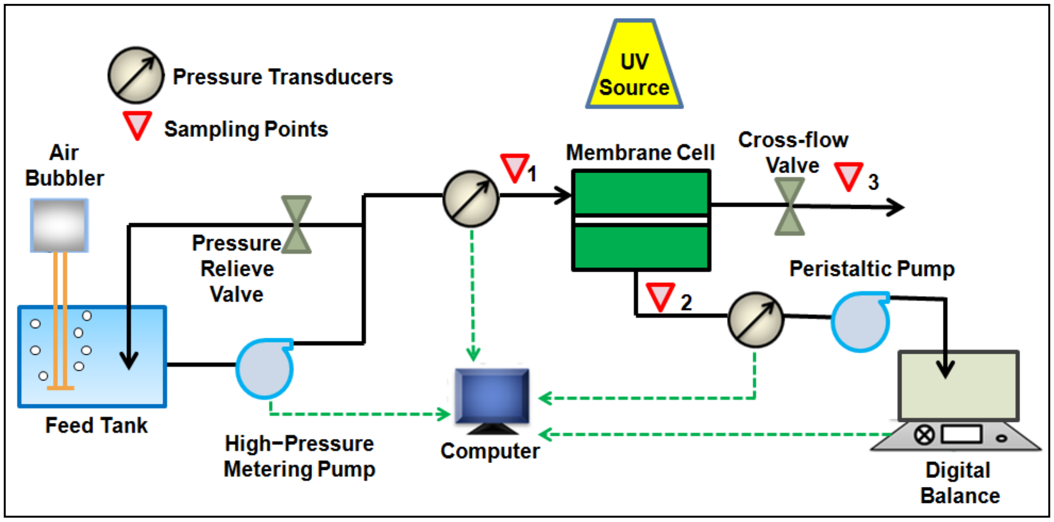

Figure 3.7 Schematic diagram of the PMR setup operating under dead-end filtration mode.

The PMR was operated under a dead-end filtration mode with constant flux. Three sampling points were designated in the setup to allow (1) sampling prior to the inlet of the membrane cell module, (2) sampling at the permeate side, and (3) sampling at the cross-flow outlet for the membrane cleaning step during the anti-bacterial experiment (Chapter 6). UV Labino 135 lamp (Fig. 3.8) (λ_{max} = 365 nm, intensity of 60 W m^{-2} measured on the surface of the RhB solution) was used as the UV-A source for the PCD reaction.

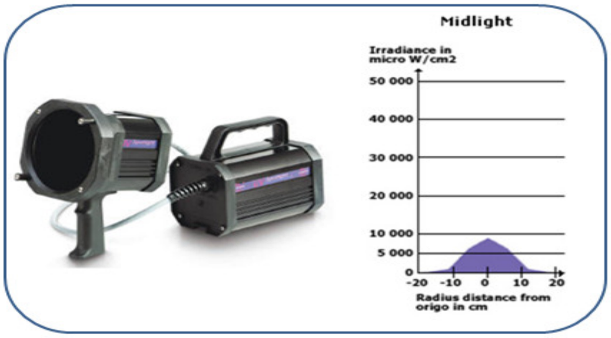

Figure 3.8 UV Labino 135 midlight lamp as the source of UV irradiation.

3.3 Characterization techniques and analytical methods

Nitrogen (N_2) adsorption/desorption isotherms for the porosimetry analysis of the TiO_2 layers were studied using Quantachrome Autosorb-1 Analyzer at liquid N_2 temperature of 77 K. The pulverized TiO_2 powders were degassed overnight at 150°C prior to the actual measurement. The Brunauer-Emmett-Teller surface area (S_{BET}) and Barrett-Joyner-Halenda (BJH) pore size distribution were derived from the result (Barrett et al. 1951, Brunauer et al. 1938).

The mineralogy and crystal structures of the TiO_2 layers were analyzed using X-rays diffractometer (Bruker D8 Advance) with a monochromated high intensity Cu-Kα (λ = 1.5418 Å) radiation over a 2θ range of 5-80° at a scan rate of 1.25° min^{-1}. Scherrer's equation (Scherrer 1918) is used to calculate TiO_2 crystallite size from the peak broadening of (101) anatase crystal plane at 25.3°.

X-ray photoelectron spectroscopy (XPS) studies were conducted using a Kratos Axis Ultra spectrophotometer with a monochromatic Kα excitation source ($h\nu$ = 1486.71 eV). All binding energies for elements of interest were corrected against an adventitious carbon C 1s core level at 284.8 eV. All XPS peaks were fitted using Shirley background together with Gaussian-Lorentzian function using CASA XPS software.

Fourier transformed infra-red (FTIR) spectra were collected using Perkin Elmer 2000 spectrophotometer to investigate the vibrational absorbance and structural characteristics of the TiO_2 layers. Samples for FTIR analysis were prepared by mixing 2 mg of sample with 275 mg of potassium bromide. The mixture was poured into the pellet pounder and was subjected to an initial hydraulic pressure of 10 kN for 1 min followed by 100 kN pressure for another 1 min using an uni-axial hydraulic press. The FTIR spectra were collected from wavenumber of 4,000 to 400 cm^{-1}.

The Raman spectra were recorded using Renishaw RM1000 Raman spectrometer equipped with a Leica x50 Nplan objective lens. The spectra were generated with 50 mW, 633 nm He-Ne laser excitation with power at the sample surface < 2 mW. The Raman spectra were analyzed using Grams32/WiRE 1.3 software.

Scanning electron microscope (SEM) micrographs and energy-dispersive X-rays (EDX) spectra were obtained using a JEOL JSM-7600 FESEM equipped with an Oxford XMX0021 EDX analytical system. Prior to the analysis, the samples were coated with platinum using sputter coater to reduce the effect of surface charging.

High resolution transmission electron microscope (HRTEM) micrographs were obtained using a JEOL JEM-2010, operating at an accelerating voltage of 200 kV. Prior to the TEM analysis, the samples were ultrasonicated in ethanol for 10 min and then transferred to the copper grid for the analysis.

An atomic force microscope (AFM) (Park System) was used to study the morphology and relative surface roughness of the resulting TiO_2 photocatalytic membrane. A non-contact cantilever (PPP-NHCR-10M) was used to scan the surface of the TiO_2 photocatalytic membrane.

Rheological characteristic of the TiO_2 sols was investigated using a rheometer (Physica MCR 101, Anton Paar). The measurements were carried out using a 25 mm measuring plate (CP25-1) under a steady-state shear rate ranging from 0.1 to 100 s^{-1} at 25 °C. The viscosity of dope solutions was recorded at the shear rate of 50 s^{-1}.

Contact angle of the TiO_2 film coated on glass substrate was measured using video contact angle device (VCA Optima, AST Products). Droplet volume of 1 μL was dispensed from a 100 μL syringe.

The extent of RhB degradation was determined by measuring its light absorbance at 553 nm with an UV/Vis spectrophotometer (Genesys 10vis, Thermo Spectronic). Full spectra of RhB visible light absorption (from 600-450 nm) over the duration of the photocatalytic degradation were collected using UV/Vis-1700 Spectrophotometer (Shimadzu).

The concentration of PEG in the membrane retention capability experiments was determined with ASI-V TOC Analyzer (Shimadzu). The total-Ag concentration in the Ag leaching experiments (Section 3.4.4) was quantified using an inductively coupled plasma-mass spectrophotometer (ICP-MS, Perkin Elmer Elan DRC-e).

3.4 Experimental procedures

3.4.1 Determination of photo-induced super-hydrophilicity

Contact angle of the TiO_2 or Ag-TiO_2 films coated on the borosilicate glass substrate was measured using video contact angle device (VCA Optima, AST Products). Prior to the contact angle measurement, the TiO_2 thin film was left in the dark for 24 h to remove any residual photo-induced super-hydrophilicity. The glass slide was then irradiated under UV for 1 h. For the measurement of the photo-induced super-hydrophilicity evolution of the representative TiO_2 thin film specimen, the contact angle was recorded at 0, 8, 24, and 48 h after the irradiation. The film was stored in the dark between each reading. For the rest of the thin film specimens, their contact angles were measured immediately after 1 h of UV irradiation.

3.4.2 Photocatalytic degradation experiments using batch photoreactors

The photocatalytic activity of TiO_2 photocatalytic ceramic membrane was evaluated in the batch photoreactor system. In a typical experiment, the membrane was fully submerged in 12 mL solution of RhB. The disk was left in the dark for 60 min to achieve RhB adsorption-desorption equilibrium. After the dark adsorption process, the TiO_2 batch photoreactor was subjected to UV irradiation (λ_{max} = 365 nm with intensity 60 W m^{-2} measured on the surface of the RhB solution). There was no stirring or oxygen bubbling during the whole duration of the experiment in the batch photoreactor. Two mL of the solutions was taken at regular time intervals to evaluate photocatalytic degradation of RhB by measuring its light absorbance at 553 nm. After the measurement, the solution was immediately returned to the batch photoreactor in order to maintain a constant working volume throughout the duration of the PCD experiment. The extent of mineralization of RhB solution was also studied using TOC.

3.4.3 Photocatalytic degradation experiments using PMR

Prior to the commencement of the experiment, the system was rinsed with Millipore ultrapure water to remove any possible impurities and to allow the permeate flux to reach a steady state. TiO_2 photocatalytic membranes were secured on the membrane cell module for performance evaluation of experiments using the PMR. The pure water permeability was determined by feeding Millipore ultrapure water into the reactor at various constant fluxes, and the resultant TMP values were recorded. PEG solutions (500 mg L^{-1}) of different molecular weights were fed into the reactor in order to determine molecular weight cut off (MWCO) of the membrane. As the standard protocol to compare the membrane retention capability, PEG solution (20,000 g mol^{-1}, 500 mg L^{-1}) was fed into the PMR setup. After the steady-state flux was achieved, permeate was collected to determine the concentration of PEG.

The TiO_2 membranes were used to treat 100 mL of 25 μM RhB solution. The PMR setup was fed with the RhB solution and was left in the dark for 60 min to achieve the RhB adsorption-desorption equilibrium. After which, the pump and UV source were turned on to commence the experiment. In this experiment, permeate was re-circulated back to the feed tank. Control experiment was performed without UV to quantify the contribution of Ads-MR on the total RhB removal by the membrane.

The TiO_2 membranes were also tested for its reusability potential. In this study, the membrane was used for 4 cycles, each to treat 100 mL of 25 μM RhB fresh solution. At the end of each cycle of 8 h experimental run, the feed was replaced with MilliQ water. This was to clean the membrane under UV irradiation for 2 h, after which the fresh 25 μM RhB solution was fed into the reactor for the subsequent cycle of the experiment run.

3.4.4 Silver leaching experiments

The as-prepared membranes were immersed in MilliQ water (30 mL) to determine the total-Ag leaching (i.e. Ag^+ ions and Ag nanoparticles) from the membrane. Prior to the total-Ag leaching test, all glasswares were soaked in 10% (v/v) HNO_3 for 24 h to prevent cross-contamination. Triplicate aliquots (0.5 mL) were taken at regular intervals (up to 168 h immersion in MilliQ water) and digested in HNO_3 (150°C, 1 h) using a Hach DRB 200 digestion unit. Total-Ag leaching from the membrane operated in the PMR was also quantified. Each type of Ag-TiO_2 membranes was secured in the membrane cell module. MilliQ water was fed into the PMR with a constant flow rate of 4 mL min^{-1}. Triplicate aliquots (0.5 mL) of permeate were taken at regular time interval (up to 480 min) and digested in HNO_3. The total-Ag concentration in the aliquots was quantified using an inductively coupled plasma- mass spectrophotometer (ICP-MS, Perkin Elmer Elan DRC-e).

3.4.5 Diffusion inhibition zone experiments

Diffusion inhibition zone of various Ag-TiO_2 membranes with different hierarchical architectures were examined according to the standard Kirby-Bauer approach (Bauer et al. 1966). The diffusion inhibition zone test provides a fast qualitative indication of the effectiveness of the Ag-TiO_2 membrane to inhibit the growth of bacteria cells. An aliquot (200 μL, 1×10^8 cfu mL^{-1}) of each bacterial inoculums were spread evenly on the triptic soy agar plates. Different types of Ag-TiO_2 membranes were placed on different agar plates with the photocatalytic layer facing down (in contact) with the agar surface. The development of the diffusion inhibition zone was examined after incubation at 37°C for 24 h.

3.4.6 Photocatalytic disinfection experiments using batch reactor

Prior to the anti-bacterial experiments, all glasswares were autoclaved (121°C, 15 min) and UV-irradiated (254 nm, 15 min) in order to avoid any contamination. Different Ag-TiO_2 membranes were immersed in 30 mL of E. *coli* bacterial suspensions (1×10^8 cfu mL^{-1}, pH 7.0 ± 0.1) which was kept in the dark. Control experiments were carried out without membrane or using Plu D membrane (which contained no Ag). Aliquots of the E. *coli* suspensions were drawn after 15 min of immersion. Serial dilutions of the aliquots were performed using 0.9 wt% NaCl solution. 100 μL of the aliquots of appropriate dilutions were streaked on the tryptic soy agar plates and incubated at 37°C for 24 h. After which, the colonies were enumerated to quantify the amount of active cells. All data were obtained from at least three replicates of experimental runs. Each membrane was used for 4 cycles of batch experiments.

3.4.7 Photocatalytic disinfection experiments using PMR

Ag-TiO_2 photocatalytic membranes were secured on the membrane cell module (Fig. 3.6) to evaluate its anti-bacterial performance in the PMR. The membrane cell was fed with 120 mL of E. *coli* bacterial suspension (1×10^7 cfu mL^{-1}, pH 7.0 ± 0.1) with a constant flux of 4 mL min^{-1}. Aliquots of permeate were collected at regular time intervals of 5, 15, and 30 min respectively. The corresponding flux values were also recorded at the same time intervals. The control experiments without UV were also performed.

After 30 min of treatment cycle, the feed was replaced with 120 mL of 0.9 wt% NaCl solution. The NaCl solution was fed at a constant flux of 8 mL min^{-1} while opening the cross-flow valve in order to dislodge any deposited bacterial cells from the surface of the membrane. At the end of 15 min cleaning cycle, an aliquot from cross-flow outlet was collected. The whole procedure was repeated 4 times in order to discern the reusability potential of the membrane. All of the collected aliquots were diluted to the appropriate concentration and enumerated on the agar plates. All data were obtained from at least three replicates of experimental runs.

3.4.8 Bacterial repair

In order to investigate the ability of bacteria to undergo repair, once the photocatalytic disinfection tests were completed, the treated bacterial suspension was collected and stored in the dark for 48 h. Aliquot of the suspension was spread evenly on the agar plate and enumerated to determine whether the bacteria could undergo dark repair after the photocatalytic disinfection.

CHAPTER 4 HIGH PERMEABILITY TiO_2 PHOTOCATALYTIC MEMBRANE WITH HIERARCHICAL POROSITY: FABRICATION, CHARACTERIZATIONS, AND PERFORMANCES

4.1 Introductions

The integration of heterogeneous photocatalysis and membrane treatment in a hybrid treatment system could be achieved either by separated membrane reactor with photoreactor operated in tandem or integrated membrane photoreactor (Lim et al. 2011). In each case, TiO_2 photocatalyst can be either used in a suspension or in an immobilized system. The former requires catalyst recovery after the photocatalytic treatment process. The latter suffers from mass transfer limitation and has a much smaller number of active sites compared to the former. By anchoring the TiO_2 photocatalyst onto a porous membrane support, or by confining it by means of a membrane, the issue of catalyst recovery can be solved. In addition, it also allows the synergistic coupling of photocatalytic reaction and membrane filtration which promotes mass transfer process through forced permeation. In this context, the crystallite size of the anchored TiO_2 photocatalyst must be optimized in order to achieve a high photocatalytic activity with low membrane resistance. Therefore, there is a need to produce a thin layer of nano-sized photocatalyst anchored on the highly porous membrane surface in order to maintain high water permeation through the membrane.

Ceramic membranes have many advantages as compared to the polymeric membranes such as excellent thermal, mechanical, chemical and biological stabilities, high permeability, easy cleaning, and resistance to UV irradiation (Anderson et al. 1988, Bhave 1991, Burggraaf and Cot 1996, Chang et al. 1994, Guizard et al. 1992). In addition, during membrane cleaning, ceramic materials are resistant to various cleaning agents (e.g., chlorine, acid, and solvent) and they can be sterilized at higher temperatures. Furthermore, ceramic membranes possess a much longer life span compared to polymeric membranes.

Synergistic coupling of photocatalytic activity and membrane filtration was first investigated by Anderson et al. (1988) in which they investigated different sol-gel synthesis techniques to obtain a membrane with controllable pore size. Since then, there are many research efforts to improving the structure and performance of photocatalytic membrane. For instance, Zhang et al. (2006) found an increasing dye removal efficiency that coupled photocatalysis with membrane separation. Wang et al. (2008) developed a pure titania membrane using porous rutile as a support for both separation and photocatalytic degradation of methylene blue. Ma et al. (2009b) synthesized a thick Si-doped TiO_2 layer onto a tubular alumina membrane that showed promising flux and dye removal performance. Ding et al. (2006) fabricated a titania ultrafiltration membrane using a nanoparticle suspension that was effective in rejection of bovine serum albumin. Bosc et al. (2006) prepared a TiO_2 membrane on asymmetric tubular alumina membrane by incorporating polystyrene latex sphere and different amphiphilic molecules as mesostructure-directing agents. Choi et al. (2006d) developed a nanocrystalline TiO_2 membrane with hierarchical properties by using different types of surfactants as the pore forming agent.

Despite these important findings, synergistic coupling of photocatalysis and membrane filtration has long-standing issues which need to be addressed, i.e. the low water permeability and adverse loss of permeation flux over a prolonged usage due to fouling. Besides, there is a need to fine-tune the photocatalytic property and porosity of the membrane in order to obtain an optimum flux and high photocatalytic performance.

In this chapter, the fabrication and performance evaluation of TiO_2 photocatalytic membrane with hierarchical porosity which consists of multiple TiO_2 sub-layers with controllable pore structure is discussed. The overall flux performance could be enhanced by coating TiO_2 sub-layers of a larger porosity on the ceramic support leaving only a thin separating top sub-layer of a smaller porosity on the surface of the photocatalytic membrane. Pluronic P-123 triblock copolymer (hereafter referred as P-123) was incorporated into the TiO_2 sol to fine-tune the microstructure of the resulting gel. P-123 contains incompatible blocks that were able to form a periodic nanostructure via microphase separation. The preliminary investigation suggested that P-123 possessed a good miscibility with the organics solvent that would allow the formation of micellar structure. The resulting pore structure of TiO_2 thin films could be controlled by varying the amount of P-123 added into the TiO_2 sol. The dissolved pollutants could be photocatalytically degraded as they move along the illuminated TiO_2 surface layers.

Various characterization techniques were utilized to understand the physico-chemical and morphological characteristics of the membrane. The performances of the membrane were evaluated both using the batch photoreactor and the continuous flow PMR operated in the dead-end filtration mode. The experiments in batch reactor were performed to provide a quick performance evaluation of each type of membrane and for some experiment that may require a longer duration, while the experiments in the PMR were performed to simulate the real operation in a scale-up reactor.

4.2 Experimental procedures

4.2.1 Membrane fabrication

Six different TiO_2 sols were prepared by acid-catalyzed sol-gel method (Section 3.1.3) using P-123 as the SDA. The sols contained 0.5, 1, 2, 3, 5, and 10 wt% of P-123 respectively. The TiO_2 sols hereafter are referred as P-123-Xwt%, where X is the weight percentage of P-123 added. The TiO_2 sol without P-123 (denoted as P-123-0wt%) was also synthesized as a control.

The hierarchically porous P-123-based TiO_2 photocatalytic membrane was fabricated using layer-by-layer coating of different TiO_2 sols onto the alumina ceramic membrane support. The preparation of the membrane support and the fabrication of the photocatalytic membrane are delineated in Sections 3.1.2 and 3.1.5 respectively. In this hierarchical porous architecture, the porosity gradient was obtained through the coating of multiple photocatalytic layers of different pore structures starting from the layer of largest pore size on the support-photocatalyst interface, followed by the coating of subsequent layers of decreasing pore sizes, leaving only a thin separation layer of smallest pore size.

Table 4.1 Types of P-123-based membrane fabricated

Types	**Sub-layers Coated**[a]			**TiO_2 Loading ($\mu g/cm^2$)**	**Thickness of TiO_2 Coating**[b] **(nm)**
	1st (bottom) Layer	**2nd Layer**	**3rd (top) Layer**		
Plu Control	0	0	0	69.1 ± 5.3	201 ± 21
Plu A	10-10-10	5-5-5	2-2-2	179.6 ± 10.0	896 ± 55
Plu B	10-10	5-5	2-2	123.4 ± 8.6	572 ± 37
Plu C	10	5	2	49.4 ± 5.2	245 ± 21
Plu D	10-10-10	5-5	2	130.3 ± 10.3	598 ± 38

[a] 0, 2, 5, and 10 indicated P-123-0wt%, 2wt%, 5wt%, and 10wt% respectively.

[b] Determined by considering different porosities of each sub-layers and assuming uniform density of anatase of 3.9 $g.cm^{-3}$.

Different types of multi-layer TiO_2 photocatalytic membranes were prepared and summarized in Table 4.1. Each membrane specimen consists of 3 photocatalytic layers. Plu A consisted of 3 sub-layers of P-123-10wt%, followed by 3 sub-layers of P-123-5wt%, and finally 3 sub-layers of P-123-2wt%. Plu B and Plu C consisted of 2 sub-layers and 1 sub-layer of each type of sol respectively. Lastly, Plu D consisted of 3 sub-layers of P-123-10wt%, 2 sub-layers of P-123-5wt%, and a single sub-layer of P-123-2wt%. Plu Control, which consisted of 3 sub-layers of P-123-0wt%, was also prepared as control for the evaluation of membrane performance.

4.2.2 Characterization techniques

Various characterization techniques were used to understand physico-chemical and morphological properties of the membrane (the detailed description of the instrumentation and methodology are presented in Section 3.3). Viscosity of the sol was determined through rheological measurement. Characterization techniques used for the pulverized TiO_2 layer were: N_2 adsorption/desorption (for porosimetry analysis) and XRD. The surface morphological characteristic of the membrane was studied using FESEM. Finally, the photo-induced super-hydrophilicity property of the membrane was observed through the contact angle measurement.

4.2.3 Evaluation of membrane performance

The photocatalytic activity of the membrane in the batch photoreactor (Section 3.4.2) and the PMR (Section 3.4.3) was evaluated against RhB, a common tracer dye and bio-marker which was used as the model pollutant in this study. In a typical experiment using the batch photoreactor, each type of membrane specimens was used to treat 12 mL of RhB solution without any stirring and oxygen bubbling. The extent of the photodegradation of RhB was monitored using UV/Vis spectrophotometer at 553 nm.

The PMR setup (Fig. 4.1) was used to evaluate the performance of the membrane while operating in the dead end filtration mode. The coated membrane disc was mounted and secured tightly in the membrane cells (Fig 3.6). The pure water permeability and the MWCO of the membrane were evaluated using the PMR. The membrane was also used to treat up to 5 cycles of 100 mL of 25 μM RhB solution. The overall RhB removal could be differentiated to 2 different processes: adsorptive-membrane retention (Ads-MR) and photocatalytic activity of TiO_2 (PCA) by the membrane. Control experiments without turning on the UV source were performed to elucidate the effect of Ads-MR on the removal of RhB. Fouling-control property of TiO_2 photocatalytic membrane was examined in the PMR setup for 12 h without re-circulation of the permeate.

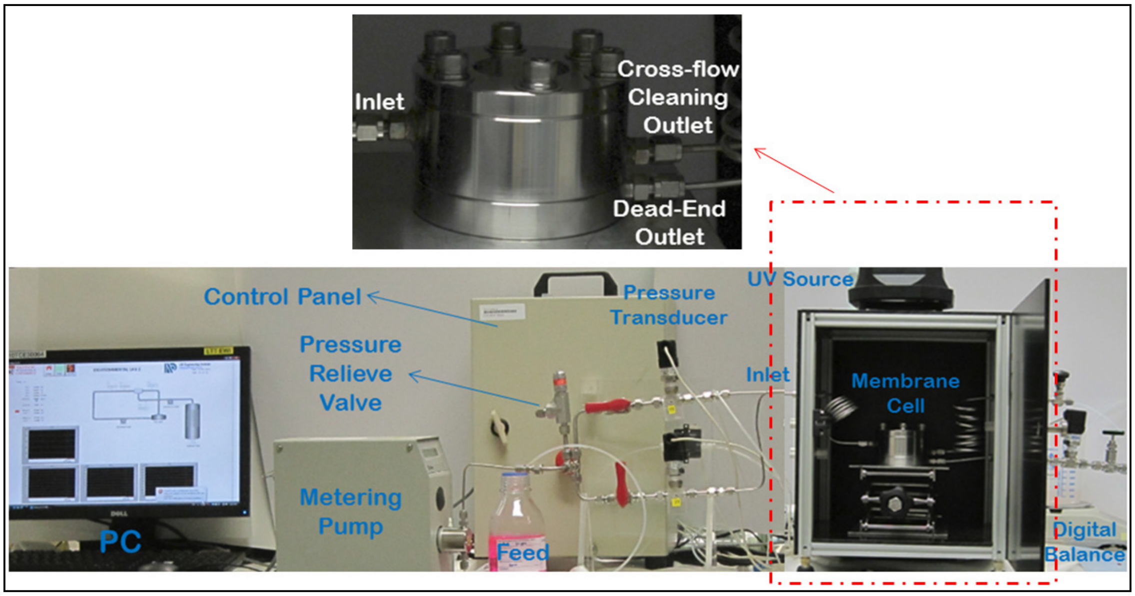

Figure 4.1 Image of the PMR reactor.

4.3 Results and discussion

4.3.1 Physico-chemical characteristics of sols

The as-synthesized TiO_2 sols were transparent and showed good stability in continuous stirring condition at room temperature. TiO_2 sols with the addition of P-123 were relatively more stable over prolonged period of time as compared with P-123-0wt% sol which was only stable for 1 d before it turned chalky. The viscosity of the sols decreased from 0.054 mPa.s for P-123-0wt% to 0.006 mPa.s for P-123-10wt%. This showed that the addition of P-123 lowered the viscosity of the resulting sol and this phenomenon was crucial in fabricating uniform TiO_2 layers with minimal cracks and pinholes.

Table 4.2 Physico-chemical characteristics of the as-synthesized TiO_2 layers

Parameters	**Layers**			
	P-123-0wt%	**P-123-2wt%**	**P-123-5wt%**	**P-123-10wt%**
BET specific surface area (m^2 g^{-1})	12.1 ± 0.4	83.3 ± 1.0	146.6 ± 1.1	200.6 ± 0.9
Pore volume (cm^3 g^{-1})[a]	0.035 ± 0.01	0.14 ± 0.02	0.27 ± 0.01	0.36 ± 0.01
BJH_{ads} pore diameter (nm)	3.11 ± 0.02	5.64 ± 0.02	6.24 ± 0.10	6.55 ± 0.10
BJH_{des} pore diameter (nm)	3.83 ± 0.30	4.36 ± 0.50	5.15 ± 0.40	5.63 ± 0.40
Average pore diameter (nm)[b]	4.28 ± 0.20	6.32 ± 0.40	6.86 ± 0.50	7.12 ± 0.40
BET porosity (%)[c]	11.9 ± 0.3	35.0 ± 0.4	51.5 ± 0.4	58.1 ± 0.4
XRD crystallite size (nm)[d]	14	11	7	6
Viscosity (mPa s)[e]	0.0535	0.0247	0.0094	0.0060

[a] Calculated from BJH desorption curve.

[b] Calculated from BJH desorption curve, and indicating average pore size between primary particles.

[c] Determined by assuming uniform density of anatase of 3.9 $g.cm^{-3}$.

[d] Calculated using Scherrer's equation with error < 1 nm.

[e] As recorded at the shear rate of 50 s^{-1}.

The values of important physico-chemical parameters of the as-synthesized TiO_2 layers are summarized in Table 4.2. Self-organized TiO_2 nanoparticles have been successfully synthesized via acid-catalyzed sol-gel method using P-123 as the SDA. P-123 formed micellar structure via microphase separation due to the difference in hydrophilicity between the polyethylene glycol and polypropylene glycol blocks of the molecules. Attractive forces between TiO_2 hydrate and P-123 formed the mesoporous structure that was crystallized at elevated temperature to form the final oxide (Lu et al. 1997, Procházka et al. 2008). During the heat treatment, P-123 and other organic residue (i.e. IPA) were removed, leaving TiO_2 nanocrystals embedded in the mesoporous structure.

The ability of the SDA to fine-tune the pore size of the synthesized TiO_2 layers was evaluated via N_2 adsorption/desorption isotherms characterization and the result is summarized in Table 4.2. Fig. 4.2a shows that P-123-based TiO_2 layers exhibited a type-IV adsorption isotherm, indicative of well developed mesoporous materials. The difference in the shapes of adsorption and desorption branches of the hysteresis loop could be ascribed to the presence of smaller pores in the titania layers which caused a sharp drop in the desorption branch (Ravikovitch and Neimark 2002). A relatively similar average pore diameter obtained from the BJH adsorption and desorption branches indicates good homogeneity of the pore structures. Table 4.2 shows that as the amount of P-123 increased, the pore size, surface area, and porosity of the TiO_2 layers increased. BET specific surface area of the TiO_2 layers were enhanced from 12.1 $m^2\ g^{-1}$ for P-123-0wt% to 200.6 $m^2\ g^{-1}$ for P-123-10wt%, a 16-fold increase in the surface area by just adding 10 wt% of P-123 as the SDA. By assuming a uniform anatase density of 3.9 $g\ cm^{-3}$, similar trend was also observed for the porosity of TiO_2 layers which showed an increase from 12% for (P-123-0wt%) to 57% (for P-123-10wt%). Higher P-123 concentration caused more pore coalescence and multi-micellar interactions during heat treatment which would result in relatively large pores and high porosity (Choi et al. 2006d).

Fig. 4.2b depicts absence of bimodal pore size distribution which suggests a good uniformity and stability of the sols. BET porosimetry results indicated that by varying the amount of P-123 added, fine-tuning the pore structure of the resulting TiO_2 layers could be achieved. This would allow the fabrication of a hierarchically porous membrane through layer-by-layer deposition of TiO_2 layers of different pore sizes.

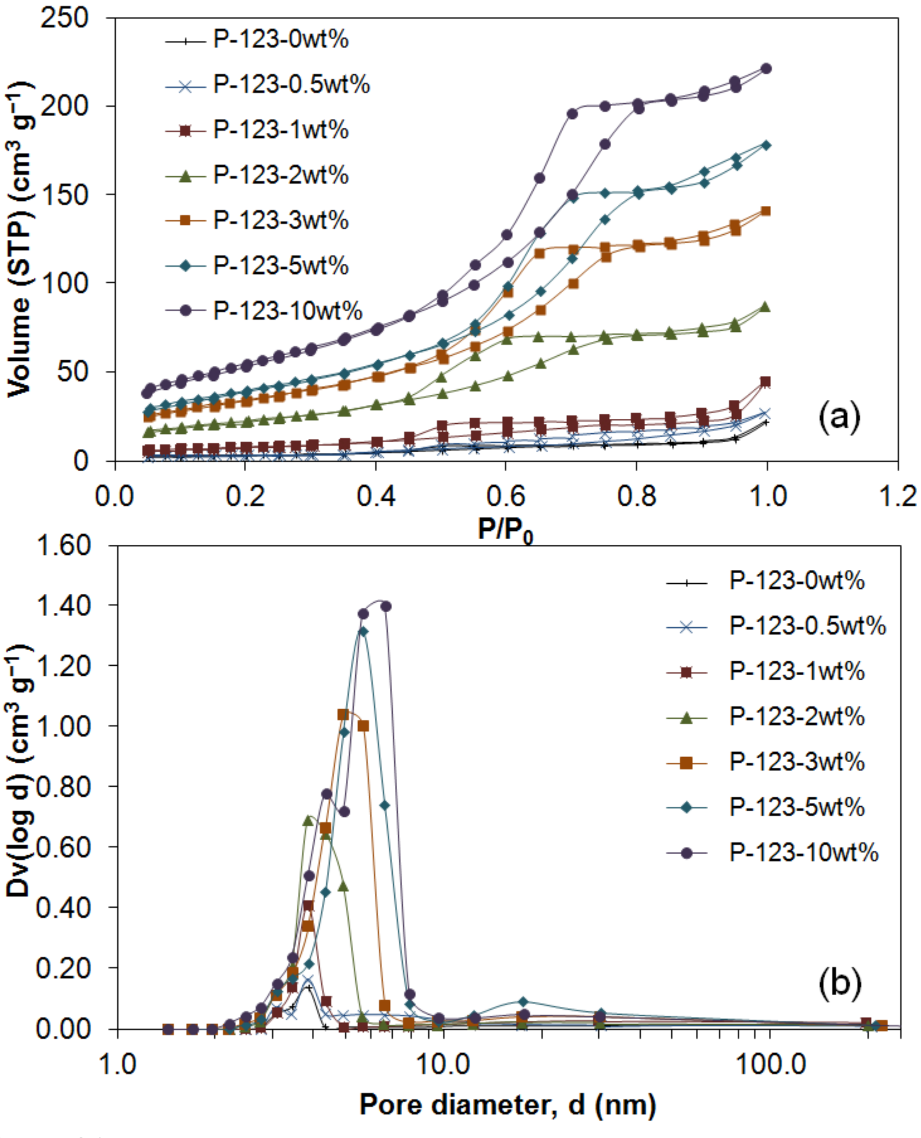

Figure 4.2 (a) N_2 adsorption/desorption curves and (b) pore size distribution of the pulverized TiO_2 layers with different amounts of P-123 added.

The wide-angle XRD spectra of the pulverized P-123-based TiO_2 sols with different amounts of P-123 added are shown in Fig. 4.3. The XRD spectra show five distinctive TiO_2 peaks at 25.3°, 37.9°, 48°, 54.6°, and 62.8° which correspond to (101), (004), (200), (105 and 211), and (204) of crystalline anatase planes respectively (JCPDS 21-1272). No rutile and brookite phases were observed. This indicates that all the P-123-based TiO_2 layers prepared were pure nanocrystalline anatase which was the most photocatalytically active and photostable form of TiO_2 (Gaya and Abdullah 2008, Tanaka et al. 1993b). No amorphous content of the TiO_2 was observed upon calcination indicating that calcination at 500°C was sufficient to induce the formation of anatase crystals (Mazzarino et al. 1999).

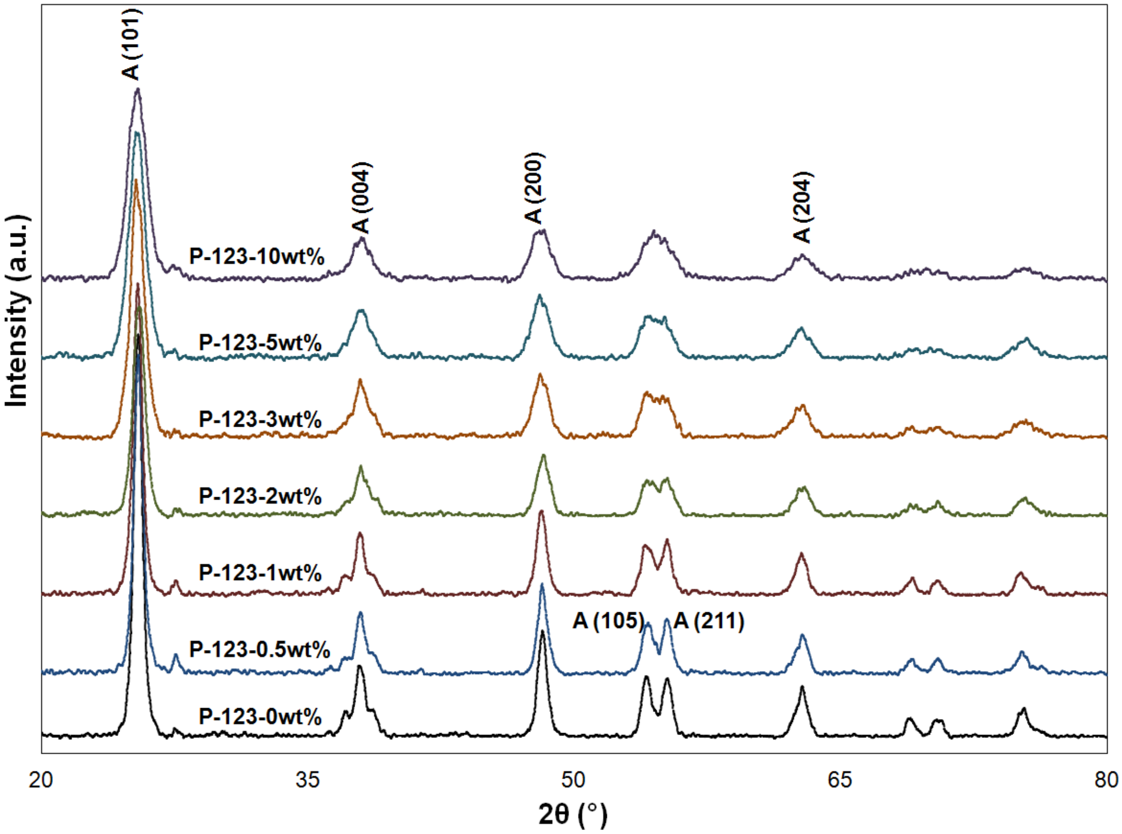

Figure 4.3 XRD spectra of the pulverized TiO_2 layers with different amounts of P-123 added.

Scherrer's equation (Scherrer 1918) is used to calculate TiO_2 crystallites size from the peak broadening of (101) anatase crystal plane at 25.3°. As shown in Fig. 4.3, with increasing concentration of P-123 loading, the intensity of (101) diffraction peak becomes weaker and the FWHM (full width at half maximum) becomes wider, indicating that the TiO_2 grain sizes become smaller. Nanocrystalline TiO_2 was synthesized to ensure a higher overall surface area or denser active catalytic sites of the photocatalyst, which is crucial for achieving a higher photocatalytic activity. However, excessively small crystallite size would cause a blue shift in the absorption spectrum and also induce surface recombination of photo-excited electrons and holes (Anpo et al. 1987, Henglein 1982). The derived TiO_2 crystallite size varied from 14.4 nm for P-123-0wt% to 6.47 nm for P-123-10wt% (Table 4.2). The sizes of as-synthesized TiO_2 crystals are close to the optimum TiO_2 crystallite size for the highest photocatalytic activity as reported in the literature (i.e. ~10 nm) (Zhang et al. 1998). It has been observed that the crystallinity of TiO_2 decreases as the amount of P-123 loading increases. This was evidenced by the overlapping of anatase (105) and (211) reflections on samples with higher P-123 loadings. This highlights the role of the P-123 in limiting the growth of TiO_2 crystals via spatial confinement mechanism (Guldin et al. 2011). TiO_2 anatase network was assembled into an ordered spatial confinement which maintained the structural integrity of the P-123 scaffold.

4.3.2 Characteristics of TiO_2 layers

TiO_2 photocatalytic membrane was fabricated via layer-by-layer deposition of TiO_2 of different porosities. Morphological study of the synthesized membrane could provide a better understanding of the coating process, which is important for tailoring the desired membrane performance. Fig 4.4a shows FESEM micrograph of unpolished support which shows a coarse packing of alumina particles. The support required polishing and PVA layering prior to the coating of TiO_2 sols. The thin PVA coating functioned both as the pores fillers, which prevent TiO_2 sol infiltration to the support, as well as the temporary binder between TiO_2 and the support material. As a binder, PVA increases the strength of the membrane layer (Alem et al. 2009b, Habibi et al. 2007a).

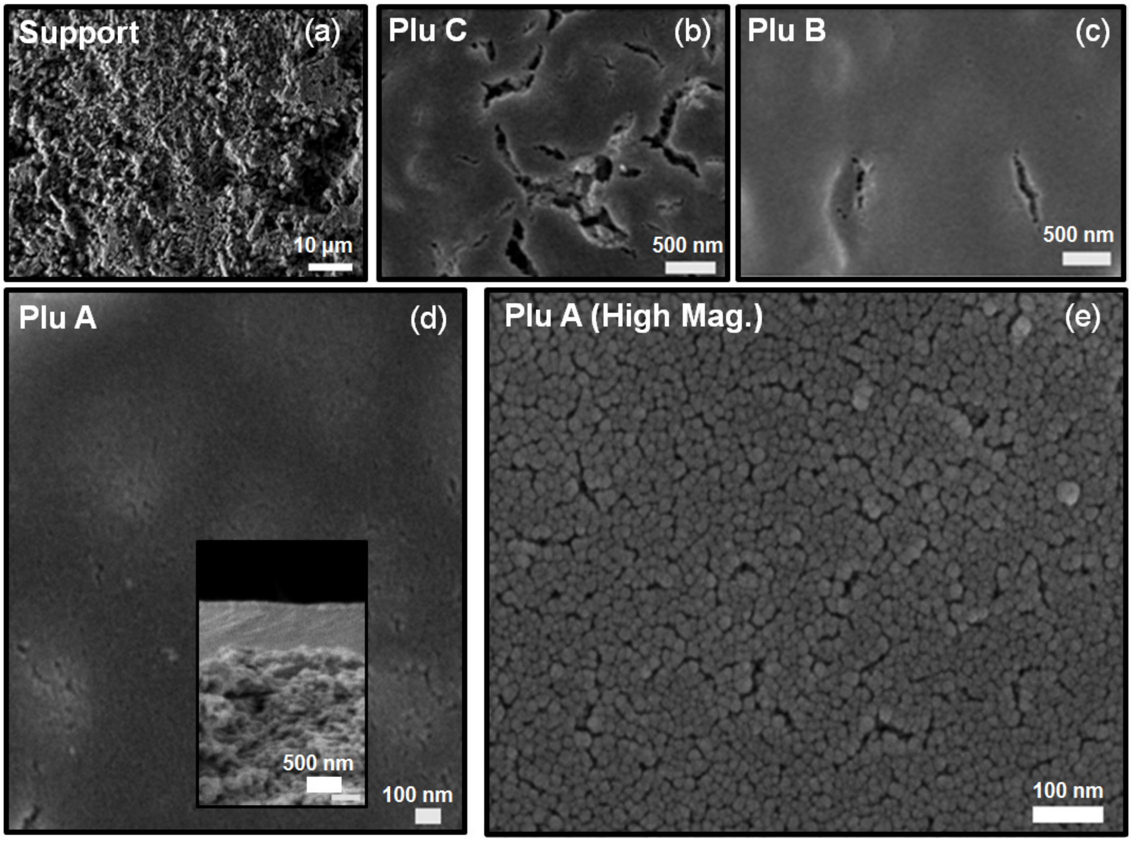

Figure 4.4 SEM micrograph of surface of (a) alumina substrate, (b) Plu C, (c) Plu B, and Plu A membrane at (d) low and (e) high magnification (the inset in (d) depicts cross-sectional view of Plu A membrane).

Figs 4.4b and 4.4c show the surface morphology of Plu C and Plu B membrane respectively. Infrequent cracks and pinholes were evident in Plu C membrane probably due to the thin TiO_2 sub-layers that expand unequally during the calcination process. The cracks and pinholes formation were greatly reduced in Plu B membrane when each type of TiO_2 sols were coated 2 times. The initial coating of the same type of sol functioned as an intermediate layer that smoothen the membrane surface for the subsequent coating. Fig 4.4d shows the FESEM micrograph of the surface of the Plu A membrane which shows a relatively smooth TiO_2 layer coating on the alumina support. The TiO_2 layer consists of ordered arrangement of TiO_2 nanocrystals (as shown in magnified micrograph of Fig. 4.4e) with minimum presence of cracks or pinholes on its surface. This is important to ensure that the membrane has a uniform permeability and membrane retention characteristics. The cross-sectional view of Plu A membrane (inset in Fig. 4.4d) shows that distinct TiO_2 layers were successfully coated on the support. The overall thickness of the TiO_2 layers is around 1 μm.

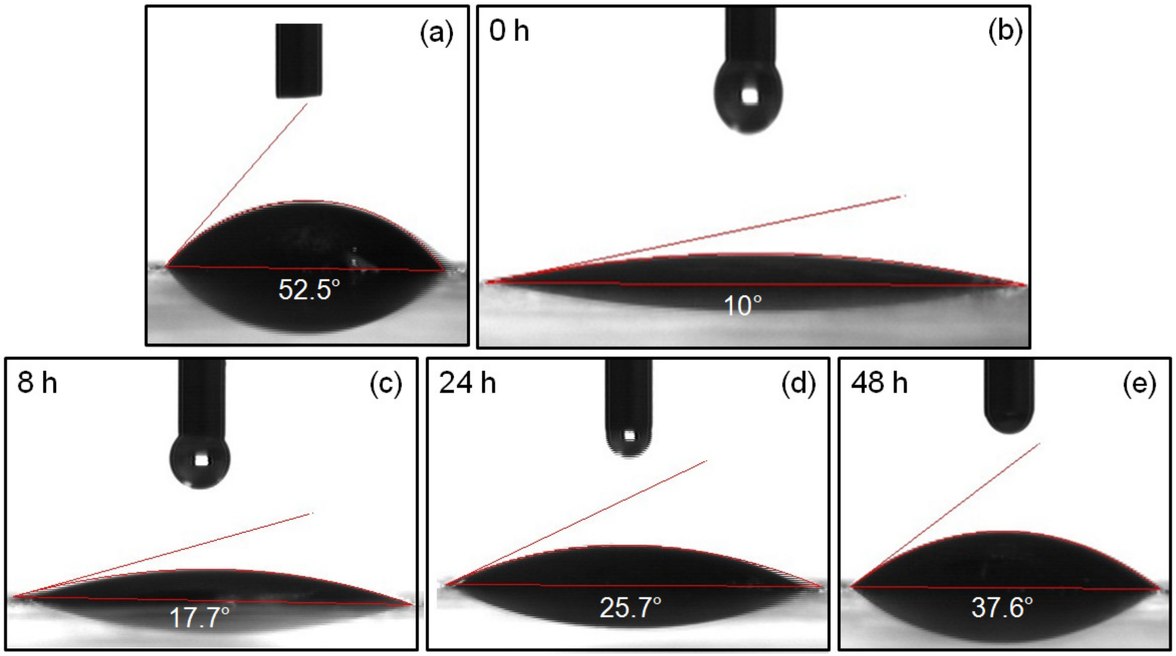

Figure 4.5 Photoinduced super-hydrophilicity behavior of Plu A film coated on a borosilicate glass as shown on **(a)** as-coated sample, **(b)** upon 1 h of UV irradiation, and after **(c)** 8 h, **(d)** 24 h, and **(e)** 48 h left in the dark.

Photo-induced super-hydrophilicity (PSH) is another important characteristic for a good TiO_2 photocatalytic membrane. The contact angle micrographs and their corresponding values are shown in Fig. 4.5. The as-coated P-123-10wt% thin film shows a contact angle of 52.5° which subsequently decreased to 10° after 1 h of UV irradiation. When the UV lamp was switched off, the contact angle increased again to 17.7°, 25.7° and 36.7° after 8, 24, and 48 h respectively. PSH is caused by the hydroxylation of film surface upon UV irradiation. Photo-generated electrons react with lattice metal ions Ti^{4+} to form Ti^{3+} defective sites. Surface-trapped electron in Ti^{3+} will react immediately with oxygen adsorbed on the surface to form O_2^{-} or O_2^{2-} ions leaving the oxygen vacancy sites (Sakai et al. 2003). Even if it was present in almost negligible amount, adsorbed water molecules would occupy the vacancy sites to reduce the surface energy, which in turn would release proton to a nearby oxygen atom and forms two hydroxyl groups at the surface of the photocatalyst.

4.3.3 Pure water permeability of P-123-based TiO_2 photocatalytic membrane

Fig. 4.6 shows the cumulative thicknesses of TiO_2 layers and the resulting pure water flux of Plu A membrane (Table 4.1) after each sub-layer coating. Layer thickness is calculated by measuring the incremental weight of the membrane after each sub-layer coating by considering the porosity of each sub-layer and assuming a uniform anatase density of 3.9 g cm^{-3}. First P-123-10wt% sub-layer is a very thin layer (37 nm) coated on the PVA-filled alumina ceramic support. The initial thin layer could be attributed to the poor adhesion of P-123-10wt% to the PVA-filled alumina support. Subsequent coatings of P-123-10wt% layers yield a relatively similar thickness of 100 nm. A more viscous P-123-5wt% sol was used for forming the subsequent 3 middle TiO_2 sub-layers with average thicknesses of 125, 140, and 134 nm respectively. At this stage, the membrane was relatively smooth so that the addition of the final 3 sub-layers of P-123-2wt% yields relatively thinner sub-layers of 82, 79, and 84 nm, bringing a total thickness of the TiO_2 layers of Plu A membrane to 0.9 µm. This estimation is consistent with the observation using SEM which shows an overall thickness of 1 µm for the TiO_2 layer coated on the alumina support. The pure water flux of Plu A membrane decreased steadily with the increased number of sub-layer coated, from initial 300 L m^{-2} h^{-1} Bar^{-1} to the final 120 L m^{-2} h^{-1} Bar^{-1} after 9 TiO_2 sub-layers being coated.

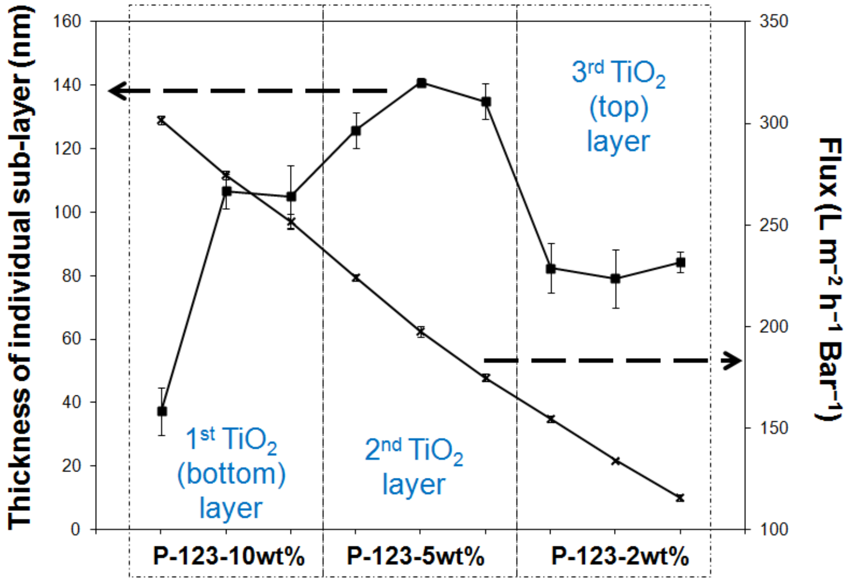

Figure 4.6 TiO_2 layer thickness and the resulting pure water flux of Plu A membrane with respect to the different sub-layers coated.

Fig. 4.7 shows pure water flux and PEG retention of the TiO_2 photocatalytic membrane. MWCO of the TiO_2 photocatalytic membrane was evaluated using 500 mg L^{-1} PEG solutions with molecular weights ranging from 1,500-20,000 g mol^{-1}. The 20,000 g mol^{-1} PEG solution corresponds to PEG molecular size of 12 nm (Choi et al. 2006a). Only Plu A membrane showed an efficient retention of PEG with MWCO of 12,000 g mol^{-1} which corresponds to pore size of 7 nm. This MWCO value is in good agreement with the result obtained from N_2 porosimetry analysis. Plu B and Plu C showed lesser retention of PEG which could be attributed to the lesser number of TiO_2 sub-layers coated (Table 4.1). Plu D showed lower

PEG retention when compared with Plu B which also consisted of a total of 6 TiO_2 layers but with a different porosity gradient. This can be explained by the thicker P-123-2wt% sub-layer in Plu B (2 sub-layers of P-123-2wt% in Plu B as compared to 1 sub-layer of P-123-2wt% in Plu D). Plu Control showed a better PEG retention as compared to Plu C which was could be attributed to the smaller pore size and porosity of Plu Control (reflected by P-123-0wt% in Table 4.2).

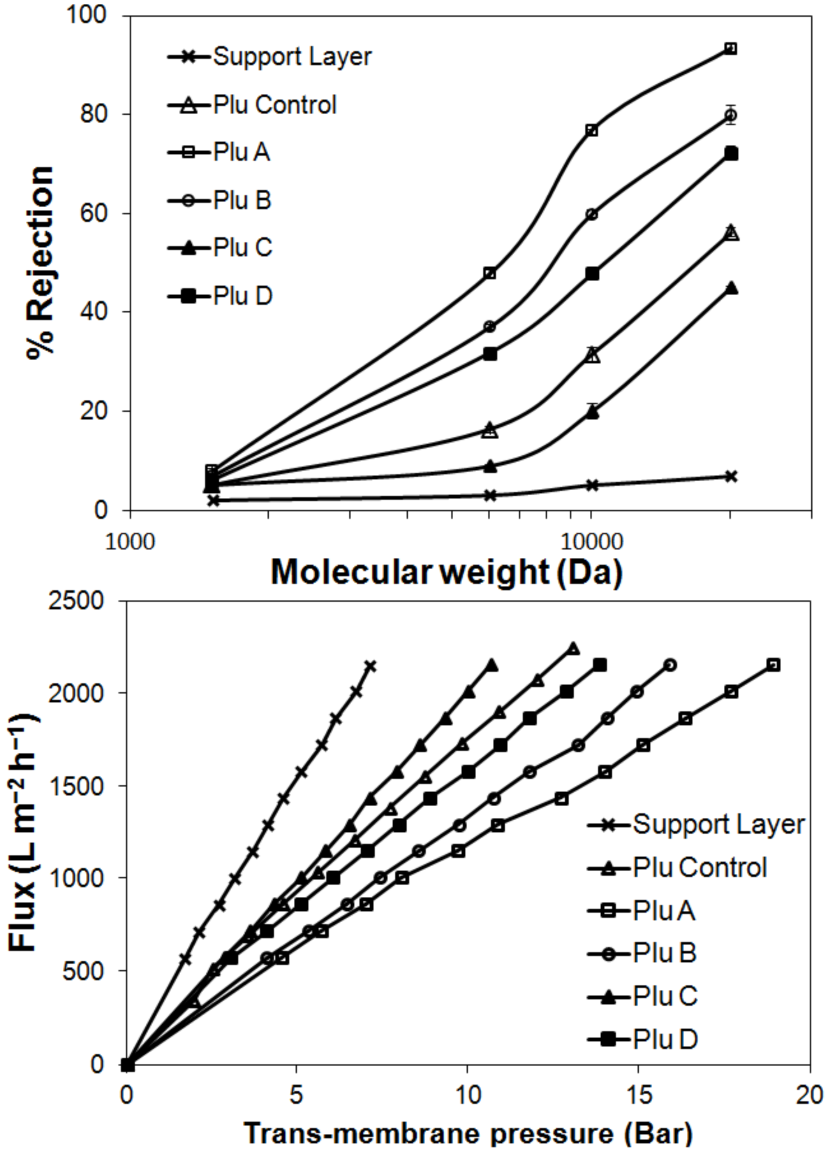

Figure 4.7 (a) PEG retention and (b) pure water permeability of P-123-based TiO_2 photocatalytic membrane.

Fig. 4.7b shows that the water permeability flux increases linearly with the TMP regardless of the type of TiO_2 layer deposited. The pure water permeability of Plu C membrane was 202 L m^2 h^{-1} Bar^{-1} which was slightly lower than that of the support layer (309 L m^2 h^{-1} Bar^{-1}). This showed that TiO_2 layers in the Plu C membrane formed a very thin porous film which only induced a minimal effect on the membrane filtration resistance. The effect of the coated layers on the pure water permeability can be evaluated by its intrinsic membrane resistance, R_m (m^{-1}), as defined below:

$$R_m = \frac{(\Delta P)At}{\mu V} \tag{4.1}$$

where ΔP is the TMP (Pa), μ is the kinematic viscosity of the liquid (1×10^{-3} Pa s), V is the volume (m^3) of liquid flowing through the membrane, A (m^2) is the surface area of the membrane and t is the filtration time (s).

The intrinsic membrane resistance of the ceramic support layer is 1.17×10^{12} m^{-1}. As the number of sub-layers of each types of the sol coated increased from 1 sub-layer (Plu C), 2 sub-layers (Plu B), and 3 sub-layers (Plu A), the corresponding intrinsic membrane resistance increased from 1.79×10^{12} m^{-1} to 3.11×10^{12} m^{-1}. As the structure of the 6 sub-layered membrane was varied, a lower intrinsic membrane resistance (higher pure water permeability) was obtained for Plu D membrane ($R_m = 2.25 \times 10^{12}$ m^{-1}) as compared to Plu B membrane ($R_m = 2.68 \times 10^{12}$ m^{-1}). This could be attributed to a thinner top separation layer (P-123-2wt%) of Plu D which allowed a higher flux. It has been found that the intrinsic membrane resistance of the P-123-based TiO_2 photocatalytic membrane is significantly lower than those reported in the literature (Choi et al. 2006d). The low intrinsic membrane resistance or high water permeability flux could be attributed to the photo-induced super-hydrophilicity property of the TiO_2 membrane. This is very important for membrane separation process, i.e.

high flux reduces the overall energy consumption in the water and wastewater treatment processes.

4.3.4 P-123-based TiO_2 photocatalytic membrane performances

4.3.4.1 Photocatalytic activity using batch photoreactor

Batch experiments were carried out to evaluate the photocatalytic activity of different structures of TiO_2 photocatalytic membrane and the results are presented in Fig. 4.8a. For a total degradation time of 8 h, Plu A membrane was able to remove > 90% RhB. Plu B and C removed 81% and 75% RhB respectively, which could be attributed to their lesser amount of TiO_2 coated on the membrane. Plu D removed 88% of initial RhB concentration, higher than that of Plu B which was also consist of 6 layers but in different structures. Plu Control showed the least amount of RhB removal (68%) which could be attributed to its smaller overall surface area of the membrane whereby RhB could be adsorbed and photodegraded. Plu A membrane was chosen as a representative sample to study the kinetics of RhB degradation and the results are presented in Fig. 4.8b. The photolysis of RhB at 25 μM under continuous UV irradiation (without the presence of the membrane) was < 5 %. In the presence of photocatalytic membrane, mass transfer rate, intra-layer pollutant diffusion, and adsorption/desorption equilibrium would affect the rate of RhB photocatalytic degradation by the membrane.

Generally, a pseudo-first order kinetic model can be used to model such photocatalytic degradation process. However, using this model, the derived reaction rate constant decreased with increasing initial concentration (6.25 to 100 μM RhB solution). Therefore, Langmuir-Hinselwood model (Eq. 4.2) is adopted to evaluate the RhB degradation kinetics.

$$\frac{1}{r_o} = \frac{1}{\kappa K}\frac{1}{C_o} + \frac{1}{\kappa} \tag{4.2}$$

where r_o is the initial reaction rate (mg L^{-1} min^{-1}), κ the Langmuir-Hinselwood reaction rate constant (mg L^{-1} min^{-1}), and K the Langmuir adsorption constant (L mg^{-1}). The inset of Fig. 4.8b shows the good fit and the derived values of κ and K was 0.219 mg L^{-1} min^{-1} and 0.06 L mg^{-1} respectively with $R^2 > 0.99$.

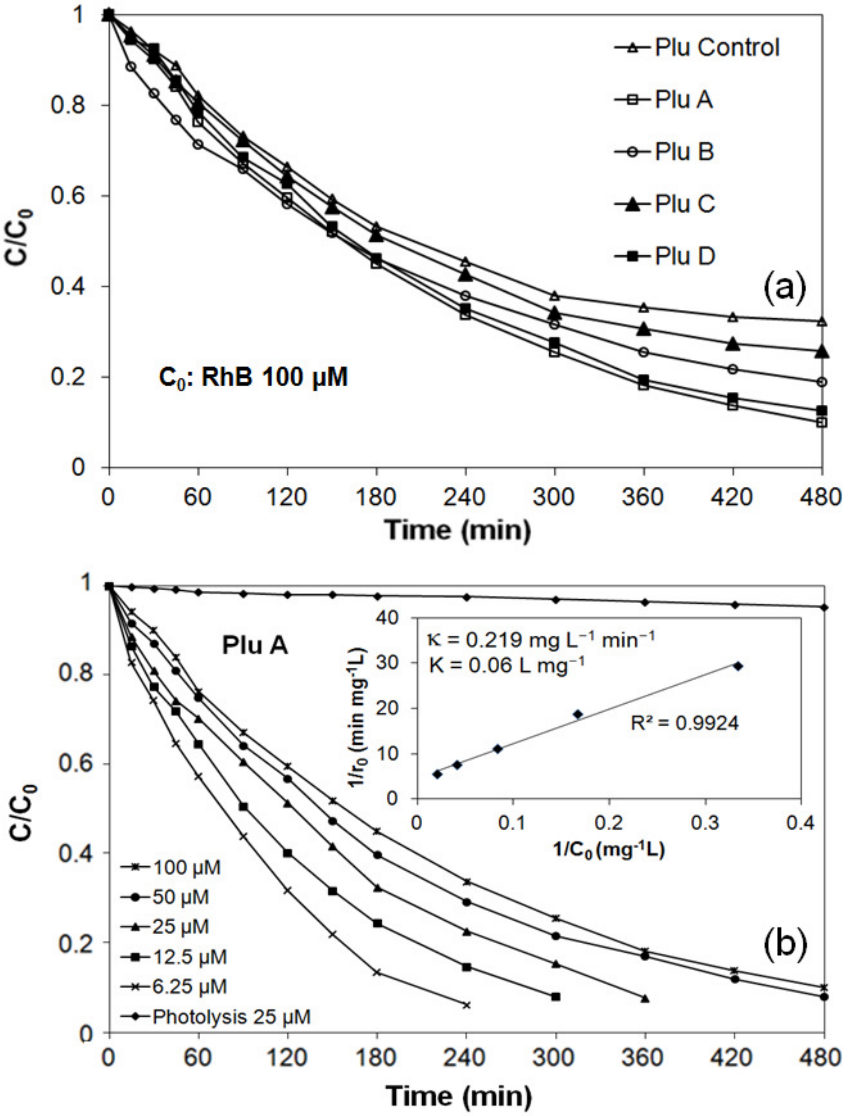

Figure 4.8 Batch result of photocatalytic activity of (a) different configurations of TiO_2 photocatalytic membrane and (b) Plu A membrane at different initial concentrations of RhB (the inset depicts the linear plot of Langmuir-Hinshelwood model).

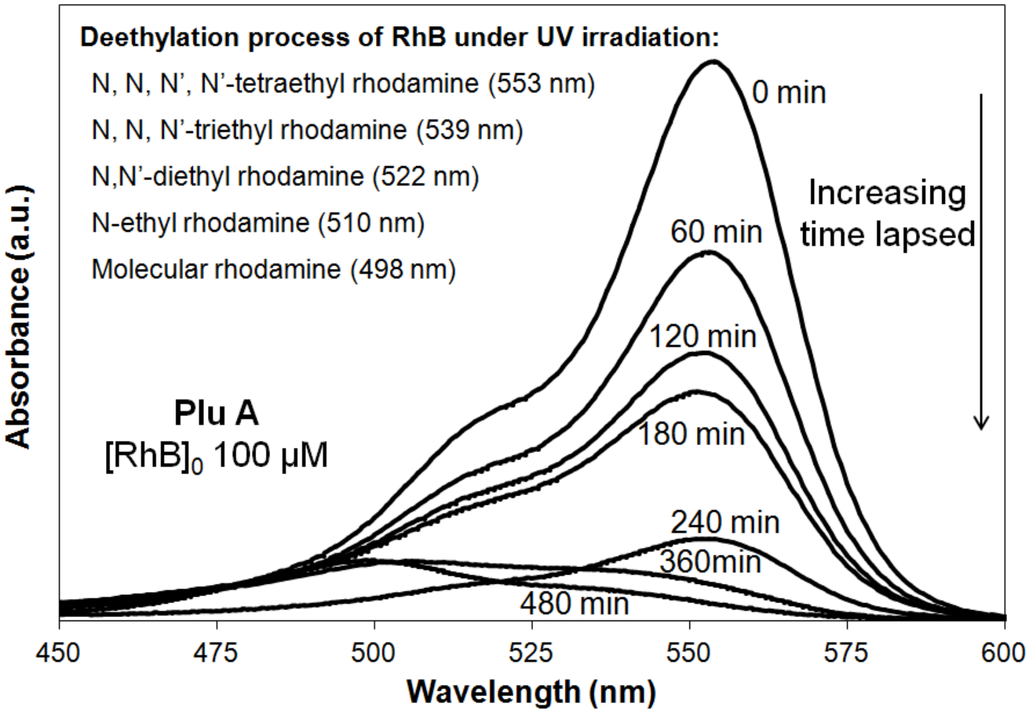

Figure 4.9 Shift of RhB maximum light absorption peak over the duration of the photocatalytic degradation process.

RhB degradation can be monitored by shifting of RhB light absorption over the duration of photocatalytic degradation experiment. Fig. 4.9 shows time-dependent profile of RhB light absorption (from 600-450 nm) for 100 μM RhB solution photodegraded using Plu A membrane in the batch photoreactor. During the degradation process under UV irradiation, the maximum RhB absorption peak shifts gradually from 553 to 498 nm. The observed color of the RhB solution also changes from the initial red to a light greenish-yellow and finally to a transparent solution. This was due to the step-wise ethyl dissociation (de−ethylation) from N, N, N', N'−tetraethyl rhodamine (553 nm), N, N, N'−triethyl rhodamine (539 nm), N, N'−diethyl rhodamine (522 nm), N−ethyl rhodamine (510 nm) to form a final rhodamine molecules (498 nm) (Xie et al. 2009). It was worth noting that the photodecolorization of chromogenic aromatic ring and dissociation of ethyl occurred simultaneously under UV irradiation. The TOC of treated RhB solutions from the batch photoreactor was measured to determine the extent of mineralization. It has been found that all the treated solutions showed a final TOC concentration < 1 mg L^{-1} which was the detection limit of the equipment. This finding indicated > 90% TOC removal from the initial RhB solution (from theoretical TOC of 33.6 mg L^{-1} for 100 µM solution).

4.3.4.2 Photocatalytic activity and flux performance using PMR

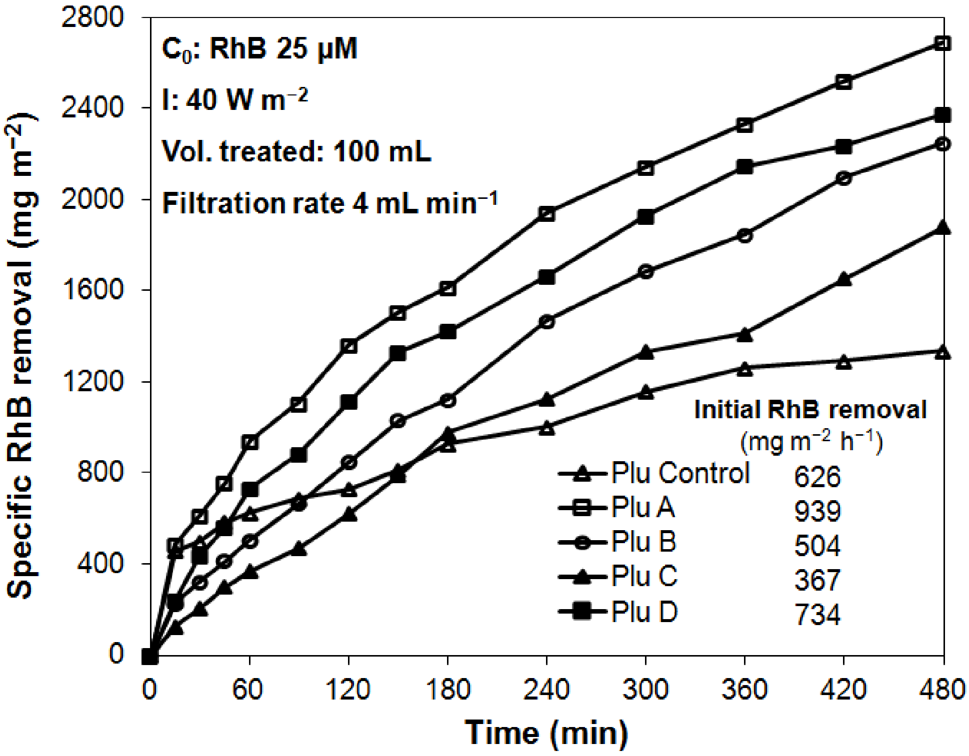

Figure 4.10 Specific RhB removal of Pluronic-based TiO_2 photocatalytic membrane (the numerical values depict kinetic value based on initial RhB removal rate within 1st hour in mg $m^{-2} h^{-1}$).

The results of PMR experiments operated in the dead-end filtration mode are shown in Figs. 4.10 to 4.12. The specific RhB removal efficiency (i.e. the cumulative RhB removal per unit area of membrane over the 8 h duration of experiments in the PMR, mg m^{-2}) by the TiO_2 photocatalytic membrane of different layered structures is illustrated in Fig. 4.10. The numerical values shown in Fig. 4.10 depict the initial rate of RhB removal. Plu A showed highest specific RhB removal of 2700 mg m^{-2} at 480 min. Plu B and Plu C showed declines in specific RhB removal (17% and 31% respectively) compared to Plu A. This can be attributed to the lesser amount of photocatalysts present on the surface of Plu B and Plu C. Plu D showed specific RhB removal of 2400 mg m^{-2}. Interestingly, although Plu D and Plu B have the same number of layers (i.e. 6 layers), the specific RhB removal of Plu D is higher than that of Plu B due to the different configurations of their layered structure.

The overall RhB removal could be itemized into 2 different phenomena i.e. photocatalytic activity (PCA) of TiO_2 and adsorptive-membrane retention (Ads-MR) and they were summarized in Table 4.3. The overall contribution of Ads-MR of RhB to the membrane was relatively small with the exception of Plu Control (47.9%) and Plu A (22.2%, due to its larger TiO_2 loading). Plu Control showed a largest percentage (47.9%) removal of RhB through Ads-MR (which could explain the high RhB removal efficiency at the initial stage of the PMR experiment) while Plu C, the thinnest membrane showed the smallest contribution of Ads-MR. The contribution of Ads-MR to the overall RhB removal by Plu D was smaller than that of Plu B which could be attributed to its hierarchical porous structure. All of the P-123-based TiO_2 photocatalytic membranes showed a large contribution (up to 88%) of PCA to the overall removal of RhB. These results suggest that by tailoring the porosity gradient of the layered structure, the overall membrane performance could be improved. Membrane with more porous layers near the support exhibited a better RhB separation and water permeability characteristic.

Table 4.3 Membrane performance in terms of its photocatalytic activity (PCA) and adsorptive-membrane retention (Ads-MR) after 8 h of operation

Types	Removal (mg m^{-2})			Removal (%)	
	PCA	Ads-MR	Total	PCA	Ads-MR
Plu Control	686 ± 36	630 ± 23	1316 ± 20	52.1	47.9
Plu A	2104 ± 31	600 ± 17	2704 ± 13	77.8	22.2
Plu B	1905 ± 21	378 ± 20	2283 ± 10	83.4	16.6
Plu C	1654 ± 18	230 ± 11	1884 ± 18	87.8	12.2
Plu D	2025 ± 24	329 ± 13	2354 ± 18	86.0	14.0

Fouling-control property of the TiO_2 photocatalytic membrane is illustrated in Fig. 4.11. The initial decline of flux rate could be attributed to the adsorption of RhB molecules onto TiO_2 photocatalytic membrane. After which, decreasing flux rate was observed until the sustainable (steady state) flux was reached. It has been observed that the PMR experiment with the presence of UV irradiation suffered only 16.5% of total flux decline over 720 min of experimental run as compared to 42% for the PMR experiment without UV irradiation. This could be attributed to a good wettability and self-cleaning induced by photocatalytic membrane surface. The results suggested that TiO_2 layers were able to minimize and control fouling as they could photodegrade the adsorbed RhB molecules and minimize the flux decline throughout the duration of the experimental run.

Reusability of membrane could significantly lower the operation cost of water and wastewater treatment plants. A Plu A membrane specimen was used for 5 treatment cycles of 25 μM RhB solutions, and the results are shown in Fig. 4.12. Plu A membrane was able to degrade a relatively same amount of RhB over multiple cycles of 8 h each. The 5th cycle of treatment still showed 91% of the initial RhB removal efficiencies (a 9% drop from 2690 to 2460 mg m^{-2} of RhB). The slight decrease in the RhB removal with increasing treatment cycle could be explained by the accumulative adsorption of RhB onto the surface of the membrane that reduced the density of active photocatalytic sites.

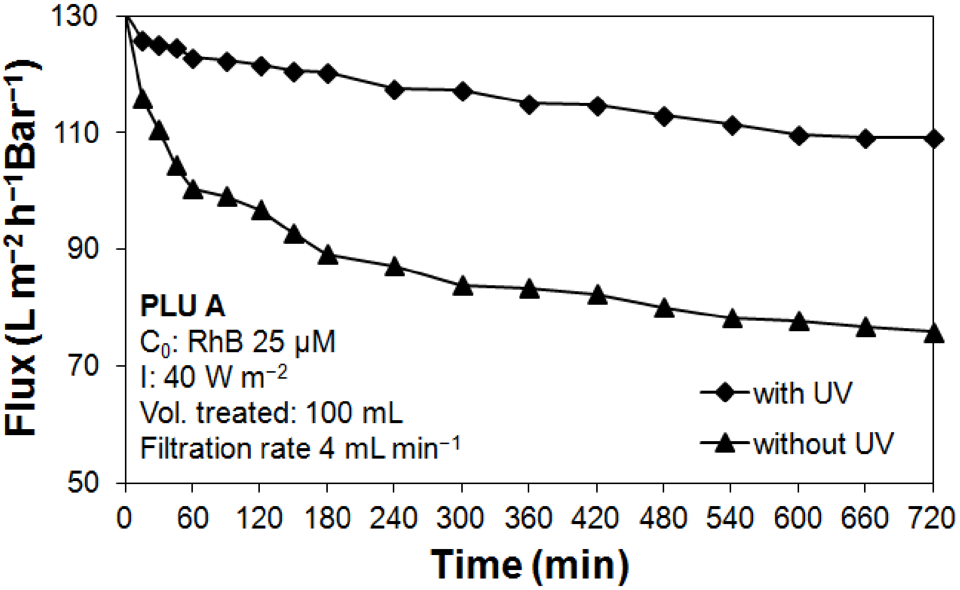

Figure 4.11 Anti-fouling property of TiO_2 photocatalytic membrane.

Similar trend was observed for the flux profile. In each cycle, the permeability flux decreased with permeation time. However, upon each cleaning cycle with DI water under UV irradiation for 2 h, more than 95% of the initial flux could be recovered. Cleaning with DI water without the presence of UV irradiation (Fig. 11(b) and (c)) only recovered about 57% of the initial flux after 5th cycle of treatment and meanwhile the RhB removal efficiency also dropped to 56% of its initial efficiency. This showed that with intermittent UV-assisted self-cleaning, the TiO_2 photocatalytic membrane was reusable over a prolonged period without a significant flux decline and deactivation.

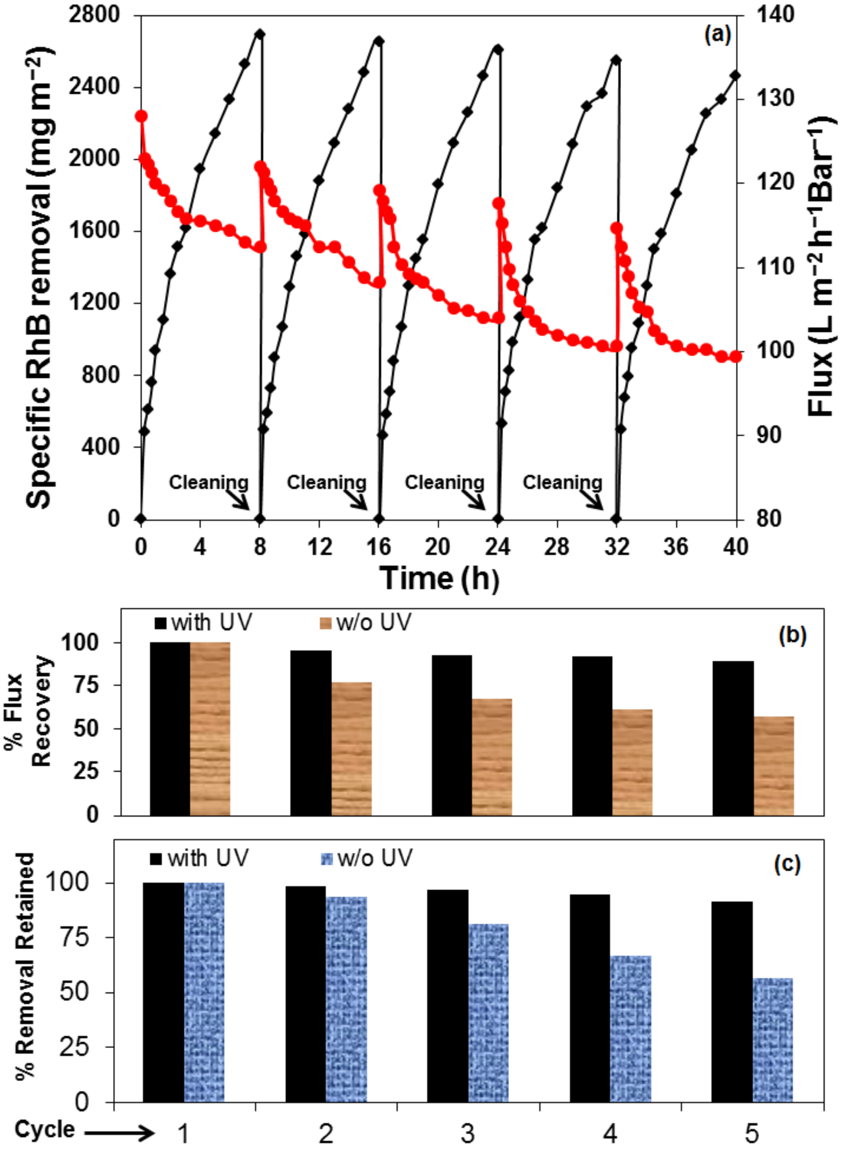

Figure 4.12 Reusability potential of the TiO_2 photocatalytic membrane: (a) specific RhB removal and flux performance with inter-cycles cleaning in the presence of UV irradiation; comparison of the effect of UV irradiation during inter-cycles cleaning in terms of (b) % flux recovery and (c) % RhB removal retained.

4.4 Conclusions

TiO_2 photocatalytic membrane was fabricated via acid-catalyzed sol-gel method incorporating Pluronic P-123 triblock-copolymer as pore forming agent and PVA as pore fillers and binder. Layer-by-layer coating of TiO_2 of different porosities and pore structures were thoroughly carried out. The resulting membranes were characterized for its physico-chemical and morphological characteristics. The membranes showed excellent photocatalytic activity when tested in the batch photoreactor. The Plu A membrane (which was coated with 3 different TiO_2 layers of different pore structures) showed a high water permeability flux of 116 L m^2 h^{-1} Bar^{-1} with the corresponding intrinsic membrane resistance of 3.1×10^{12} m^{-1}. Plu A membrane also possessed excellent specific RhB removal of 2700 mg m^{-2}. The membrane with a thinner top separation layer (Plu D) showed a higher water permeability flux and specific RhB removal when compared with the membrane with the same number of layers but a thicker separation layer (Plu B).

The result suggested that by tailoring the layered structures (porosity gradient), an optimum membrane performance could be obtained. The as-synthesized hybrid photocatalytic membrane has a great potential for use in water and wastewater treatment owing to its fouling-control capability, high intrinsic permeability, good photocatalytic activity, and reusability potential. These properties are favorable for practical applications of membrane separation processes. The integration of the heterogeneous photocatalysis and membrane process in the membrane photoreactor offers simultaneous photodegradation and membrane separation, simpler system configuration with less mechanical and hydraulic fittings, and smaller overall footprint (Lim et al. 2011).

CHAPTER 5 EFFECT OF DIFFERENT STRUCTURE DIRECTING AGENTS ON THE PERFORMANCES OF THE HIERARCHICALLY POROUS TiO_2 PHOTOCATALYTIC CERAMIC MEMBRANES

5.1 Introductions

The porous structure of the TiO_2 layer could be formed and fine-tuned by incorporating different structure directing agents (SDAs) during the preparation of the TiO_2 sols. SDAs are molecules that possess both hydrophobic and hydrophilic segments that exhibit partial affinity toward both polar and non-polar surfaces. Various SDAs that have been incorporated in the preparation of TiO_2 sols were Pluronic P-123 (P-123) (Goei et al. 2013, Liu et al. 2009, Procházka et al. 2008, Sun et al. 2009, Wu and Rankin 2011), Triton X-100 (Lei et al. 2011, Sanguanruang et al. 2011, Xu et al. 2013), Tween 20 (Chen and Dionysiou 2008, García-Benjume et al. 2009), and Tween 80 (Choi et al. 2006d, Choi et al. 2006c, Han et al. 2011). The important properties of these SDAs are summarized in Table 5.1. At a very low loading concentration, there is no assembly of the SDA molecules. At the higher concentration known as the critical micelle concentration (CMC), the SDA molecules would aggregate to form a unimolecular layer. Above the CMC, the SDA molecules would self- assemble into a micelle. In the TiO_2 sols, the SDA would form the self-assembled micelles that could be removed during the calcination step, leaving behind a mesoporous TiO_2 nano-structure. Non-ionic SDAs such as Triton X-100, Tween 20 and Tween 80 generally have the advantages over ionic SDAs in term of its compatibility with other types of SDA and the stability over a wider pH range (Attwood and Florence 1985, Porter 1994). P-123 is an amphiphilic triblock copolymer that exhibits a similar micellar assembly as the non-ionic SDA. The hydrophile-lipophile balance (HLB) number (with values range from 0-20) describes the amphiphilic nature of the SDAs. All the SDAs have a relatively high HLB number which suggests the hydrophilic characteristic of the SDA.

Table 5.1 Properties of different SDAs used

SDA	**Pluronic® P-123**	**Triton X-100™**	**Tween® 20**	**Tween® 80**
Structure	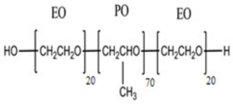 $HO-[CH_2CH_2O]_{20}-[CH_2CH(CH_3)O]_{70}-[CH_2CH_2O]_{20}-H$	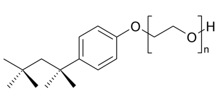	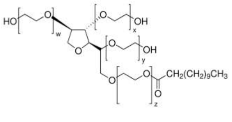	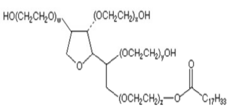
MW (g mol^{-1})	5,800	647	1,228	1,310
CMC[a] (µM)	4.4	220-240	60	12
HLB[b]	8.0	13.5	16.7	15.0
Hydrophobic group	Propylene	Phenyl ether	Lauric acid	Oleic acid
Density (g cm^{-3})	1.04	1.07	1.10	1.06

[a] Critical micelle concentration

[b] Hydrophile-lipophile balance

The hierarchically porous TiO_2 hybrid photocatalytic ceramic membrane could be constructed by multilayer coating of TiO_2 layers, starting with the layer of largest porosity, following a decreasing porosity gradient profile, ending with the thinnest separation layer of the smallest porosity. The performances of the resulting TiO_2 photocatalytic ceramic membrane could be controlled and optimized by coating an appropriate TiO_2 layer chosen from a wide range of the as-prepared TiO_2 sols. This fabrication scheme allows the flexibility of tailoring the porosity gradient of the membrane to obtain desired membrane performances.

In this chapter, the fabrication of the hierarchically porous TiO_2 photocatalytic ceramic membrane that possessed different porosity gradient configurations is discussed. Four specimens of the TiO_2 photocatalytic membranes were prepared each with multilayer coating of different TiO_2 sols prepared using one type of SDA. Two of the membrane specimens were prepared by coating TiO_2 sub-layers prepared with different SDAs, which was made possible by a good compatibility among the non-ionic SDAs. The physico-chemical and morphological properties of the membrane were elucidated using various characterization tools (i.e. N_2 porosimetry analysis, powder X-ray diffraction, scanning electron microscope, and video contact angle measurement). The performances of the membranes were evaluated using the batch photoreactor and photocatalytic membrane reactor (PMR). It was also the aim of this phase of study to optimize the performance of the membrane by fine-tuning its pore structure configuration.

5.2 Experimental procedures

5.2.1 Membrane fabrication

Four different SDAs (i.e. P-123, Triton X-100, Tween 20 and Tween 80) were used to modify the microstructure of the resulting TiO_2 layer. The properties of the SDAs used are summarized in Table 5.1. Twelve different TiO_2 sols were prepared by acid-catalyzed sol-gel method (Section 3.1.3). The final sols had a constant molar ratio of IPA:HCl:TTIP:H_2O equals to 60:4:1:4 but contained 0.5, 1.0, or 2.0 mol% of SDAs (with respect to TiO_2). The resulted TiO_2 layers hereafter are referred as X-Y where X is the type of SDA added (P, X, T20, and T80 for P-123, Triton X-100, Tween 20 and Tween 80 respectively) and Y is the amounts of SDA added in mol% with respect to TiO_2.

Six different SDA-modified membrane specimens of different porosity gradients were fabricated and they are summarized in Table 5.2. Each membrane specimen consists of 3 photocatalytic layers. The first photocatalytic layer was formed through 3 coatings of the similar sol resulting into the formation of 3-sub-layers of the largest porosity. The intermediate layer which consists of 2-sub-layers was formed through 2 coating of the similar sol. Finally, a thin top-layer of smallest porosity was coated onto the membrane as the top separation layer. The first 4 membranes (Plu, X, T20, and T80) were fabricated from the sols prepared using only one type of SDA (hereafters are referred as one-SDA-type membranes). Membranes M1 and M2 were fabricated from the TiO_2 sols prepared using different types of SDAs (i.e. P-2.0, T20-1.0, T80-0.5 and T80-2.0, X-2.0, P-0.5 for membranes M1 and M2 respectively). A control membrane specimen consisting of 6 sub-layers of SDA-free TiO_2 sols was also prepared for comparisons.

Table 5.2 Types of TiO_2 photocatalytic ceramic membranes fabricated

Types	**Layers coated**			**TiO_2 loading ($\mu g\ cm^{-2}$)**	**Thickness of TiO_2 layer (nm)[a]**	**PEG rejection (%)[b]**	**Pure water permeance ($L\ m^{-2}\ h^{-1}\ Bar^{-1}$)**
	1st (bottom) 3-sub-layers	**2nd 2-sub-layers**	**3rd (top) 1-layer**				
Plu	P-2.0	P-1.0	P-0.5	117.4 ± 0.7	532 ± 23	91.8 ± 0.5	116 ± 2
X	X-2.0	X-1.0	X-0.5	100.7 ± 0.5	408 ± 12	84.9 ± 0.7	127 ± 3
T20	T20-2.0	T20-1.0	T20-0.5	95.9 ± 1.0	455 ± 19	79.0 ± 0.4	141 ± 2
T80	T80-2.0	T80-1.0	T80-0.5	105.9 ± 0.5	511 ± 18	76.4 ± 0.3	149 ± 3
M1	P-2.0	T20-1.0	T80-0.5	107.9 ± 0.5	536 ± 16	76.0 ± 0.3	155 ± 3
M2	T80-2.0	X-2.0	P-0.5	104.7 ± 0.6	471 ± 10	89.5 ± 0.8	121 ± 1
Control	Control	Control	Control	107.3 ± 0.4	312 ± 6	94.1 ± 0.4	109 ± 1

Note: All numbers after ± indicate the standard deviation.

[a] Determined by considering different porosities of each sub-layers and assuming uniform density of anatase of $3.9\ g\ cm^{-3}$.

[b] Determined using PEG of MW 20,000 $g\ mol^{-1}$.

5.2.2 Characterization techniques

Various characterization techniques were used to understand physico-chemical and morphological properties of the membrane (the detailed description of the instrumentation and methodology can be found in Section 3.3). Characterization techniques used for the pulverized TiO_2 layer were: FTIR, N_2 adsorption/desorption porosimetry analysis, Raman spectroscopy, and XRD. The surface morphological characteristic of the membrane was studied using FESEM. Finally, the photo-induced super-hydrophilicity property of the membrane was observed through the contact angle measurement.

5.2.3 Evaluation of membrane performance

The photocatalytic activity of the membrane was evaluated both using the batch photoreactor (Section 3.4.2) and the PMR (Section 3.4.3) against photocatalytic degradation of RhB. In a typical experiment in the batch photoreactor, each types of membrane were used to treat 12 mL of RhB solution without any stirring and oxygen bubbling. The extent of the photodegradation of RhB was monitored using UV/Vis spectrophotometer at 553 nm.

The PMR setup was used to evaluate the performance of the membrane in the dead end filtration mode. The coated membrane disc was mounted and secured tightly in the membrane cells. The pure water permeability and the MWCO of the membrane were evaluated using the PMR. The membrane was also used to treat up to 5 cycles of 100 mL, 25 μM RhB solutions. The overall RhB removal could be itemized into 2 different processes: Ads-MR and PCA by the membrane. Control experiments without turning on the UV source were performed to elucidate the effect of Ads-MR on the removal of RhB. Fouling-control property of TiO_2 photocatalytic membrane was tested in the PMR setup for 12 h without re-circulation of permeate.

5.3 Results and discussion

5.3.1 Physico-chemical characteristics of TiO_2 layers.

A total of 12 different TiO_2 layers of varying types and amounts of SDAs incorporated were prepared, producing 6 different SDA-modified membrane specimens (Table 5.2). The important physico-chemical characteristics of the as-prepared TiO_2 layers are summarized in Table 5.3.

Table 5.3 Physico-chemical characteristics of the as-prepared TiO_2 layers

Surfactant		**BET Surface Area**	**Porosity**	**XRD Crystallite Size**
Types	**Loading**	**(m^2 g^{-1})**	**(%)[a]**	**(nm)[b]**
TiO_2 Control	Control	11.9 ± 0.3	12.1 ± 0.4	14.4
Pluronic® P-123	P-0.5	27.6 ± 0.4	22.0 ± 0.6	13.3
	P-1.0	83.3 ± 1.0	35.0 ± 0.4	10.8
	P-2.0	146.7 ± 1.1	51.5 ± 0.4	7.3
Triton™ X-100	X-0.5	102.5 ± 1.2	30.5 ± 0.3	7.4
	X-1.0	107.7 ± 0.3	35.5 ± 0.4	7.2
	X-2.0	123.9 ± 0.9	38.9 ± 0.2	6.6
Tween® 20	T20-0.5	134.9 ± 1.0	35.6 ± 0.7	7.3
	T20-1.0	140.0 ± 0.4	45.1 ± 0.3	6.9
	T20-2.0	150.4 ± 0.9	48.9 ± 0.1	6.3
Tween® 80	T80-0.5	134.5 ± 1.1	40.8 ± 0.4	7.7
	T80-1.0	141.8 ± 0.5	44.8 ± 0.4	6.9
	T80-2.0	154.2 ± 1.1	49.4 ± 0.1	6.4

Note: All numbers after ± indicate the standard deviation.

[a] Determined assuming uniform density of anatase of 3.9 g cm^{-3}.

[b] Calculated using Scherrer's equation with error < 1 nm.

The formation of the mesoporous structure in the P-123-based TiO_2 layer was due to microphase separation caused by the difference in the hydrophilicity of the polyethylene glycol and polypropylene glycol blocks of P-123. The incorporation of P-123 into the preparation of TiO_2 sols also lowered the viscosity and increased the stability of the sols allowing the coating of uniform TiO_2 thin layers with minimum presence of cracks and pinholes (Goei et al. 2013). A non-ionic surfactant such as Triton X-100, Tween 20, and Tween 80 formed the self-assembled micelles via solvent evaporation during drying and ageing period. The TiO_2 mesoporous structure was formed as the result of hydrogen bonding between the surfactant and the titanium hydrates. Besides, in the case of T20 (a hydrophilic SDA), the addition of surfactant could decrease the rate of solvent evaporation and minimize the development of tensile stress of the TiO_2 layer during the calcination resulting in a TiO_2 layers with minimum presence of cracks and pinholes (Chen et al. 2011).

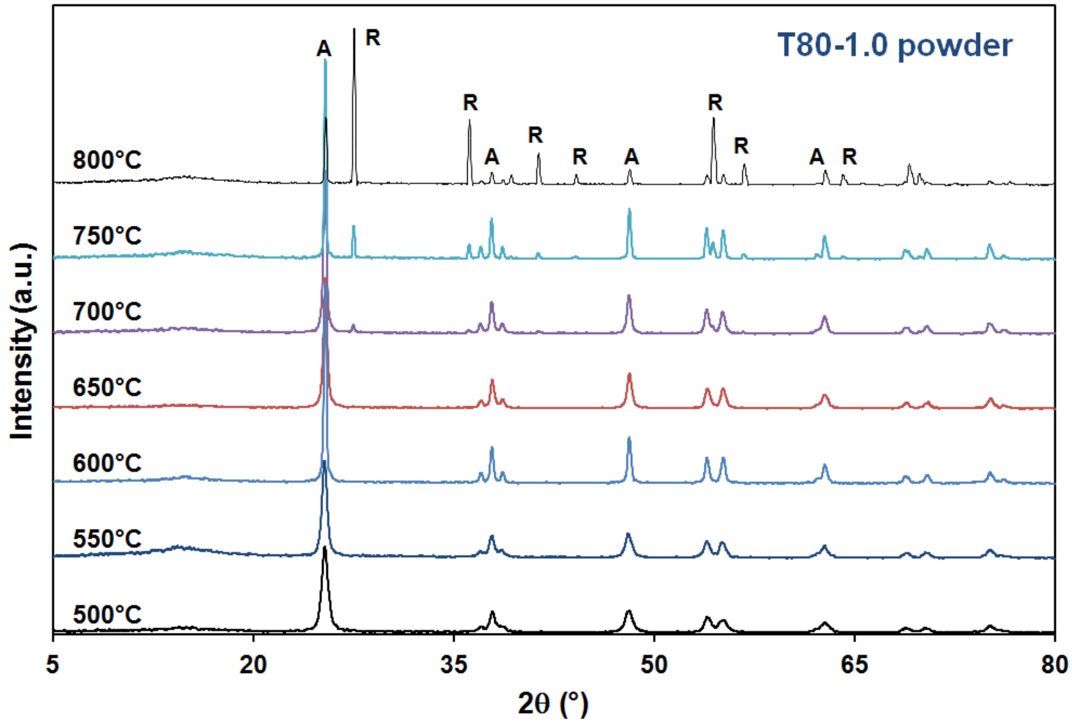

Figure 5.1 XRD spectra of the pulverized T80-1.0 TiO_2 layers calcined at different temperatures.

The wide-angle XRD spectra of different TiO_2 layers are shown in Figs. 5.1 and 5.2. The effect of calcination temperature on the purity and crystal phase of TiO_2 is shown in Fig. 5.1. At calcination temperature of 500°C, pure anatase phase is successfully formed. Five distinctive anatase-TiO_2 peaks at 25.3°, 37.9°, 48.0°, 54.6°, and 62.8° which correspond to (101), (004), (200), (105 and 211), and (204) reflections of crystalline anatase-TiO_2 planes respectively (JCPDS 21-1272) can be observed. The crystallization process of TiO_2 occurred when the calcination temperature was higher than 350°C. No other peaks other than characteristic peaks of anatase could be observed on the XRD spectra showing that calcination temperature of 500°C was sufficient to remove surfactant used in the synthesis process. As the calcination temperature increased, the FWHM decreased and the crystallites size increased. For the calcination temperature higher than 700°C, 3 characteristics rutile peaks at 25.34°, 30.31°, and 25.69° corresponding to (120), (121) and (111) crystal planes respectively (JCPDS 82-0514) were observed, signifying that anatase-rutile phase transformation had occurred. At higher calcination temperatures, the rutile peaks intensified to replace the anatase peaks.

The XRD spectra of different types of SDA-modified TiO_2 layers calcined at 500°C are presented in Fig. 5.2. No amorphous or other TiO_2 polymorphs peak can be observed in all of the spectra indicating a successful formation of anatase. TiO_2 crystallite sizes are calculated from the peak broadening of (101) anatase crystal plane at 25.3° using Scherrer's equation (Scherrer 1918) and are summarized in Table 5.3. The relatively wide (101) peak indicates a small TiO_2 crystallite size. TiO_2 layers with varying crystallite sizes from 6.3 nm (T20-2.0) to 14.4 nm (control) could be fabricated. The sizes of TiO_2 crystal decreased as the amount of SDAs loading increased for all types of the SDA incorporated. This phenomenon was caused by the decrease in the hydrolysis and condensation rate of the titanium alkoxide resulting in the smaller TiO_2 crystallites (Pelaez et al. 2010). For the case of P-123-based TiO_2, this phenomenon could be attributed to the spatial confinement mechanism through which TiO_2-anatase crystals were assembled while maintaining the integrity of the P-123 scaffold (Guldin et al. 2011). The crystallinity of resulting TiO_2 layer decreased as the amount of SDAs loading increased. This was evidenced by the overlapping of anatase (105) and (211) reflections from samples with a higher SDA loading.

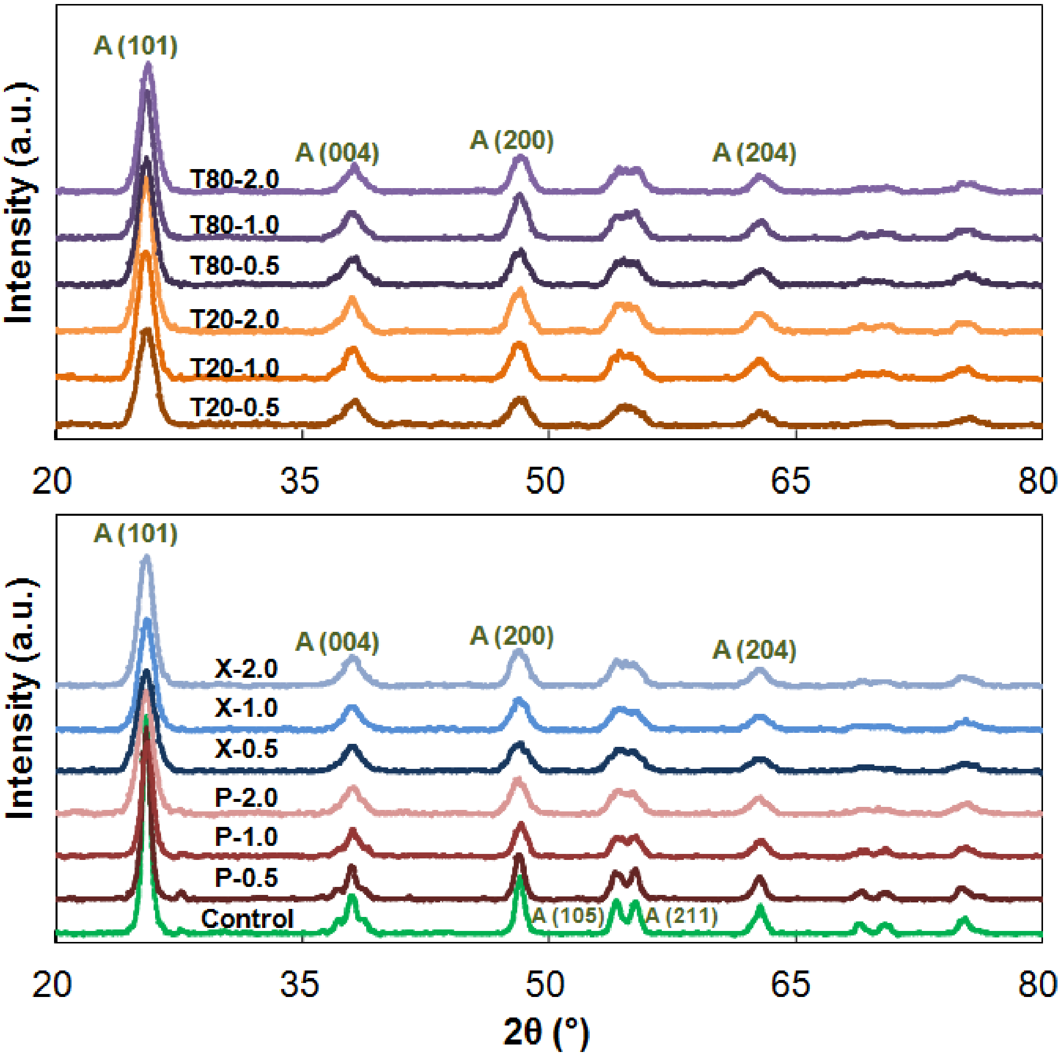

Figure 5.2 XRD spectra of the pulverized TiO_2 layers prepared with different SDAs.

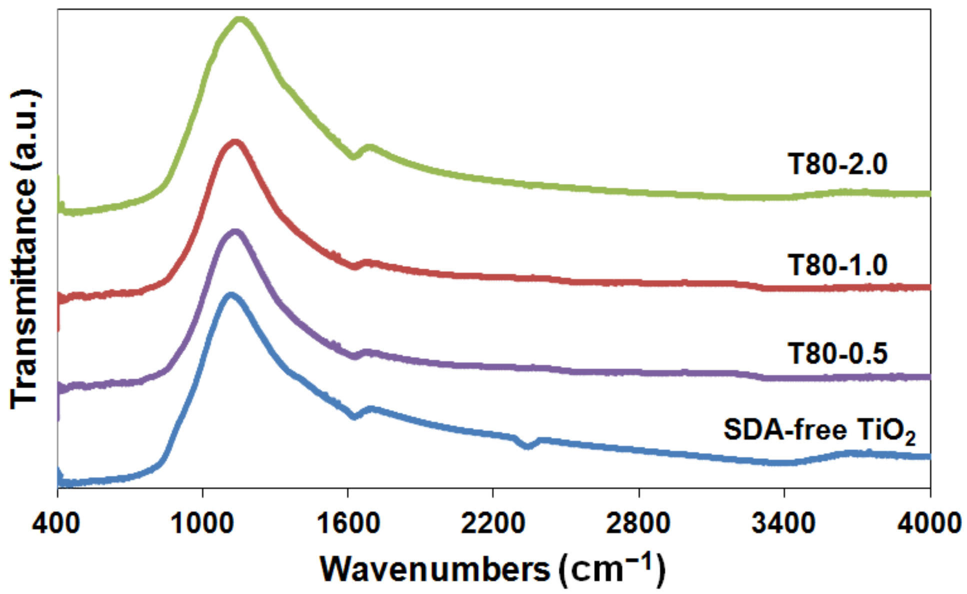

Figure 5.3 FTIR spectra of the pulverized TiO_2 layers prepared with T80.

The FTIR spectra of the representative TiO_2 layers prepared using T80 SDA is shown in Fig. 5.3. FTIR spectra observed in this study were compared with the literature (Bradley et al. 1978, Kumar et al. 2000, Pavia et al. 2009, Vinodgopal et al. 1996, Yu et al. 2003). The spectra show the main bands at 400–700 cm^{-1}, which could be attributed to Ti-O bond stretching and Ti–O–Ti bridging stretching modes. The relatively weak band at 1400 cm^{-1} could be attributed to a relatively weak OH– bending vibration. The bending vibration of the adsorbed water could be observed at 1630 cm^{-1}. The broadband at 3100–3700 cm^{-1} could be assigned to stretching vibration of the hydrogen bonded hydroxyl group and the titanium hydroxide. The titanium hydroxide was formed by hydrolysis of titanium alkoxide source with band at 3400 cm^{-1} associated with weakly chemisorbed hydroxyl group. The peaks for carbonyl bonding are located at 1635, 1638, 2360, and 2922 cm^{-1} corresponding to C=C, –C=O, –CH and –CH_2 respectively. For the SDA-free TiO_2 layer, the only carbonyl peak observable from the FTIR spectra is –CH peak. As no other significant organic content could be observed in the FTIR spectra for all of the as-synthesized TiO_2 layers, the calcination temperature of 500°C as adopted in this study was deemed sufficient to remove the organic component present in the sol. The presence of a small peak at 1630 cm^{-1} shows that hydroxyl groups in the TiO_2 thin films could never be removed completely which was beneficial to enhance the surface hydrophilicity of the TiO_2 photocatalytic membrane.

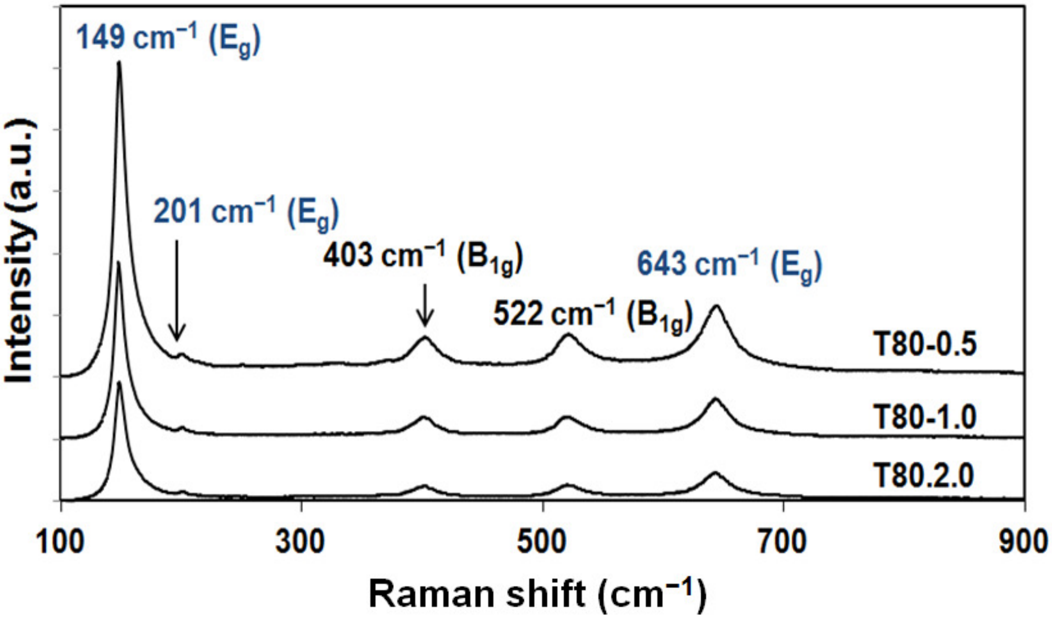

Figure 5.4 Raman spectra of the pulverized TiO_2 layers prepared with T80.

The Raman spectra of the representative TiO_2 layers prepared using T80 SDA is shown in Fig. 5.4. Anatase is a tetragonal structure (space group $D_{19}^{4h}(I4/amd)$) with 2 formula units per unit cell. Information about the structure of anatase can be represented in 10 optical modes which are $1A_{1g} + 1A_{2u} + 2B_{1g} + 1B_{2u} + 3E_g + 2E_u$. The A_{2u} and E_u modes are active in the infrared spectra while A_{1g}, B_{1g}, and E_g modes are in the Raman spectra. The peaks of the bulk anatase are observed at Raman shift at 149 cm^{-1} (E_g), 201 cm^{-1} (E_g), 403 cm^{-1} (B_{1g}), 522 cm^{-1} (B_{1g}), and 643 cm^{-1} (E_g). No rutile peaks (143 cm^{-1} (B_{1g}), 447 cm^{-1} (E_g), 612 cm^{-1} (A_{1g}), and 399 cm^{-1} (B_{2g})) could be observed in all the analyzed TiO_2 layers. It could be observed from the main anatase peak located at 149 cm^{-1} that as the amount of T80 in the sol increased, the relative intensity of the peak decreased. This indicated that a larger TiO_2 crystal was resulted from the enhancement of the Ti-O bonding, illustrating the effectiveness of T80 (or other SDAs) in controlling the TiO_2 crystallite size. This trend was in a good agreement with the crystallite size derived from XRD result.

The Raman peaks observed in this study are compared with the literature (Ohsaka et al. 1979). There is a blue shift in the Raman spectra of the as-prepared TiO_2 layers. As reported before, the peak shift could be caused either by oxygen deficiency of the non-stoichiometric TiO_2 (Parker and Siegel 1990), or the dimensional effect known as phonon confinement, in the case of stoichiometric TiO_2, (Bersani et al. 1998).

The ability of SDA to fine-tune the resulting microstructure of the TiO_2 layers is further evidenced from the N_2 adsorption/desorption isotherm. The result is summarized in Table 5.3 and Fig. 5.5. All samples exhibited the type-IV adsorption isotherm indicating their well developed mesoporous structures. The narrow distribution of TiO_2 pore sizes (4-6 nm) are evidenced from the sharp hysteresis loops. The SDA-modified TiO_2 was highly porous with highly interconnected network which yielded TiO_2 layer with high porosity. It has been observed that as the amount of SDAs loading increased, the BET surface area and porosity of the resulting TiO_2 layers increased for all types of the SDAs incorporated.

The increases in the BET surface area and the overall porosity of the TiO_2 layers were caused by the pore coalescence and the multi-micellar interactions during the calcination step (Choi et al. 2006d). The increase in the pore size of the TiO_2 layer would result in a thinner mesoporous wall. This observation was in a good agreement with the decreasing XRD crystallite size for the layer with of a higher amount of SDA added. Smaller TiO_2 crystals would result in a larger overall surface area as measured by N_2 adsorption/desorption. The increase in BET surface area and the overall porosity was the most significant in the P-123-

based TiO_2 layer. TiO_2 layer prepared using P-123 at 0.5 mol%, showed the smallest surface area (27.6 m^2 g^{-1}) and porosity (22 %). The surface area and porosity of the P-123-based TiO_2 would eventually increase to 146.7 m^2 g^{-1} and 51.5 % respectively for the P-2.0 layer. This is in agreement with the greater variation observed in the TiO_2 crystallite size of P-123-based TiO_2 (from 13.3 nm for P-0.5 to 7.3 nm for P-2.0).

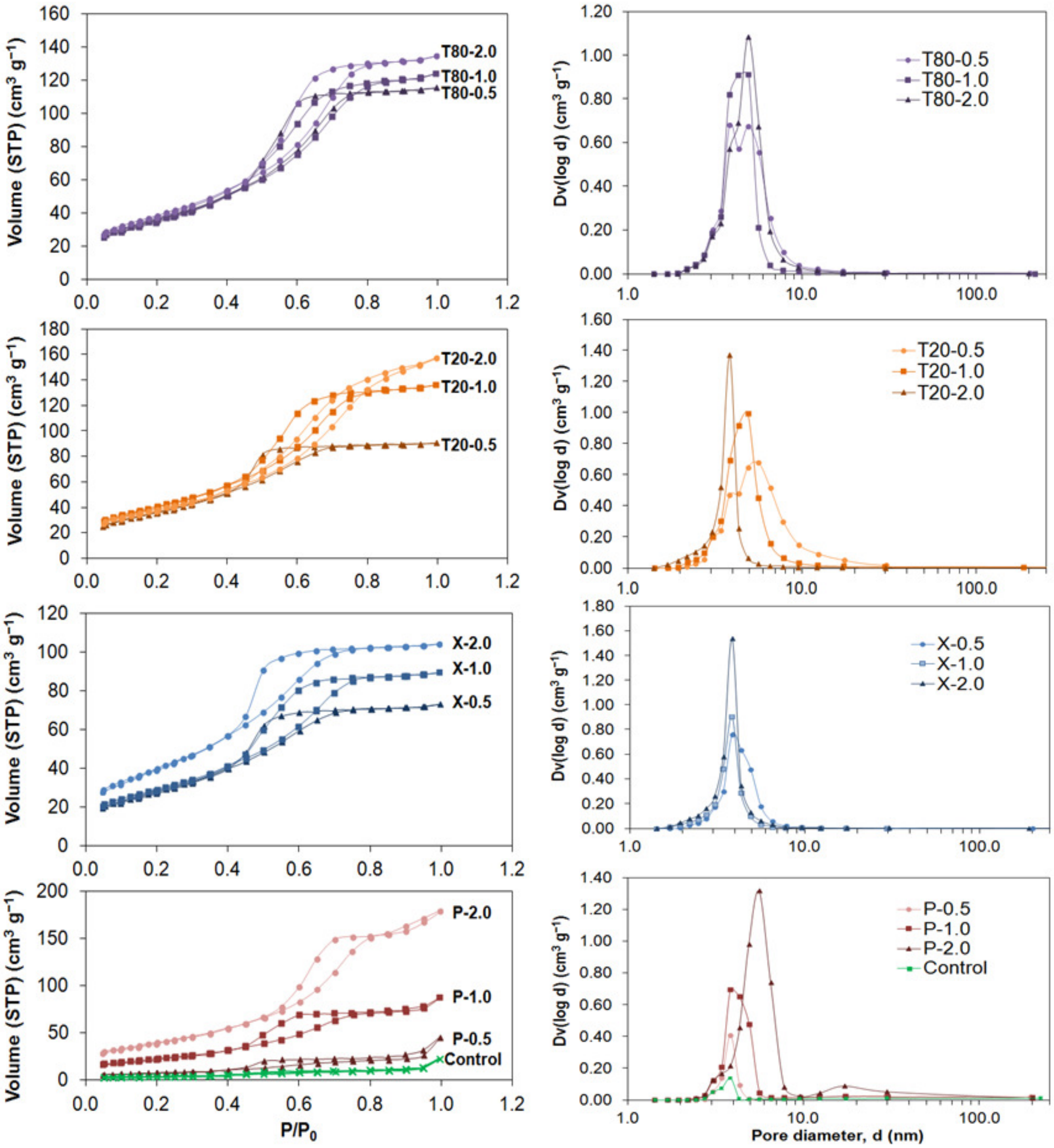

Figure 5.5 (a) N_2 adsorption/desorption isotherms and (b) pore size distributions of the pulverized TiO_2 layers prepared with different SDAs.

There was only a small variation of BET surface area and porosity observed for TiO_2 layers prepared using T20 and T80. This was due to the small difference in their molecular weights and HLB. The only difference between T20 and T80 was the type of its hydrophobic group, lauric acid and oleic acid respectively. Triton-based TiO_2 showed the smallest surface area and porosity at 2 mol% SDA loading which could be attributed to its small molecular weight. Also, SDA with longer chain length (e.g. Tween SDA, 20 ether groups) would produce TiO_2 layer with higher porosity and larger pore size when compared to the SDA with shorter chain length (e.g. Triton X-100, 10 ether groups). The XRD, Raman and N_2 porosimetry analysis have exhibited the successful formation of the SDA-modified TiO_2 layer with controllable mesoporous structure.

5.3.2 Characteristics of TiO_2 photocatalytic ceramic membranes

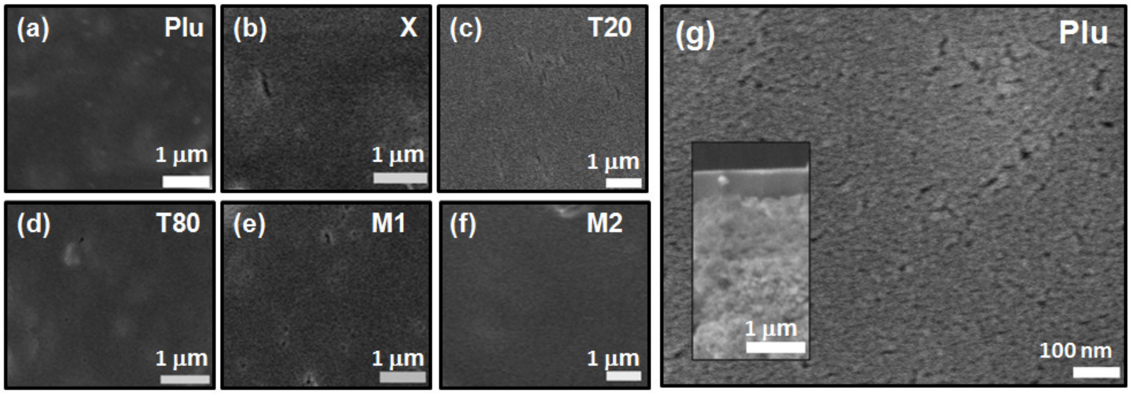

Figure 5.6 FESEM micrographs of the surface of: (a) Plu, (b) X, (c) T20, (d) T80, (e) M1 and (f) M2 membrane. (g) a high magnification FESEM micrograph of Plu membrane (the inset depicts cross-sectional view of Plu membrane).

All the membranes were prepared to produce the following porosity gradient configuration scheme: the first (bottom) 3-sub-layers were the most porous, followed by the subsequent less porous 2-sub-layers, and finally a thin least porous separating (top) layer. Figs. 5.6a-f show the FESEM micrographs of the membrane surface. It can be observed from the FESEM micrographs that relatively smooth TiO_2 layers were successfully coated onto the finished membranes. The presence of cracks and pinholes are minimal in all the membrane specimens. This is an important observation to ensure uniform permeability and good separation performance across the membrane area.

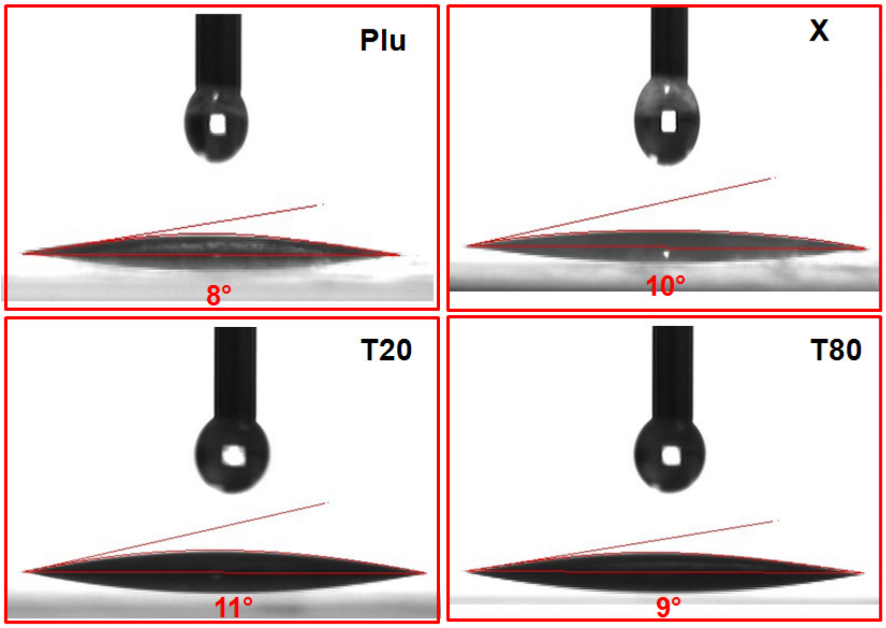

Figure 5.7 Photoinduced super-hydrophilicity (PSH) property of TiO_2 thin films prepared using different SDAs.

The TiO_2 membranes exhibited a photoinduced super-hydrophilicity (PSH) phenomenon. The contact angle micrographs of TiO_2 layers prepared using different SDAs and its corresponding contact angle values are shown in Fig. 5.7. Upon UV irradiation, all the TiO_2 layers coated on a borosilicate glass slides shows a relatively small contact angle $\leq 11°$. This was caused by hydroxylation of TiO_2 thin film surface when subjected to the UV irradiation. Ti^{3+} defective sites are formed when lattice metal ions Ti^{4+} interact with photogenerated electrons. Surface-trapped electron Ti^{3+} would react with oxygen adsorbed on the surface to form O_2^- or O_2^{2-} ions leaving the oxygen vacancy sites (Sakai et al. 2003). Adsorbed water molecules would occupy the oxygen vacancy sites to reduce the overall surface energy, releasing proton to a nearby oxygen atom and forming two hydroxyl groups on the surface of the TiO_2 photocatalyst.

The hierarchical configuration of different types of the TiO_2 photocatalytic ceramic membranes and some important characteristics are summarized in Table 5.2. The thickness of TiO_2 layer of the Control membrane specimen (312 nm) is relatively smaller than the other membrane specimens. The incorporation of SDA into the TiO_2 sols would increase the overall viscosity of the sol, resulting in a thicker TiO_2 layer. Plu membrane contained the highest amount of TiO_2 loading among the one-SDA-type membrane specimens and consequently had the thickest TiO_2 layer (Table 5.2).

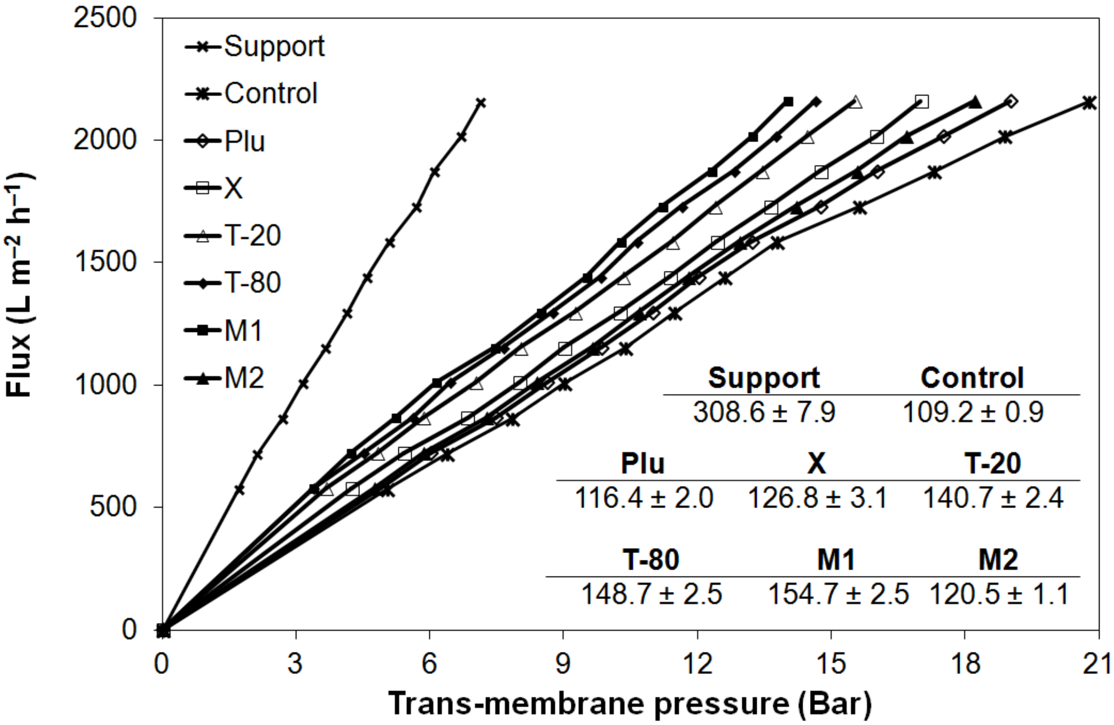

Figure 5.8 Pure water permeability of different types of TiO_2 photocatalytic ceramic membranes (the numerical values depict average pure water permeance in L m^{-2} h^{-1} Bar^{-1}).

Fig. 5.8 shows the pure water permeability of different types of the TiO_2 membranes. The macroporous alumina ceramic support could allow average pure water permeance of 309 L m^{-2} h^{-1} Bar^{-1}. The resulting pure water permeability of the membranes is strongly dependent on the thickness and the porous structure of the TiO_2 membranes. T80 membrane showed the highest pure water permeability among the one-SDA-type membrane which could be attributed to its most porous top separation layer (T80-0.5). On the other hand, Plu membrane showed the lowest pure water permeability among the SDA-modified membranes due to its least porous separating layer (P-0.5). M1 membrane was constructed such that each of its photocatalytic layers was of the most porous TiO_2 layers (3 P-2.0 sub-layers, followed by 2 T20-1.0 sub-layers and a thin T80-0.5 top separation layer). As expected, M1 membrane showed the highest pure water permeance of 155 L m^{-2} h^{-1} Bar^{-1}. Consequently, M1 membrane showed the least PEG rejection of 76%. The other mixed membrane (M2) showed a relatively high pure water permeance of 121 L m^{-2} h^{-1} Bar^{-1}. Although the Control membrane possessed the thinnest TiO_2 photocatalytic layer, the pure water permeance was the lowest among the membrane specimens (109 L m^{-2} h^{-1} Bar^{-1}) which could be attributed to the low porosity TiO_2 layers. The pure water permeability of the SDA-modified TiO_2 membranes is generally higher than those reported in the literature (Choi et al. 2006d, Qi et al. 2013, Romanos et al. 2013). The relatively high pure water permeability of the membranes could be also attributed to the PSH phenomena of the membrane. This is a very important aspect for the operation of membrane separation process whereby high permeability would reduce the overall energy consumption in the water and wastewater treatment processes. The trend observed for the pure water permeability is also in agreement with the PEG rejection profile, i.e. the least porous membrane rejected the highest percentage of the PEG solution.

5.3.3 Photocatalytic degradation of RhB using batch photoreactor

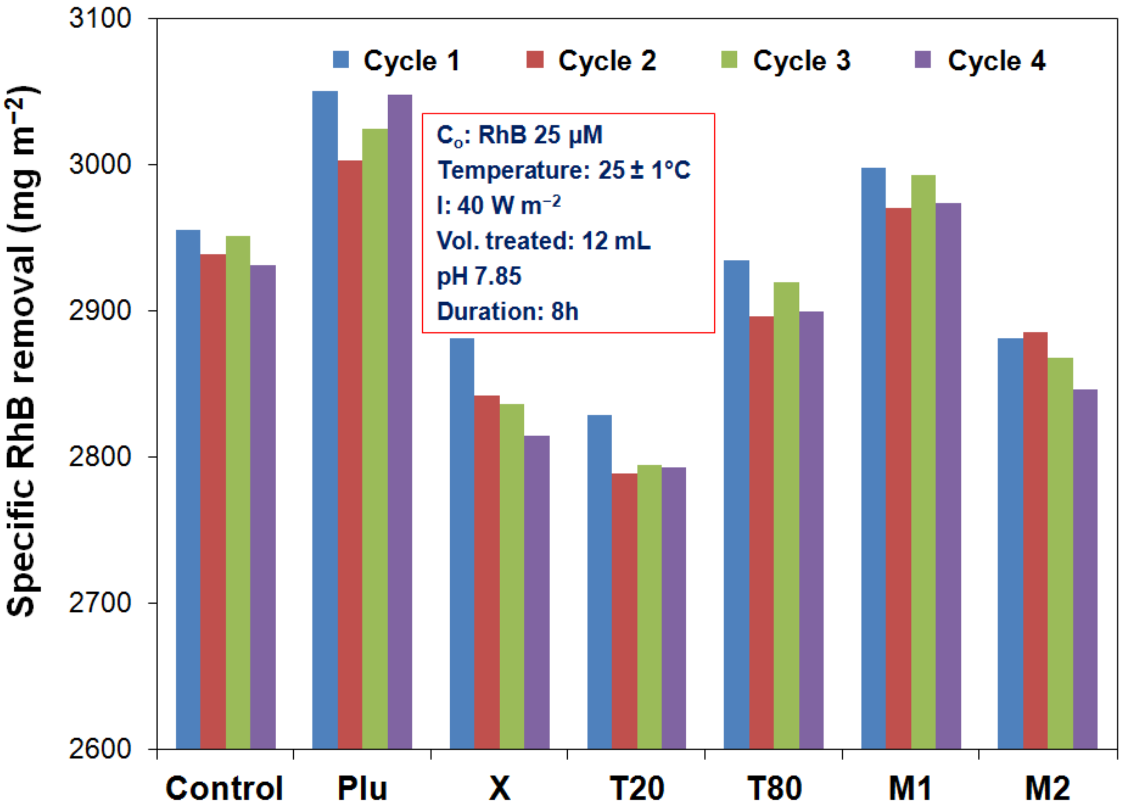

Figure 5.9 Performances of different types of TiO_2 photocatalytic ceramic membranes in the batch photoreactor.

Fig. 5.9 shows the performances of different types of the TiO_2 membranes using the batch photoreactor for 8 h. The photolysis of 25 μM RhB under continuous UV irradiation (without the presence of the membrane) was < 5 %. In the presence of TiO_2 coated membrane, the rate of RhB degradation in the batch photoreactor was controlled by mass transfer rate, intra-layer pollutant diffusion, and adsorption/desorption equilibrium. It could be observed that the Plu membrane removed the highest amount of RhB (3,000 mg m^{-2}) over the 8 h duration of treatment in the batch photoreactor. This could be explained by its highest TiO_2 content in the top layer of the membrane. The membrane with the least amount of TiO_2, T20, could remove up to 2,800 mg m^{-2} of RhB from its solution over the same treatment duration. The small variation in the RhB removal efficiency among the TiO_2 membranes suggested that the effect of thickness and porous structure of the TiO_2 layers on the RhB removal efficiency in the batch photoreactor was marginal.

The degradation of RhB could be monitored by UV-Vis spectrophotometer as the maximum absorbance of the RhB solution would shifts gradually from 553 nm to 498 nm. The gradual shift was caused by the step-wise de-ethylation of RhB to form the rhodamine solution (from the initial N, N, N', N'-tetraethyl rhodamine to the final rhodamine molecules). The observed color of the RhB solution also changes from the initial pinkish-red to a light greenish-yellow and finally to a transparent solution. The photodecolorization of the chromogenic aromatic ring and the dissociation of ethyl branches from RhB occurred simultaneously (Xie et al. 2009). In order to determine the extent of mineralization of RhB solution, the TOC of the treated RhB solutions from the batch photoreactor was measured. It was found that all the treated solutions showed a final TOC concentration smaller than 1 mg L^{-1} after 8 h, which was the detection limit of the equipment. This finding indicated > 90% TOC removal from the initial RhB solution (from the initial TOC of 8.6 mg L^{-1} corresponding to 25 µM solution). The membranes were also used up to 4 cycles of treatment in the batch photoreactor. There was no significant drop of RhB removal efficiency (Fig. 5.9), indicating that the TiO_2 membranes could be re-used.

5.3.4 Photocatalytic degradation of RhB using PMR.

The results of experiments using the PMR are shown in Figs. 5.10-5.12 and Table 5.3. The efficacy of different membranes to remove RhB is illustrated in Fig. 5.10 and reported as specific RhB removal. The numerical values shown in Fig. 5.10 depict the initial rate of RhB removal. All membranes showed a rapid initial RhB removal which could be attributed by initial RhB adsorption by the membrane. After which the photocatalytic degradation initiated by UV irradiation would take place. Plu membrane showed the highest specific RhB removal of 2,657 mg m^{-2} for 8 h of treatment duration in the PMR. Interestingly, M2 membrane shows the second highest removal (2,577 mg m^{-2}) followed by X, M1, T80, and T20 membranes. It is shown that a membrane constructed from TiO_2 layers prepared using different SDAs exhibited no compatibility issue among the different SDA-modified TiO_2 layers thus also exhibited a good RhB removal efficiency.

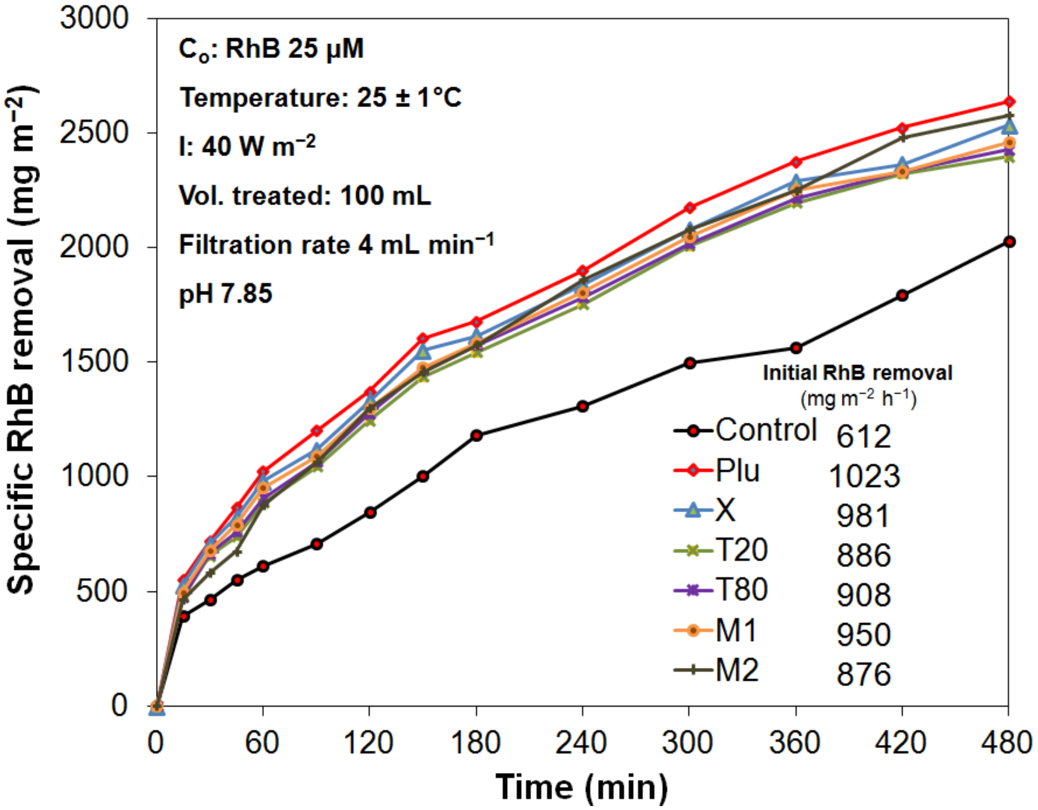

Figure 5.10 Performances of different types of TiO_2 photocatalytic ceramic membrane in the PMR (the numerical values depict kinetic value based on initial RhB removal rate within 1st hour in mg m^{-2} h^{-1}).

The contributions of different phenomena (i.e. PCA and Ads-MR) that were responsible for the overall removal of RhB in the PMR are summarized in Table 5.4. Prior to the light on of UV source, the PMR cell module was filled with RhB solution and left in the dark for 1 h in order to reach the adsorption-desorption equilibrium. Among the SDA-modified membranes, Plu membrane showed the highest contribution of Ads-MR (501 mg m^{-2}) due to its thickest TiO_2 layer. The contribution of Ads-MR on the overall efficiency of RhB removal varied from 9.5 to 17.5% (235 to 466 mg m^{-2}) for the SDA-modified membranes. The highest contribution of Ads-MR among the SDA-modified membranes was observed for Plu membrane, followed by M2, T-20, T-80, X and M1 membranes. For M1 membrane, the lowest contribution of Ads-MR could be caused by its most porous structure (M1 membrane also showed the highest pure water permeability among the tested membrane specimens). The Control membrane showed the highest overall contribution of Ads-MR (529 mg m^{-2}, 26.4%) compared to the SDA-modified membrane due to its least porous configuration hence a smaller overall surface area for adsorption. The overall contribution of adsorptive-membrane retention was lower than the result reported on author's previous work (Goei et al. 2013). This is due to the porosity gradient configuration that was shown to improve the flux and overall PCA efficiency was adopted for the present work.

RhB molecules were photocatalytically degraded as their travelled through the porosity gradient of TiO_2 layers. All the SDA-modified TiO_2 photocatalytic ceramic membranes showed more than 81% contribution of photocatalytic degradation to the overall RhB removal. M1 membrane showed the largest contribution of PCA (2,234 mg m^{-2}, 89.9%) to the overall RhB removal. This could be attributed to its most porous structure, allowing a higher flux through the membrane and hence higher photocatalytic degradation. Even the

Control membrane with a relatively small porous structure could remove 1,476 mg m^{-2} of RhB through the photocatalytic degradation.

Table 5.4 Performance of TiO_2 photocatalytic ceramic membrane in terms of its photocatalytic activity (PCA) and adsorptive-membrane retention (Ads-MR) and percentage of initial flux retained after 8 h of operation

Types	**Removal (mg m^{-2})**			**Removal (%)**		**Flux Decline**
	PCA	**Ads-MR**	**Total**	**PCA**	**Ads-MR**	**(%)**
Plu	2156 ± 32	501 ± 16	2657 ± 30	81.1	18.9	93.3
X	2185 ± 70	364 ± 36	2549 ± 34	88.9	11.1	90.9
T20	2088 ± 48	319 ± 26	2407 ± 24	86.7	13.7	93.6
T80	2129 ± 27	302 ± 12	2431 ± 22	87.6	12.4	93.9
M1	2234 ± 32	249 ± 30	2483 ± 13	89.9	10.1	94.3
M2	2121 ± 40	456 ± 30	2577 ± 11	82.3	17.7	91.9
Control	1476 ± 14	529 ± 13	2005 ± 21	73.6	26.4	79.0

Fouling control is an important requisite of an efficient membrane process. The overall flux declines of different TiO_2 membranes over the duration of RhB photocatalytic degradation experiment are listed in Table 5.4. The SDA-modified TiO_2 photocatalytic ceramic membranes exhibited only a small percentage (maximum of 10 %) of flux decline over the duration of 8 h of photocatalytic degradation of RhB. The higher initial flux decline could be attributed to the cumulative adsorption of RhB molecules onto the membrane. After which, the smaller flux decline would be observed and the final steady-state flux would be achieved and maintained. The initial flux could be recovered by inter-cycle cleaning steps by replacing the feed with MilliQ water for 2 h with UV irradiation. Fig. 5.11 illustrates the reusability potential of the TiO_2 photocatalytic membrane. Over the duration of the first treatment cycle, 92% of the initial flux was maintained with 98% of the initial flux was recovered after the first cleaning step. Even after 4th cycle of usage, 83% of the initial flux was maintained. The results suggest the potential of TiO_2 photocatalytic ceramic membrane to be reused over a prolonged period.

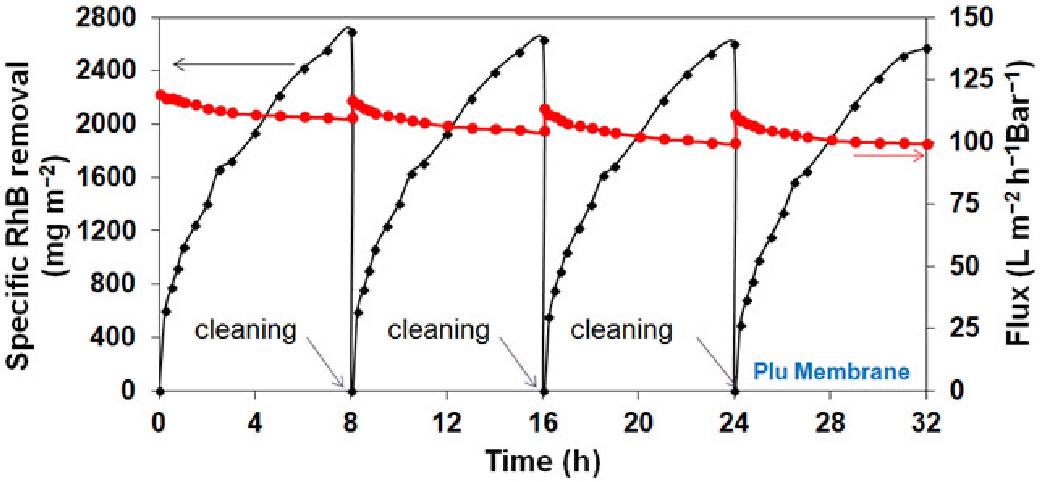

Figure 5.11 Reusability potential of the TiO_2 photocatalytic ceramic membrane in terms of flux and specific RhB removal performance with UV-assisted inter-cycle cleaning.

Fig. 5.12 summarizes the performances of different TiO_2 membranes when they were utilized over 4 cycles of treatment with the inter-cycles cleaning steps. The highest decrease of total RhB removal and % flux retained showed by the Control membrane. Only 85% of the initial RhB removal capacity and 79% of the initial could be retained. Better performance was shown by the membranes with porosity gradient configuration. Plu membranes could retain the highest (95.9%) total RhB removal capability respectively after 4 treatment cycles followed by X, T-20, T-80, M1 and M2 membranes respectively. The percentages of the initial flux retained after 4 treatment cycles for Plu, X, T-20, T-80, M1 and M2 membranes are 93.3, 90.9, 93.6, 93.9, 94.3, and 91.9% respectively. The results suggested the ability of the membrane to control fouling via UV-assisted self-cleaning mechanism that preserved the removal capability and flux flowing through the membrane. It can also be observed from Fig. 5.12 that the decline of flux and overall RhB removal capability of the subsequent treatment cycle is decreasing. This indicated the possibility of attaining a steady-state sustainable flux and overall RhB removal capability in the subsequent treatment cycles.

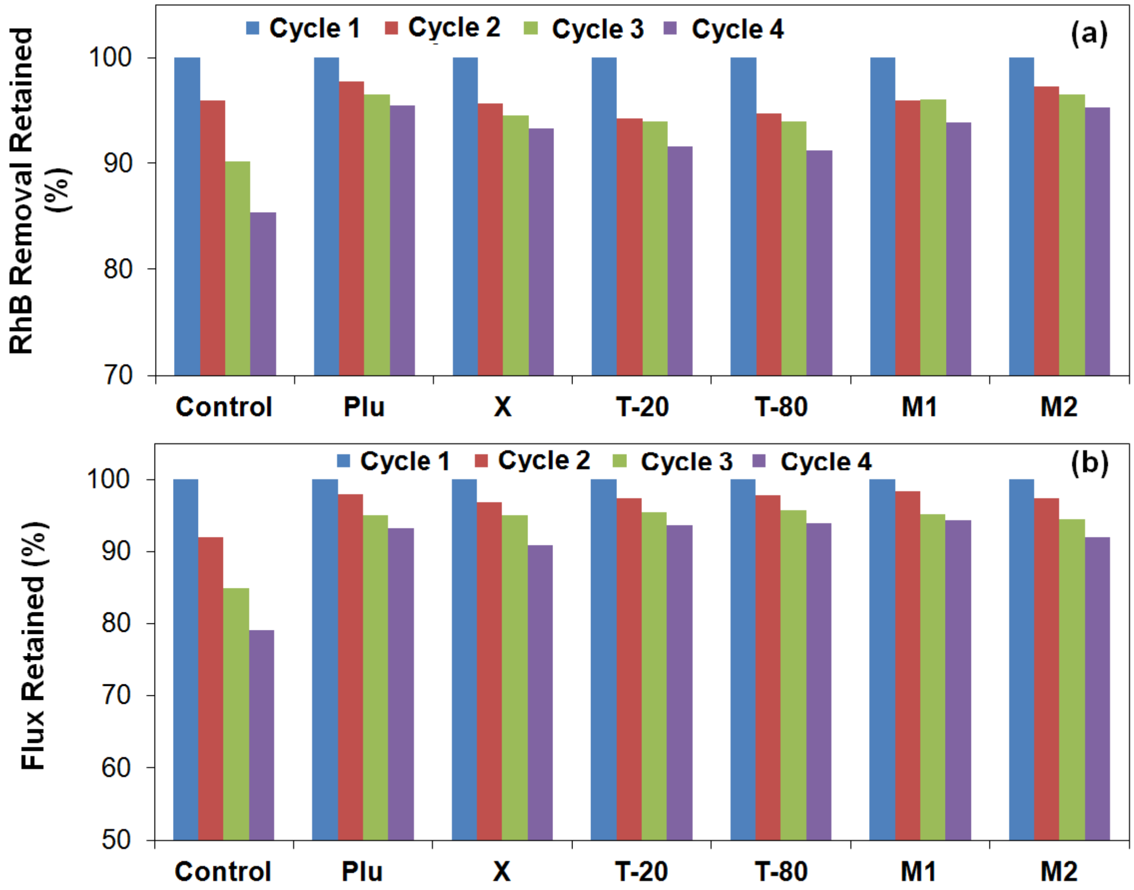

Figure 5.12 Reusability potential of different types of TiO_2 photocatalytic ceramic membranes in terms of (a) specific RhB removal retained and (b) flux retained after each UV-assisted inter-cycles cleaning (8h for each cycle).

5.4 Conclusions

The hierarchically porous TiO_2 photocatalytic ceramic membranes have been successfully constructed by using TiO_2 layer prepared with different SDAs. The membranes possessed a porosity gradient configuration that was achieved by multilayer coating of TiO_2 layers of unique porous structures. 4 different SDAs were used in the preparation of the TiO_2 sol i.e. Pluronic P-123, Triton X-100, Tween 20 and Tween 80. Six types of membranes were prepared, 2 of which consisted of TiO_2 layers prepared incorporating different types of SDAs. The TiO_2 sols prepared using different SDAs exhibited a good compatibility among them, allowing the flexibility of constructing the TiO_2 membrane that exhibited favorable operating parameters, i.e., high permeability, good separation or both. Membrane M1 exhibited the highest flux performance while membrane Plu exhibited the largest RhB removal. The TiO_2 photocatalytic membrane could remove RhB from its solution through different processes which were classified as Ads-MR and PCA. The reusability potential of the TiO_2 membranes has been showed using both the batch photoreactor and flow-through PMR which would reduce the overall operating cost of the treatment system.

CHAPTER 6 SILVER-DECORATED TiO_2 PHOOCATALYTIC CERAMIC MEMBRANE WITH HIERARCHICAL ARCHITECTURE: PHOTOCATALYTIC AND ANTIBACTERIAL ACTIVITIES

6.1 Introductions

In order to improve the photocatalytic activity of TiO_2, doping of various metallic and non-metallic element was advocated (Chen and Mao 2007). Among the possible metal dopants, Ag is favorable due to its remarkable catalytic, electric, and specific optical characteristics (Morones et al. 2005, Roucoux et al. 2002). Also, Ag nanoparticles have exhibited the highest bactericidal activity and biocompatibility among other bactericidal nanoparticles (Akhavan and Ghaderi 2010, Gumy et al. 2006, Li et al. 2008). The synergistic coupling of Ag and TiO_2 is attributed to the Schottky barriers that are formed due to the difference in their work function. The Schottky barriers facilitate electron transfer from a higher Fermi energy level TiO_2 to Ag which would then reduce molecular oxygen to produce reactive oxygen radicals. This phenomenon would lead to a better charge separation thus inhibiting photogenerated electrons and holes recombination (Kubacka et al. 2008, Seery et al. 2007, Subba et al. 2003, Yu et al. 2005). Furthermore, Ag doping would add an additional functionality of anti-bacterial/anti-biofouling property to the already robust TiO_2 photocatalyst. However, there exists an optimum level of Ag doping, beyond which photohole trapping effect (increase in the probability of recombination by suppressing active photogenerated charge transfer to the reactant species at the surface) would happen (Ma et al. 2009a, Yin et al. 2004).

Recently, there are many research efforts to incorporate Ag nanoparticles into a membrane filtration setup (including some treatment systems that combine Ag anti-bacterial property, TiO_2 photocatalysis, and membrane filtration). For instance, Krylova et al. (2009) have deposited Ag nanoparticles onto different ceramic support (such as silica, titania, and zirconia) by sol-gel method. Liu et al. (2013a) fabricated Ag-loaded nanocomposite nanofiltration (NF) and forward osmosis (FO) membranes via layer-by-layer assembly method. Ma et al. (2009a) prepared a Ag-TiO_2/HAP/Al_2O_3 composite to that exhibited improved adsorption of bacterial cells and good anti bacterial property. Ma et al. (2010) also fabricated Ag-TiO_2/HAP microfiltration (MF) membrane to treat humic acid solutions. Liu et al. (2013b) designed a direct observation experiment to study the effect of Ag nanoparticles on the bacteria deposition and its associated detachment kinetics from a polysulfone membrane. Lei et al. (2011) synthesized Ag/AgCl coated polyacrylonitrile nanofiber membranes that posses a high photocatalytic activity. Lv and coworkers (Lv et al. 2009a, Lv et al. 2009b) have fabricated Ag-decorated porous ceramic composite for the inactivation of E. *coli.* Yin et al. (2013) have attached Ag nanoparticles to the surface of polyamide membrane that showed an anti biofouling property.

In this chapter, the fabrication of different types of Ag-decorated TiO_2 photocatalytic membranes that posses a hierarchically porous architecture was described. Hierarchically porous architecture is a preferred structure to allow optimum operating parameters of photocatalytic membrane (Colombo et al. 2010). In this architecture, porosity gradient was obtained through coating of multi- photoactive layers of different pore structures (coating with larger pore size on the support-photocatalyst interface). Pluronic P-123 triblock copolymer was incorporated into the preparation of TiO_2 sol to control the microstructure of the resulting gel. This was achieved by the formation of a periodic nanostructure caused by microphase separation of the incompatible polymer blocks of P-123. Besides, EO-type nonionic surfactants such as P-123 could assist reduction of Ag^+ to Ag^0 through the oxidation of their oxythylene group to aldehydes (Andersson et al. 2002, Liz-Marzán and Lado-Touriño 1996). Various characterization techniques were employed to elucidate the physico-chemical and morphological characteristics of the membranes. Different performance parameters were used to evaluate the photocatalytic activity and anti-bacterial action of the membranes. Finally, it was the objective of this chapter to gain an insight into different phenomena that govern the performance of the Ag-TiO_2 membranes including their various anti-bacterial actions and its reusability potential.

The potential applications of the Ag-TiO_2 membranes are not only limited to remove turbidity and pathogen in the water and wastewater treatment but also to remove organic pollutants as a hybrid UF/NF photocatalytic membrane in the filtration system (as a reactive membrane). The multi-functionality of the Ag-TiO_2 membrane and its reusability potential are important criteria for the application of low cost yet effective photocatalytic membrane treatment system.

6.2 Experimental procedures

6.2.1 Membrane fabrication

Ag-decorated TiO_2 (Ag-TiO_2) sols were prepared with the incorporation of Pluronic P-123 as the SDA (Section 3.1.4). $AgNO_3$ was used as the Ag source. The Ag-TiO_2 sols had a molar ratio of IPA:HNO_3:TTIP:H_2O equals to 60:4:1:4. Variable amounts of P-123 and $AgNO_3$ were used in the preparation of different sols to obtain Ag-TiO_2 sols that contained 0.5, 1.0, 2.0, 5.0, or 10 wt% of P-123 and 0.5, 1.0, 2.0, 3.0 mol% of Ag (with respect to TiO_2) respectively. The resulted TiO_2 layers hereafter are referred as PX-AgY where X and Y are the amounts of P-123 and Ag added respectively.

Table 6.1 Types of Ag-TiO_2 photocatalytic membrane fabricated

Types	**Layers coated**			**TiO_2 loading ($\mu g\ cm^{-2}$)**	**Thickness of Ag-TiO_2 layer (nm)**[a]	**PEG rejection (%)**[b]	**Water Permeance ($L\ m^{-2}\ h^{-1}\ Bar^{-1}$)**
	1st (bottom) 3-sub-layers	**2nd 2-sub-layers**	**3rd (top) 1-layer**				
R1	P10-Ag0.0	P5.0-Ag0.0	P2.0-Ag0.5	58.6 ± 7.1	323 ± 39	75.2 ± 0.6	159 ± 1
R2	P10-Ag0.5	P5.0-Ag0.5	P2.0- Ag0.5	48.3 ± 7.7	260 ± 41	76.4 ± 2.6	146 ± 2
R3	P5.0-Ag0.0	P2.0-Ag0.0	P1.0-Ag0.5	70.3 ± 5.2	341 ± 25	78.8 ± 0.6	142 ± 3
R4	P5.0-Ag0.5	P2.0-Ag0.5	P1.0-Ag0.5	65.8 ± 9.9	298 ± 45	82.5 ± 1.3	129 ± 3
R5	P5.0-Ag0.0	P2.0-Ag0.0	P1.0-Ag1.0	78.5 ± 5.6	355 ± 24	80.1 ± 1.2	134 ± 2
R6	P5.0-Ag1.0	P2.0-Ag1.0	P1.0-Ag1.0	72.9 ± 10.8	325 ± 40	84.8 ± 0.5	123 ± 2
Plu D[c]	P10-Ag0.0	P5.0-Ag0.0	P2.0-Ag0.0	130.3 ± 10.3	598 ± 38	72.3 ± 1.4	160 ± 1

[a] Determined by considering different porosities of each sub-layers and assuming uniform density of anatase and metallic silver of 3.9 and 10.5 g cm^{-3} respectively.

[b] Determined using PEG of MW 20,000 g mol^{-1}.

[c] Obtained from author's previous work [Goei et al. (2013)] as control.

The hierarchical architecture of Ag-TiO_2 membrane was obtained by coating different sols on the alumina support. Prior to the coating, the alumina support was coated with 5 wt% PVA solution and air dried to prevent possible infiltration of TiO_2 sol into the alumina support. One side of the alumina support was covered to allow only single-side coating of Ag-TiO_2 sols. The alumina support was then dipped into the designated Ag-TiO_2 sol for 60 s using a home-fabricated dip-coater, and withdrawn at a rate of 2 mm s^{-1}. The coated membrane was first oven dried (103°C, 15 min), then calcined in the muffle furnace (Nabertherm LHT04/16) at 500°C for 1 h (3°C min^{-1} heating rate). Six different membrane specimens of different hierarchical architectures were fabricated and they are summarized in Table 6.1. The first photocatalytic layer was formed through 3 coatings of the similar sol resulting into the formation of 3-sub-layers. The intermediate layer which consists of 2-sub-layers was formed through 2 coating of another sol. Finally, a thin top-layer was coated once with Ag-containing sol. R1, R3, and R5 were decorated with Ag only in the top-most layer while R2, R4, and R6 were decorated with Ag in all sub-layers. All the membranes were UV irradiated (λ_{max} = 365 nm, 60 W m^{-2}) for 1 h (after the heat treatment of each coated sub-layers) in order to reduce Ag^+ species in the membrane to metallic Ag^0. A previously prepared Ag-free TiO_2 membrane, Plu D, was included in the present study for comparison (Goei et al. 2013). In order to characterize the microstructure of the Ag-TiO_2, a thick Ag-TiO_2 layer was also coated onto a Petri dish. The resulting layer was then scrapped off, heat treated, pulverized, and stored for its subsequent characterizations.

6.2.3 Evaluation of membrane performance

The photocatalytic activity of the membrane was evaluated both using the batch photoreactor (Section 3.4.2) and the PMR (Section 3.4.3) against photocatalytic degradation of RhB. In a typical experiment in the batch photoreactor, each types of membrane were used to treat 12 mL of RhB solution without any stirring and oxygen bubbling. The extent of the photodegradation of RhB was monitored using UV/Vis spectrophotometer at 553 nm.

The PMR setup was used to evaluate the performance of the membrane in the dead end filtration mode. The coated membrane disc was mounted and secured tightly in the membrane cells. The pure water permeability and the MWCO of the membrane were evaluated using the PMR. The membrane was also used to treat up to 5 cycles of 100 mL of 25 µM RhB solutions. Control experiments without turning on the UV source were performed to elucidate the effect of Ads-MR on the removal of RhB. The overall RhB removal could be attributed to 2 different processes: PCA of the TiO_2 layer and Ads-MR by the membrane.

The total amount of Ag leaching from the Ag-TiO_2 photocatalytic membrane was quantified using ICP-MS (Section 3.4.4). The study of diffusion inhibition zone of the Ag-TiO_2 photocatalytic membrane was performed (Section 3.4.5). The anti-bacterial performance of Ag-TiO_2 photocatalytic membrane was also evaluated by the means of photocatalytic disinfection of E. *coli* both in the batch reactor (Section 3.4.6) and PMR (Section 3.4.7). Lastly, the ability of bacteria to undergo repair after the disinfection reaction was evaluated (Section 3.4.8).

6.3 Results and discussion

6.3.1 Characterization of Ag-TiO_2 layers

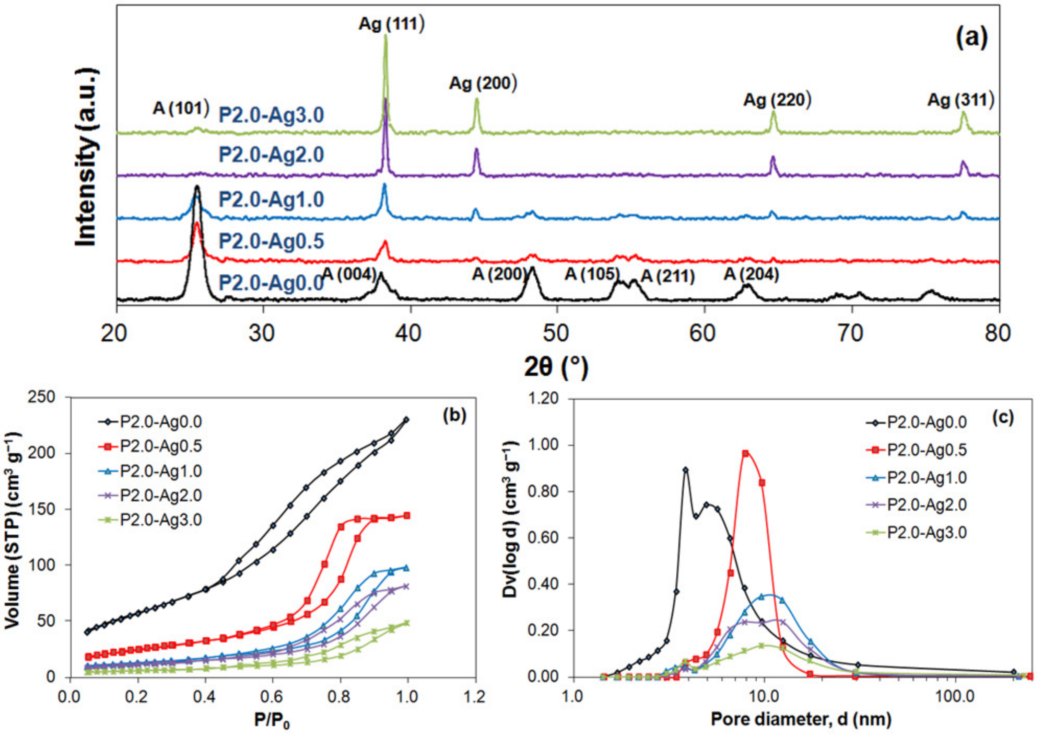

Figure 6.1 (a) XRD spectra, (b) N_2 adsorption/desorption curves, and (c) pore size distribution of the pulverized Ag-TiO_2 layers with different amounts of Ag added.

The important physico-chemical characteristics of the as prepared Ag-TiO_2 layers are summarized in Table 6.2. Various types of Ag-TiO_2 materials have been prepared by acid-catalyzed sol-gel method. Thirty types of Ag-TiO_2 layers were prepared by varying its

Pluronic P-123 and $AgNO_3$ content of the sols. The difference in the hydrophilicity of the polyethylene glycol and polypropylene glycol blocks of P-123 would cause a microphase separation. This phenomenon was responsible for micellar structure that would leads to the mesoporous structure formation of the resulting Ag-TiO_2 layers. The mesoporous structure was formed by attractive forces between titanium dioxide hydrate and P-123 and would crystallize during the calcination stage to obtain the final Ag-TiO_2 layers (Lu et al. 1997, Procházka et al. 2008).

The wide-angle XRD patterns of the representative Ag-TiO_2 sols are shown in Fig. 6.1a. It showed the XRD patterns of the pulverized Ag-TiO_2 with increasing Ag content (from 0 up to 3 mol% Ag) while the amount of P-123 added was kept constant. The XRD spectra show five distinctive anatase TiO_2 peaks at 25.3°, 37.9°, 48°, 54.6°, and 62.8° which correspond to (101), (004), (200), (105 and 211), and (204) reflections of crystalline TiO_2 anatase planes respectively (JCPDS 21-1272). No amorphous content was observed in the spectra indicating a successful formation of anatase crystals upon calcination at 500°C. Anatase phase was the most photocatalytically active form among the TiO_2 polyforms (Gaya and Abdullah 2008, Tanaka et al. 1993a). Four distinctive peaks of face-centered cubic metallic Ag at 38.1°, 44.3°, 64.5°, and 77.4° which correspond to (111), (200), (220), and (311) reflection were also observed in the spectra of Ag-containing sample (JCPDS 04-783). The result from XRD analysis confirmed the successful deposition of Ag on TiO_2 nanocrystals.

A high atom density facet of (111) crystal plane of metallic Ag was found to be a favorable condition for effective disinfections upon interaction with bacterial cell (Morones et al. 2005, Pal et al. 2007). TiO_2 crystallites size was calculated from the peak broadening of (101) anatase crystal plane at 25.3° using Scherrer's equation (Scherrer 1918) and are summarized in Table 6.2. The size of TiO_2 crystal decreased as the amount of P-123 loading increased. This could be attributed to spatial confinement mechanism of P-123 scaffold (Guldin et al. 2011). The concentration of Ag doping would also affect the resulting TiO_2 crystallite size. Ag was found to suppress the growth of anatase crystal by inclusion of Ag nanoparticles on the mesoporous TiO_2 layer (Ma et al. 2011).

Table 6.2 Physico-chemical characteristics of synthesized Ag-TiO_2 materials: (a) TiO_2 crystallite size, (b) BET surface area, and (c) BET porosity

(a) TiO_2 Crystallite Size (nm)[a]

↓ P-123 | Ag → (wt%) | (mol%)	0.0	0.5	1.0	2.0	3.0
0.0	14.8	14.6	12.9	10.8	8.9
0.5	14.4	13.4	12.8	10.5	8.3
1.0	13.3	12.7	10.8	9.8	7.7
2.0	7.7	6.8	6	5.2	4.7
5.0	5.5	5.3	4.6	3.7	3.6
10	5	4.5	3.7	3.4	2.6

(b) BET Surface Area (m^2 g^{-1})

P-123 | Ag	0.0	0.5	1.0	2.0	3.0
0.0	27.68 ± 0.71	20.15 ± 0.70	17.55 ± 0.57	5.83 ± 0.13	1.61 ± 0.01
0.5	51.29 ± 0.76	35.15 ± 1.07	24.07 ± 0.25	13.81 ± 0.08	9.36 ± 0.23
1.0	82.19 ± 0.51	46.29 ± 0.57	34.91 ± 0.93	19.97 ± 0.14	10.84 ± 0.09
2.0	127.06 ± 2.95	49.33 ± 0.59	45.64 ± 0.29	36.33 ± 0.40	20.79 ± 0.27
5.0	139.41 ± 1.08	56.08 ± 0.47	53.59 ± 0.61	40.84 ± 0.18	30.51 ± 0.30
10	146.84 ± 1.07	75.52 ± 0.42	68.58 ± 0.52	48.72 ± 0.36	38.32 ± 0.28

(c) BET Porosity (%)[b]

P-123 | Ag	0.0	0.5	1.0	2.0	3.0
0.0	14.19 ± 0.17	13.22 ± 0.22	11.23 ± 0.13	5.79 ± 0.21	3.97 ± 0.04
0.5	29.84 ± 0.19	28.53 ± 0.23	23.38 ± 0.26	16.35 ± 0.36	12.02 ± 0.14
1.0	34.60 ± 0.39	33.49 ± 0.26	29.86 ± 0.12	18.09 ± 0.17	14.05 ± 0.05
2.0	45.63 ± 0.32	40.52 ± 0.42	37.27 ± 0.43	33.05 ± 0.19	22.82 ± 0.09
5.0	47.98 ± 0.23	46.67 ± 0.33	43.86 ± 0.16	35.18 ± 0.07	32.26 ± 0.06
10	58.20 ± 0.21	51.41 ± 0.42	50.02 ± 0.07	45.70 ± 0.30	21.19 ± 0.10

[a] Calculated using Scherrer's equation with error < 1 nm.

[b] Determined assuming uniform densities of anatase and metallic silver of 3.9 and 10.5 g cm^{-3} respectively.

Further evidence of the ability to fine-tuning the resulting microstructure of Ag-TiO_2 layers just by altering the amount of P-123 and $AgNO_3$ added into the sol were obtained from N_2 adsorption/desorption isotherm characterization. The result is summarized in Table 6.2a-b, and Fig. 6.1b-c. A well developed mesoporous material was evidenced from a type-IV adsorption isotherm. The sharp hysteresis loops indicate that pore sizes in the Ag-TiO_2 layers are of narrow distribution. It has been observed that as the amount of P-123 added increased, the BET surface area and porosity of the resulting Ag-TiO_2 increased. More pore coalescence and multi-micellar interaction during calcination are expected for higher P-123 loading which would result in increase in pore size and overall porosity (Choi et al. 2006d). However, as the amount of Ag doping increased, the decreased in BET surface area and overall porosity was observed. This could be attributed to the inclusion of Ag nanoparticles into the mesoporous TiO_2 layers. The control of surface area and porosity profile is important to maximize the numbers of catalytic active sites.

XPS analyses were carried out to understand the chemical states of element in Ag-TiO_2 layers. Two samples of the pulverized Ag-TiO_2 layers (P2Ag0.5 and P2Ag2.0) were chosen as representative for the XPS analysis. The high resolution XPS spectra of C 1s, O 1s, Ti 2p, and Ag 3d core levels are presented in Fig. 6.2. There were 2 main peaks observed in O 1s, the dominant peak at 529.6 eV which was characteristics of metallic oxide and a smaller peak at 531.8 eV which was attributed to chemisorbed oxygen on the surface of Ag-TiO_2 layer. The adsorbed oxygen allows the H^+ hydroxylation to form –Ti(OH)-O-Ti-(OH)- bond which would generate hydroxyl radical that are beneficial for photocatalysis (Hoffmann et al. 1995). A separation of 5.7 eV of Ti 2p doublet indicates that Ti exists in Ti^{4+} oxidation state. Distinct doublet was also observed at Ag 3d core level. A spin-orbit splitting energy of 6.0 eV for the 3d doublet of Ag indicates the formation of metallic Ag^0 (Moulder et al. 1992). No peak from other form of Ag oxide (i.e. AgO or Ag_2O) were observed) indicates the successful photoreduction of Ag species to Ag^0.

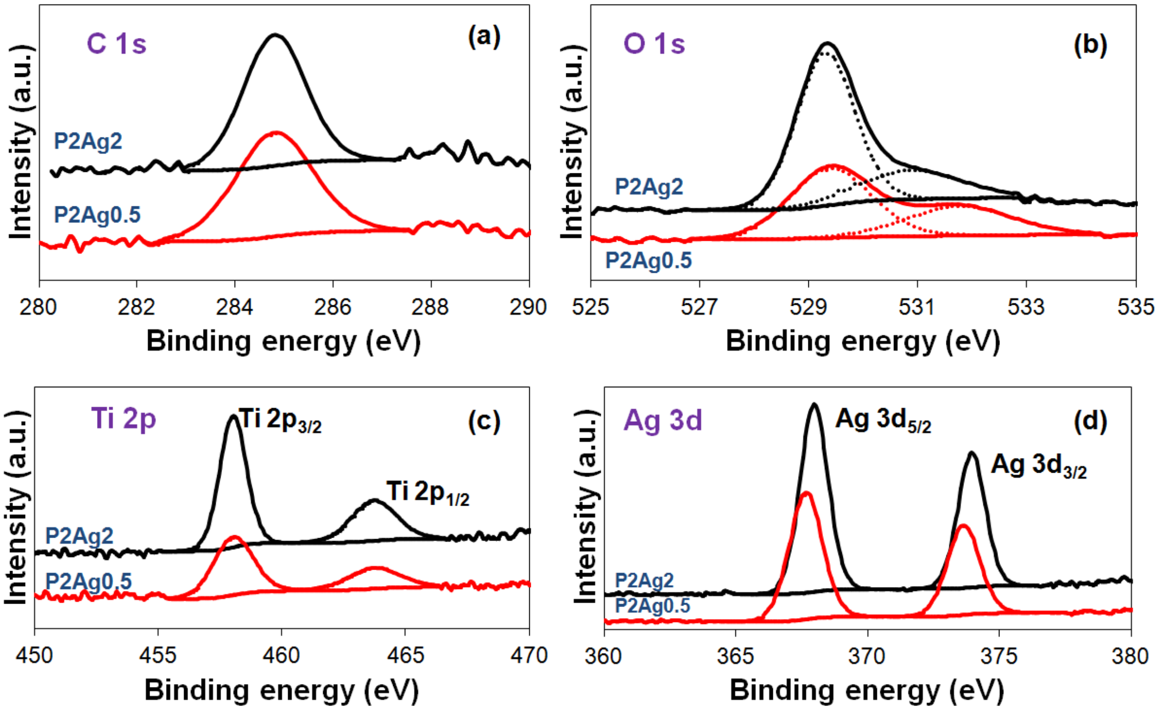

Figure 6.2 High resolution XPS spectra of (a) C 1s, (b) O 1s, (c) Ti 2p and (d) Ag 3d regions of the pulverized Ag-TiO_2 layers.

6.3.2 Characteristics of Ag-TiO_2 membranes.

Six types of Ag-TiO_2 membrane with hierarchical architecture were fabricated. All membranes followed the following hierarchical architecture scheme: the first 3 sub-layers were the most porous, followed by subsequent 2 less porous sub-layers, and finally a thin least porous separating layer was coated. For comparisons, Plu D membrane from author's previous study (Goei et al. 2013) was also fabricated. R1 and R2 membranes were prepared similar to Plu D by using P10, P5, and P2 sols. R1 used TiO_2 sol doped with 0.5 mol% Ag only on the top-most sub-layer, while R2 used TiO_2 sols doped with 0.5 mol% Ag in all of its sub-layers. R3 and R4 membranes were prepared using P5, P2, and P1 sols which structure were analogous to R1 and R2. Finally, R5 and R6 membranes were prepared using P5, P2, and P1 sols which structure analogous to R3 and R4 but using instead a 1 mol% of Ag-decorated TiO_2 sol.

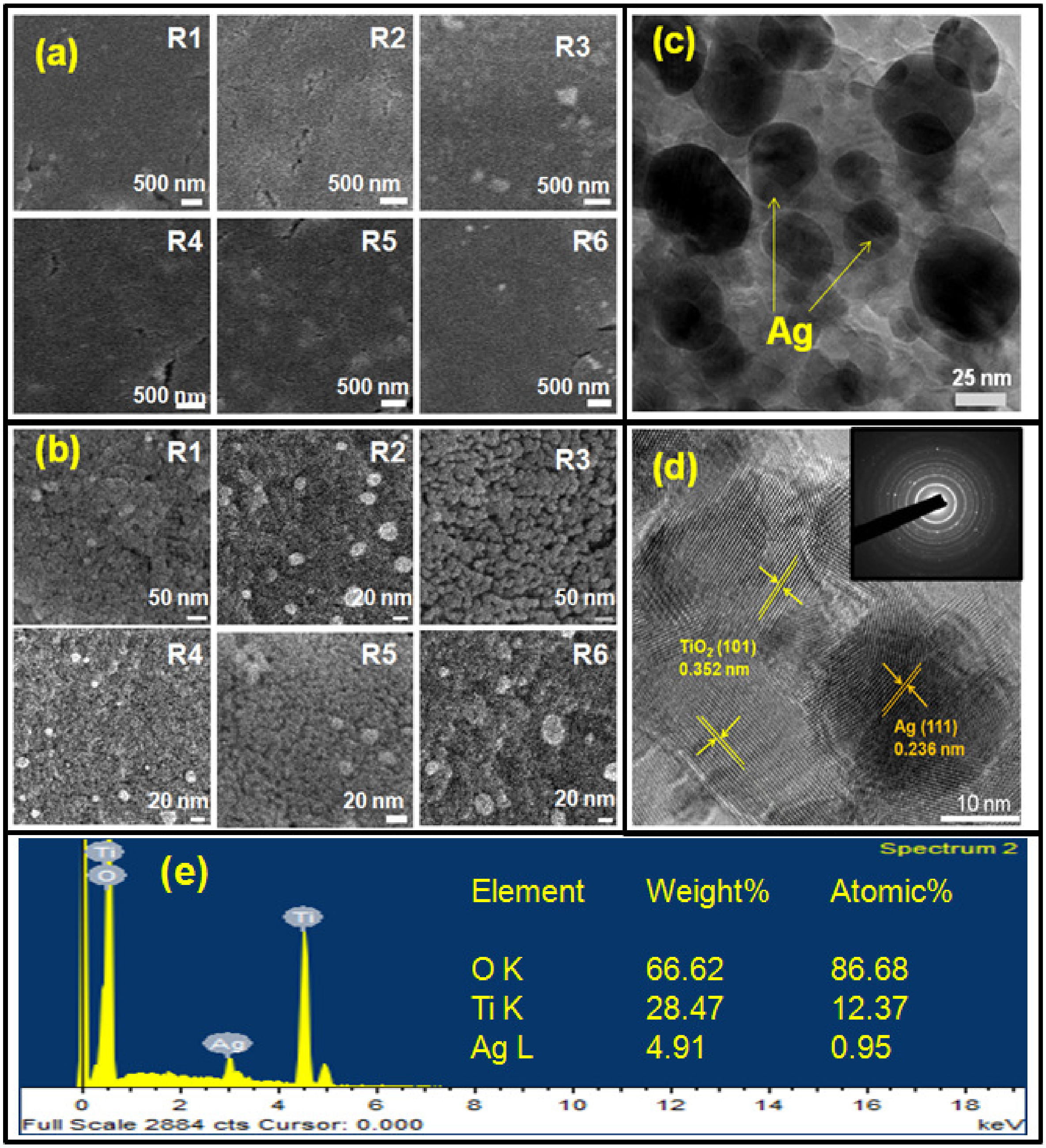

Element	Weight%	Atomic%
O K	66.62	86.68
Ti K	28.47	12.37
Ag L	4.91	0.95

Figure 6.3 FESEM micrographs of Ag-TiO_2 photocatalytic membrane at (a) low and (b) high magnifications. (c) TEM and (d) HRTEM micrographs of R2 membrane (the inset depicts the corresponding SAED pattern). (e) EDX of the surface of R2 membrane.

Fig. 6.3a shows FESEM micrographs of the membrane surface with the corresponding high magnification micrograph shown in Fig. 6.3b. The FESEM images suggest that a relatively smooth Ag-TiO_2 layer has been successfully coated onto the surface of the alumina support. The coated layers showed a minimal presence of cracks and pinholes which was important to ensure uniform permeability and good separation performance. Apparent presence of well-dispersed Ag nanoparticles (particles that appear brighter) could be observed from the high magnification FESEM micrographs of the membrane. It showed a successful dispersion of Ag nanoparticles (approximately 20 nm in diameter) onto TiO_2 matrix.

TEM micrograph of scrapped photoactive layers of R2 membrane (Fig. 6.3c.) revealed a dispersion of spherical Ag nanoparticles into the cluster of smaller TiO_2 nanoparticles. This is in agreement with earlier FESEM observation. However, some of the Ag nanoparticles were found in the agglomerated form. Ag nanoparticles are more prone to agglomeration at a higher Ag loading (Herrmann et al. 1988). HRTEM micrograph of the same membrane R2 (Fig. 6.3d.) confirms the successful formation of TiO_2 anatase crystals and deposition of Ag^0 nanoparticles. Fig. 6.3e depicts an EDX elemental analysis spectrum of a randomly selected area on the surface of R2 membrane. Ag loading was 0.5 mol% at all the sub-layers coating of R2. However, the elemental analysis showed a slightly higher Ag concentration. This indicates that Ag tends to agglomerate at the surface of the membrane. This observation is important to explain a high anti-bacterial activity of the Ag-TiO_2 membrane.

The hierarchical architecture of the Ag-TiO_2 membrane and some important characteristics are summarized in Table 6.1. Few trends could be observed from the characteristics of membranes of different hierarchical architectures. Firstly, membrane decorated with Ag tends to possess a thinner photoactive layer than the one without (323 nm of R1 vs 598 of Plu D). In the same manner, membrane with all sub-layers decorated with Ag was thinner than the one decorated with Ag only on the top-most layer. Consequently, membrane with thinner photoactive layer had a smaller amount of TiO_2 loading. This might due to different in the viscosity of the sols. TiO_2 sol with higher P-123 and Ag loading tends to be less viscous, thus a thinner layer would be coated.

Secondly, R2, R4, and R6 membranes showed a higher PEG (MW 20,000 g mol^{-1}) rejection than R1, R3, and R5 membranes respectively. This showed the effect of Ag doping that would lower the porosity and overall surface area of the TiO_2 layers that eventually affect the resulting PEG rejection profile. The 20,000 g mol^{-1} PEG solution correspond to PEG molecular size of 12 nm (Choi et al. 2006a) which is in a good agreement with the porosity profile obtained from N_2 porosimetry analysis.

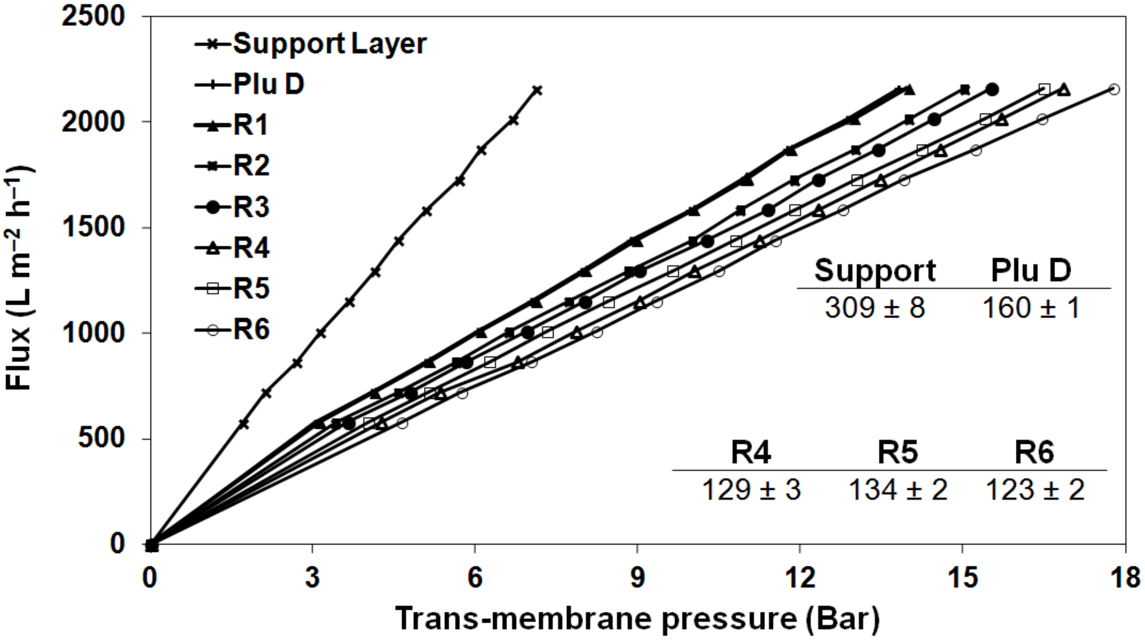

Figure 6.4 Pure water permeability of Ag-TiO_2 photocatalytic membrane (The numerical values depict average pure water permeance in L m^{-2} h^{-1} Bar^{-1}).

Thirdly, membranes with a more porous photocatalytic layer would exhibit larger pure water permeability. The numerical value of pure water fluxes of different membranes as a function of TMPs (Fig. 6.4) are listed in Table 6.1. It can be observed that the pure water permeability flux of the membranes increased linearly with the TMP regardless of the types of their hierarchical architectures. R1 and R2 membranes showed higher fluxes due to their more porous structure. All the membranes with Ag in all of its sub-layers showed a marginally smaller flux (< 10% difference) when compared with its counterpart which was consistent with the observation from N_2 porosimetry analysis. This suggests that by altering the amount of Ag incorporated would only marginally affect the resulting pure water permeability performance. Even the 'tightest' membrane (R6) showed a relatively high pure water permeability of 123 L m^{-2} h^{-1} Bar^{-1} which could be attributed to the photo-induced super-hydrophilicity (PSH) of the membrane.

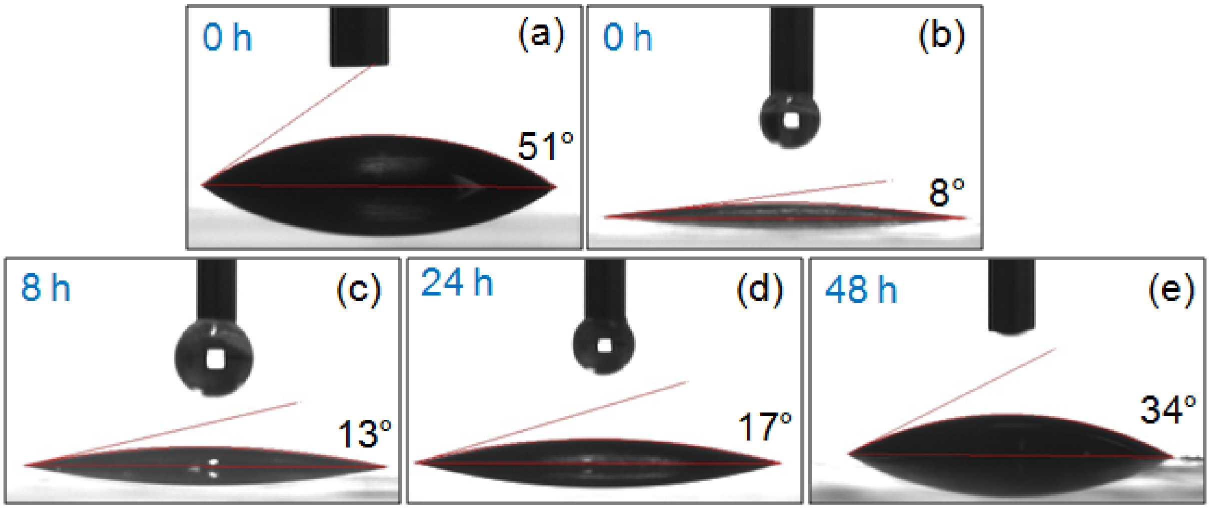

Figure 6.5 Photo-induced super-hydrophilicity of R6-like thin film coated on a borosilicate glass as shown on (a) as coated thin film, (b) upon 1 h of UV irradiation, and after (c) 8 hr, (d) 24 h, and (e) 48 h left in the dark.

The evidence of PSH property of the membrane is shown in Fig. 6.5. The coated R6-like thin film shows a contact angle of 51° which subsequently decreased to 8° after 1 h of UV irradiation. This result illustrated the photo-induced super-hydrophilicity property of Ag-TiO_2 thin film. When the UV source was switched off, the contact angle increased again to 13°, 17° and 34° after 8, 24 and 48 h respectively.

6.3.3 Photocatalytic degradation of RhB in the PMR reactor

Fig. 6.6 shows the specific RhB removal (i.e. the cumulative RhB removal per unit area of membrane over a period of time, mg m^{-2}) of the Ag- TiO_2 membrane. The photolysis of RhB at 25 μM under continuous UV irradiation (without the presence of the membrane) was < 5 %. All the membranes with Ag in all of its sub-layers showed a higher specific RhB removal as compared to the membrane with Ag only on its top-most layer. R6 showed the highest specific RhB removal owing to its tightest pore structure and highest amount of Ag incorporated. R5 and R6 membranes, which contained higher amount of Ag, showed a higher specific RhB removal as compared to their respective counterparts, R3 and R4 membranes. R1 and R2 showed a higher specific RhB removal than the control specimen Plu D.

The overall RhB removal could be attributed to two different phenomena: photocatalytic activity (PCA) of the TiO_2 layer and adsorptive-membrane retention (Ads-MR) of the membrane. The contribution of each of these phenomena is summarized in Table 6.3. It can be observed that the RhB removal through the adsorptive-retention by the membrane was lower than the removal through photocatalytic degradation. R2, R4, and R6 membranes showed a higher removal through adsorptive-retention as compared with its R1, R3, and R5 counterparts respectively. Incorporation of Ag in all sub-layers of R2, R4, and R6 caused RhB to pass through the more tortuous path of the membrane smaller porous architecture.

When compared with Plu D, the Ag-TiO_2 membrane showed (with the exception of R3) a higher specific RhB removal which was attributed to the Ag-enhanced photocatalytic activity. The incorporation of Ag could enhance the overall photocatalytic activity of the membrane by acting as an electron sink at the Schottky barrier formed at the Ag-TiO_2 interface. It was found that all the treated solutions showed a final TOC concentration < 1 mg L^{-1}, after 8 h, which was the detection limit of the equipment. This finding indicated > 88% TOC removal in the RhB solution (from the theoretical TOC concentration of 8.4 mg L^{-1} for 25 μM solution).

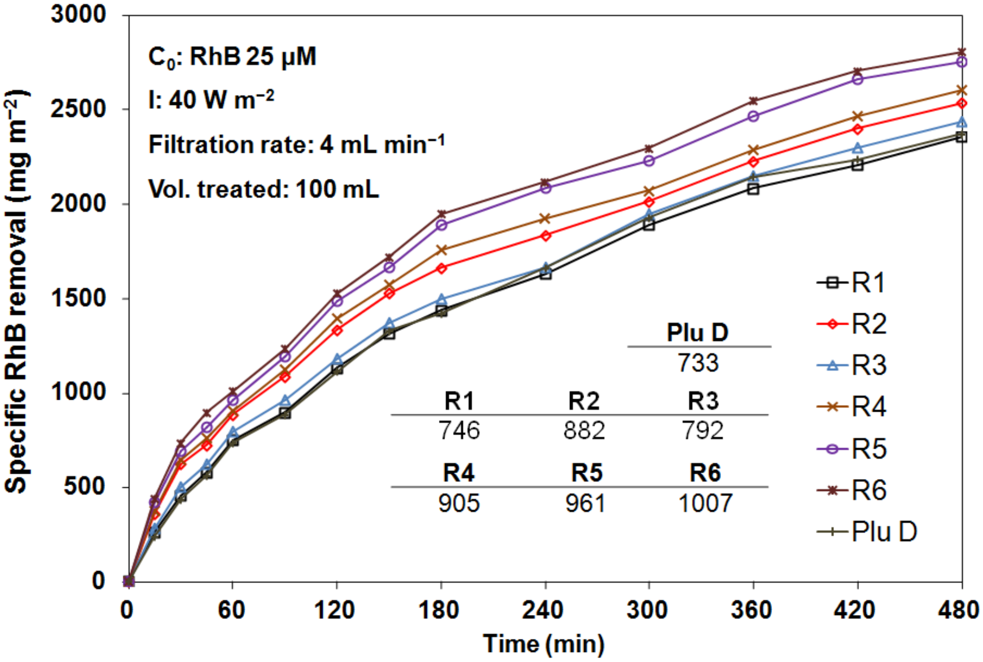

Figure 6.6 Specific RhB removal of Ag-TiO_2 photocatalytic membrane (the numerical values depict kinetic value based on initial RhB removal rate within 1st hour in mg m^{-2} h^{-1}).

Fouling control is an important property of any membrane process. The overall values of flux decline over the treatment duration of 480 min were listed in Table 6.3. The Ag-TiO_2 membrane suffered only a small fraction (up to 17 %) of flux decline over the duration of 480 min treatment of RhB. The higher initial decline of the flux could be contributed by the adsorption of RhB molecules onto the membrane. After which, the steady state flux was reached.

Table 6.3 Performance of TiO_2 photocatalytic ceramic membrane in terms of its photocatalytic activity (PCA) and adsorptive-membrane retention (Ads-MR) after 8 h of operation and percentage of initial flux retained after 4 cycles of treatment

Types	**Removal (mg m^{-2})**			**Removal (%)**		**Flux Decline**
	PCA	**Ads-MR**	**Total**	**PCA**	**Ads-MR**	**(%)**
R1	2048 ± 52	331 ± 26	2379 ± 29	86.1	13.9	13.9
R2	2169 ± 35	351 ± 22	2520 ± 13	86.1	13.9	15.1
R3	1999 ± 56	407 ± 11	2406 ± 46	83.1	16.9	16.4
R4	2048 ± 71	558 ± 23	2606 ± 74	78.6	21.4	16.8
R5	2252 ± 30	486 ± 29	2738 ± 52	82.2	17.8	16.0
R6	2203 ± 52	577 ± 56	2780 ± 29	79.2	20.8	17.1
Plu D	2025 ± 24	329 ± 13	2354 ± 18	86.0	14.0	13.8

6.3.4 Total Ag leaching of Ag-TiO_2 membranes

The usage of Ag nanoparticles as an anti-bacterial agent might release a significant amount of Ag into the treated water. Significant Ag^+ ions release would also have an adverse effect on the aqueous ecosystems and shorten the overall life-span of the Ag-TiO_2 membrane. The time-dependent Ag leaching profiles of the Ag-TiO_2 membranes are studied (Tables 6.4). Total Ag releases of R1 and R3 are small (2.0 and 1.5 μg L^{-1} respectively) which could be attributed to their relatively small Ag content at the top-most layer of the membrane. Generally, the membranes with Ag incorporated in all their sub-layers showed a higher total Ag release. Membrane R4 released more Ag^+ than R2 (despite the same amount of Ag loading on their sub-layers) because of its tighter porous structure, thus more Ag nanoparticles were concentrated near the surface of TiO_2 clusters. The highest Ag concentration leached out from the Ag-TiO_2 membrane (i.e. R6 of 27 μg L^{-1} after 168 h of immersion) was still 4 times lower than the highest tolerable Ag concentration in drinking water of 100 μg L^{-1} as prescribed by USEPA regulation and WHO guideline (USEPA 2009, WHO 2011). This showed that the Ag-TiO_2 membrane possessed a good chemical stability.

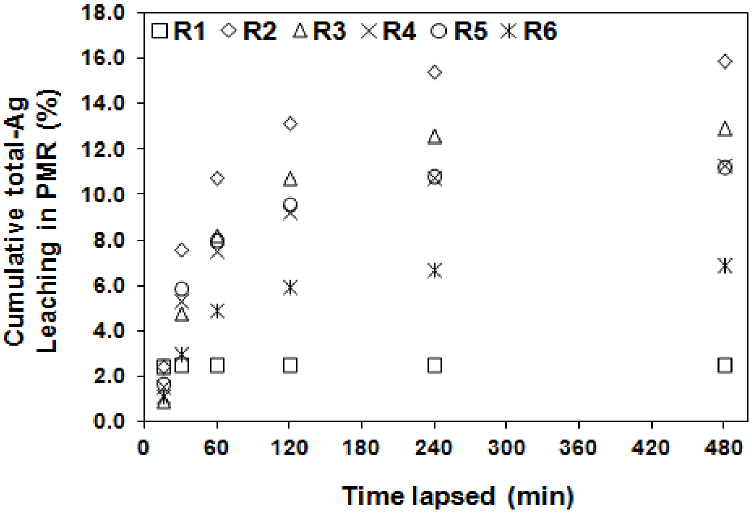

Figure 6.7 Cumulative total-Ag leached from Ag-TiO_2 membrane operated in the PMR.

Total-Ag leaching experiments were also performed in the PMR. Most of the Ag (a maximum of 8 μg L^{-1} for R6) was leached out from the membrane within the first 120 min of membrane operation (Table 6.4 and Fig. 6.7). It was evident that the additional amount of Ag leachate for the last 360 min of operation was marginal (about one-fifth of the amount released in the first 120 min) indicating the chemical stability of the membrane (Fig. 6.7). The release of Ag^+ ions was governed by the diffusion rate of both Ag^+ ions and water. At the early stage of the test, the Ag release was mainly contributed from the dissolution of surface Ag nanoparticles into water and the possibility of dislodgment of Ag nanoparticles from the membrane. After which, the rate of release was slower. The slower release of the Ag nanoparticles located inside the TiO_2 matrix could be attributed to the slow diffusion rate inside the pores (Ma et al. 2011).

Table 6.4 Time-dependent total-Ag leaching of Ag-TiO_2 membrane reported in (a) % of initial Ag loading and (b) in µg L^{-1}

(a)

Types	**Ag loading (µg)**	**Cumulative time-dependent total-Ag leaching (%) in batch reactor**			**Cummulative total-Ag leaching (%) in PMR**		
		24 h	**96 h**	**168 h**	**30 min**	**120 min**	**480 min**
R1	0.47 ± 0.03	3.30 ± 0.02	6.78 ± 0.09	12.79 ± 0.23	2.45 ± 0.02	2.46 ± 0.02	2.47 ± 0.03
R2	1.36 ± 0.22	2.27 ± 0.04	5.02 ± 0.08	7.29 ± 0.03	7.56 ± 0.13	13.16 ± 0.22	15.84 ± 0.26
R3	0.76 ± 0.01	2.46 ± 0.03	4.16 ± 0.09	5.74 ± 0.05	4.75 ± 0.08	10.73 ± 0.18	12.95 ± 0.24
R4	1.85 ± 0.28	12.37 ± 0.25	19.52 ± 0.18	26.59 ± 0.21	5.28 ± 0.04	9.21 ± 0.11	11.24 ± 0.15
R5	1.53 ± 0.16	3.64 ± 0.01	15.53 ± 0.20	24.53 ± 0.15	5.86 ± 0.09	9.54 ± 0.12	11.23 ± 0.17
R6	4.09 ± 0.61	6.31 ± 0.02	13.10 ± 0.27	19.82 ± 0.59	2.94 ± 0.04	5.88 ± 0.08	6.91 ± 0.11

(b)

Types	**Cumulative time-dependent total-Ag leaching (µg L^{-1}) in batch reactor**			**Cummulative total-Ag leaching (µg L^{-1}) in PMR**		
	24 h	**96 h**	**168 h**	30 min	120 min	480 min
R1	0.52 ± 0.01	1.07 ± 0.01	2.03 ± 0.04	2.14 ± 0.02	3.84 ± 0.03	4.66 ± 0.05
R2	1.03 ± 0.02	2.27 ± 0.04	3.30 ± 0.01	3.42 ± 0.06	5.95 ± 0.10	7.16 ± 0.12
R3	0.62 ± 0.01	1.05 ± 0.02	1.45 ± 0.01	1.20 ± 0.02	2.71 ± 0.05	3.27 ± 0.06
R4	7.62 ± 0.16	12.02 ± 0.11	16.37 ± 0.13	3.25 ± 0.03	5.67 ± 0.07	6.92 ± 0.10
R5	1.86 ± 0.01	7.92 ± 0.10	12.52 ± 0.07	2.99 ± 0.04	4.87 ± 0.06	5.73 ± 0.08
R6	8.61 ± 0.02	17.87 ± 0.37	27.04 ± 0.80	4.00 ± 0.05	8.02 ± 0.10	9.42 ± 0.15

6.3.5 Anti-bacterial performance of Ag-TiO_2 membranes

6.3.5.1 Diffusion inhibition zone test

Diffusion inhibition zone of various Ag-TiO_2 membranes with different hierarchical architectures were performed according to a standard Kirby-Bauer approach (Bauer et al. 1966) and are presented in Fig. 6.8. Ag-free Plu D membrane did not show any apparent inhibition effect against the growth of E. *coli*. R1 and R3 membranes showed a small inhibition zone due to its smaller Ag content while R5 membrane showed an observable inhibition zone (diameter of 27 mm) which highlights the significant of Ag content on the thin photoactive layer of the membrane. R2, R4 and R6 membranes which contained Ag in all of its 6 sub-layers, showed the most prominent inhibition effect with diameter of the inhibition zone measured to 36, 31, and 38 mm respectively. R2 membrane showed a larger inhibition zone as compared to R4 membrane which could be attributed to more Ag^+ ions leaching due to its larger porous structure. R6 membrane showed the largest inhibition zone owing to its largest Ag content hence more Ag^+ ions diffusion into the agar plate that restrained the bacteria growth. It was understood that diffused Ag^+ ions possessed more effective anti-bacteria property as compared with Ag nanoparticles (Lv et al. 2009b)

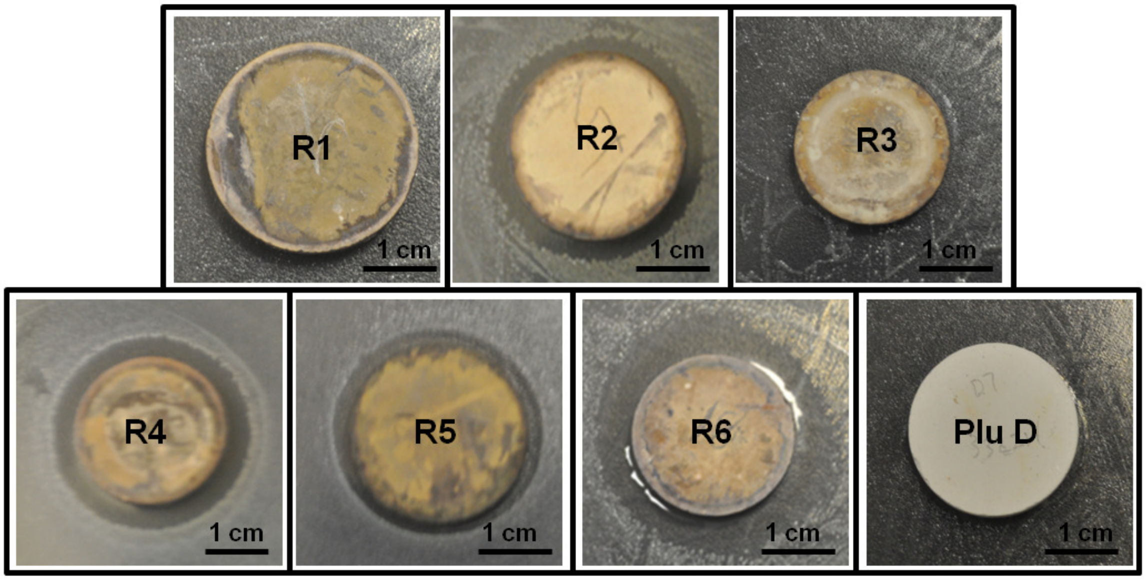

Figure 6.8 Diffusion inhibition zones of Ag-TiO_2 photocatalytic membrane against E. *coli* after 24 h incubation.

.

6.3.5.2 Anti-bacterial performance using batch reactor

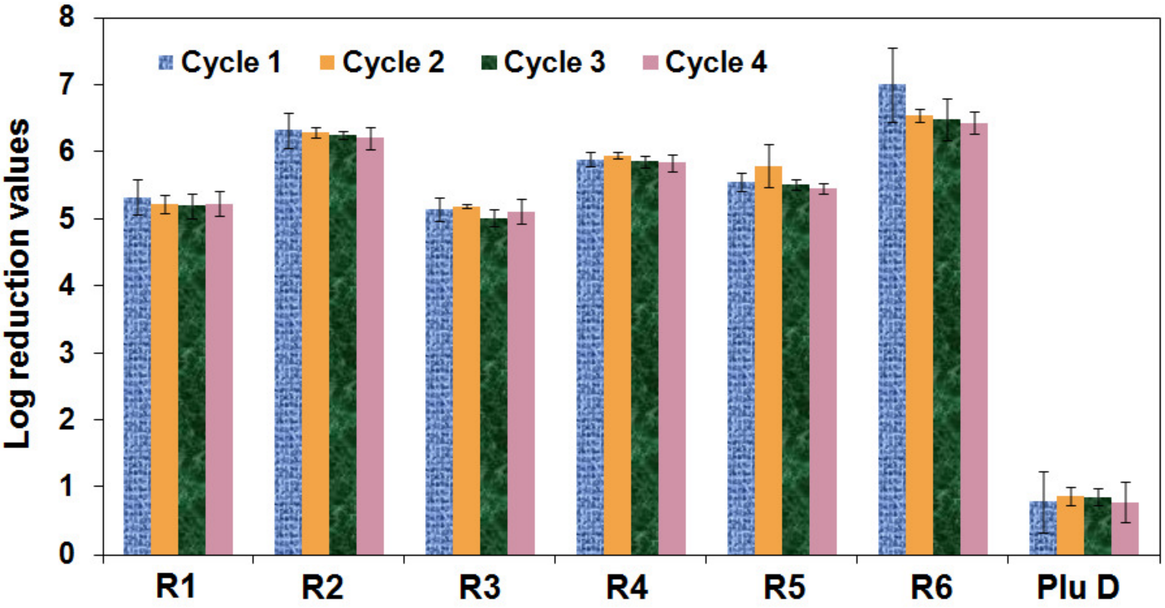

Figure 6.9 E. *coli* log reduction value of Ag-TiO_2 photocatalytic membrane showing its reusability over 4 cycles (duration of 8 h each cycle) of operation in a batch reactor. Error bars represent one standard deviation of at least three replicates of experimental runs.

Fig. 6.9 shows log reduction values of E. *coli* suspension when subjected to the Ag-TiO_2 membrane at a batch reactor operating at dark under continuous stirring. The Ag-TiO_2 membranes were able to remove a minimum of 5-logs of E. *coli* from it suspension within 15 min contact time. This suggests that the Ag-TiO_2 membrane exhibited an excellent anti-bacterial activity even when operating in the dark. The overall reduction of E. *coli* was caused by the snit-bacterial activity of Ag. R1, R2, R3, R4, R5, and R6 membranes reduce the E. *coli* viable cells count up to 5.3, 6.3, 5.2, 6.0, 5.8, and 7.0 logs respectively. R2, R4, and R6 showed more E. *coli* removal efficiency due to a higher Ag loading on its sub-layers. This is consistent with earlier observation from the total Ag-leaching study. R1 and R2 showed a slightly higher E. *coli* removal efficiency than its R3 and R4 counterpart. This could be attributed to their more porous structure that allowed more interaction between Ag species and bacteria cells. 1-log removal of E. *coli* suspension when treated with Plu D suggests that TiO_2-anatase posses, to some extent, a bactericidal activity (Kubacka et al. 2009). Repeated usages (up to 4 cycles) of the membrane showed a good consistency of E. *coli* removal efficiency. This suggests a reusability potential of the Ag-TiO_2 membrane.

6.3.5.3 Anti-bacterial performance using PMR

The anti-bacterial performances of the various membranes used in the PMR are illustrated in Figs. 6.10-6.13. Prior to any of the experiments, the PMR was flushed thoroughly with 0.9 wt% NaCl solution. After which, the feed was replaced with E. *coli* suspension. A control sampling was taken regularly at the sampling point 1 (Fig. 1) to ensure that the concentration of E. *coli* suspension entering the membrane cell was the same as the concentration at the feed tank. Upon entering the membrane cell, E. *coli* started to be deposited onto the surface of the membrane. This was evidenced from a declining permeate flux as the experiment progressed (Fig. 6.10a and b). The fouling was expected as the size of E. *coli* cell (± 1 μm length) was much larger than the pore size of the Ag-TiO_2 membrane (between 4–12 nm depending on the amount of P-123 and Ag loading).

The membrane fouling could be caused by the adhesion and accumulation of dead bacteria cells on the membrane surface (Yao et al. 2008). However, as the experiment progressed, the rate of declining flux was progressively reduced. The experiments that were carried out in the presence of UV irradiation exhibited a much smaller flux decline. After 30 min of operation, the feed was replaced by an equal-volume 0.9 wt% NaCl solution and the cross-flow cleaning valve was opened. This was a cross-flow cleaning step that helped to recover the permeate flux by dislodging any deposited dead-bacteria cells.

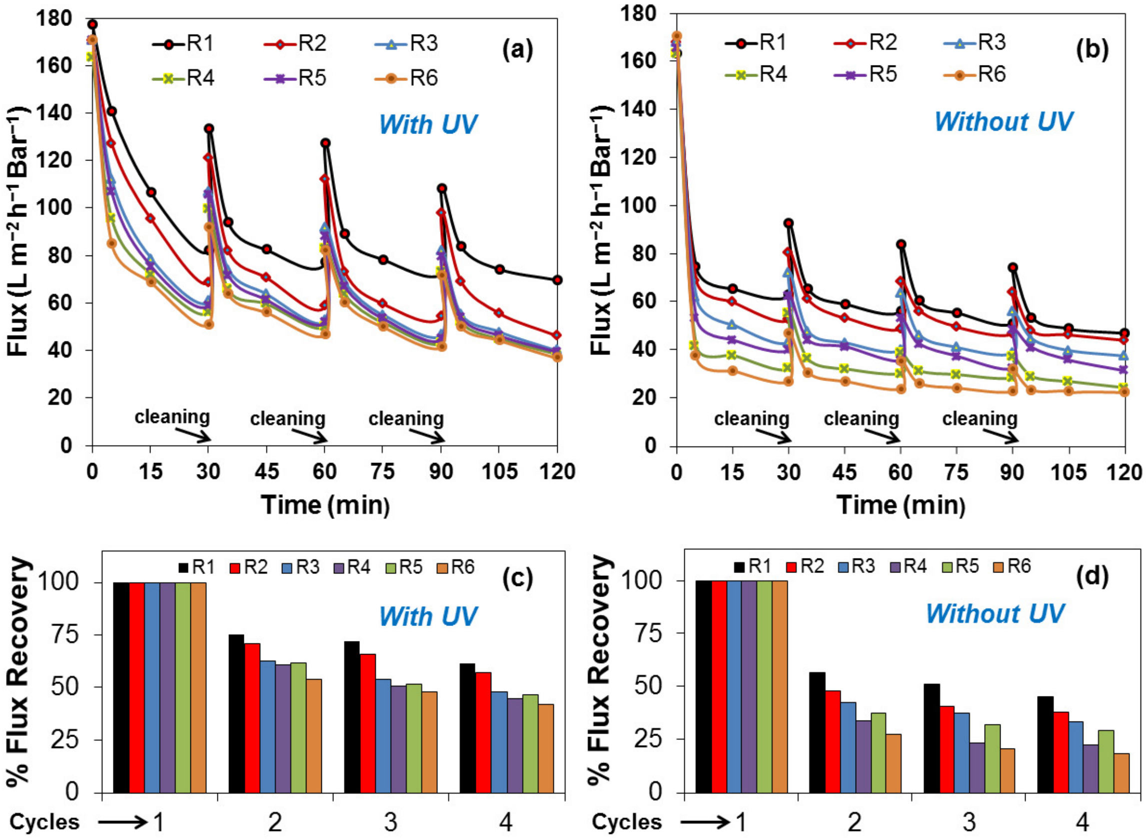

Figure 6.10 Flux performance of Ag-TiO$_2$ photocatalytic membrane in the dead-end filtration mode of PMR with inter-cycle cleaning operating (a) with UV and (b) without UV. Percent flux recovery after each cleaning cycles when operating (c) with UV and (d) without UV.

The percentages of flux recovery after each cleaning cycle are shown in Fig. 6.10c and d. The membranes operated under UV irradiation showed higher flux recoveries. R1 and R2 (possessed more porous structure) exhibited the least flux decline. In general, the membranes with larger porosity exhibited lesser flux decline than their counterparts. From the decreasing rate of flux decline after each operation-cleaning cycle, it could be hypothesized that a steady-state sustainable flux would be achieved after a certain number of operation-cleaning cycles.

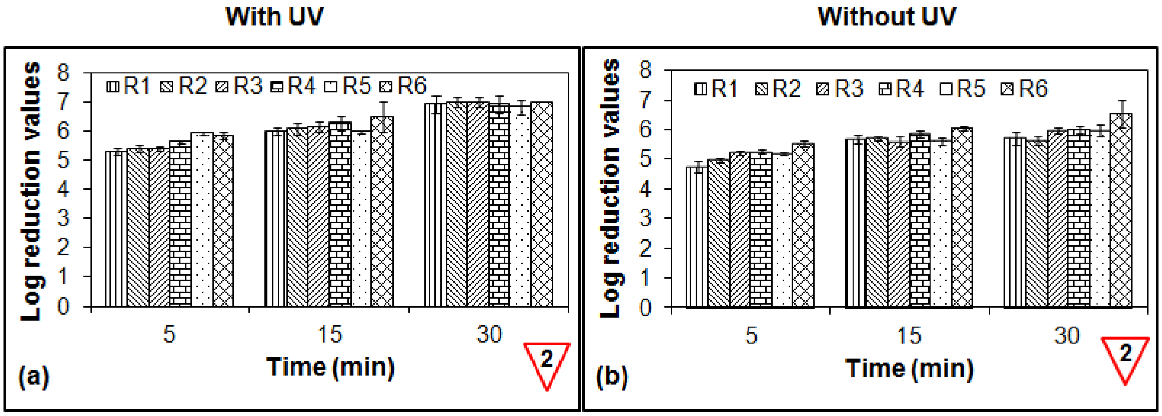

Figure 6.11 E. *coli* log reduction values of Ag-TiO_2 photocatalytic membrane operating in a photocatalytic membrane reactor: at sampling point (2) when operating (a) with and (b) without UV. Error bars represent one standard deviation of at least three replicates of experimental runs.

The log reduction value of E. *coli* was evaluated during the PMR operation (aliquots taken from the sampling point 2, Fig. 6.11) and after each cleaning cycle (aliquots taken from the sampling point 3, Fig. 6.12). In the presence of UV irradiation (λ_{max} = 365 nm) alone, only 1.9 ± 0.2 log of bacteria cells was killed. Sample aliquots taken from the sampling point 2 during operation should contain a negligible concentration of E. *coli* (< 0.002% of the initial feed concentration) as most of the bacteria cells (>99.998%) would be retained or inactivated by the membrane. The membranes operating under UV irradiation generally showed a higher E. *coli* reduction values. Also, the membranes with higher amounts of Ag content showed a higher E. *coli* reduction values.

Sample aliquots (Fig. 6.12a and b) taken from sampling point 3 (after each cleaning cycle) showed a clearer trend. It can be observed that the membranes operating under UV irradiation showed a higher overall E. *coli* removal. This could be attributed to three synergistic processes that were taking place, i.e. Ag anti-bacteria activity, Ag-enhanced TiO_2 photocatalytic disinfection, and, to the lesser extent, direct UV disinfection. Reduction of viable E. *coli* counts for experiments that were carried out in the dark could be ascribed to the inherent Ag anti-bacterial activity only.

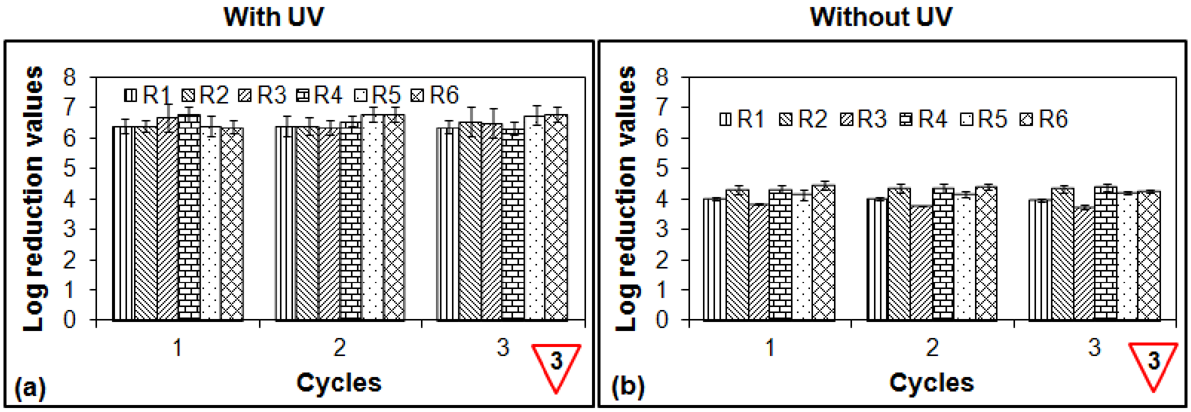

Figure 6.12 E. *coli* log reduction values of Ag-TiO_2 photocatalytic membrane operating in a photocatalytic membrane reactor: at sampling point (3) after each cross-flow cleaning cycles when operating (a) with and (b) without UV. Error bars represent one standard deviation of at least three replicates of experimental runs.

6.3.5.4 Anti-bacterial mechanisms of Ag-TiO_2 membranes

In order elucidate the contribution of each anti-bacterial processes, selected results from the PMR experiment (taken at sampling point 3) are tabulated in Fig. 6.13. Alumina support disk show no anti-bacterial capability. Plu D membrane showed some degree of antibacterial capability of TiO_2-anatase. When operating Plu D under UV irradiation, the synergistic effect of TiO_2 photocatalytic disinfection and direct UV disinfection could be observed (by almost 4-log increase in *E. coli* removal). Same effect was evidenced when different Ag-TiO_2 membrane operating under UV irradiation. Membrane with higher amount of Ag loading, showed higher E. coli reduction values (e.g. R2 > R1, R5 >R1, and R6>R5). This could be attributed to additional process of Ag anti-bacterial activity as well as enhanced TiO_2 photocatalytic degradation.

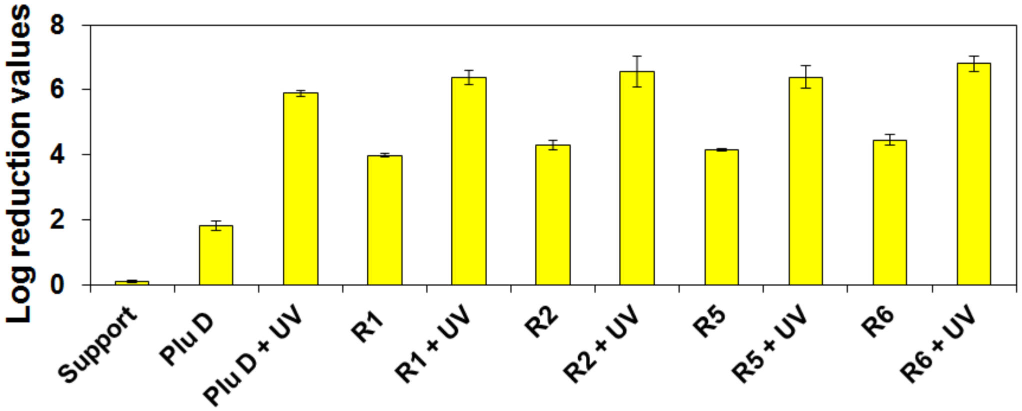

Figure 6.13 Log reduction values of E. *coli* at sampling point 3 after cross-flow cleaning cycle for various membranes. Error bars represent one standard deviation of at least three replicates of experimental runs.

It is not an easy task to pin-point which process has a larger contribution on the overall anti-bacteria/anti-biofouling activity of the Ag-TiO_2 membrane. Some possible anti-bacteria mechanisms are illustrated in Fig. 6.14. They are: direct UV disinfection, membrane rejection, interaction of bacteria cells with Ag^+ ions, direct interaction with Ag nanoparticles, and TiO_2 photocatalytic disinfection.

The important processes could be explained as followed: Ag^0 tends to be lightly bonded to oxygen, which would readily oxidized to Ag^+, interact with the disulfide or thiol (-S-H) groups enzyme or DNA of the bacteria, while removing H as water. This would cause the formation of R-S-S-R bond that would disrupt respiration and other metabolic processes, interrupt DNA replication, and causing the death of bacteria cells (bactericidal effect) (Feng et al. 2000, Russell and Hugo 1994, Siva Kumar et al. 2004). It was also reported that Ag^+ ions are able to change the permeability of the negatively charged-cell wall, causing cell lysis and the eventual death (Samuel and Guggenbichler 2004). Some surviving bacteria that are already contaminated with Ag^+ ions cannot grow into colonies because their growth signaling pathway has been disturbed by penetrating Ag^+ ions (bacteriostatic effect) (Lv et al. 2009b, Shrivastava et al. 2007).

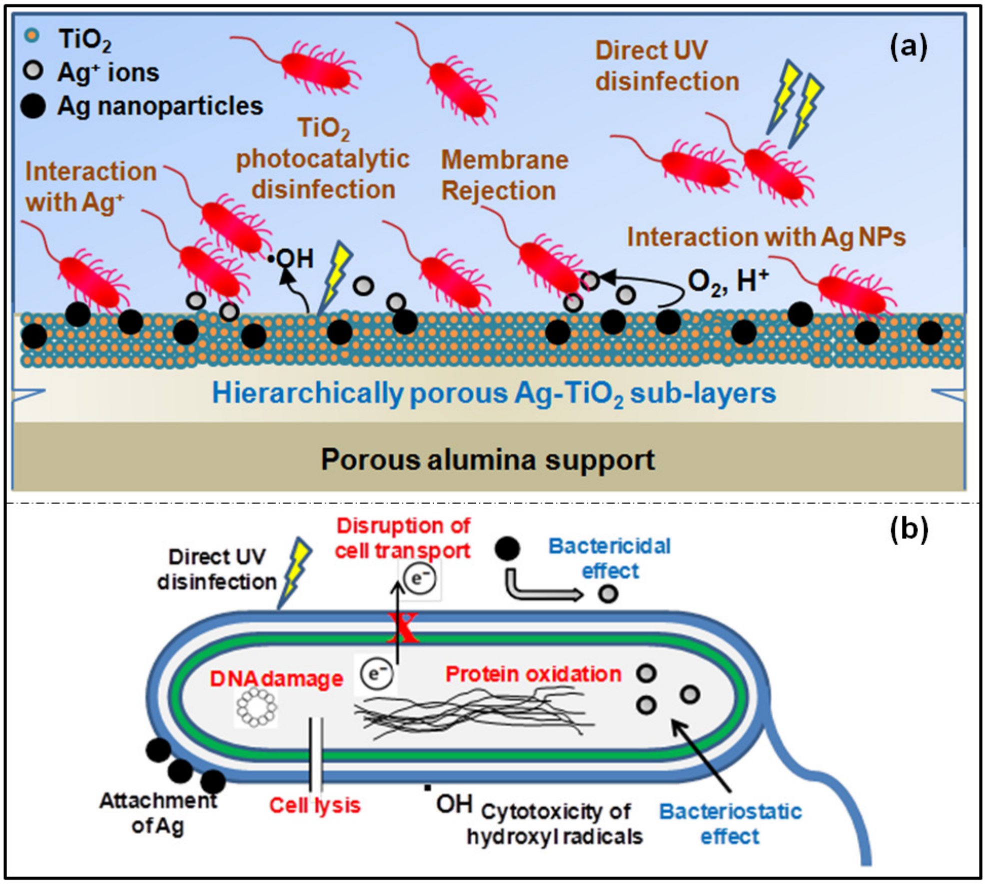

Figure 6.14 (a) Possible mechanisms of anti-bacterial action inside the photocatalytic membrane reactor: direct UV disinfection (when subjected to a high UV intensity), membrane rejection, interaction with Ag^+ ions, interaction with Ag nanoparticles, and bactericidal action of TiO_2 and (b) Summary of different actions of bacteria inactivation.

Ag nanoparticles could directly attached to the surface of bacteria cell membrane, destabilize the outer membrane, disrupt the plasma membrane potential and decrease the concentration of intracellular ATP (Choi et al. 2008, Lok et al. 2006, Sondi and Salopek-Sondi 2004).

Hydroxyl radicals are the cytotoxic agent produced at the surface of TiO_2 photocatalyst that directly attacks the cytoplasmic membrane of the bacteria and resulting in the leakage of the intracellular components. A Gram-negative bacterium such as E. *coli* is protected only by a thin peptidoglycan layer (a relatively open polymeric network of N-acetylmuramic and N-acetylglucosamine polysaccharide chains with peptide bridges). However, it is the outer membrane (consist of complex layer of lipids, lipopolysaccharides and proteins) that hinders the passage of hydroxyl radicals (Huang et al. 2000, Lu et al. 2003, Page et al. 2007).

Finally, the ability of bacteria to undergo repair after photocatalytic disinfection were investigated both in the dark and in the presence of UV irradiation. Bacteria cells could repair themselves either through dark repair or photo-reactivation (Rincón and Pulgarin 2004) after irradiation to light with wavelength of 300-500 nm (Kashimada et al. 1996). No bacterial growth could be detected after the bacterial repairing period for both tested solutions. This suggests that photocatalytic disinfection caused a permanent damage to the bacterial cells unless a provision of favorable conditions for bacteria repair were given (Dunlop et al. 2002).

6.4 Conclusions

Ag-TiO_2 photocatalytic membranes have been fabricated using P-123 as the pore forming and structure-directing agent. The different membranes possessed their unique hierarchical architectures that were achieved by multilayer coating of Ag-TiO_2 of different porous structures. Ag incorporation enhanced the photocatalytic activity of TiO_2 by hindering the recombination of photo-generated electrons and holes. Furthermore, the incorporation of Ag imparted anti-bacterial functionality to the membranes. The Ag-TiO_2 membrane possessed a multi-functionality of membrane retention, Ag-enhanced TiO_2 photocatalytic activity and multiple anti-bacterial actions. The reusability potential of the Ag-TiO_2 membranes has been demonstrated both in the batch and flow-through PMR which would reduce the overall operating cost of the treatment system.

CHAPTER 7 CONCLUSIONS AND RECOMMENDATIONS

7.1 Conclusions

Different types of TiO_2 layers with controllable porous structure were prepared by acid-catalyzed sol-gel method employing P-123 as the SDA. TiO_2 sols were dip-coated on a macroporous alumina ceramic membrane support. Layer-by-layer coatings were performed to obtain a hybrid TiO_2 photocatalytic ceramic membrane with a hierarchical porous architecture. Extensive characterization of the resulting membrane has been carried out. The membrane displayed a photo-induced super-hydrophilicity. Plu D membrane with 3-2-1 layers configuration was found to display an optimum membrane and photocatalytic degradation of RhB performances.

Four types of SDAs were employed to fabricate a hierarchically porous TiO_2 photocatalytic membrane. TiO_2 layers prepared using different SDAs could be used in the composite membrane fabrication without any compatibility issue. This allow flexibility of constructing a membrane that exhibit favorable operating parameters such as high permeability, good membrane separation, good photocatalytic degradation capability, or any combination of the parameters.

Ag-decorated hierarchically porous TiO_2 photocatalytic membrane has been fabricated. The amount of Ag incorporated, together with the amount of SDA (P-123), could be used to control the porosity structure of the resulting Ag-TiO_2 layer. Membranes with different configurations (different porosities and location of Ag doping) were fabricated. The incorporation of Ag had caused enhancement in the photocatalytic activity of TiO_2 and introduced an additional anti-bacterial functionality. The anti-bacterial functionality of the Ag-TiO_2 membrane was tested against E. *coli*, a common water-borne pathogen. Multiple anti-bacterial actions have also been postulated.

The integration of TiO_2 photocatalysis, membrane separation, and Ag-induced anti-bacterial actions has offered a multi-functional one-stop treatment system with simpler configuration and smaller overall footprint. The hybrid membrane displayed a great potential to be used in water and wastewater treatment and many other potential environmentally important applications.

7.2 Recommendations for future research

To further enhance and extend the potential application of the hierarchically porous TiO_2 photocatalytic ceramic membrane for wastewater treatment and water reclamation, several recommendations for the future research are proposed:

1. Hierarchically porous TiO_2 photocatalytic membrane
    - A more versatile techniques can be developed for the preparation and coating of the TiO_2 sol onto the ceramic disk support. Different ceramic supports (e.g. supports that made of macroporous ZnO or TiO_2) can be considered to enhance the functionality of the composite membrane.
    - A more thorough investigation of TiO_2 photocatalytic membrane can be carried out to fully understand the microstructure of the photocatalytic layer
    - An intermediate molecular sieve layer can be introduced to enhance the molecular size-selectivity and permeability of the composite membranes.
    - To prepare a hybrid membrane with top layer having a smaller pore sizes (in the NF range or down to ~1 nm) to investigate the efficacy of the hybrid membrane in treating small recalcitrant molecules.
    - Some analytical techniques could be employed to investigate the generation of reactive oxygen species, to fully elucidate the mechanism of photocatalytic

  degradation reaction (i.e. electron paramagnetic resonance (EPR), electron spin resonance (ESR), cyclic voltammetry, etc).

  - The possibility of up-scaling the operation of TiO_2 photocatalytic membrane can be considered. Several ideas for the up-scaling include fabrication of a larger composite membrane, simultaneous operation of the parallel PMRs, etc.

2. Metal/non-metal decorated TiO_2 photocatalytic membrane
   - The possibility of exploiting surface plasmon resonance induced by Ag-TiO_2 can be investigated for operation of Ag-TiO_2 membrane using a visible light as the irradiation source.
   - Ag^+ leaching in a continuous flow through setup can be monitored for a longer period to study the temporal Ag^+ leaching from the membrane.
   - The possibility of incorporation of other metal (e.g. Er, Si, Zn, Zr, etc) or non-metal (e.g. C, N, S, etc) dopants or co-dopants into the TiO_2 matrix can be investigated.
3. Hybrid photocatalytic membrane reactor
   - The configuration of the PMR can be adjusted to provide insight of the effect of various operation parameters (such as different irradiation sources, different operation modes, different flow rate, etc) to the efficiency of the treatment process.
   - The possibility of introducing a more versatile irradiation source can be considered (e.g. through the use of fiber optics) to overcome the challenge of PMR reactor design.
   - The setup and control of the automated PMR can be enhanced to allow continuous operation. The safety feature can be enhanced to minimize

interruption of the continuous operation. Round-the-clock operation of the PMR can provide interesting insight onto the real-scale operation of the TiO_2 photocatalytic membrane.

- The removal efficiency of TiO_2 photocatalytic membrane can be evaluated against a wider range of pollutants as well as possibility of treating a real wastewater. Different parameters such as pH of the solution and the effect of various aqueous matrix species can be studied.
- Various pre-treatments can be considered to be operated in tandem with PMR system to allow a wider range of application for wastewater treatment.
- Various membrane operation parameters such as critical flux determination and the effect of backwashing can be investigated to enhance the understanding of the operation of TiO_2 photocatalytic membrane in the PMR.
- The economy of the treatment process (including fixed and operating cost) can be evaluated for comparisons with other similar treatment system.

4. Anti-bacterial action of Ag-TiO_2 membrane
    - The effect of pH and inorganic matrix species on the anti-bacterial action against E. *coli* can be investigated.
    - Various operating parameters such as different constant fluxes, irradiation sources, operation modes, etc can be investigated to understand the extent of the anti-bacterial action of Ag-TiO_2 membrane.
    - The efficacy of the anti-bacteria property of the membrane can be tested against other type of bacteria including gram positive bacteria (e.g. *S. aureus*).

REFERENCES

Abellán, M.N., Bayarri, B., Giménez, J. and Costa, J. (2007) Photocatalytic degradation of sulfamethoxazole in aqueous suspension of TiO_2. Applied Catalysis B: Environmental 74(3-4), 233-241.

Akhavan, O. (2009) Lasting antibacterial activities of Ag-TiO_2/Ag/a-TiO_2 nanocomposite thin film photocatalysts under solar light irradiation. Journal of Colloid And Interface Science 336(1), 117-124.

Akhavan, O. and Ghaderi, E. (2010) Self-accumulated Ag nanoparticles on mesoporous TiO_2 thin film with high bactericidal activities. Surface and Coatings Technology 204(21-22), 3676-3683.

Aksu, Z. (2005) Application of biosorption for the removal of organic pollutants: A review. Process Biochemistry 40(3-4), 997-1026.

Alem, A., Sarpoolaky, H. and Keshmiri, M. (2009a) Sol-gel preparation of titania multilayer membrane for photocatalytic applications. Ceramics International 35(5), 1837-1843.

Alem, A., Sarpoolaky, H. and Keshmiri, M. (2009b) Titania ultrafiltration membrane: Preparation, characterization and photocatalytic activity. Journal of the European Ceramic Society 29(4), 629-635.

Almeida, J.C., Castro, A.G.B., Lancastre, J.J.H., Miranda Salvado, I.M., Margaça, F.M.A., Fernandes, M.H.V., Ferreira, L.M. and Casimiro, M.H. (2014) Structural characterization of PDMS-TEOS-CaO-TiO_2 hybrid materials obtained by sol-gel. Materials Chemistry and Physics 143(2), 557-563.

Amama, P.B., Itoh, K. and Murabayashi, M. (2004) Photocatalytic degradation of trichloroethylene in dry and humid atmospheres: Role of gas-phase reactions. Journal of Molecular Catalysis A: Chemical 217(1-2), 109-115.

Anderson, M.A., Gieselmann, M.J. and Xu, Q. (1988) Titania and alumina ceramic membranes. Journal of Membrane Science 39(3), 243-258.

Andersson, M., Alfredsson, V., Kjellin, P. and Palmqvist, A.E.C. (2002) Macroscopic alignment of silver nanoparticles in reverse hexagonal liquid crystalline templates. Nano Letters 2(12), 1403-1407.

Anpo, M., Shima, T., Kodama, S. and Kubokawa, Y. (1987) Photocatalytic hydrogenation of CH_3CCH with H_2O on small-particle TiO_2: size quantization effects and reaction intermediates. Journal of Physical Chemistry 91(16), 4305-4310.

Antoniou, M.G., Shoemaker, J.A., de la Cruz, A.A. and Dionysiou, D.D. (2008) LC/MS/MS structure elucidation of reaction intermediates formed during the TiO_2 photocatalysis of microcystin-LR. Toxicon 51(6), 1103-1118.

Ao, Y., Xu, J., Fu, D. and Yuan, C. (2008) Preparation of Ag-doped mesoporous titania and its enhanced photocatalytic activity under UV light irradiation. Journal of Physics and Chemistry of Solids 69(11), 2660-2664.

Appels, L., Baeyens, J., Degrève, J. and Dewil, R. (2008) Principles and potential of the anaerobic digestion of waste-activated sludge. Progress in Energy and Combustion Science 34(6), 755-781.

Arabatzis, I.M., Stergiopoulos, T., Bernard, M.C., Labou, D., Neophytides, S.G. and Falaras, P. (2003) Silver-modified titanium dioxide thin films for efficient photodegradation of methyl orange. Applied Catalysis B: Environmental 42(2), 187-201.

Arconada, N., Durán, A., Suárez, S., Portela, R., Coronado, J.M., Sánchez, B. and Castro, Y. (2009) Synthesis and photocatalytic properties of dense and porous TiO_2-anatase thin films prepared by sol-gel. Applied Catalysis B: Environmental 86(1-2), 1-7.

Arconada, N., Castro, Y. and Durán, A. (2010) Photocatalytic properties in aqueous solution of porous TiO_2-anatase films prepared by sol-gel process. Applied Catalysis A: General 385(1-2), 101-107.

Arconada, N., Castro, Y., Durán, A. and Héquet, V. (2011) Photocatalytic oxidation of methyl ethyl ketones over sol-gel mesoporous and meso-structured TiO_2 films obtained by EISA method. Applied Catalysis B: Environmental 107(1-2), 52-58.

Artale, M.A., Augugliaro, V., Drioli, E., Golemme, G., Grande, C., Loddo, V., Molinari, R., Palmisano, L. and Schiavello, M. (2001) Preparation and characterisation of membranes with entrapped TIO_2 and preliminary photocatalytic tests. Annali di Chimica 91(3-4), 127-136.

Attwood, D. and Florence, A.T. (1985) Surfactant System Their chemistry, pharmacy and biology., Chapman and Hall, London.

Awitor, K.O., Rivaton, A., Gardette, J.L., Down, A.J. and Johnson, M.B. (2008) Photo-protection and photo-catalytic activity of crystalline anatase titanium dioxide sputter-coated on polymer films. Thin Solid Films 516(8), 2286-2291.

Azrague, K., Puech-Costes, E., Aimar, P., Maurette, M.T. and Benoit-Marquie, F. (2005) Membrane photoreactor (MPR) for the mineralisation of organic pollutants from turbid effluents. Journal of Membrane Science 258(1-2), 71-77.

Bailey, S.E., Olin, T.J., Bricka, R.M. and Adrian, D.D. (1999) A review of potentially low-cost sorbents for heavy metals. Water Research 33(11), 2469-2479.

Baker, R.W. (2004) Membrane Technology and Applications, John Wiley & Sons Ltd., Chichester, England.

Barboux-Doeuff, S. and Sanchez, C. (1994) Synthesis and characterization of titanium oxide-based gels synthesized from acetate modified titanium butoxide precursors. Materials Research Bulletin 29(1), 1-13.

Barrett, E.P., Joyner, L.G. and Halenda, P.P. (1951) The determination of pore volume and area distributions in porous substances. I. Computations from nitrogen isotherms. Journal of the American Chemical Society 73(1), 373-380.

Bauer, A.W., Kirby, W.M., Sherris, J.C. and Turck, M. (1966) Antibiotic susceptibility testing by a standardized single disk method. American Journal of Clinical Pathology 45(4), 493-496.

Bersani, D., Lottici, P.P. and Ding, X.Z. (1998) Phonon confinement effects in the Raman scattering by TiO_2 nanocrystals. Applied Physics Letters 72(1), 73-75.

Beyers, E., Cool, P. and Vansant, E.F. (2005) Anatase formation during the synthesis of mesoporous titania and its photocatalytic effect. Journal of Physical Chemistry B 109(20), 10081-10086.

Bhatkhande, D.S., Pangarkar, V.G. and Beenackers, A.A.C.M. (2002) Photocatalytic degradation for environmental applications - A review. Journal of Chemical Technology and Biotechnology 77(1), 102-116.

Bhatkhande, D.S., Pangarkar, V.G. and Beenackers, A.A.C.M. (2003) Photocatalytic degradation of nitrobenzene using titanium dioxide and concentrated solar radiation: Chemical effects and scaleup. Water Research 37(6), 1223-1230.

Bhave, P.R. (1991) Inorganic Membrane Synthesis, Characteristics, and Applications, Van Nostrand Reinhold, New York.

Boissiere, C., Grosso, D., Lepoutre, S., Nicole, L., Bruneau, A.B. and Sanchez, C. (2005) Porosity and mechanical properties of mesoporous thin films assessed by environmental ellipsometric porosimetry. Langmuir 21(26), 12362-12371.

Bosc, F., Ayral, A., Albouy, P.A. and Guizard, C. (2003) A simple route for low-temperature synthesis of mesoporous and nanocrystalline anatase thin films. Chemistry of Materials 15(12), 2463-2468.

Bosc, F., Lacroix-Desmazes, P. and Ayral, A. (2006) TiO_2 anatase-based membranes with hierarchical porosity and photocatalytic properties. Journal of Colloid and Interface Science 304(2), 545-548.

Bosco, M.V., Garrido, M. and Larrechi, M.S. (2006) Determination of phenol in the presence of its principal degradation products in water during a TiO_2-photocatalytic degradation process by three-dimensional excitation-emission matrix fluorescence and parallel factor analysis. Analytica Chimica Acta 559(2), 240-247.

Bradley, D.C., Mehrotra, R.C. and Gaur, D.P. (1978) Metal alkoxides, Academic Press, London.

Brunauer, S., Emmett, P.H. and Teller, E. (1938) Adsorption of gases in multimolecular layers. Journal of the American Chemical Society 60(2), 309-319.

Buekenhoudt, A. (2008) Inorganic Membranes: Synthesis, Characterisation and Applications. Mallada, R. and Menendez, M. (eds), pp. 1-31, Elsevier B.V., Jaca, Spain.

Burggraaf, A.J. and Cot, L. (eds) (1996) Fundamental of Inorganic Membrane Science and Technology, Elsevier Science, Amsterdam.

Byrappa, K., Lokanatha Rai, K.M. and Yoshimura, M. (2000) Hydrothermal preparation of TiO_2 and photocatalytic degradation of hexachlorocyclohexane and dichlorodiphenyltrichloromethane. Environmental Technology 21(10), 1085-1090.

Calza, P., Sakkas, V.A., Medana, C., Baiocchi, C., Dimou, A., Pelizzetti, E. and Albanis, T. (2006) Photocatalytic degradation study of diclofenac over aqueous TiO_2 suspensions. Applied Catalysis B: Environmental 67(3-4), 197-205.

Carp, O., Huisman, C.L. and Reller, A. (2004) Photoinduced reactivity of titanium dioxide. Progress in Solid State Chemistry 32(1-2), 33-177.

Castro, Y. and Durán, A. (2013) Mesoporous and mesostructured TiO_2 coatings for photocatalytic applications. Journal of Sol-Gel Science and Technology, 1-9.

Chang, C.H., Gopalan, R. and Lin, Y.S. (1994) A comparative study on thermal and hydrothermal stability of alumina, titania and zirconia membranes. Journal of Membrane Science 91(1-2), 27-45.

Chang, Y.L. and Hsiang, H.I. (2010) A surfactant-assisted solid-state synthesis of $BaTiO_3$ from $BaCO_3$ and TiO_2, pp. 9-22.

Chao, H.E., Yun, Y.U., Xingfang, H.U. and Larbot, A. (2003) Effect of silver doping on the phase transformation and grain growth of sol-gel titania powder. Journal of the European Ceramic Society 23(9), 1457-1464.

Chen, G. (2004) Electrochemical technologies in wastewater treatment. Separation and Purification Technology 38(1), 11-41.

Chen, L., Tian, J., Qiu, H., Yin, Y., Wang, X., Dai, J., Wu, P., Wang, A. and Chu, L. (2009) Preparation of TiO_2 nanofilm via sol-gel process and its photocatalytic activity for degradation of methyl orange. Ceramics International 35(8), 3275-3280.

Chen, X. and Mao, S.S. (2007) Titanium dioxide nanomaterials: Synthesis, properties, modifications and applications. Chemical Reviews 107(7), 2891-2959.

Chen, Y. and Dionysiou, D.D. (2007) A comparative study on physicochemical properties and photocatalytic behavior of macroporous TiO_2-P25 composite films and macroporous TiO_2 films coated on stainless steel substrate. Applied Catalysis A: General 317(1), 129-137.

Chen, Y. and Dionysiou, D.D. (2008) Bimodal mesoporous TiO_2-P25 composite thick films with high photocatalytic activity and improved structural integrity. Applied Catalysis B: Environmental 80(1-2), 147-155.

Chen, Y., Lunsford, S.K., Song, Y., Ju, H., Falaras, P., likodimos, V., Kontos, A.G. and Dionysiou, D.D. (2011) Synthesis, characterization and electrochemical properties of mesoporous zirconia nanomaterials prepared by self-assembling sol-gel method with Tween 20 as a template. Chemical Engineering Journal 170(2-3), 518-524.

Cho, S.H. and Yoon, Y.J. (2013) Multi-layer TiO_2 films prepared by aerosol deposition method for dye-sensitized solar cells. Thin Solid Films 547, 91-94.

Choi, H., Stathatos, E. and Dionysiou, D.D. (2006a) Sol-gel preparation of mesoporous photocatalytic TiO_2 films and TiO_2/Al_2O_3 composite membranes for environmental applications. Applied Catalysis B: Environmental 63(1-2), 60-67.

Choi, H., Stathatos, E. and Dionysiou, D.D. (2006b) Synthesis of nanocrystalline photocatalytic TiO_2 thin films and particles using sol-gel method modified with nonionic surfactants. Thin Solid Films 510(1-2), 107-114.

Choi, H., Kim, Y.J., Varma, R.S. and Dionysiou, D.D. (2006c) Thermally Stable Nanocrystalline TiO_2 Photocatalysts Synthesized via Sol–Gel Methods Modified with Ionic Liquid and Surfactant Molecules. Chem Mater 18(22), 5377-5384.

Choi, H., Sofranko, A.C. and Dionysiou, D.D. (2006d) Nanocrystalline TiO_2 photocatalytic membranes with a hierarchical mesoporous multilayer structure: Synthesis, characterization, and multifunction. Advanced Functional Materials 16(8), 1067-1074.

Choi, O., Deng, K.K., Kim, N.J., Ross Jr, L., Surampalli, R.Y. and Hu, Z. (2008) The inhibitory effects of silver nanoparticles, silver ions, and silver chloride colloids on microbial growth. Water Research 42(12), 3066-3074.

Choi, W. (2006a) Pure and modified TiO_2 photocatalysts and their environmental applications/. Catalysis Surveys from Asia 10(1), 16-28.

Choi, W. (2006b) Pure and modified TiO_2 photocatalysts and their environmental applications. Catalysis Surveys from Asia 10(1), 16-28.

Chong, M.N., Jin, B., Chow, C.W.K. and Saint, C. (2010) Recent developments in photocatalytic water treatment technology: A review. Water Research 44(10), 2997-3027.

Choo, K.H., Tao, R. and Kim, M.J. (2008) Use of a photocatalytic membrane reactor for the removal of natural organic matter in water: Effect of photoinduced desorption and ferrihydrite adsorption. Journal of Membrane Science 322(2), 368-374.

Chrysicopoulou, P., Davazoglou, D., Trapalis, C. and Kordas, G. (1998) Optical properties of very thin (< 100 nm) sol-gel TiO_2 films. Thin Solid Films 323(1-2), 188-193.

Colombo, P., Vakifahmetoglu, C. and Costacurta, S. (2010) Fabrication of ceramic components with hierarchical porosity. Journal of Materials Science 45(20), 5425-5455.

Coquil, T., Reitz, C., Brezesinski, T., Nemanick, E.J., Tolbert, S.H. and Pilon, L. (2010) Thermal conductivity of ordered mesoporous titania films made from nanocrystalline building blocks and sol-gel reagents. Journal of Physical Chemistry C 114(29), 12451-12458.

Costerton, J.W., Stewart, P.S. and Greenberg, E.P. (1999) Bacterial biofilms: A common cause of persistent infections. Science 284(5418), 1318-1322.

Cot, L., Ayral, A., Durand, J., Guizard, C., Hovnanian, N., Julbe, A. and Larbot, A. (2000) Inorganic membranes and solid state sciences. Solid State Sciences 2(3), 313-334.

Crepaldi, E.L., Soler-Illia, G.J.D.A.A., Grosso, D., Cagnol, F., Ribot, F. and Sanchez, C. (2003) Controlled formation of highly organized mesoporous titania thin films: From mesostructured hybrids to mesoporous nanoanatase TiO_2. Journal of the American Chemical Society 125(32), 9770-9786.

Dag, Ö., Soten, I., Çelik, Ö., Polarz, S., Coombs, N. and Ozin, G.A. (2003) Solventless acid-free synthesis of mesostructured titania: Nanovessels for metal complexes and metal nanoclusters. Advanced Functional Materials 13(1), 30-36.

De Lange, R.S.A., Hekkink, J.H.A., Keizer, K. and Burggraaf, A.J. (1995) Formation and characterization of supported microporous ceramic membranes prepared by sol-gel modification techniques. Journal of Membrane Science 99(1), 57-75.

Dholam, R., Patel, N., Adami, M. and Miotello, A. (2008) Physically and chemically synthesized TiO_2 composite thin films for hydrogen production by photocatalytic water splitting. International Journal of Hydrogen Energy 33(23), 6896-6903.

Di Paola, A., Bellardita, M., Ceccato, R., Palmisano, L. and Parrino, F. (2009) Highly active photocatalytic TiO_2 powders obtained by thermohydrolysis of $TiCl_4$ in water. Journal of Physical Chemistry C 113(34), 15166-15174.

Di Valentin, C., Finazzi, E., Pacchioni, G., Selloni, A., Livraghi, S., Paganini, M.C. and Giamello, E. (2007) N-doped TiO_2: Theory and experiment. Chemical Physics 339(1-3), 44-56.

Diesen, V., Jonsson, M. and Parkin, I.P. (2013) Improved Texturing and Photocatalytic Efficiency in TiO_2 Films Grown Using Aerosol-Assisted CVD and Atmospheric Pressure CVD. Chemical Vapor Deposition.

Ding, X., Fan, Y. and Xu, N. (2006) A new route for the fabrication of TiO_2 ultrafiltration membranes with suspension derived from a wet chemical synthesis. Journal of Membrane Science 270(1-2), 179-186.

Dunlop, P.S.M., Byrne, J.A., Manga, N. and Eggins, B.R. (2002) The photocatalytic removal of bacterial pollutants from drinking water. Journal of Photochemistry and Photobiology A: Chemistry 148(1-3), 355-363.

Egerton, T.A. and Christensen, P.A. (2004). Parsons, S. (ed), pp. 167-184, IWA Publishing, London, UK.

Emadi, R. and Raeissi, K. (2011) Antibacterial and biocompatibility properties of nano-silver/titania thin layer. International Journal of Modern Physics B 25(27), 3647-3653.

Ennaoui, A., Sankapal, B.R., Skryshevsky, V. and Lux-Steiner, M.C. (2006) TiO_2 and TiO_2-SiO_2 thin films and powders by one-step soft-solution method: Synthesis and characterizations. Solar Energy Materials and Solar Cells 90(10), 1533-1541.

Fattakhova-Rohlfing, D., Wark, M., Brezesinski, T., Smarsly, B.M. and Rathouský, J. (2007) Highly organized mesoporous TiO_2 films with controlled crystallinity: A Li-insertion study. Advanced Functional Materials 17(1), 123-132.

Feng, Q.L., Wu, J., Chen, G.Q., Cui, F.Z., Kim, T.N. and Kim, J.O. (2000) A mechanistic study of the antibacterial effect of silver ions on Escherichia coli and Staphylococcus aureus. Journal of Biomedical Materials Research 52(4), 662-668.

Foster, H.A., Ditta, I.B., Varghese, S. and Steele, A. (2011) Photocatalytic disinfection using titanium dioxide: Spectrum and mechanism of antimicrobial activity. Applied Microbiology and Biotechnology 90(6), 1847-1868.

Fox, M.A. and Dulay, M.T. (1993) Heterogeneous photocatalysis. Chemical Reviews 93(1), 341-357.

Frank, S.N. and Bard, A.J. (1977a) Heterogeneous photocatalytic oxidation of cyanide ion in aqueous solutions at TiO_2 powder. Journal of the American Chemical Society 99(1), 303-304.

Frank, S.N. and Bard, A.J. (1977b) Heterogeneous photocatalytic oxidation of cyanide and sulfite in aqueous solutions at semiconductor powders. Journal of Physical Chemistry 81(15), 1484-1488.

Fretwell, R. and Douglas, P. (2001) An active, robust and transparent nanocrystalline anatase TiO_2 thin film - Preparation, characterisation and the kinetics of photodegradation of model pollutants. Journal of Photochemistry and Photobiology A: Chemistry 143(2-3), 229-240.

Fujishima, A. and Honda, K. (1972) Electrochemical photolysis of water at a semiconductor electrode. Nature 238(5358), 37-38.

Fujishima, A., Rao, T.N. and Tryk, D.A. (2000) Titanium dioxide photocatalysis. Journal of Photochemistry and Photobiology C: Photochemistry Reviews 1(1), 1-21.

Fujishima, A. and Zhang, X. (2006) Titanium dioxide photocatalysis: present situation and future approaches. Comptes Rendus Chimie 9(5-6), 750-760.

Gander, M., Jefferson, B. and Judd, S. (2000) Aerobic MBRs for domestic wastewater treatment: A review with cost considerations. Separation and Purification Technology 18(2), 119-130.

Gao, B., Lim, T.M., Subagio, D.P. and Lim, T.T. (2010) Zr-doped TiO_2 for enhanced photocatalytic degradation of bisphenol A. Applied Catalysis A: General 375(1), 107-115.

García-Benjume, M.L., Espitia-Cabrera, M.I. and Contreras-García, M.E. (2009) Hierarchical macro-mesoporous structures in the system TiO_2-Al_2O_3, obtained by hydrothermal synthesis using Tween-20® as a directing agent. Materials Characterization 60(12), 1482-1488.

Gaya, U.I. and Abdullah, A.H. (2008) Heterogeneous photocatalytic degradation of organic contaminants over titanium dioxide: A review of fundamentals, progress and problems. Journal of Photochemistry and Photobiology C: Photochemistry Reviews 9(1), 1-12.

Gerischer, H. and Heller, A. (1991) The role of oxygen in photooxidation of organic molecules on semiconductor particles. Journal of Physical Chemistry 95(13), 5261-5267.

Ghanem, A.F., Badawy, A.A., Ismail, N., Rayn Tian, Z., Abdel Rehim, M.H. and Rabia, A. (2014) Photocatalytic activity of hyperbranched polyester/TiO_2 nanocomposites. Applied Catalysis A: General 472, 191-197.

Giri, A.S. and Golder, A.K. (2014) Fenton, photo-fenton, H_2O_2 Photolysis, and TiO_2 Photocatalysis for Dipyrone Oxidation: Drug Removal, Mineralization, Biodegradability, and Degradation Mechanism. Industrial and Engineering Chemistry Research 53(4), 1351-1358.

Goei, R., Dong, Z. and Lim, T.T. (2013) High-permeability pluronic-based TiO_2 hybrid photocatalytic membrane with hierarchical porosity: Fabrication, characterizations and performances. Chemical Engineering Journal 228, 1030-1039.

Gogate, P.R. and Pandit, A.B. (2004) A review of imperative technologies for wastewater treatment II: Hybrid methods. Advances in Environmental Research 8(3-4), 553-597.

Guillén-Santiago, A., Mayén, S.A., Torres-Delgado, G., Castanedo-Pérez, R., Maldonado, A. and Olvera, M.D.L.L. (2010) Photocatalytic degradation of methylene blue using undoped and Ag-doped TiO_2 thin films deposited by a sol-gel process: Effect of the ageing time of the starting solution and the film thickness. Materials Science and Engineering B: Solid-State Materials for Advanced Technology 174(1-3), 84-87.

Guizard, C., Julbe, A., Larbot, A. and Cot, L. (1992) Nanostructures in sol-gel derived materials: application to the elaboration of nanofiltration membranes. Journal of Alloys and Compounds 188(C), 8-13.

Guldin, S., Hüttner, S., Tiwana, P., Orilall, M.C., Ülgüt, B., Stefik, M., Docampo, P., Kolle, M., Divitini, G., Ducati, C., Redfern, S.A.T., Snaith, H.J., Wiesner, U., Eder, D. and Steiner, U. (2011) Improved conductivity in dye-sensitised solar cells through block-copolymer confined TiO_2 crystallisation. Energy and Environmental Science 4(1), 225-233.

Gumy, D., Morais, C., Bowen, P., Pulgarin, C., Giraldo, S., Hajdu, R. and Kiwi, J. (2006) Catalytic activity of commercial of TiO_2 powders for the abatement of the bacteria (E. coli) under solar simulated light: Influence of the isoelectric point. Applied Catalysis B: Environmental 63(1–2), 76-84.

Gutiérrez, D.J.R., Mathews, N.R. and Martínez, S.S. (2013) Photocatalytic activity enhancement of TiO_2 thin films with silver doping under visible light. Journal of Photochemistry and Photobiology A: Chemistry 262, 57-63.

Ha, H.Y., Nam, S.W., Lim, T.H., Oh, I.H. and Hong, S.A. (1996) Properties of the TiO_2 membranes prepared by CVD of titanium tetraisopropoxide. Journal of Membrane Science 111(1), 81-92.

Habibi, M.H., Esfahani, M.N. and Egerton, T.A. (2007a) Photochemical characterization and photocatalytic properties of a nanostructure composite TiO_2 film. International Journal of Photoenergy 2007.

Habibi, M.H., Nasr-Esfahani, M. and Egerton, T.A. (2007b) Preparation, characterization and photocatalytic activity of TiO_2 / Methylcellulose nanocomposite films derived from nanopowder TiO_2 and modified sol-gel titania. Journal of Materials Science 42(15), 6027-6035.

Habibi, M.H. and Nasr-Esfahani, M. (2007) Preparation, characterization and photocatalytic activity of a novel nanostructure composite film derived from nanopowder TiO_2 and sol-gel process using organic dispersant. Dyes and Pigments 75(3), 714-722.

Han, C., Pelaez, M., Likodimos, V., Kontos, A.G., Falaras, P., O'Shea, K. and Dionysiou, D.D. (2011) Innovative visible light-activated sulfur doped TiO_2 films for water treatment. Applied Catalysis B: Environmental 107(1-2), 77-87.

Han, C., Andersen, J., Likodimos, V., Falaras, P., Linkugel, J. and Dionysiou, D.D. (2014) The effect of solvent in the sol-gel synthesis of visible light-activated, sulfur-doped TiO_2 nanostructured porous films for water treatment. Catalysis Today 224, 132-139.

Hanaor, D.A.H. and Sorrell, C.C. (2011) Review of the anatase to rutile phase transformation. Journal of Materials Science 46(4), 855-874.

Haque, M.M., Muneer, M. and Bahnemann, D.W. (2006) Semiconductor-mediated photocatalyzed degradation of a herbicide derivative, chlorotoluron, in aqueous suspensions. Environmental Science and Technology 40(15), 4765-4770.

Haque, M.M. and Muneer, M. (2007) TiO_2-mediated photocatalytic degradation of a textile dye derivative, bromothymol blue, in aqueous suspensions. Dyes and Pigments 75(2), 443-448.

Haritash, A.K. and Kaushik, C.P. (2009) Biodegradation aspects of Polycyclic Aromatic Hydrocarbons (PAHs): A review. Journal of Hazardous Materials 169(1-3), 1-15.

Hashizume, M. and Kunitake, T. (2003) Preparation of self-supporting ultrathin films of titania by spin coating. Langmuir 19(24), 10172-10178.

Hata, S., Kai, Y., Yamanaka, I., Oosaki, H., Kazuo, H. and Yamazaki, S. (2000) Development of hydrophilic outside mirror coated with titania photocatalyst. JSAE review 21(1), 97-102.

Henglein, A. (1982) Colloidal TiO_2 catalysed photo-and radiation chemical processes in aqueous solution. Physical Chemistry Chemical Physics 86(3), 241-246.

Hepel, M. and Kumarihamy, I.D. (2007) Nanocrystalline structure and nanopore formation in modified thermal TiO_2 films. International Journal of Hydrogen Energy 32(14), 2693-2702.

Herrmann, J.M., Disdier, J. and Pichat, P. (1988) Photocatalytic deposition of silver on powder titania: Consequences for the recovery of silver. Journal of Catalysis 113(1), 72-81.

Herrmann, J.M. (1999) Heterogeneous photocatalysis: Fundamentals and applications to the removal of various types of aqueous pollutants. Catalysis Today 53(1), 115-129.

Herrmann, J.M. (2005) Heterogeneous photocatalysis: State of the art and present applications. Topics in Catalysis 34(1-4), 49-65.

Hoffmann, M.R., Martin, S.T., Choi, W. and Bahnemann, D.W. (1995) Environmental applications of semiconductor photocatalysis. Chemical Reviews 95(1), 69-96.

Horikoshi, S., Hidaka, H. and Serpone, N. (2001) Photocatalyzed degradation of polymers in aqueous semiconductor suspensions: V. Photomineralization of lactam ring-pendant polyvinylpyrrolidone at titania/water interfaces. Journal of Photochemistry and Photobiology A: Chemistry 138(1), 69-77.

Hou, D., Goei, R., Wang, X., Wang, P. and Lim, T.T. (2012) Preparation of carbon-sensitized and Fe-Er codoped TiO_2 with response surface methodology for bisphenol A photocatalytic degradation under visible-light irradiation. Applied Catalysis B: Environmental 126, 121-133.

Hou, X.G., Huang, M.D., Wu, X.L. and Liu, A.D. (2009) Preparation and studies of photocatalytic silver-loaded TiO_2 films by hybrid sol-gel method. Chemical Engineering Journal 146(1), 42-48.

Houas, A., Lachheb, H., Ksibi, M., Elaloui, E., Guillard, C. and Herrmann, J.M. (2001) Photocatalytic degradation pathway of methylene blue in water. Applied Catalysis B: Environmental 31(2), 145-157.

Hsieh, H.P. (ed) (1996) Materials and preparation of inorganic membrane, Elsevier.

Hu, C., Guo, J., Qu, J. and Hu, X. (2007) Photocatalytic Degradation of Pathogenic Bacteria with AgI/TiO_2 under Visible Light Irradiation. Langmuir 23(9), 4982-4987.

Huang, X., Leal, M. and Li, Q. (2008) Degradation of natural organic matter by TiO_2 photocatalytic oxidation and its effect on fouling of low-pressure membranes. Water Research 42(4-5), 1142-1150.

Huang, Z., Maness, P.C., Blake, D.M., Wolfrum, E.J., Smolinski, S.L. and Jacoby, W.A. (2000) Bactericidal mode of titanium dioxide photocatalysis. Journal of Photochemistry and Photobiology A: Chemistry 130(2-3), 163-170.

Hung, I.M., Wang, Y., Lin, L.T. and Huang, C.F. (2010) Preparation and characterization of mesoporous TiO_2 thin film. Journal of Porous Materials 17(4), 509-513.

Irie, H., Washizuka, S., Yoshino, N. and Hashimoto, K. (2003) Visible-light induced hydrophilicity on nitrogen-substituted titanium dioxide films. Chemical Communications 9(11), 1298-1299.

Ivanda, M., Musić, S., Gotić, M., Turković, A., Tonejc, A.M. and Gamulin, O. (1999) The effects of crystal size on the Raman spectra of nanophase TiO_2. Journal of Molecular Structure 480-481, 641-644.

Jahromi, H.S., Taghdisian, H., Afshar, S. and Tasharrofi, S. (2009) Effects of pH and polyethylene glycol on surface morphology of TiO_2 thin film. Surface and Coatings Technology 203(14), 1991-1996.

Jamieson, J.C. and Olinger, B. (1968) High-pressure polymorphism of titanium dioxide. Science 161(3844), 893-895.

Jardim, W.F., Moraes, S.G. and Takiyama, M.M.K. (1997) Photocatalytic degradation of aromatic chlorinated compounds using TiO_2: Toxicity of intermediates. Water Research 31(7), 1728-1732.

Jiang, X., Herricks, T. and Xia, Y. (2003) Monodispersed spherical colloids of titania: Synthesis, characterization, and crystallization. Advanced Materials 15(14), 1205-1209.

Jing, L., Qu, Y., Wang, B., Li, S., Jiang, B., Yang, L., Fu, W., Fu, H. and Sun, J. (2006) Review of photoluminescence performance of nano-sized semiconductor materials and its relationships with photocatalytic activity. Solar Energy Materials and Solar Cells 90(12), 1773-1787.

Joo, J., Kwon, S.G., Yu, T., Cho, M., Lee, J., Yoon, J. and Hyeon, T. (2005) Large-scale synthesis of TiO_2 nanorods via nonhydrolytic sol-gel ester elimination reaction and their application to photocatalytic inactivation of E. coli. Journal of Physical Chemistry B 109(32), 15297-15302.

Joya, Y.F., Liu, Z., Joya, K.S. and Wang, T. (2012) Preparation and antibacterial properties of laser-generated silver-anatase nanocomposite film against Escherichia coli and Staphylococcus aureus. Nanotechnology 23(49).

Kabra, K., Chaudhary, R. and Sawhney, R.L. (2004) Treatment of hazardous organic and inorganic compounds through aqueous-phase photocatalysis: A review. Industrial and Engineering Chemistry Research 43(24), 7683-7696.

Kashimada, K., Kamiko, N., Yamamoto, K. and Ohgaki, S. (1996) Assessment of photoreactivation following ultraviolet light disinfection, pp. 261-269.

Kavan, L. and Grätzel, M. (1995) Highly efficient semiconducting TiO_2 photoelectrodes prepared by aerosol pyrolysis. Electrochimica Acta 40(5), 643-652.

Keizer, K., Leenaars, A.F.M. and Burggraaf, A.J. (1984) Porous alumina as a membrane material in separation processes, pp. 101-106.

Kermanpur, A., Ghassemali, E. and Salemizadeh, S. (2008) Synthesis and characterisation of microporous titania membranes by dip-coating of anodised alumina substrates using sol-gel method. Journal of Alloys and Compounds 461(1-2), 331-335.

Klavarioti, M., Mantzavinos, D. and Kassinos, D. (2009) Removal of residual pharmaceuticals from aqueous systems by advanced oxidation processes. Environment International 35(2), 402-417.

Kment, S., Kmentova, H., Kluson, P., Krysa, J., Hubicka, Z., Cirkva, V., Gregora, I., Solcova, O. and Jastrabik, L. (2010) Notes on the photo-induced characteristics of transition metal-doped and undoped titanium dioxide thin films. Journal of Colloid And Interface Science 348(1), 198-205.

Konstantinou, I.K. and Albanis, T.A. (2003) Photocatalytic transformation of pesticides in aqueous titanium dioxide suspensions using artificial and solar light: Intermediates and degradation pathways. Applied Catalysis B: Environmental 42(4), 319-335.

Konstantinou, I.K. and Albanis, T.A. (2004) TiO_2-assisted photocatalytic degradation of azo dyes in aqueous solution: Kinetic and mechanistic investigations: A review. Applied Catalysis B: Environmental 49(1), 1-14.

Kouloumbos, V.N., Tsipi, D.F., Hiskia, A.E., Nikolic, D. and Van Breemen, R.B. (2003) Identification of photocatalytic degradation products of diazinon in TiO_2 aqueous suspensions using GC/MS/MS and LC/MS with quadrupole time-of-flight mass spectrometry. Journal of the American Society for Mass Spectrometry 14(8), 803-817.

Krylova, G.V., Gnatyuk, Y.I., Smirnova, N.P., Eremenko, A.M. and Gun'Ko, V.M. (2009) Ag nanoparticles deposited onto silica, titania, and zirconia mesoporous films synthesized by sol-gel template method. Journal of Sol-Gel Science and Technology 50(2), 216-228.

Kubacka, A., Ferrer, M., Martínez-Arias, A. and Fernández-García, M. (2008) Ag promotion of TiO_2-anatase disinfection capability: Study of Escherichia coli inactivation. Applied Catalysis B: Environmental 84(1-2), 87-93.

Kubacka, A., Ferrer, M., Cerrada, M.L., Serrano, C., Sánchez-Chaves, M., Fernández-García, M., de Andrés, A., Riobóo, R.J.J. and Fernández-Martín, F. (2009) Boosting TiO_2-anatase antimicrobial activity: Polymer-oxide thin films. Applied Catalysis B: Environmental 89(3-4), 441-447.

Kubacka, A., Ferrer, M., Fernández-García, M., Serrano, C. and Cerrada, M.L. (2011) Tailoring polymer-TiO_2 film properties by presence of metal (Ag, Cu, Zn) species:

Optimization of antimicrobial properties. Applied Catalysis B: Environmental 104(3-4), 346-352.

Kubo, M., Ishihara, Y., Mantani, Y. and Shimada, M. (2013) Evaluation of the factors that influence the fabrication of porous thin films by deposition of aerosol nanoparticles. Chemical Engineering Journal 232, 221-227.

Kumar, P.M., Badrinarayanan, S. and Sastry, M. (2000) Nanocrystalline TiO_2 studied by optical, FTIR and X-ray photoelectron spectroscopy: Correlation to presence of surface states. Thin Solid Films 358(1), 122-130.

Kyriacou, S.V., Brownlow, W.J. and Xu, X.H.N. (2004) Using Nanoparticle Optics Assay for Direct Observation of the Function of Antimicrobial Agents in Single Live Bacterial Cells. Biochemistry 43(1), 140-147.

Lahiri, D., Subramanian, V., Bunker, B.A. and Kamat, P.V. (2006) Probing photochemical transformations at TiO_2/Pt and TiO_2/Ir interfaces using x-ray absorption spectroscopy. Journal of Chemical Physics 124(20).

Landmann, M., Rauls, E. and Schmidt, W.G. (2012) The electronic structure and optical response of rutile, anatase and brookite TiO_2. Journal of Physics Condensed Matter 24(19).

Langmuir, I. (1932) Vapor pressures, evaporation, condensation and adsorption. The Journal of the American Chemical Society 54(7), 2798-2832.

Larbot, A., Fabre, J.P., Guizard, C. and Cot, L. (1988) Inorganic membranes obtained by sol-gel techniques. Journal of Membrane Science 39(3), 203-212.

Le-Clech, P., Chen, V. and Fane, T.A.G. (2006) Fouling in membrane bioreactors used in wastewater treatment. Journal of Membrane Science 284(1-2), 17-53.

Lee, H.U., Lee, S.C., Seo, J.H., Hong, W.G., Kim, H., Yun, H.J., Kim, H.J. and Lee, J. (2013) Room temperature synthesis of nanoporous anatase and anatase/brookite TiO_2 photocatalysts with high photocatalytic performance. Chemical Engineering Journal 223, 209-215.

Lee, J., Christopher Orilall, M., Warren, S.C., Kamperman, M., Disalvo, F.J. and Wiesner, U. (2008) Direct access to thermally stable and highly crystalline mesoporous transition-metal oxides with uniform pores. Nature Materials 7(3), 222-228.

Leenaars, A.F.M., Keizer, K. and Burggraaf, A.J. (1984) The preparation and characterization of alumina membranes with ultra-fine pores - Part 1 Microstructural investigations on non-supported membranes. Journal of Materials Science 19(4), 1077-1088.

Leenaars, A.F.M. and Burggraaf, A.J. (1985) The preparation and characterization of alumina membranes with ultrafine pores. 2. The formation of supported membranes. Journal of Colloid And Interface Science 105(1), 27-40.

Lei, J., Wang, W., Song, M., Dong, B., Li, Z., Wang, C. and Li, L. (2011) Ag/AgCl coated polyacrylonitrile nanofiber membranes: Synthesis and photocatalytic properties. Reactive and Functional Polymers 71(11), 1071-1076.

Li, H., Xu, H., Wang, S., Pan, Y., Wu, Q. and Liu, C. (2011) Preparation of nano-TiO_2 using a sol-gel process mediated in reverse microemulsion combined with a solvent thermal technique, pp. 1731-1734.

Li, Q., Mahendra, S., Lyon, D.Y., Brunet, L., Liga, M.V., Li, D. and Alvarez, P.J.J. (2008) Antimicrobial nanomaterials for water disinfection and microbial control: Potential applications and implications. Water Research 42(18), 4591-4602.

Li, S. and Sun, W. (2014) Photocatalytic degradation of 17α-ethinylestradiol in mono- and binary systems of fulvic acid and Fe(III): Application of fluorescence excitation/emission matrixes. Chemical Engineering Journal 237, 101-108.

Lim, T.T., Yap, P.S., Srinivasan, M. and Fane, A.G. (2011) TiO_2/AC composites for synergistic adsorption-photocatalysis processes: Present challenges and further developments for water treatment and reclamation. Critical Reviews in Environmental Science and Technology 41(13), 1173-1230.

Linsebigler, A.L., Lu, G. and Yates Jr, J.T. (1995) Photocatalysis on TiO_2 surfaces: Principles, mechanisms, and selected results. Chemical Reviews 95(3), 735-758.

Liu, J., An, T., Li, G., Bao, N., Sheng, G. and Fu, J. (2009) Preparation and characterization of highly active mesoporous TiO_2 photocatalysts by hydrothermal synthesis under weak acid conditions. Microporous and Mesoporous Materials 124(1-3), 197-203.

Liu, K., Fu, H., Shi, K., Xiao, F., Jing, L. and Xin, B. (2005) Preparation of large-pore mesoporous nanocrystalline TiO_2 thin films with tailored pore diameters. Journal of Physical Chemistry B 109(40), 18719-18722.

Liu, S.X., Qu, Z.P., Han, X.W. and Suna, C.L. (2004) A mechanism for enhanced photocatalytic activity of silver-loaded titanium dioxide. Catalysis Today 93, 877-884.

Liu, X., Qi, S., Li, Y., Yang, L., Cao, B. and Tang, C.Y. (2013a) Synthesis and characterization of novel antibacterial silver nanocomposite nanofiltration and forward osmosis membranes based on layer-by-layer assembly. Water Research 47(9), 3081-3092.

Liu, Y., Li, J., Qiu, X. and Burda, C. (2006) Novel TiO_2 nanocatalysts for wastewater purification: Tapping energy from the sun, pp. 47-54.

Liu, Y., Wang, X., Yang, F. and Yang, X. (2008) Excellent antimicrobial properties of mesoporous anatase TiO_2 and Ag/TiO_2 composite films. Microporous and Mesoporous Materials 114(1-3), 431-439.

Liu, Y., Rosenfield, E., Hu, M. and Mi, B. (2013b) Direct observation of bacterial deposition on and detachment from nanocomposite membranes embedded with silver nanoparticles. Water Research 47(9), 2949-2958.

Liz-Marzán, L.M. and Lado-Touriño, I. (1996) Reduction and stabilization of silver nanoparticles in ethanol by nonionic surfactants. Langmuir 12(15), 3585-3589.

Loeb, S. and Sourirajan, S. (1963) Saline Water Conversion-II, Advance in Chemistry Series, pp. 117-132, American Chemical Society, Washington DC.

Lok, C.N., Ho, C.M., Chen, R., He, Q.Y., Yu, W.Y., Sun, H., Tam, P.K.H., Chiu, J.F. and Che, C.M. (2006) Proteomic analysis of the mode of antibacterial action of silver nanoparticles. Journal of Proteome Research 5(4), 916-924.

Lu, Y., Ganguli, R., Drewien, C.A., Anderson, M.T., Jeffrey Brinker, C., Gong, W., Guo, Y., Soyez, H., Dunn, B., Huang, M.H. and Zink, J.I. (1997) Continuous formation of supported cubic and hexagonal mesoporous films by sol-gel dip-coating. Nature 389(6649), 364-368.

Lu, Z.X., Zhou, L., Zhang, Z.L., Shi, W.L., Xie, Z.X., Xie, H.Y., Pang, D.W. and Shen, P. (2003) Cell Damage Induced by Photocatalysis of TiO_2 Thin Films. Langmuir 19(21), 8765-8768.

Lv, L., Luo, Y., Ng, W.J. and Zhao, X.S. (2009a) Bactericidal activity of silver nanoparticles supported on microporous titanosilicate ETS-10. Microporous and Mesoporous Materials 120(3), 304-309.

Lv, Y., Liu, H., Wang, Z., Liu, S., Hao, L., Sang, Y., Liu, D., Wang, J. and Boughton, R.I. (2009b) Silver nanoparticle-decorated porous ceramic composite for water treatment. Journal of Membrane Science 331(1–2), 50-56.

Ma, J., Xiong, Z., David Waite, T., Ng, W.J. and Zhao, X.S. (2011) Enhanced inactivation of bacteria with silver-modified mesoporous TiO_2 under weak ultraviolet irradiation. Microporous and Mesoporous Materials 144(1-3), 97-104.

Ma, N., Fan, X., Quan, X. and Zhang, Y. (2009a) Ag-TiO_2/HAP/Al_2O_3 bioceramic composite membrane: Fabrication, characterization and bactericidal activity. Journal of Membrane Science 336(1-2), 109-117.

Ma, N., Quan, X., Zhang, Y., Chen, S. and Zhao, H. (2009b) Integration of separation and photocatalysis using an inorganic membrane modified with Si-doped TiO_2 for water purification. Journal of Membrane Science 335(1-2), 58-67.

Ma, N., Zhang, Y., Quan, X., Fan, X. and Zhao, H. (2010) Performing a microfiltration integrated with photocatalysis using an Ag-TiO_2/HAP/Al_2O_3 composite membrane for water treatment: Evaluating effectiveness for humic acid removal and anti-fouling properties. Water Research 44(20), 6104-6114.

Magdeburg, A., Stalter, D., Schlüsener, M., Ternes, T. and Oehlmann, J. (2014) Evaluating the efficiency of advanced wastewater treatment: Target analysis of organic contaminants and (geno-)toxicity assessment tell a different story. Water Research 50, 35-47.

Malato, S., Cáceres, J., Fernández-Alba, A.R., Piedra, L., Hernando, M.D., Agüera, A. and Vial, I. (2003) Photocatalytic treatment of diuron by solar photocatalysis: Evaluation of main intermediates and toxicity. Environmental Science and Technology 37(11), 2516-2524.

Malato, S., Fernández-Ibáñez, P., Maldonado, M.I., Blanco, J. and Gernjak, W. (2009) Decontamination and disinfection of water by solar photocatalysis: Recent overview and trends. Catalysis Today 147(1), 1-59.

Matsunaga, T., Tomoda, R., Nakajima, T. and Wake, H. (1985) Photoelectrochemical sterilization of microbial cells by semiconductor powders. FEMS Microbiology Letters 29(1-2), 211-214.

Mazzarino, I., Piccinini, P. and Spinelli, L. (1999) Degradation of organic pollutants in water by photochemical reactors. Catalysis Today 48(1-4), 315-321.

Meulenberg, W.A., Mertens, J., Bram, M., Buchkremer, H.-P. and Stöver, D. (2006) Graded porous TiO_2 membranes for microfiltration. Journal of the European Ceramic Society 26(4-5), 449-454.

Mills, A. and Le Hunte, S. (1997) An overview of semiconductor photocatalysis. Journal of Photochemistry and Photobiology A: Chemistry 108(1), 1-35.

Mills, A., Elliott, N., Parkin, I.P., O'Neill, S.A. and Clark, R.J. (2002) Novel TiO_2 CVD films for semiconductor photocatalysis. Journal of Photochemistry and Photobiology A: Chemistry 151(1-3), 171-179.

Molinari, R., Mungari, M., Drioli, E., Di Paola, A., Loddo, V., Palmisano, L. and Schiavello, M. (2000) Study on a photocatalytic membrane reactor for water purification. Catalysis Today 55(1-2), 71-78.

Molinari, R., Pirillo, F., Falco, M., Loddo, V. and Palmisano, L. (2004) Photocatalytic degradation of dyes by using a membrane reactor. Chemical Engineering and Processing: Process Intensification 43(9), 1103-1114.

Molinari, R., Pirillo, F., Loddo, V. and Palmisano, L. (2006) Heterogeneous photocatalytic degradation of pharmaceuticals in water by using polycrystalline TiO_2 and a nanofiltration membrane reactor. Catalysis Today 118(1-2), 205-213.

Morones, J.R., Elechiguerra, J.L., Camacho, A., Holt, K., Kouri, J.B., Ramírez, J.T. and Yacaman, M.J. (2005) The bactericidal effect of silver nanoparticles. Nanotechnology 16(10), 2346-2353.

Moser, E.M., Chappuis, S. and Olleros, J. (2013) Production of photocatalytically active titania layers: A comparison of plasma processes and coating properties. Surface and Coatings Technology 227, 2-9.

Moulder, J.F., Stickle, W.F., Sobol, P.E. and Bomben, K.D. (1992) Handbook of X-Ray photoelectron spectroscopy, Perkin Elmer, Eden Prairie, MN, USA.

Mulder, M. (1996) Basic Principles of Membrane Technology, Kluwer Academic Publisher, Dordrecht, The Netherlands.

Nash, M. (2008) An investigation into the photocatalytic properties of microporous titanosilicate materials, University of Delaware.

Nasr-Esfahani, M. and Habibi, M.H. (2008) Silver doped TiO_2 nanostructure composite photocatalyst film synthesized by sol-gel spin and dip coating technique on glass. International Journal of Photoenergy 2008.

Navrotsky, A., Jamieson, J.C. and Kleppa, O.J. (1967) Enthalpy of transformation of a high-pressure polymorph of titanium dioxide to the rutile modification. Science 158(3799), 388-389.

Niederberger, M., Bartl, M.H. and Stucky, G.D. (2002) Benzyl alcohol and titanium tetrachloride - A versatile reaction system for the nonaqueous and low-temperature preparation of crystalline and luminescent titania nanoparticles. Chemistry of Materials 14(10), 4364-4370.

Obalová, L., Reli, M., Lang, J., Matějka, V., Kukutschová, J., Lacný, Z. and Kočí, K. (2013) Photocatalytic decomposition of nitrous oxide using TiO_2 and Ag-TiO_2 nanocomposite thin films. Catalysis Today 209, 170-175.

Ohsaka, T., Yamaoka, S. and Shimomura, O. (1979) Effect of hydrostatic pressure on the Raman spectrum of anatase (TiO_2). Solid State Communications 30(6), 345-347.

Ollis, D.F. and Al-Ekabi, H. (eds) (1993) Photocatalytic Purification, and Treatment of Water and Air, Elsevier, Amsterdam.

Oppenländer, T. (2003) Photochemical purification of water and air, WILEY-VCH, Darmstadt, Germany.

Ortel, E., Sokolov, S., Zielke, C., Lauermann, I., Selve, S., Weh, K., Paul, B., Polte, J. and Kraehnert, R. (2012a) Supported mesoporous and hierarchical porous Pd/TiO_2 catalytic coatings with controlled particle size and pore structure. Chemistry of Materials 24(20), 3828-3838.

Ortel, E., Fischer, A., Chuenchom, L., Polte, J., Emmerling, F., Smarsly, B. and Kraehnert, R. (2012b) New triblock copolymer templates, PEO-PB-PEO, for the synthesis of titania films with controlled mesopore size, wall thickness, and bimodal porosity. Small 8(2), 298-309.

Owen, G., Bandi, M., Howell, J.A. and Churchouse, S.J. (1995) Economic assessment of membrane processes for water and waste water treatment. Journal of Membrane Science 102(1-3), 77-91.

Ozdemir, S.S., Buonomenna, M.G. and Drioli, E. (2006) Catalytic polymeric membranes: Preparation and application. Applied Catalysis A: General 307(2), 167-183.

Page, K., Palgrave, R.G., Parkin, I.P., Wilson, M., Savin, S.L.P. and Chadwick, A.V. (2007) Titania and silver-titania composite films on glass - Potent antimicrobial coatings. Journal of Materials Chemistry 17(1), 95-104.

Pal, S., Tak, Y.K. and Song, J.M. (2007) Does the antibacterial activity of silver nanoparticles depend on the shape of the nanoparticle? A study of the gram-negative bacterium Escherichia coli. Applied and Environmental Microbiology 73(6), 1712-1720.

Palmas, S., Polcaro, A.M., Ruiz, J.R., Da Pozzo, A., Mascia, M. and Vacca, A. (2010) TiO_2 photoanodes for electrically enhanced water splitting. International Journal of Hydrogen Energy 35(13), 6561-6570.

Pan, J.H. and Lee, W.I. (2006) Preparation of highly ordered cubic mesoporous WO_3/TiO_2 films and their photocatalytic properties. Chemistry of Materials 18(3), 847-853.

Park, J.-Y., Lee, C., Jung, K.-W. and Jung, D. (2009) Structure related photocatalytic properties of TiO_2. Bulletin Korean Chemical Society 30(2), 402-404.

Parker, J.C. and Siegel, R.W. (1990) Raman microprobe study of nanophase TiO_2 and oxidation-induced spectral changes. Journal of Materials Research 5(6), 1246-1252.

Pavia, D.L., Lampman, G.M., Kriz, G.S. and Vyvyan, J.a. (2009) Introduction to Spectroscopy, Brooks/Cole, Minnesota.

Pelaez, M., Falaras, P., Likodimos, V., Kontos, A.G., de la Cruz, A.A., O'Shea, K. and Dionysiou, D.D. (2010) Synthesis, structural characterization and evaluation of sol-gel-based NF-TiO_2 films with visible light-photoactivation for the removal of microcystin-LR. Applied Catalysis B: Environmental 99(3-4), 378-387.

Pirkanniemi, K. and Sillanpää, M. (2002) Heterogeneous water phase catalysis as an environmental application: A review. Chemosphere 48(10), 1047-1060.

Piwoński, I., Kdzioła, K., Kisielewska, A., Soliwoda, K., Wolszczak, M., Lisowska, K., Wrońska, N. and Felczak, A. (2011) The effect of the deposition parameters on size, distribution and antimicrobial properties of photoinduced silver nanoparticles on titania coatings. Applied Surface Science 257(16), 7076-7082.

Porter, M.R. (1994) Handbook of Surfactants, Chapman and Hall, London.

Procházka, J., Kavan, L., Shklover, V., Zukalová, M., Frank, O., Kalbáč, M., Zukal, A., Pelouchová, H., Janda, P., Mocek, K., Klementová, M. and Carbone, D. (2008) Multilayer films from templated TiO_2 and structural changes during their thermal treatment. Chemistry of Materials 20(9), 2985-2993.

PUB (2014) Four national taps provide water for all, p. http://www.pub.gov.sg/water/Pages/default.aspx.

Puhlfürß, P., Voigt, A., Weber, R. and Morbé, M. (2000) Microporous TiO_2 membranes with a cut off <500 Da. Journal of Membrane Science 174(1), 123-133.

Qi, H., Niu, S., Jiang, X. and Xu, N. (2013) Enhanced performance of a macroporous ceramic support for nanofiltration by using α-Al_2O_3 with narrow size distribution. Ceramics International 39(3), 2463-2471.

Rahimi, R., Moghaddas, M.M., Zargari, S. and Rahimi, R. (2013) Synthesis of mesoporous V-TiO_2 with different surfactants: The effect of surfactant type on photocatalytic properties, pp. 56-61.

Răileanu, M., Crişan, M., Drăgan, N., Crişan, D., Galtayries, A., Brăileanu, A., Ianculescu, A., Teodorescu, V.S., Niţoi, I. and Anastasescu, M. (2009) Sol-gel doped TiO_2 nanomaterials: A comparative study. Journal of Sol-Gel Science and Technology 51(3), 315-329.

Rajeshwar, K., Osugi, M.E., Chanmanee, W., Chenthamarakshan, C.R., Zanoni, M.V.B., Kajitvichyanukul, P. and Krishnan-Ayer, R. (2008) Heterogeneous photocatalytic treatment of organic dyes in air and aqueous media. Journal of Photochemistry and Photobiology C: Photochemistry Reviews 9(4), 171-192.

Rashad, M.M. and Shalan, A.E. (2013) Surfactant-assisted hydrothermal synthesis of titania nanoparticles for solar cell applications. Journal of Materials Science: Materials in Electronics 24(9), 3189-3194.

Raut, N.C., Mathews, T., Sundari, S.T., Sairam, T.N., Dash, S. and Tyagi, A.K. (2009) Structural and morphological characterization of TiO_2 thin films synthesized by spray pyrolysis technique. Journal of Nanoscience and Nanotechnology 9(9), 5298-5302.

Ravikovitch, P.I. and Neimark, A.V. (2002) Density functional theory of adsorption in spherical cavities and pore size characterization of templated nanoporous silicas with cubic and three-dimensional hexagonal structures. Langmuir 18(5), 1550-1560.

Rincón, A.-G. and Pulgarin, C. (2004) Bactericidal action of illuminated TiO_2 on pure Escherichia coli and natural bacterial consortia: post-irradiation events in the dark and assessment of the effective disinfection time. Applied Catalysis B: Environmental 49(2), 99-112.

Rivero, M.J., Parsons, S.A., Jeffrey, P., Pidou, M. and Jefferson, B. (2006) Membrane chemical reactor (MCR) combining photocatalysis and microfiltration for grey water treatment, pp. 173-180.

Romanos, G.E., Athanasekou, C.P., Likodimos, V., Aloupogiannis, P. and Falaras, P. (2013) Hybrid ultrafiltration/photocatalytic membranes for efficient water treatment. Industrial and Engineering Chemistry Research 52(39), 13938-13947.

Rothenberger, G., Moser, J., Grätzel, M., Serpone, N. and Sharma, D.K. (1985) Charge carrier trapping and recombination dynamics in small semiconductor particles. Journal of the American Chemical Society 107(26), 8054-8059.

Roucoux, A., Schulz, J. and Patin, H. (2002) Reduced transition metal colloids: A novel family of reusable catalysts? Chemical Reviews 102(10), 3757-3778.

Russell, A.D. and Hugo, W.B. (1994) 7 Antimicrobial Activity and Action of Silver, pp. 351-370.

Ryu, J., Hahn, B.D., Choi, J.J., Yoon, W.H., Lee, B.K., Choi, J.H. and Park, D.S. (2010) Porous photocatalytic TiO_2 thin films by aerosol deposition. Journal of the American Ceramic Society 93(1), 55-58.

Sakai, N., Fujishima, A., Watanabe, T. and Hashimoto, K. (2003) Quantitative evaluation of the photoinduced hydrophilic conversion properties of TiO_2 thin film surfaces by the reciprocal of contact angle. Journal of Physical Chemistry B 107(4), 1028-1035.

Samuel, U. and Guggenbichler, J.P. (2004) Prevention of catheter-related infections: The potential of a new nano-silver impregnated catheter. International Journal of Antimicrobial Agents 23(SUPPL. 1), S75-S78.

Sanchez, C., Livage, J., Henry, M. and Babonneau, F. (1988) Chemical modification of alkoxide precursors. Journal of Non-Crystalline Solids 100(1-3), 65-76.

Sanguanruang, S., Leotphayakkarat, R., Fangern, N., Koonsaeng, N. and Chawengkijwanich, C. (2011) Preparation and characterization of thin films TiO_2 prepared by various amount of triton X-100 surfactant for photodegradation of a dye pollutant, pp. 2863-2870.

Scherrer, P. (1918) Göttinger Nachrichten. Math. Phys. 2, 98-100.

Schindler, K.M. and Kunst, M. (1990) Charge-carrier dynamics in TiO_2 powders. Journal of Physical Chemistry 94(21), 8222-8226.

Seery, M.K., George, R., Floris, P. and Pillai, S.C. (2007) Silver doped titanium dioxide nanomaterials for enhanced visible light photocatalysis. Journal of Photochemistry and Photobiology A: Chemistry 189(2-3), 258-263.

Seidel, A. and Elimelech, M. (2002) Coupling between chemical and physical interactions in natural organic matter (NOM) fouling of nanofiltration membranes: Implications for fouling control. Journal of Membrane Science 203(1-2), 245-255.

Sekulic-Kuzmanovic, J. (2004) Mesoporous and Microporous Titania Membranes.

Sekulic, J., Ten Elshof, J.E. and Blank, D.H.A. (2004) Synthesis and characterization of microporous titania membranes. Journal of Sol-Gel Science and Technology 31(1-3 SPEC.ISS.), 201-204.

Shamaila, S., Leghari Sajjad, A.K., Chen, F. and Zhang, J. (2011) Mesoporous titania with high crystallinity during synthesis by dual template system as an efficient photocatalyst. Catalysis Today 175(1), 568-575.

Shankar, M.V., Cheralathan, K.K., Arabindoo, B., Palanichamy, M. and Murugesan, V. (2004) Enhanced photocatalytic activity for the destruction of monocrotophos pesticide by TiO_2/H[beta]. Journal of Molecular Catalysis A: Chemical 223(1-2), 195-200.

Shao, C., Zhou, G., Li, Z., Wu, Y., Xu, D. and Sun, B. (2013) Fabrication of large-diameter tube-like mesoporous TiO_2 via homogeneous precipitation and photocatalytic decomposition of papermaking wastewater. Chemical Engineering Journal 230, 227-235.

Sharma, S.K., Vishwas, M., Rao, K.N., Mohan, S., Reddy, D.S. and Gowda, K.V.A. (2009) Structural and optical investigations of TiO_2 films deposited on transparent substrates by sol-gel technique. Journal of Alloys and Compounds 471(1-2), 244-247.

Shen, P.S., Tai, Y.C., Chen, P. and Wu, Y.C. (2014) Clean and time-effective synthesis of anatase TiO_2 nanocrystalline by microwave-assisted solvothermal method for dye-sensitized solar cells. Journal of Power Sources 247, 444-451.

Shrivastava, S., Bera, T., Roy, A., Singh, G., Ramachandrarao, P. and Dash, D. (2007) Characterization of enhanced antibacterial effects of novel silver nanoparticles. Nanotechnology 18(22).

Sin, J.C., Lam, S.M., Mohamed, A.R. and Lee, K.T. (2012) Degrading endocrine disrupting chemicals from wastewater by TiO_2 photocatalysis: A review. International Journal of Photoenergy 2012.

Siva Kumar, V., Nagaraja, B.M., Shashikala, V., Seetharamulu, P., Padmasri, A.H., David Raju, B. and Rama Rao, K.S. (2004) Role of acidic and basic sites of Al_2O_3 in predicting the reaction pathway of isophorone transformation. Journal of Molecular Catalysis A: Chemical 223(1-2), 283-288.

Sleiman, M., Conchon, P., Ferronato, C. and Chovelon, J.M. (2009) Photocatalytic oxidation of toluene at indoor air levels (ppbv): Towards a better assessment of conversion, reaction intermediates and mineralization. Applied Catalysis B: Environmental 86(3-4), 159-165.

Smyth, J. (2009) Mineral Structure and Property Data: TiO_2 Group, Colorado.

Sondi, I. and Salopek-Sondi, B. (2004) Silver nanoparticles as antimicrobial agent: A case study on E. coli as a model for Gram-negative bacteria. Journal of Colloid and Interface Science 275(1), 177-182.

Stathatos, E., Lianos, P. and Tsakiroglou, C. (2004) Highly efficient nanocrystalline titania films made from organic/inorganic nanocomposite gels. Microporous and Mesoporous Materials 75(3), 255-260.

Stylidi, M., Kondarides, D.I. and Verykios, X.E. (2004) Visible light-induced photocatalytic degradation of Acid Orange 7 in aqueous TiO_2 suspensions. Applied Catalysis B: Environmental 47(3), 189-201.

Subagio, D.P., Srinivasan, M., Lim, M. and Lim, T.T. (2010) Photocatalytic degradation of bisphenol-A by nitrogen-doped TiO_2 hollow sphere in a vis-LED photoreactor. Applied Catalysis B: Environmental 95(3-4), 414-422.

Subba, K.V., Lavédrine, B. and Boule, P. (2003) Influence of metallic species on TiO_2 for the photocatalytic degradation of dyes and dye intermediates. Journal of Photochemistry and Photobiology A: Chemistry 154(2-3), 189-193.

Subramanian, V., Wolf, E. and Kamat, P.V. (2001) Semiconductor-metal composite nanostructures. To what extent do metal nanoparticles improve the photocatalytic activity of TiO_2 films? Journal of Physical Chemistry B 105(46), 11439-11446.

Subramanian, V., Wolf, E.E. and Kamat, P.V. (2004) Catalysis with TiO_2/Gold Nanocomposites. Effect of Metal Particle Size on the Fermi Level Equilibration. Journal of the American Chemical Society 126(15), 4943-4950.

Sun, H., Ma, C., Yuan, B., Wang, T., Xu, Y., Xue, Q., Li, P. and Kong, Y. (2014a) Cardo polyimides/TiO_2 mixed matrix membranes: Synthesis, characterization, and gas separation property improvement. Separation and Purification Technology 122, 367-375.

Sun, L., An, T., Wan, S., Li, G., Bao, N., Hu, X., Fu, J. and Sheng, G. (2009) Effect of synthesis conditions on photocatalytic activities of nanoparticulate TiO_2 thin films. Separation and Purification Technology 68(1), 83-89.

Sun, X., Dyballa, M., Yan, J., Li, L., Guan, N. and Hunger, M. (2014b) Solid-state NMR investigation of the 16/17O isotope exchange of oxygen species in pure-anatase and mixed-phase TiO_2. Chemical Physics Letters 594, 34-40.

Syafei, A.D., Lin, C.F. and Wu, C.H. (2008) Removal of natural organic matter by ultrafiltration with TiO_2-coated membrane under UV irradiation. Journal of Colloid And Interface Science 323(1), 112-119.

Tanaka, K., Hisanaga, T., Riviera, A.P., Ollis, D.F. and Al-Ekabi, H. (1993a) Photocatalytic Purification and Treatment of Water and Air., Elsevier, Amsterdam, Netherlands.

Tanaka, K., Hisanaga, T., Riviera, A.P., Ollis, D.F. and Al-Ekabi, H. (eds) (1993b) Photocatalytic Purification and Treatment of Water and Air., Elsevier, Amsterdam.

Thiruvenkatachari, R., Vigneswaran, S. and Moon, I.S. (2008) A review on UV/TiO_2 photocatalytic oxidation process. Korean Journal of Chemical Engineering 25(1), 64-72.

Tsoukleris, D.S., Maggos, T., Vassilakos, C. and Falaras, P. (2007) Photocatalytic degradation of volatile organics on TiO_2 embedded glass spherules. Catalysis Today 129(1-2 SPEC. ISS.), 96-101.

Tsuru, T., Hino, T., Yoshioka, T. and Asaeda, M. (2001a) Permporometry characterization of microporous ceramic membranes. Journal of Membrane Science 186(2), 257-265.

Tsuru, T. (2001) Inorganic porous membranes for liquid phase separation. Separation and Purification Methods 30(2), 191-220.

Tsuru, T., Hironaka, D., Yoshioka, T. and Asaeda, M. (2001b) Titania membranes for liquid phase separation: Effect of surface charge on flux. Separation and Purification Technology 25(1-3), 307-314.

Turchi, C.S. and Ollis, D.F. (1989) Mixed reactant photocatalysis: Intermediates and mutual rate inhibition. Journal of Catalysis 119(2), 483-496.

USEPA (2009) National Secondary Drinking Water Regulations, United States Environmental Protection Agency, Washington DC, USA.

Valencia, S., Marín, J.M., Restrepo, G. and Frimmel, F.H. (2013) Application of excitation-emission fluorescence matrices and UV/Vis absorption to monitoring the photocatalytic degradation of commercial humic acid. Science of the Total Environment 442, 207-214.

Valencia, S., Marín, J.M., Restrepo, G. and Frimmel, F.H. (2014) Evaluation of natural organic matter changes from Lake Hohloh by three-dimensional excitation-emission matrix fluorescence spectroscopy during TiO_2/UV process. Water Research 51, 124-133.

Van Gestel, T., Vandecasteele, C., Buekenhoudt, A., Dotremont, C., Luyten, J., Leysen, R., Van der Bruggen, B. and Maes, G. (2002) Alumina and titania multilayer membranes for nanofiltration: preparation, characterization and chemical stability. Journal of Membrane Science 207(1), 73-89.

Van Gestel, T., Sebold, D., Hauler, F., Meulenberg, W.A. and Buchkremer, H.P. (2010) Potentialities of microporous membranes for H_2/CO_2 separation in future fossil fuel power plants: Evaluation of SiO_2, ZrO_2, Y_2O_3-ZrO_2 and TiO_2-ZrO_2 sol-gel membranes. Journal of Membrane Science.

Vankelecom, I.F.J., Smet, K.D., Gevers, L.E.M. and Jacobs, P.A. (2005) Nanofiltration - Principles and Applications. Schafer, A.I., Fane, A.G. and Waite, T.D. (eds), Elsevier, Oxford.

Vinod, V.P. and Anirudhan, T.S. (2002) Photocatalytic degradation for environmental applications - A review. Journal of Chemical Technology and Biotechnology 77(1), 102-116.

Vinodgopal, K., Wynkoop, D.E. and Kamat, P.V. (1996) Environmental photochemistry on semiconductor surfaces: Photosensitized degradation of a textile azo dye, Acid Orange 7, on TiO_2 particles using visible light. Environmental Science and Technology 30(5), 1660-1666.

Wang, J., Li, H., Li, H., Wang, H. and Cai, Q. (2013) Preparation, characterization, and photocatalytic activity of mesoporous TiO_2 thin films. Journal of Nanoscience and Nanotechnology 13(2), 1493-1497.

Wang, P., Yap, P.S. and Lim, T.T. (2011a) C-N-S tridoped TiO_2 for photocatalytic degradation of tetracycline under visible-light irradiation. Applied Catalysis A: General 399(1-2), 252-261.

Wang, X. and Lim, T.T. (2010) Solvothermal synthesis of C-N codoped TiO_2 and photocatalytic evaluation for bisphenol A degradation using a visible-light irradiated LED photoreactor. Applied Catalysis B: Environmental 100(1-2), 355-364.

Wang, X., Tang, Y., Leiw, M.Y. and Lim, T.T. (2011b) Solvothermal synthesis of Fe-C codoped TiO_2 nanoparticles for visible-light photocatalytic removal of emerging organic contaminants in water. Applied Catalysis A: General.

Wang, Y.H., Liu, X.Q. and Meng, G.Y. (2008) Preparation and properties of supported 100% titania ceramic membranes. Materials Research Bulletin 43(6), 1480-1491.

Wang, Y.L., Wan, Y.Z., Dong, X.H., Cheng, G.X., Tao, H.M. and Wen, T.Y. (1998) Preparation and characterization of antibacterial viscose-based activated carbon fiber supporting silver. Carbon 36(11), 1567-1571.

Wang, Z., Helmersson, U. and Käll, P.O. (2002) Optical properties of anatase TiO_2 thin films prepared by aqueous sol-gel process at low temperature. Thin Solid Films 405, 50-54.

Watanabe, T., Nakajima, A., Wang, R., Minabe, M., Koizumi, S., Fujishima, A. and Hashimoto, K. (1999) Photocatalytic activity and photoinduced hydrophilicity of titanium dioxide coated glass. Thin Solid Films 351(1-2), 260-263.

Weng, K.W. and Huang, Y.P. (2013) Preparation of TiO_2 thin films on glass surfaces with self-cleaning characteristics for solar concentrators. Surface and Coatings Technology 231, 201-204.

WHO (2011) Guidelines for Drinking-water Quality, Geneva, Switzerland.

Wu, D., You, H., Jin, D. and Li, X. (2011) Enhanced inactivation of Escherichia coli with Ag-coated TiO_2 thin film under UV-C irradiation. Journal of Photochemistry and Photobiology A: Chemistry 217(1), 177-183.

Wu, J.M. (2007) Photodegradation of rhodamine B in water assisted by titania nanorod thin films subjected to various thermal treatments. Environmental Science and Technology 41(5), 1723-1728.

Wu, Q.L. and Rankin, S.E. (2011) Tuning the wall thickness and pore orientation in mesoporous titania films prepared with low-temperature aging. Journal of Sol-Gel Science and Technology 60(1), 81-90.

Wu, T., Liu, G., Zhao, J., Hidaka, H. and Serpone, N. (1998) Photoassisted degradation of dye pollutants. V. Self-photosensitized oxidative transformation of Rhodamine B under visible light irradiation in aqueous TiO_2 dispersions. Journal of Physical Chemistry B 102(30), 5845-5851.

Xiao, Y., Fan, R., Zhang, L., Yue, J., Webster, R.D. and Lim, T.T. (2014) Photodegradation of iodinated trihalomethanes in aqueous solution by UV 254 irradiation. Water Research 49, 275-285.

Xie, J., Lü, X., Liu, J. and Shu, H. (2009) Brookite titania photocatalytic nanomaterials: Synthesis, properties, and applications. Pure and Applied Chemistry 81(12), 2407-2415.

Xu, H., Wu, F., Li, M. and Liang, Z. (2013) Application of response surface methodology for optimization of nano-TiO_2 preparation using modified sol-gel method. Journal of Sol-Gel Science and Technology 67(2), 394-405.

Xu, Y. and Langford, C.H. (2001) UV- or visible-light-induced degradation of X3B on TiO_2 nanoparticles: The influence of adsorption. Langmuir 17(3), 897-902.

Yao, F., Fu, G.D., Zhao, J., Kang, E.T. and Neoh, K.G. (2008) Antibacterial effect of surface-functionalized polypropylene hollow fiber membrane from surface-initiated atom transfer radical polymerization. Journal of Membrane Science 319(1-2), 149-157.

Yao, N. and Lun Yeung, K. (2011) Investigation of the performance of TiO_2 photocatalytic coatings. Chemical Engineering Journal 167(1), 13-21.

Yigit, Z. and Inan, H. (2009) A study of the photocatalytic oxidation of humic acid on anatase and mixed-phase anatase-rutile TiO_2 nanoparticles. Water, Air, and Soil Pollution: Focus 9(3), 237-243.

Yin, J., Yang, Y., Hu, Z. and Deng, B. (2013) Attachment of silver nanoparticles (AgNPs) onto thin-film composite (TFC) membranes through covalent bonding to reduce membrane biofouling. Journal of Membrane Science 441, 73-82.

Yin, S., Hasegawa, H., Maeda, D., Ishitsuka, M. and Sato, T. (2004) Synthesis of visible-light-active nanosize rutile titania photocatalyst by low temperature dissolution-reprecipitation process. Journal of Photochemistry and Photobiology A: Chemistry 163(1-2), 1-8.

Yoshitake, H., Sugihara, T. and Tatsumi, T. (2002) Preparation of wormhole-like mesoporous TiO_2 with an extremely large surface area and stabilization of its surface by chemical vapor deposition. Chemistry of Materials 14(3), 1023-1029.

Yu, B., Leung, K.M., Guo, Q., Lau, W.M. and Yang, J. (2011) Synthesis of Ag-TiO_2 composite nano thin film for antimicrobial application. Nanotechnology 22(11).

Yu, J., Xiong, J., Cheng, B. and Liu, S. (2005) Fabrication and characterization of Ag-TiO_2 multiphase nanocomposite thin films with enhanced photocatalytic activity. Applied Catalysis B: Environmental 60(3-4), 211-221.

Yu, J.G., Yu, H.G., Cheng, B., Zhao, X.J., Yu, J.C. and Ho, W.K. (2003) The Effect of Calcination Temperature on the Surface Microstructure and Photocatalytic Activity of TiO_2 Thin Films Prepared by Liquid Phase Deposition. Journal of Physical Chemistry B 107(50), 13871-13879.

Yu, L.Y., Shen, H.M. and Xu, Z.L. (2009) PVDF-TiO_2 composite hollow fiber ultrafiltration membranes prepared by TiO_2 sol-gel method and blending method. Journal of Applied Polymer Science 113(3), 1763-1772.

Yuan, Y., Li, H., Luo, M., Qin, S., Luo, W., Li, L. and Yan, H. (2014) TiO_2-Mediated Photodegradation of Aqueous Trinitrophenol Irradiated by an Artificial Light Source. Water, Air and Soil Pollution 225(3), 1-9.

Zakaria, M.B., Suzuki, N., Torad, N.L., Matsuura, M., Maekawa, K., Tanabe, H. and Yamauchi, Y. (2013) Preparation of mesoporous titania thin films with well-crystallized frameworks by using thermally stable triblock copolymers. European Journal of Inorganic Chemistry (13), 2330-2335.

Zaspalis, V.T., Van Praag, W., Keizer, K., Ross, J.R.H. and Burggraaf, A.J. (1992) Synthesis and characterization of primary alumina, titania and binary membranes. Journal of Materials Science 27(4), 1023-1035.

Zhan, W.T., Ni, H.W., Chen, R.S., Wang, Z.Y., Li, Y.W. and Li, J.H. (2013) One-step hydrothermal preparation of TiO_2/WO_3 nanocomposite films on anodized stainless steel for photocatalytic degradation of organic pollutants. Thin Solid Films 548, 299-305.

Zhang, H., Quan, X., Chen, S., Zhao, H. and Zhao, Y. (2006) Fabrication of photocatalytic membrane and evaluation its efficiency in removal of organic pollutants from water. Separation and Purification Technology 50(2), 147-155.

Zhang, J., Wang, Z.-L., Liu, J., Chen, S. and Liu, G.-Y. (2003a) Self-Assembled nanostructure, Kluwer Cademic/Plenum Publishers, New York.

Zhang, L., Zhu, Y., He, Y., Li, W. and Sun, H. (2003b) Preparation and performances of mesoporous TiO_2 film photocatalyst supported on stainless steel. Applied Catalysis B: Environmental 40(4), 287-292.

Zhang, R., Tu, B. and Zhao, D. (2010) Synthesis of highly stable and crystalline mesoporous anatase by using a simple surfactant sulfuric acid carbonization method. Chemistry - A European Journal 16(33), 9977-9981.

Zhang, S., Fu, R., Dingcai, W., Xu, W., Ye, Q. and Chen, Z. (2004) Preparation and characterization of antibacterial silver-dispersed activated carbon aerogels. Carbon 42(15), 3209-3216.

Zhang, Z., Wang, C.C., Zakaria, R. and Ying, J.Y. (1998) Role of particle size in nanocrystalline TiOi-based photocatalysts. Journal of Physical Chemistry B 102(52), 10871-10878.

Zhao, B. and Chen, Y.W. (2011) Ag/TiO_2 sol prepared by a solgel method and its photocatalytic activity. Journal of Physics and Chemistry of Solids 72(11), 1312-1318.

Zhao, L., Yu, Y., Song, L., Ruan, M., Hu, X. and Larbot, A. (2004) Preparation of mesoporous titania film using nonionic triblock copolymer as surfactant template. Applied Catalysis A: General 263(2), 171-177.

Zhao, L., Yu, Y., Song, L., Hu, X. and Larbot, A. (2005) Synthesis and characterization of nanostructured titania film for photocatalysis. Applied Surface Science 239(3-4), 285-291.

Zhao, Y., Zhai, J., Tan, S., Wang, L., Jiang, L. and Zhu, D. (2006) TiO_2 micro/nano-composite structured electrodes for quasi-solid-state dye-sensitized solar cells. Nanotechnology 17(9), 2090-2097.

Zhao, Y., Zhang, X., Zhai, J., He, J., Jiang, L., Liu, Z., Nishimoto, S., Murakami, T., Fujishima, A. and Zhu, D. (2008) Enhanced photocatalytic activity of hierarchically micro-/nano-porous TiO_2 films. Applied Catalysis B: Environmental 83(1-2), 24-29.

Zhong, Z., Ang, T.P., Luo, J., Gan, H.C. and Gedanken, A. (2005) Synthesis of one-dimensional and porous TiO_2 nanostructures by controlled hydrolysis of titanium alkoxide via coupling with an esterification reaction. Chemistry of Materials 17(26), 6814-6818.

Znamirowski, Z., Nitsch, K. and Pawłowski, L. (2013) The electric charge transport in titania-alumina composite cold cathodes made using atmospheric plasma spraying and laser engraving. Surface and Coatings Technology 220, 271-275.

Zong, W., Sun, F. and Sun, X. (2013) Evaluation on the generative mechanism and biological toxicity of microcystin-LR disinfection by-products formed by chlorination. Journal of Hazardous Materials 252-253, 293-299.

Zou, J.J., He, H., Cui, L. and Du, H.Y. (2007) Highly efficient Pt / TiO_2 photocatalyst for hydrogen generation prepared by a cold plasma method. International Journal of Hydrogen Energy 32(12), 1762-1770.